



Article

Finite Element Analysis of Microwave Tumor Ablation Based on Open-Source Software Components

Nikola Bošković , Marija Radmilović-Radjenović *  and Branislav Radjenović

Institute of Physics, University of Belgrade, Pregrevica 118, 11080 Belgrade, Serbia; nikolab@ipb.ac.rs (N.B.)

* Correspondence: marija@ipb.ac.rs

Abstract: Microwave ablation is a procedure for treating various types of cancers during which a small needle-like probe is inserted inside the tumor, which delivers microwave energy, causes tissue heating, and effectively produces necrosis of the tumor tissue. Mathematical models of microwave ablation involve the modeling of multiple physical phenomena that occur during the procedure, including electromagnetic wave propagation, heat transfer, and tissue damage. In this study, a complete model of a microwave ablation procedure based on open-source software components is presented. First, the comprehensive procedure of mesh creation for the complete geometric arrangement of the microwave ablation, including a multi-slot coaxial antenna, a real liver tumor taken from the database, and the surrounding liver tissue, is described. It is demonstrated that utilizing smart meshing procedures significantly reduces the usage of computational resources and simulation time. An accurate custom explicit Euler time loop was designed to obtain temperature values and estimate tissue necrosis across the computational domain during the time of microwave ablation. The simulation results obtained by solving the electromagnetic field using the finite element method in the frequency domain are presented and analyzed. The simulation was performed for a microwave frequency of 2.45 GHz, and the volumetric distribution of temperature and estimation of cell damage over 600 s are presented.



Citation: Bošković, N.; Radmilović-Radjenović, M.; Radjenović, B. Finite Element Analysis of Microwave Tumor Ablation Based on Open-Source Software Components. *Mathematics* **2023**, *11*, 2654. <https://doi.org/10.3390/math11122654>

Academic Editors: Yuri Vassilevski, Vitaly Volpert and Cristina I. Muresan

Received: 30 March 2023

Revised: 26 May 2023

Accepted: 1 June 2023

Published: 10 June 2023



Copyright: © 2023 by the authors. Licensee MDPI, Basel, Switzerland. This article is an open access article distributed under the terms and conditions of the Creative Commons Attribution (CC BY) license (<https://creativecommons.org/licenses/by/4.0/>).

Keywords: computational physics; microwave ablation; necrotic tissue; open-source software

MSC: 92-10

1. Introduction

Microwave ablation (MWA) has been shown to be effective in treating certain types of cancer, including liver, lung, and kidney tumors [1–4]. It is a minimally invasive medical procedure with a short recovery time, making it a viable alternative to traditional surgical methods [5–7]. During MWA, a small needle-like probe is inserted into the tumor, and microwave energy is delivered to heat and destroy cancer cells [8,9]. Multi-slot coaxial antennas are commonly used for the delivery of microwave radiation because of their simplicity, low complexity, and ability to generate highly spherical ablation zones [10,11]. To improve the safety and efficacy of the procedure, modeling MWA is an important tool for predicting the size and shape of the ablation zone and optimizing treatment for individual patients [12,13].

Modeling MWA as a multiphysics problem involves modeling multiple physical phenomena that occur during the procedure, including electromagnetic wave propagation, heat transfer, and tissue damage [14,15]. These phenomena are interrelated, and modeling them together can provide a more accurate and comprehensive understanding of tissue behavior during the procedure [16,17]. The first stage encompasses the accurate modeling of the microwave radiation of the antenna. The second stage involves modeling the interaction between tissue and antenna radiation and heat transfer under the influence of blood flow effects. The third stage requires an estimation of cell death due to heating. While

the material parameters of the antenna components can generally be observed as constant during ablation, the material properties of the healthy tissue and tumor are temperature (time) dependent [18,19]. Tumor shape is patient-specific, so a general approach using a spherical or static tumor model is inaccurate [20]. The water concentration in the tissue changes with increasing temperature, effectively altering the physical properties of the tissue [21,22].

From a numerical modeling perspective, modeling MWA represents a closed boundary problem with the required results in a narrow frequency bandwidth [23]. The three-dimensional (3D) finite element method (FEM) is an excellent choice for solving all the required electromagnetic and heat transfer equations, as implemented in widely used software such as the COMSOL Multiphysics simulation package [24,25]. Ideal software solutions for MWA practitioners should enable users to input tumor scan data obtained from the computerized tomography (CT) scan of a patient [26], select the probe model with the antenna from the available library, and set the input power and geometric location of the probe inside the tumor. Commercially available packages can be used to develop such a solution, but software based on open-source code would be far more beneficial [27–30], since commercially based packages typically have high price and usage limitations.

Physical processes can be described using partial differential equations (PDE). FEM is a numerical method in which the PDE is numerically converted into a set of linear algebraic equations to obtain approximate solutions for a specific physical problem [31]. In FEM, the geometry is divided into many small subdomains, known as finite elements, on which the approximation of the unknowns can be performed using simple functions. The division of the geometry into finite elements is called meshing [32]. The two basic types of FEM meshing are unstructured and structured meshing. Mixed meshing, with a combination of these two types of meshing with the same geometry, is also possible. Solving the PDE using the finite element method requires computational resources, which are directly governed by the number of elements and quality of the finite element mesh.

In this paper, we present a complete model of the MWA procedure based on open-source software components, which was one of the most important goals. We shall describe the comprehensive procedure of mesh creation of the complete MWA geometric arrangement, including a multi-slot coaxial antenna, a real liver tumor taken from the database [26], and surrounding liver tissue. We used a smart meshing procedure to significantly reduce the use of computational resources and simulation time. For geometry and mesh creation, we used Gmsh, an open-source package that implements multiple state-of-the-art solutions for automatic mesh creation [33–43]. Gmsh can create complex geometries using the OpenCASCADE computer-aided design (CAD) engine [44]. The mesh created with Gmsh can be used with many FEM solvers, but the most suitable is a general FEM solver called GetDP [45,46]. It is free and developed by the same team that works on Gmsh, and it is a compiled bundle with Gmsh in the Open Numerical Engineering LABoratory (ONELAB), an open-source, lightweight interface for finite element software [47]. We designed an accurate custom explicit Euler time loop to obtain temperature values and estimate tissue necrosis across the computational domain during MWA. Finally, the simulation results obtained by solving the electromagnetic field with FEM in the frequency domain will be presented and analyzed.

2. Methodology

The proposed solution consists of implementing the physics of the MWA procedure, generating geometry, and meshing in a form suitable for FEM simulation. We show these methods in this section.

2.1. Physics of the MWA Procedure

In MWA, the electromagnetic field and tissue heating are coupled. To model MWA, we first need to calculate the electromagnetic field distribution originating from the antenna and spread across the computational domain. Human tissues have approximately equal

magnetic properties, and the MWA process is performed through electric field interaction; hence, we need to calculate only the electric field distribution. The calculated field was then used as an external heat source in the bio-heat equation [48]. Tissue heating is a slow process that can occur within a few seconds. In comparison, electric field propagation is extremely fast and occurs in nanoseconds; therefore, we calculated the electric field in the frequency domain and used the results to calculate the temperature distribution in the time domain. Subsequently, we estimated the fraction of necrotic tissue over time during MWA.

2.1.1. EM Field Calculations

The MWA system electromagnetic field generated by the antenna is usually described by the well-known frequency domain wave equation for electric field, derived from Maxwell's equations [31], given as:

$$\nabla^2 \vec{E} - \mu_r k_0^2 \left(\epsilon_r - \frac{j\sigma}{\omega \epsilon_0} \right) \vec{E} = 0, \quad (1)$$

where μ_r is the relative permeability (its value is 1 for a non-magnetic environment), $\omega = 2\pi f$ is the angular frequency, \vec{E} is the electric field vector generated by the antenna, σ is the electric conductivity, ϵ_0 is the permittivity of vacuum, and k_0 is the vacuum propagation constant.

Propagation of the electric field in coaxial cable in cylindrical coordinate system can be expressed as:

$$\vec{E} = \vec{e}_r \frac{C}{r} e^{j(\omega t - kz)}, \quad (2)$$

where z is the direction of propagation, \vec{e}_r is the radial vector, r is the radius, and C represents a constant that can be expressed as:

$$C = \sqrt{\frac{Z P_{av}}{\pi \ln \frac{r_0}{r_i}}}, \quad (3)$$

$$Z = \frac{1}{2\pi} \sqrt{\frac{\mu}{\epsilon}} \ln \frac{r_0}{r_i}, \quad (4)$$

where P_{av} is the time-averaged power flow in the cable, Z is the impedance of the coaxial cable, r_0 and r_i are the outer and inner radii of the dielectric, respectively; μ is the permeability and ϵ is the permittivity.

The boundary condition on the conductor surface is given by $\vec{n} \times \vec{E} = 0$. This represents the PEC boundary condition; the tangential component of the electric field is zero, only the normal component exists, and it is perfectly reflected from the boundary. The electric field does not penetrate the volume within the PEC boundary; hence, such a volume is of no interest in electric-field calculations.

The SAR represents the amount of radiation absorbed by a tissue [25]. It can identify which part of the tissue will be the most affected by radiation and how the electric field propagation interacts with the tissue. It can be determined from the electric field, electric conductivity σ , and density of the observed domain ρ , as follows:

$$SAR = \frac{\sigma}{2\rho} \left| \vec{E} \right|^2. \quad (5)$$

The scattering parameter S_{11} is one of the fundamental parameters of antennas. This parameter represents the extent to which the antenna matches the power source. A value below -10 dB at the working frequency was considered good. A high S_{11} value is dangerous in MWA for both the equipment and patients. The power source can be damaged, and antenna conductors can produce very high temperatures, essentially burning tissue in close

proximity, whereas radiation can be very poor. It can be calculated by solving the surface integral at the port boundary as follows [25]:

$$S_{11} = \frac{\iint_{PORT} \left(\vec{E} - \vec{E}_{PORT} \right) \cdot \vec{E}_{PORT}^* dS}{\iint_{PORT} \vec{E}_{PORT} \cdot \vec{E}_{PORT}^* dS}, \quad (6)$$

where \vec{E} is the electric field vector calculated in the observed domain, \vec{E}_{PORT} is the electric field vector defined at the port, and its conjugate is \vec{E}_{PORT}^* [25].

The wave Equation (1) is in its strong form and generally has no closed-form solution. Such a formulation cannot be used in FEM approach [31], and it needs to be written in so-called weak form, where the weak solution satisfies the integral equation when “tested” with a well-defined set of test functions:

$$\iiint_V \left[(\nabla \times W) \cdot \frac{1}{\mu_r} (\nabla \times \vec{E}) - W \cdot k_0^2 \left(\epsilon_r - \frac{j\sigma}{\omega\epsilon_0} \right) \vec{E} \right] dV - \iint_S W \cdot \left[\vec{n} \times \left(\frac{1}{\mu_r} \nabla \times \vec{E} \right) \right] dS = 0, \quad (7)$$

where W represents the weighting test function, V is the volume in which the electric field calculation is performed, S is the surface boundary of V , and \vec{n} is the unit normal vector. Here, S represents the combination of the port boundary surface and absorbing boundary surface (ABS). Here, $\mu_r = 1$ and the second part of (7) can be written as an absorbing boundary condition [31]:

$$\iint_{ABS} W \cdot \left[\vec{n} \times \left(\nabla \times \vec{E} \right) \right] dS + \iint_{ABS} W \cdot \left[jk_0 \sqrt{\epsilon_r} \cdot \left[\vec{n} \times \left(\vec{n} \times \vec{E} \right) \right] \right] dS = 0. \quad (8)$$

Similarly, the port boundary condition defined at the port surface can be written as [31]:

$$\iint_{PORT} W \cdot \left[\vec{n} \times \left(\nabla \times \vec{E} \right) \right] dS + \iint_{PORT} W \cdot \left[jk_0 \sqrt{\epsilon_r} \cdot \left[\vec{n} \times \left(\vec{n} \times \vec{E} \right) \right] \right] dS + \iint_{PORT} W \cdot \left[2jk_0 \sqrt{\epsilon_r} \vec{E}_{PORT} \right] dS = 0. \quad (9)$$

By solving the previous equations, we can obtain a FEM approximation of the electric field vector in the defined volume.

2.1.2. Heat Transfer Calculation

The transfer of the heat generated by the electromagnetic field in MWA is described by Pennes’s bio-heat equation [48]:

$$\rho c \frac{\partial T}{\partial t} = \nabla \cdot (k \nabla T) + \rho_b \omega_b c_b (T_b - T) + Q_{ext} + Q_{met}, \quad (10)$$

where t is the time, ρ , c , and T are the density, specific heat capacity, and temperature of the tissue, respectively. ρ_b , c_b , and ω_b are the density, specific heat capacity, and perfusion rate of the blood, $T_b = 37^\circ\text{C}$ denotes the arterial blood temperature, Q_{met} is the metabolic heat, and Q_{ext} represents the external heat source. Q_{ext} represents the heat generated from MWA, and considering that $Q_{ext} \gg Q_{met}$, in practical MWA use cases, Q_{met} can be neglected. The coupling with an electric field is given as:

$$Q_{ext} = \frac{\sigma \left| \vec{E} \right|^2}{2}, \quad (11)$$

where σ is electrical conductivity of the tissue. The dependence of the thermal conductivity of the tissue k on the temperature is given by the following relation [10,14]:

$$k(T) = k_0 + \Delta k |T - T_0|, \quad (12)$$

where k_0 is the thermal conductivity of the tissue measured at temperature T_0 and $\Delta k = 0.001161 \text{ (K}^{-1}\text{)}$ characterizes the change in k as a function of temperature. The blood perfusion rate is assumed to stop when coagulation occurs above 60°C and is expressed as [10]:

$$\omega_b(T) = \begin{cases} 0.000021 \cdot T + 0.0035, & T \leq 60^\circ\text{C} \\ 0, & T > 60^\circ\text{C} \end{cases}. \quad (13)$$

A heterogeneous model of blood perfusion [49,50] based on clinical measurements [51,52] can give a more accurate MWA calculation. Liver tissue contains a high concentration of water (approximately 78%). Owing to the rise in temperature during MWA, a change in water content occurs and can be expressed as [53]:

$$W(T) = \begin{cases} 0.778 \cdot \left(1 - e^{\frac{T-106}{3.42}}\right), & 70^\circ\text{C} \leq T \leq 100^\circ\text{C} \\ 7.053 - 0.064096 \cdot T, & 100^\circ\text{C} \leq T \leq 104^\circ\text{C} \\ 0.778 \cdot e^{\frac{T-80}{34.37}}, & T > 104^\circ\text{C} \end{cases}. \quad (14)$$

Above 100°C , the evaporation of water content may decrease concentration of the water to less than 20%, which will cause a significant change in all tissue parameters. Hence, the specific heat capacity used in (10) should be replaced with an effective value [54]:

$$c' = c - \frac{\alpha}{\rho} \frac{\partial W}{\partial T}, \quad (15)$$

where $\alpha = 2,260,000 \text{ (J/kg)}$ is the water latent heat constant, ρ is the water density, and c is the specific heat of the tissue.

Based on Equations (15) and (12), the specific heat capacity and thermal conductivity in relation to the temperature change are calculated and shown in Figure 1a. Values of the specific heat capacity and thermal conductivity in tumors are around 10% higher than the ones in the liver tissue. This is beneficial for the processes of MWA because, under the same conditions, tumor tissue will heat faster than liver tissue. Thermal conductivity is a simple linear function of the temperature. Based on Equation (13), the blood perfusion rate in relation to the temperature is given in Figure 1b.

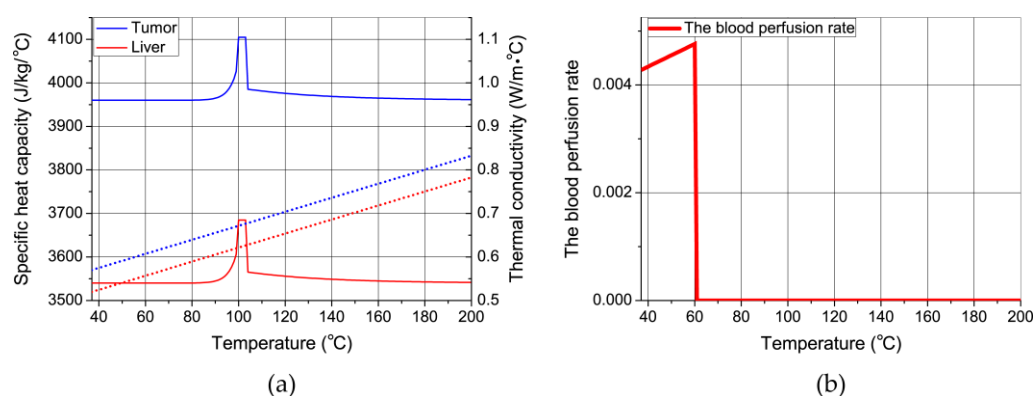


Figure 1. (a) Change in the specific heat capacity (full line) and thermal conductivity (dots) with the temperature. (b) Change in the blood perfusion rate with the temperature.

Specific heat capacity below 70°C is constant; above 70°C due to change in water content, there is a rise with a maximum value between 100°C and 104°C , and above 104°C , specific heat capacity becomes stable again.

The dielectric constant of the tissue ε_r and electrical conductivity σ can be expressed as [14]:

$$\varepsilon_r = a_1 \cdot \left(1 - \frac{1}{1 + e^{(a_2 - a_3 T)}} \right), \quad (16)$$

$$\sigma = b_1 \cdot \left(1 - \frac{1}{1 + e^{(b_2 - b_3 T)}} \right). \quad (17)$$

The values of the coefficients in Equations (16) and (17) are given in Table 1.

Table 1. Values of the coefficients used in the calculation of ε_r and σ for the liver tissue and tumor.

Coefficients	Tissue	
	Liver	Tumor
a_1	44.3	54.8
a_2	5.223	5.223
a_3	0.0524	0.0524
b_1	1.69	2
b_2	6.583	6.583
b_3	0.0598	0.0598

Tissue damage is a function of temperature and time, and can be approximated using the Arrhenius equation [55,56]:

$$\frac{\partial \Omega}{\partial t} = A e^{\left(-\frac{\Delta E}{RT}\right)}, \quad (18)$$

where $A = 7.39 \times 10^{39}$ 1/s and $\Delta E = 2.577 \times 10^5$ J/mol represent the frequency factor and activation energy for the irreversible damage reaction, respectively; T is the temperature calculated at each point of the model region, and R is the universal gas constant. By solving differential Equation (18), the fraction of necrotic tissue can be calculated as follows [55,56]:

$$\theta_d = 1 - e^{-\Omega}. \quad (19)$$

From Equation (19), a value of 1 represents total tissue damage, and a value of 0 indicates that there is no damage. The values of the thermo-physiological parameters used in this work are given in Table 2.

Table 2. Thermo-physiological parameters used in this work.

Parameter	Tissue		
	Liver	Tumor	Blood
Density, [kg/m ³]	1079	1040	1060
Specific heat, [J/kg/°C]	3540	3960	3600
Thermal conductivity, [W/m·°C]	0.52	0.57	0.5

2.2. Geometry and Mesh Generation

Gmsh comprises two modules for geometry creation. The built-in module requires model creation from lower to higher dimensions (points < curves < surfaces < volumes). However, for complex structures, this type of modeling can quickly get out of control. The OpenCASCADE module supports work with solids and has the same capabilities as any commercially available CAD design package. Three-dimensional models can be directly composed of defined volumes, and the most important factor is complete Boolean support, which means that multiple solid models can be united and intersected, effectively creating new volumes. Geometry can be manipulated in any way: translated, rotated, copied, scaled, and so on. The OpenCASCADE module supports the import, export, and processing of the STEP and IGES file formats, which are commonly used 3D geometry formats, and the BREP file format, which is native to OpenCASCADE.

The Gmsh mesh module is extremely versatile and powerful. Gmsh can operate with most standard FEM shapes, such as lines, triangles, quadrangles, tetrahedrons, hexahedrons, prisms, and pyramids [32,33], as shown in Figure 2. The standard Gmsh unstructured mesh algorithm comprises planar (2D) elements that are generally meshed with triangles (some structures can be recombined into quadrangles), whereas 3D elements are meshed with tetrahedrons or tetrahedrons and pyramids when quadrangles are present [43].

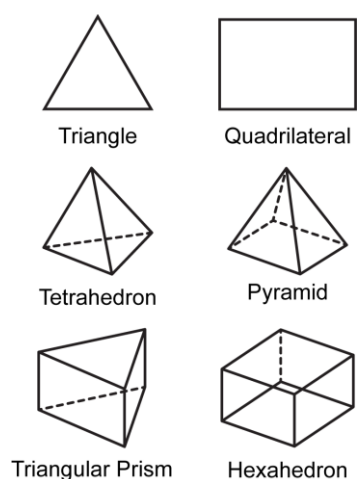


Figure 2. Standard FEM shapes: two-dimensional (triangle and quadrilateral) and three-dimensional (tetrahedron, pyramid, triangular prism, and hexahedron).

Global control of the mesh size can be achieved by specifying the minimal and maximal cell sizes that can be specified at any point, curve, volume, etc. The mesh can be interpolated linearly at the geometric edge or with geometric progression. The mesh size can be adapted to the geometric curvature. The quality of each created element is determined, and appropriate adaptive and refinement algorithms can be applied. An equilateral triangle has a quality of 1, and a degenerated shape with a zero area has a quality of 0. Similarly, for a tetrahedron, the maximum quality is obtained when the tetrahedron is constructed from equilateral triangles, whereas zero quality occurs when the element is shattered and has zero volume.

The major advantage of unstructured meshing is that it can be applied to any shape. However, for good quality meshing, multiple refinement steps are often necessary, with a massive increase in the number of elements, computing time, and resource demands, and generally lower accuracy in FEM simulations in comparison with structured meshing. Hexahedrons with small aspect ratios are ideal mesh elements in FEM and should be used whenever possible. Some geometrically highly irregular structures, such as tumors, are difficult to represent using this algorithm, whereas probes with antennas can be represented using structured meshing. There are numerous advantages of structured meshing in FEM simulations. The number of elements in the same structure with structured meshing was several times smaller. With accurately defined structured meshing, mesh quality is superior, mesh generation is very quick because the best quality mesh is already defined, and there is no need for multiple refinement steps.

In MWA, the liver represents the computational domain where the process of MWA takes place, as seen in Figure 3a. In MWA, we are interested in simulating the processes around the tumor, which is usually much smaller than the entire liver volume; hence, the computational domain does not have to consider the whole liver, and it can be a part of the liver around the tumor in the form of a regular geometrical shape. The most commonly used shape is a cylinder. However, for structured meshing, the hexahedron domain is a better choice because of the possibility of using mostly identical hexahedrons as finite elements across the entire domain. Two models were developed in this study. One had

an unstructured tetrahedral mesh and a cylindrical computational domain with a radius of 30 mm and height of 90 mm, and the other had a mixed meshing and hexahedral computational domain with dimensions of 60 mm \times 60 mm \times 90 mm.

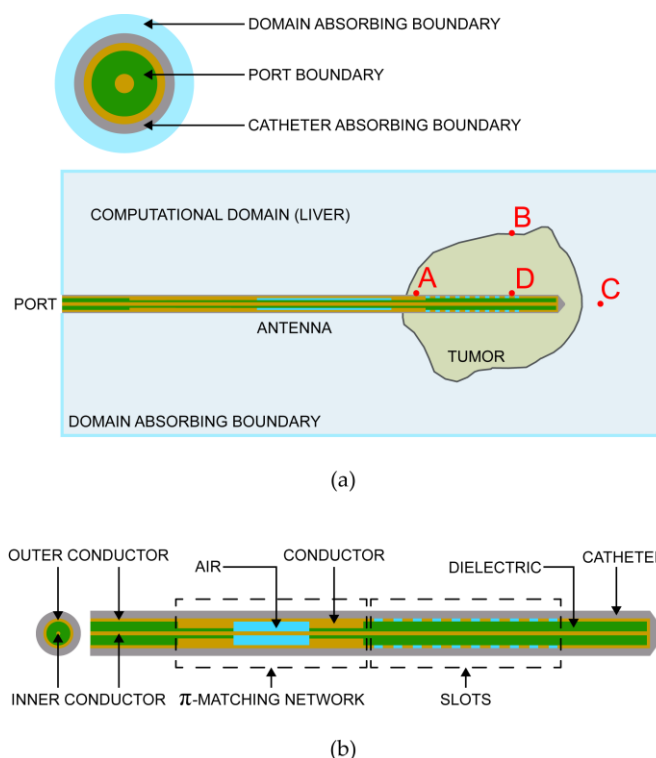


Figure 3. (a) Geometry of the problem, points A, B, C, and D are used as a reference in the simulation algorithm, and (b) probe with the antenna geometry.

Figure 3b shows the geometry of the probe used for MWA [10,13]. The antenna was a coaxial slot antenna, where the inner conductor passed through the center of the geometry and was connected to the outer conductor at the end of the antenna. Radiation occurred through 10 slots in the outer conductor. A matching network exists in front of the radiating slots. The entire antenna is placed inside the catheter. There are four different material regions in the probe structure: the metal conductor, the dielectric in the antenna between conductors, air, and the dielectric material of the catheter (Table 3). The basic geometry of the antenna was a long cylindrical volume. From electromagnetic analysis through the FEM, the value of the electric field is necessary for heat transfer estimation. From electromagnetic theory, we can assume that there is no field propagation inside the conductor volume, and that the faces of the conductor volume behave as field boundaries. Field propagation occurs only through dielectric materials. Based on this, there is no need for volume meshing of the conductor part; therefore, the basic geometry for the meshing of the antenna consists of multiple concentric hollow cylinders.

Table 3. Materials used in the probe construction.

Material	Dielectric Constant
Air	1
Dielectric	2.05
Catheter	2.1

An arbitrary hollow cylinder is shown in Figure 4. Using the OpenCASCADE module, the geometry can be created with a few commands, and the cylinder can be defined by specifying its position in space, radius, and height. All other geometric components of lower

orders, such as surfaces, curves, and nodes, were automatically created. All elements of the same order have unique tags in Gmsh that are necessary for any geometrical manipulation.

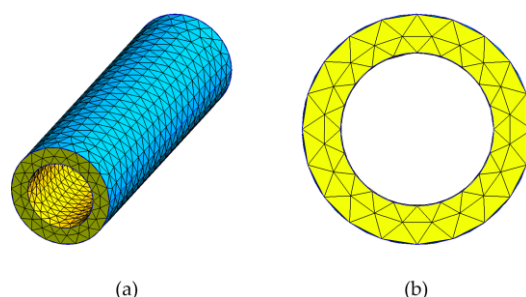


Figure 4. Unstructured meshing of a cylinder with dimensions of 1 mm, 1.5 mm, and 10 mm for the inner radius, outer radius, and length, respectively. (a) Volume view and (b) planar projection view.

The construction of the unstructured mesh was simple. It can be seen that the mesh from the curvature is 20, which means that the circular cross-section is represented by 20 segments, which is sufficient for an accurate circle geometry representation, and the maximal size of the cells is specified at 2 mm. The number of tetrahedrons in the volume per quality factor is listed in Table 4. After the two mesh optimization steps, the mesh became suitable for the simulation. In the second iteration, all elements with a quality lower than 0.3 are eliminated, and the average mesh quality is now 0.76, which is very good. The mesh contained 3969 tetrahedrons and 2704 triangles.

Table 4. The number of elements in a specific quality factor range in two mesh iterations shown in Figure 4.

Quality Factor Range	Number of Elements per Iteration	
	First	Second
0.0–0.1	8	0
0.1–0.2	15	0
0.2–0.3	4	0
0.3–0.4	13	13
0.4–0.5	30	28
0.5–0.6	92	87
0.6–0.7	1235	1232
0.7–0.8	1493	1502
0.8–0.9	327	328
0.9–1.0	779	779

Structured meshing cannot be applied directly to arbitrary geometries. The basic condition in Gmsh is that the volume must have five or six faces. Neighboring volumes must follow a defined grid pattern. Geometric volumes must be sliced or adjusted to conform to the structured meshing. In this case, the geometry has four faces. The simplest way to conform this geometry to structured meshing is to slice the geometry through the symmetry plane to form two half-ring volumes, as shown in Figure 5a. Instead of a full cylinder, two symmetrical half-cylinders were created, each with six faces, as displayed in Figure 5b.

The number of segments per curve has to be specified for each plane. The desired meshing parameters were the same as before, with 20 segments for circular representation and a maximal cell size of 2 mm. There are no automatic meshing algorithms for structured meshing; however, the process of specifying the number of segments per curve can be easily automated with simple scripting. There are various options for dividing the physical length of the residual curves by 2 mm; therefore, the number of segments can be obtained. The curves that define the half circumference should be divided into 10 segments. We obtained a meshing composed of 250 quadrangles and 100 identical hexahedrons. The base

of the hexahedron had a very small deviation from the rectangle, and the structure was elongated in a single direction. The mesh quality of this element was close to perfect.

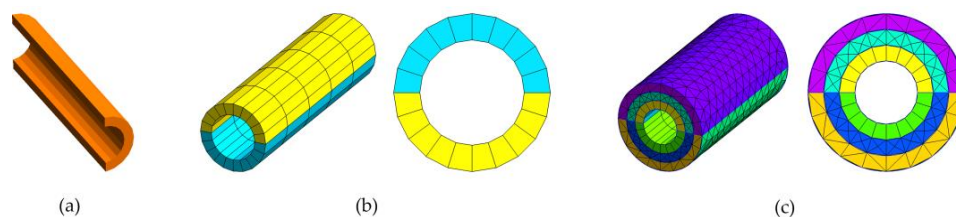


Figure 5. (a) Half-ring volume, (b) two half-ring volumes with structured meshing, and (c) volume with a combination of structured meshing, unstructured meshing, and mixed meshing.

The difference in the number of finite elements for these two types of meshing is large. In unstructured meshing, there are 11 times more planar elements and 40 times more volume elements. All volume elements in the structured elements are identical, which is highly desirable, and the mesh quality is superior, resulting in a shorter simulation time, smaller resource usage, and higher accuracy. In this simple example, it is clear that there is a significant benefit to using structured meshing.

In Gmsh, it is possible to combine both structured and unstructured meshing with a transitional layer of pyramids between hexahedrons and tetrahedrons. In this model, the tumor represents an irregular unpredictable geometry, which is meshed with unstructured meshing, and the catheter volume layer is between the antenna and the tumor and can have a layer of pyramids. Figure 5c shows an example of a hollow cylinder comprising an internal ring meshed with structured meshing (hexahedrons) and an outer ring meshed with unstructured meshing. The middle ring contains pyramids, which are transitional layers between two types of meshing.

The geometry of the probe can be simply constructed as a group of solid objects directly in Gmsh based on the antenna dimensions. The geometry is clearly defined and does not change during the analysis. Tumor geometry can be obtained from medical scans in the STL format, which represents an object in the form of a shell made from multiple triangles [17,32]. STL geometry represents the surface meshing of an object with triangles. The STL file does not represent solid geometry; therefore, it cannot be used with OpenCASCADE. The built-in module can work with the STL format and create a surface and volume geometry based on it, after which meshing can be performed. The geometry of STL files typically has a very high resolution and can consist of a very large number of triangles. A tumor is a live structure with blood circulation and other metabolic processes, and its geometry can undergo slow and fast changes over time. For the purpose of accurate simulation of MWA, extremely high resolution is not required as long as the tumor volume boundaries are accurately represented.

In Gmsh, it is possible to use STL remeshing, where the surface geometry can be reconstructed in a much smaller number of triangles with higher mesh quality. In Figure 6a, an STL file of the live liver tumor with the dimensions of 21.9 mm × 22.7 mm × 25.4 mm is shown. The original model contained 3000 triangles. Remeshing can be performed, depending on the required resolution. In Figure 6b, one version of remeshing is shown, with 1122 triangles. With all the details, this model provides a good representation of the tumor for adequate analysis. In Figure 6c, the more aggressive remeshing model has 336 triangles, and some details are lost. The number of smaller triangles is decreased; hence, the resolution is lower, but the basic geometry is still present.

The built-in Gmsh module can create the geometry and mesh for the STL file, but it does not support Boolean operations. The geometry of the probe with the antenna is inserted into the tumor, and the tumor is inside the liver tissue, so new geometries must be created based on the interaction of the probe, tumor, and liver tissue. Therefore, it was necessary to use the OpenCASCADE module. For this, STL must be converted to a format that is suitable for the OpenCASCADE module, such as the BREP file format. In Gmsh,

there is no direct way for STL conversion, but it can be achieved through external scripting, for example, with the Python API. The BREP file of the tumor can then be imported and used to create a solid volume that can be used in the OpenCASCADE module as any other solid geometry.

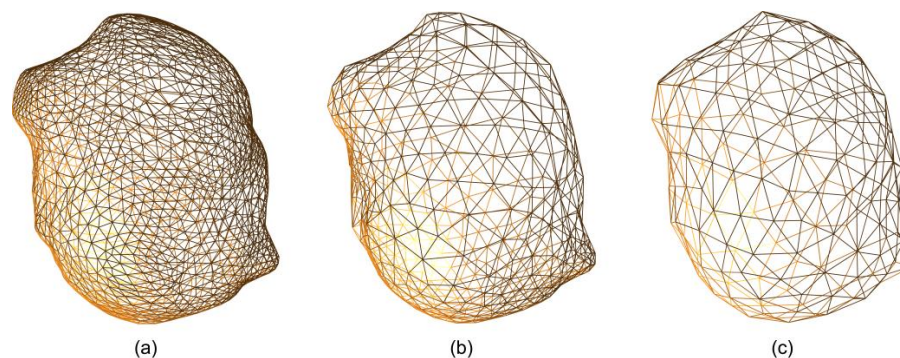


Figure 6. (a) STL representation of the tumor: (a) original with 3000 triangles, (b) remeshed with 1122 triangles, and (c) remeshed with 336 triangles.

A very important operation for simulation preparation is grouping finite element volumes and surfaces based on whether they belong to a particular material or have the same boundary conditions. Each material listed in Table 3 belonged to a unique physical zone. In addition, there are tumor and liver volumes; hence, there are five physical volume zones. There is no electric field in the conductor; hence, the volume meshing of the conductors is not required.

There are three specific surface boundary regions: absorbing, port, and Perfect Electric Conductor (PEC) boundaries. The largest is the absorbing boundary, which consists of two parts: the surface at the exterior of the computational domain (liver) (Figure 3a) and a small ring surface at the exterior of the catheter, which represents the catheter's absorbing boundary. The absorbing boundary has a very important purpose in the FEM simulation. The electric field intensity decreases with distance from the source; for infinite or very large domain spaces (relative to wavelength), the entire electric field is negligible, and there is no reflection from domain surface boundaries. The purpose of the absorbing boundary is to absorb the electric field, which essentially enables the small computational domain to behave in a manner similar to that of a much larger domain (the entire liver).

The port boundary was defined as the planar ring surface on the exterior of the antenna dielectric (Figure 3a). This is where the electric-field source is defined. The conductor surfaces played a major role in the simulation. This essentially represents a reflective boundary that controls the direction of propagation of the electric field. The PEC boundary is a region consisting of surface zones at the interface between the dielectric and the conductors. Three surface zones define the PEC interface: the antenna dielectric conductor, air conductor, and catheter conductor.

The frequency of interest here is 2.45 GHz, and the approximate value of the dielectric constant for the liver tissue is 44, which indicates that the finite element size in the given domain should be $\lambda_g/10 \approx 2$ mm. The dielectric constant is a critical parameter for electromagnetic simulations. A higher value of the dielectric constant requires a higher meshing density.

Figure 7a shows a cylindrical domain cross-section with the probe (dark), tumor (yellow), and liver (blue). The total volume of the domain was 254.47 cm^3 , and the total number of tetrahedrons was 640,604. In Figure 7b, we show a view of the location where the probe with the antenna exits the domain. The conductors are not meshed. The inside parts of the geometry can be seen: air (green), which is further inside, and the catheter (purple), which is at the end of the antenna. The port boundary surface (orange) and the absorbing boundary of the catheter (red) are shown. The blue surface around the catheter represents the absorbing boundary of the domain on the exterior of the liver.

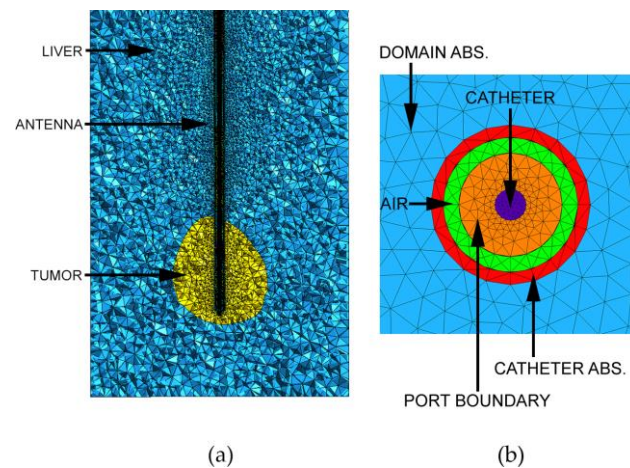


Figure 7. The geometry of the unstructured meshing shown in Figure 3; the cylindrical domain radius was 30 mm, and the height was 90 mm. (a) Cross-sectional top view (tumor zone is yellow, liver domain is blue, and antenna is dark) and (b) projection view of the port surface.

As shown in Figure 8, the model has a hexahedron domain meshed with a combination of structured and unstructured meshing. The total volume of this domain was 324 cm^3 , which was 27% higher than that of the cylindrical domain. The total number of hexahedrons was 49,552 (green), the total number of tetrahedrons was 99,063 (red), and the total number of pyramids was 2709 (blue). Even with larger volumes, the total number of volume elements is much smaller; the number of tetrahedrons is 6.46 times smaller, and the total number of volume elements is 4.38 times smaller. The hexahedrons used in the domain are mostly identical cubes, which are perfect elements for FEM analysis. For higher mesh control in the geometry, we can create dummy objects whose purpose is to facilitate a specific mesh pattern. Around the tumor, a dummy hexahedron volume is created; the volume was meshed with tetrahedrons (red) in the same manner as the tumor, which enabled a smooth transition to structured meshing (Figure 8a). A similar dummy object was placed around the catheter, as shown in Figure 8b,c. The catheter was meshed with a small layer of pyramids intertwined with surrounding tetrahedrons. The boundary regions are the same as those shown in Figure 7b.

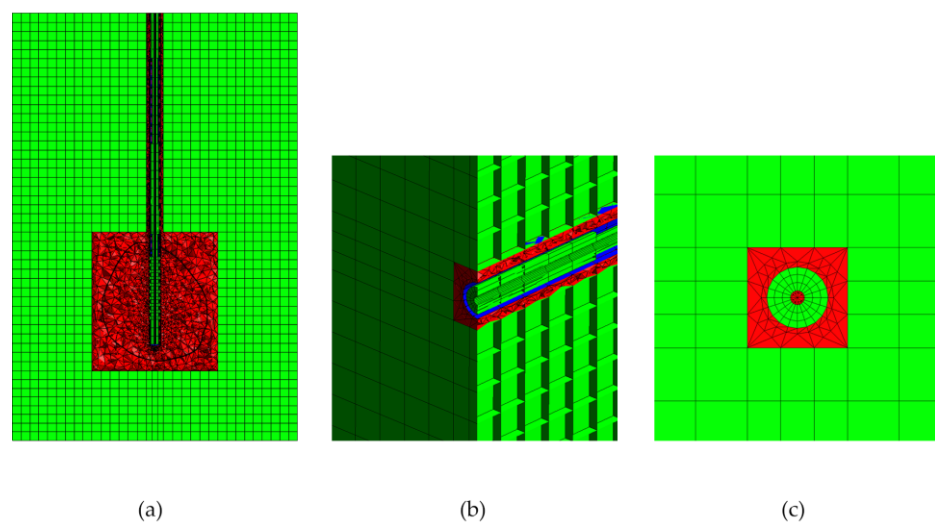


Figure 8. Mixed meshing of the geometry from Figure 2, a hexahedral domain with dimensions of $60 \text{ mm} \times 60 \text{ mm} \times 90 \text{ mm}$. (a) Cross-sectional top view: the tumor zone is marked with a black line, and meshing is performed with three types of geometry: hexahedrons (green), tetrahedrons (red), pyramids (blue), (b) cross-sectional side view and (c) projection view at the port surface.

3. Results

Solving the previously defined equations in the domain of interest with the FEM was performed using GetDP. The mesh generated by Gmsh contains a list of nodes with their coordinates, a list of finite elements with defined element type (line, triangle, quadrangle, tetrahedron, hexahedron, prism, etc.) with a number tag characterizing the physical region to which a particular element belongs and the list of its nodes. The only necessary connection between the mesh and the GetDP is a unique tag of the physical zone defined in the mesh and linked as a group of regions inside the GetDP [45]. All physical definitions were expressed in the GetDP scripting language. All the volume physical zones are joined in a group called a domain. Additionally, the liver and tumor tissues were grouped into a heat zone. We can configure the temperature to only be calculated in the heat zone because we are only interested in the tissue temperature. By solving the electric field vector in the frequency range of 2 GHz to 3 GHz and using Equation (6), we can obtain the values of S_{11} versus the frequency, as can be seen in Figure 9. Simulations were carried out for the models in Figures 7 and 8, with unstructured and mixed meshing, respectively. We can see that S_{11} values in both cases are quite similar, and the antenna has good reflection below -10 dB at 2.45 GHz. The rest of the analyses is focused only on a frequency of 2.45 GHz and an input power of 13 W.

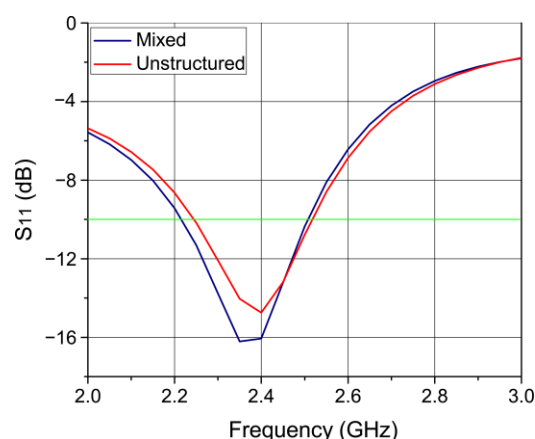


Figure 9. S_{11} parameters at the antenna port for unstructured meshing (Figure 7) and mixed meshing (Figure 8). Green horizontal line represents -10 dB limit.

To obtain the temperature originating from MWA, we must acquire the value of the electric field across the domain and use it as an external source in the bio-heat Equation (10). Solving these coupled equations is challenging. The best approach is to solve the equations for the electric field and then use the solution in the bio-heat equation. In this manner, there is no difference in solving coupled problems compared to uncoupled problems. The only thing that matters is a good definition of the association between the coupled problems and the proper order for solving the equations. To calculate temperature, a transient simulation must be implemented [57].

Many schemes with various levels of complexity and stability can be used to solve this coupled problem. Some of the most famous are the Crank–Nicholson, Implicit Euler, and Explicit Euler methods. Crank–Nicholson and Explicit Euler are predefined in GetDP. One of the major differences between these schemes is the method used. Crank–Nicholson and Explicit Euler used an explicit resulting method. They typically use various predictor–corrector formulations, where the value of a function in the future time step $f(t_{n+1})$ is predicted and then corrected by solving the system of non-linear equations. This is a costly and slow process, particularly with higher-order schemes. The advantage of these schemes is the solution stability, which does not depend on the size of the time step.

The Explicit Euler method is a simple and fast explicit scheme. For each time step, we solve the equations and use the solution in the next time step. The electric field must

be solved for each time step because the material parameters are temperature dependent, as shown in Equations (16) and (17). The time derivative at a particular time step can be determined using the first-order approximation of the first partial derivative as follows:

$$\frac{df}{dt}(t_n) \approx \frac{f(t_n) - f(t_{n-1})}{\Delta t}, \quad (20)$$

where $f(t_n)$ represents a function that contains the value of interest, the temperature in this case, which is calculated at this time step, and $f(t_{n-1})$ is already known from the previous time step. The Explicit Euler scheme uses known and calculated values. The problem with the Explicit Euler equation is the accuracy of the approximation in (20), which is directly correlated with the size of the time step. Smaller time steps yield smaller errors, but they increase the number of time steps and, consequently, the duration of the simulation. In GetDP, predefined variables such as \$Time, \$DTime, and \$TimeStep, which define the current time, current time increment, and current time step, respectively, are necessary for the construction, control, and modification of the transient schemes. The time step value that ensures numerical stability can be determined by calculating the largest eigenvalue of the global thermal stiffness over the global thermal mass values [58,59]. This process is computationally expensive for large thermal matrices [58].

The optimal solution is to have a reasonable starting value for the time step as a fraction of the total observed time, and then use the test function to check the change in the observed value in comparison with the previous time step and adapt the time step size. If the change is greater than the specified value, we can repeat the time loop with a smaller time step and use this simple iterative procedure until the condition is satisfied.

In this study, we defined four points inside the heat domain (liver and tumor) in which we observed the calculated temperature (see Figure 3a). Points A, B, C, and D are in the plane with maximum transverse and longitudinal dimensions [10,13]. The initial temperature of the heat domain was set at 37 °C. If the absolute temperature difference between successive time steps is larger than one, the loop repeats with a halved time step. Tests will occur at the defined time values. The starting time step was 10 s, and the value of 2.5 s in the current models satisfied the defined conditions.

After obtaining the temperature, we were particularly interested in calculating the tissue damage estimated using Equation (19). The standard approach is to define a third system of coupled equations to calculate the time integration of Equation (18). This is not necessary, and powerful post-processing functionality and post-operation objects can be used [45]. Any calculated unknown can be used to define expressions, such as the integration of the calculated unknown through the surface or volume. In post-processing, the result of the expression can be written as an internal variable and used in the next time step. We can use a simple scalar value (for the temperature at a specific point in the domain) or a matrix calculated across the entire domain (for the definition of the temperature values in the heat domain).

$$C_i = Ae^{(-\frac{\Delta E}{RT_i})}, \quad (21)$$

$$\Omega = \int_0^T C dt = \int_0^{\Delta T} C_1 dt + \int_{\Delta T}^{2\Delta T} C_2 dt + \cdots + \int_{(N-1)\Delta T}^{N\Delta T} C_N dt = C_1 \Delta T + C_2 \Delta T + \cdots + C_N \Delta T. \quad (22)$$

For tissue damage, the equation is very simple, and all values inside the integral are known and constant C_i in Equation (21). In the observed time steps (C_1, C_2, \dots, C_N), we can simply add a call inside the time loop for post-processing, which stores the calculated $C_1 \Delta T$. In the next time step, we add the calculated $C_2 \Delta T$, and so on, until the final step is completed, as in Equation (22). At each time step, we used a current value of Ω in θ_d to obtain the fraction of necrotic tissue. One particular aspect that needs to be addressed is that, while values are known, there are multiple exponents in the expressions that can produce extremely large values. Calculations using coupled equations are particularly sensitive

and can easily break the entire numerical approximation. The maximum exponent value that can be used in the double-precision floating-point format is 2^{1023} , and the minimum exponent value is 2^{-1022} . In θ_d , this can be exceeded, which would cause errors; therefore, we can limit the maximal value of Ω which can be used for θ_d , as a simple expression, such as if $\Omega > 10$, we use $\Omega = 10$. Factor e^{-10} has a very small value, and in this case, there is not much difference if an even smaller value is used since, here, $\theta_d \approx 1$, which indicates total tissue necrosis.

The simulation was performed using a SuperMicro workstation with a Threadripper 3975WX processor. A comparison of the simulation parameters for the two meshing types is presented in Table 5. The degree of freedom (DOF) in the FEM represents the number of unknowns. This depends on the type of elements used (number of nodes) and the number of dependent variables.

Table 5. Comparison of the DOFs for the electric field (E) and temperature (T), elements, and time per iteration, for model with unstructured and mixed meshing.

	DOF T	DOF E	Hexahedron	Tetrahedron	Pyramids	Time
Unstructured	68,449	697,730	0	639,658	0	170 s
Mixed	67,573	274,352	49,552	99,063	2709	47 s

It should be noted that the volume of the geometry with mixed meshing is 27% larger than the volume of the geometry with unstructured meshing, but again, we can see that the number of DOFs for the temperature calculation is smaller for 876 and 2.54 times smaller for the electric field calculation. Thus, the simulation time is 3.62 times faster for mixed meshing.

The SAR simulation is shown in Figure 10. In both models, the results were identical. The SAR results essentially represent the MWA propagation and shape. The SAR shape was symmetrical and spherical in all planes, and the strongest intensity was in the proximity of the antenna slots.

In Figure 11, we can see a fast growth of the ablation area until 360 s, after which the growth is much subtler. The tumor area and temperature isocontours correspond to areas at approximately 50 °C and 60 °C, respectively. Above 60 °C, rapid cell death would happen [10]. Temperatures above 42 °C for moderate periods cause damage to cellular functions [14]. The level of damage depends on temperature and duration of exposure. At 600 s, the entire tumor was at 50 °C, which was sufficient for its destruction.

Figure 12 shows the actual ablation shape calculated using Equation (22). This follows the rise in temperature and saturation patterns. At 600 s, the entire tumor was in the ablation area with a fraction of tissue damage close to 1, which accounts for total necrosis.

The fraction of necrotic tissue damage at 600 s for multiple planes and for both meshing models is shown in Figure 13. The shape of the MWA follows the same pattern as that of the SAR, and they are visually identical. The tumor was completely located in an area of total necrosis.

In Figures 14 and 15, we can see continuous estimations of the temperature, fraction of necrotic tissue, and tissue damage at four control points for mixed-meshing, since extremely small differences were observed between the two meshing models. The results were very stable, and there was no abrupt change in the values, suggesting that the time scheme used was accurate. Point D, which is near the slots, shows a very rapid rise of the temperature and achieves around 86 °C at 600 s; we can see that total necrosis happens exactly when the temperature passes 60 °C at 130 s, which is in accordance with previous reports [10]. Point B is at the edge of the tumor and has a temperature slightly below 60 °C at 600 s, while total necrosis occurs at around 350 s. Point A is near the antenna but is moved away from the slots toward the antenna port. It shows a similar temperature as point B, with a value of around 55 °C at 600 s and total necrosis at around 450 s. Point C is placed on the same axis as the antenna, but away from it and outside of the tumor, and achieves a

value of around 48 °C at 600 s. Here, the fraction of necrotic tissue damage is around 0.88 at 600 s. With additional time, total tissue damage would occur; therefore, it is essential to have an antenna that is able to cover the entire tumor in a short time frame. The MWA should originate from radiation, and extremely high temperatures around the antenna should be avoided because they can cause rapid heating of the antenna surface, causing tissue damage along the entire antenna structure.

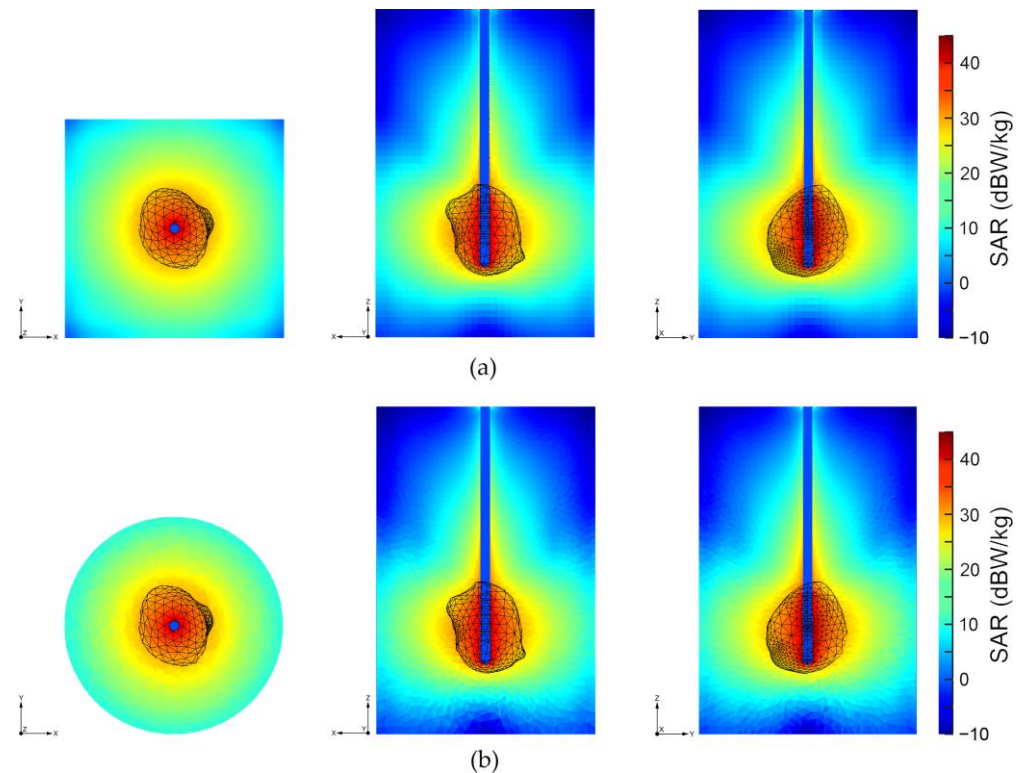


Figure 10. SAR simulation results for different cross-sections at 600 s with tumor structure designated by black color: (a) mixed meshing and (b) unstructured meshing.

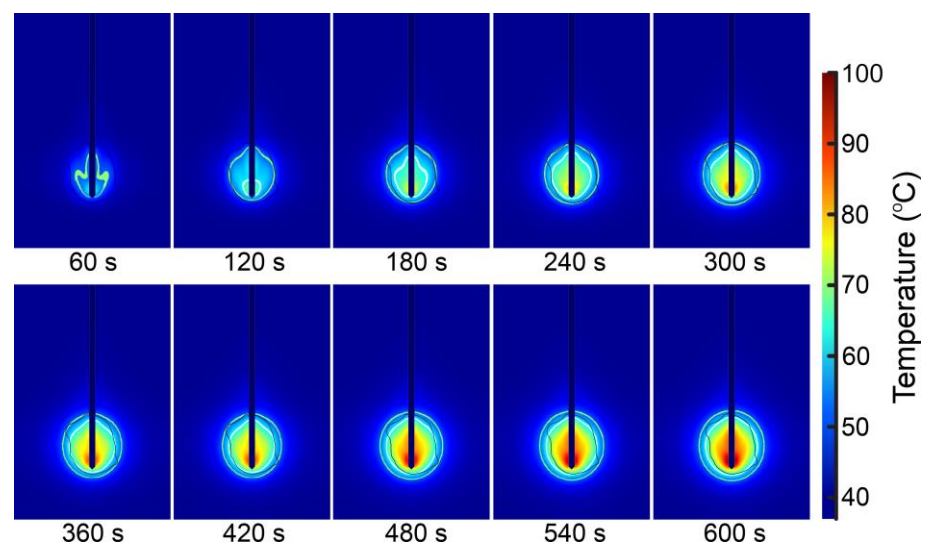


Figure 11. Temperature change with time for mixed meshing in the x-z cut plane. The tumor boundaries are marked with black lines, and the temperature isocontours corresponding to 50 °C and 60 °C are marked with light green and white, respectively.

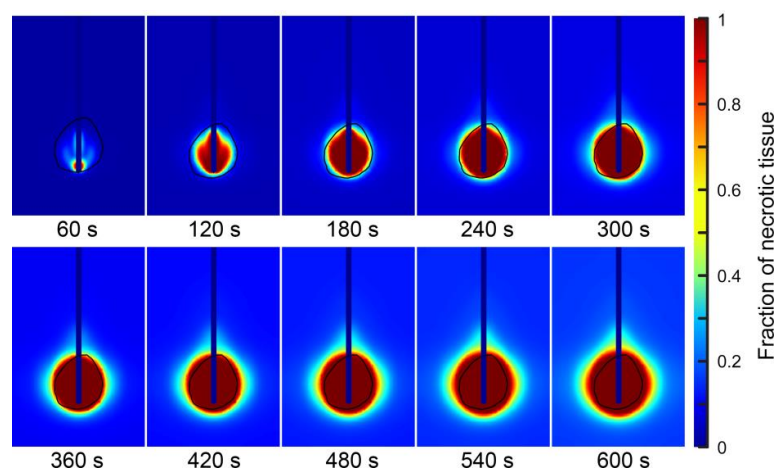


Figure 12. Fraction of the necrotic tissue change with time for mixed meshing in z-y cut plane. Tumor boundaries are marked with a black line.

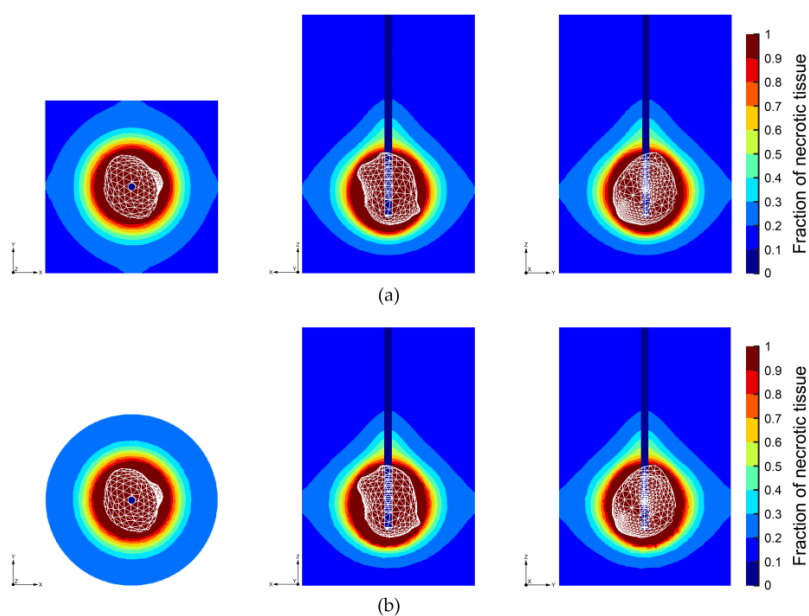


Figure 13. Fraction of necrotic tissue at different cross-sections at 600 s for (a) mixed meshing and (b) unstructured meshing. Tumor shape is designated by white color.

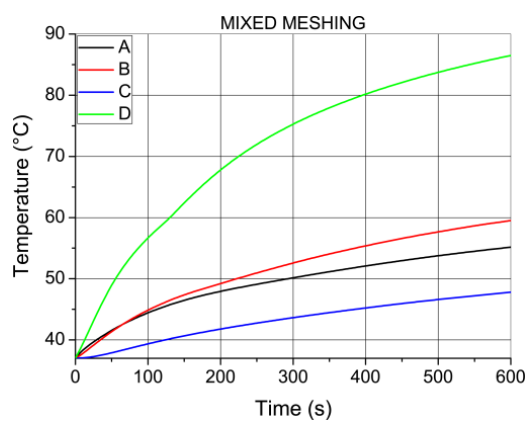


Figure 14. The dependence of temperature on time at the four points (A, B, C, and D) for mixed meshing.

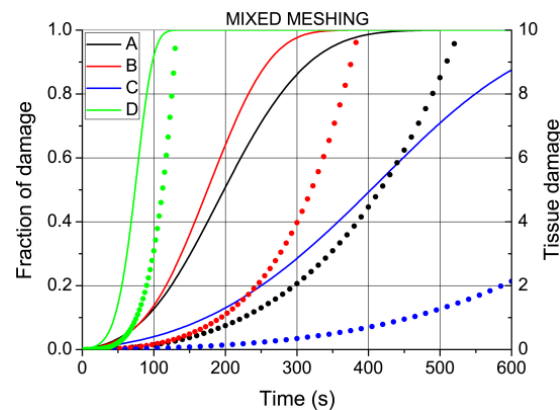


Figure 15. The fraction of necrotic tissue changes with time at the four points (A, B, C, and D) for mixed meshing (full lines) and tissue damage (dots of the same color).

4. Discussion

The tissue damage parameter is sometimes used for the estimation of damage during MWA [60,61]. The value of $\Omega = 10$ is equivalent to the value of 0.99995 for the fraction of necrotic damage, which in practice can be considered as 1 or 100% cell damage; hence, values of Ω above 10 do not add a significant change in the fraction of necrotic damage [60,62]. In MWA, there are two general objectives: irreversible damage to tumor cells and minimal damage to the surrounding healthy tissue. Two expressions were used to estimate the damage to healthy tissue. The volumetric damage (VD) is calculated as the ratio of the volume of the damaged healthy tissue ($V_{DAMAGED}$) and tumor tissue (V_{TUMOR}) [60,63]:

$$VD = \frac{V_{DAMAGED}}{V_{TUMOR}} \cdot 100\%. \quad (23)$$

The amount of damaged healthy tissue (DT) was calculated as the ratio between the volume of the damaged healthy tissue and the total volume of the liver (V_{LIVER}) without tumor tissue (V_{TUMOR}) [64,65]:

$$DT = \frac{V_{DAMAGED}}{V_{LIVER} - V_{TUMOR}} \cdot 100\%. \quad (24)$$

The boundary of damaged healthy tissue was estimated by using different parameters. The most common is the volume of the tissue inside certain limits of tissue damage, such as $\Omega \geq 4$ or $\Omega \geq 4.6$, which corresponds to 98.17% and 98.99% of the cell damage, respectively [60–65]. In this study, the volume of the tumor was 5.38 cm³, and the volume of the tissue inside the $\Omega \geq 4.6$ was 7.13 cm³. Thus, the volumetric damage was $(7.13 - 5.38)/5.38 = 32.53\%$. The mean volume of the human liver is around 1750 cm³ [66]; hence, the amount of damaged healthy tissue, in this case, was $0.175/1750 = 0.1\%$, which is negligible.

In the MWA simulation, there would generally be two convergence operations. One relates to whether mesh refinement yield changes in the observed quantity below certain limits, and the second one relates to the stability of the time loop, which is related to the size of the used time step. The convergence criterion for the time loop is that the absolute value of the temperature change, calculated in control points between successive time steps, is below 1. This is implemented directly in the Explicit Euler scheme; resulting curves are stable, there is no abrupt change, and curves have a similar shape as the one in the related literature obtained with commercial software.

Mesh convergence represents a standard topic in the FEM simulation. This was related to the effect of the smaller size of the finite elements used in the solution. The convergence criterion corresponds to the maximum variation in the observed solution between simulations involving smaller finite elements. It is typically set as the relative

change (e.g., 1%). Thus, the estimation of convergence involves multiple full simulations with successive mesh refinement steps. Mesh refinement is typically performed in an adaptive manner, where parts of the volume with a higher variation of the observed quantity, between successive refinement steps, are meshed with more elements in the next step [25]. Increasing the number of elements will have a significant effect on the simulation time, and with sufficient refinement steps, it will eventually reach the limit of the available computation resources, so the number of iterations is typically limited. In the current model, we did not use mesh refinement after the FEM calculation began. In order to estimate how our mesh settings were based on limiting the maximal element size to 2 mm, compared to the mesh model generated with smaller finite elements, we repeated the simulation of the model with mixed meshing with a maximal element size of 1 mm, as shown in Figure 16. This resulted in a massive increase in the number of elements and the simulation time, as listed in Table 6.

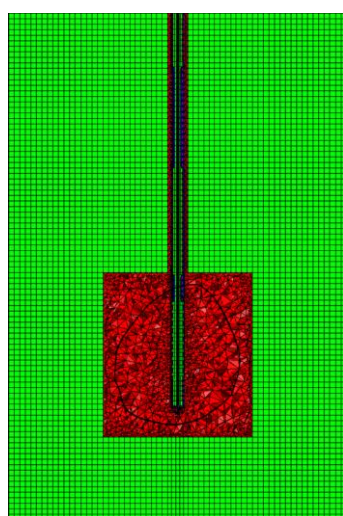


Figure 16. Meshing of the model with mixed meshing for a maximal element size of 1 mm and the same projection of the same model for a maximum element size of 2 mm are shown in Figure 8a.

Table 6. Comparison of the DOFs for the electric field (E) and temperature (T), elements, and time per iteration for models with mixed meshing and maximal mesh element sizes of 1 mm and 2 mm, respectively.

	DOF T	DOF E	Hexahedron	Tetrahedron	Pyramids	Time
1 mm	399,449	1,328,615	352,623	196,577	7389	393 s
2 mm	67,573	274,352	49,552	99,063	2709	47 s

The total number of DOFs is 1,728,064 in this case, which is more than five times as many compared to the previous case, and the total number of elements is 3.68 times higher. The simulation time is 8.36 times longer. The temperature obtained at the control points from this simulation was compared with the previous one, as can be seen in Figure 17. The relative absolute temperature difference (*Ratd*) was calculated as

$$Ratd = \frac{|T_{2mm} - T_{1mm}|}{T_{2mm}} \cdot 100\%, \quad (25)$$

where T_{2mm} and T_{1mm} are the temperature values at the control point for the models with maximal mesh sizes of 2 mm and 1 mm, respectively. As shown in Figure 17, the maximal absolute relative temperature difference is around 0.2% which is acceptable in this and most other models, and is below the typically desired value of 1% [60,67]. Hence, the new

mesh model does not give any significant difference compared to the initial one, at the cost of much more DOFs and simulation time.

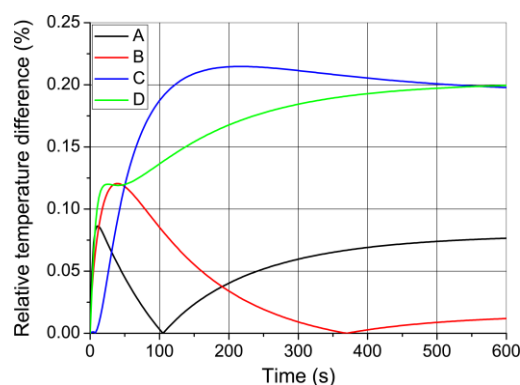


Figure 17. Relative absolute temperature difference in control points during MWA simulation for model with mixed meshing when the maximal size of finite elements is 1 mm and 2 mm.

5. Conclusions

In this study, we demonstrated that all steps in the modeling and simulation of MWA can be replaced with open-source solutions [33–47]. The geometry of a multi-slot coaxial antenna [10,13] is created using the open-source solution Gmsh [33], and the geometry of the real tumor is constructed in Gmsh from a CT scan of a patient [26]. We presented a detailed meshing procedure for both mixed and unstructured meshing [32] using Gmsh, and a significant advantage of mixed meshing is displayed. Simulation of MWA requires the calculation of the electromagnetic field and tissue heating as a coupled problem. Tissue heating is an extremely slow process in comparison with electric field propagation; therefore, we calculated the electric field in the frequency domain, and we used these results to calculate the temperature distribution in the time domain. To solve equations describing the physics of MWA, we used the FEM method implemented in the open-source solution GetDP [45,46]. Solving the coupled equations for the electric field and bio-heat is difficult, and the best approach is to solve the equations for the electric field and then use the solution in the bio-heat equation as an external heat source. In this manner, there is no difference in solving coupled problems compared to uncoupled problems. To calculate the temperature, a transient simulation was required [57]. There are many schemes with various levels of complexity and stability to solve this coupled problem, such as the Crank–Nicholson, implicit Euler, and explicit Euler schemes. One of the major differences between these schemes is the time-stepping method used. The explicit Euler method is a simple and fast explicit scheme based on using known values from the current and previous time steps, but the problem can be the accuracy of the approximation, which is directly correlated with the size of the time step. The time-step value that ensures numerical stability can be determined by calculating the largest eigenvalue of the global thermal stiffness over the global thermal mass values [58,59]. This process is computationally expensive for large thermal matrices [58]. We derived a custom, fully explicit, accurate, and stable time scheme based on an Explicit Euler, which is much faster than implicit schemes and has a considerably lower usage of computational resources.

The results presented in this paper agree well with our previously published results (temperature, microwave powers, and time of exposure) obtained using the COMSOL Multiphysics software package [25]. One of the main goals of this paper is to demonstrate that this type of simulation can be performed successfully using open-source software. The novelty of this study is the accurate modeling of the full MWA process, which is on par with commercial software such as COMSOL Multiphysics [25]. Our approach includes a superior meshing procedure designed to significantly reduce computational time and memory requirements, and a fully explicit stable Euler scheme for temperature time marching based on carefully chosen control points. The limitation of the presented

algorithm is the fact that we used the simplest tissue model. In future work, the complete model of MWA with multiple antennas and domain decomposition algorithm to achieve a significant reduction in the simulation time through parallelization will be implemented. More complex effects, such as a change in the interstitial space (porosity) of tissue during MWA, will be studied.

Author Contributions: Conceptualization, N.B., B.R. and M.R.-R.; methodology, N.B. and B.R.; software, N.B. and B.R.; investigation and data interpretation, N.B. and B.R.; original draft preparation, N.B., B.R. and M.R.-R.; writing—review, and editing, all of the authors; supervision, B.R. and M.R.-R. All authors have read and agreed to the published version of the manuscript.

Funding: All authors acknowledge that this research was supported by the Science Fund of the Republic of Serbia, The Program IDEAS, GRANT No. 7739583, SimSurgery.

Data Availability Statement: The data are available from the corresponding authors upon reasonable request.

Conflicts of Interest: The authors declare no conflict of interest.

References

- Villanueva, A. Hepatocellular Carcinoma. *N. Engl. J. Med.* **2019**, *380*, 1450–1462. [\[CrossRef\]](#)
- Arnold, M.; Abnet, C.C.; Neale, R.E.; Vignat, J.; Giovannucci, E.L.; McGlynn, K.A.; Bray, F. Global Burden of 5 Major Types of Gastrointestinal Cancer. *Gastroenterology* **2020**, *159*, 335–349. [\[CrossRef\]](#)
- Llovet, J.M.; Kelley, R.K.; Villanueva, A.; Singal, A.G.; Pikarsky, E.; Roayaie, S.; Lencioni, R.; Koike, K.; Zucman-Rossi, J.; Finn, R.S. Hepatocellular carcinoma. *Nat. Rev. Dis. Prim.* **2021**, *7*, 6. [\[CrossRef\]](#)
- Radmilović-Radjenović, M.; Radjenović, D.; Radjenović, B. Finite element analysis of the effect of microwave ablation on the liver, lung, kidney, and bone malignant tissues. *Europhys. Lett.* **2021**, *135*, 3500. [\[CrossRef\]](#)
- Izzo, F.; Granata, V.; Grassi, R.; Fusco, R.; Palaia, R.; Delrio, P.; Carrafiello, G.; Azoulay, D.; Petrillo, A.; Curley, S.A. Radiofrequency Ablation and Microwave Ablation in Liver Tumors: An Update. *Oncologist* **2019**, *24*, e990–e1005. [\[CrossRef\]](#) [\[PubMed\]](#)
- Tan, W.; Deng, Q.; Lin, S.; Wang, Y.; Xu, G. Comparison of microwave ablation and radiofrequency ablation for hepatocellular carcinoma: A systematic review and meta-analysis. *Int. J. Hyperth.* **2019**, *36*, 264–272. [\[CrossRef\]](#) [\[PubMed\]](#)
- Li, W.; Ni, C.F. Current status of the combination therapy of transarterial chemoembolization and local ablation for hepatocellular carcinoma. *Abdom. Radiol.* **2019**, *44*, 2268–2275. [\[CrossRef\]](#) [\[PubMed\]](#)
- Hojjatollah, F.; Punit, P. Antenna Designs for Microwave Tissue Ablation. *Crit. Rev. Biomed. Eng.* **2018**, *46*, 495–521. [\[CrossRef\]](#)
- Huang, H.; Zhang, L.; Moser, M.A.J.; Zhang, W.; Zhang, B. A review of antenna designs for percutaneous microwave ablation. *Phys. Med.* **2021**, *84*, 254–264. [\[CrossRef\]](#)
- Ge, M.; Jiang, H.; Huang, X.; Zhou, Y.; Zhi, D.; Zhao, G.; Chen, Y.; Wang, L.; Qiu, B. A multi-slot coaxial microwave antenna for liver tumor ablation. *Phys. Med. Biol.* **2018**, *63*, 175011. [\[CrossRef\]](#)
- Wang, T.; Zhao, G.; Qiu, B. Theoretical evaluation of the treatment effectiveness of a novel coaxial multi-slot antenna for conformal microwave ablation of tumors. *Int. J. Heat Mass Transf.* **2015**, *90*, 81–91. [\[CrossRef\]](#)
- Vogl, T.J.; Basten, L.M.; Nour-Eldin, N.-E.A.; Kaltenbach, B.; Bodelle, B.; Wichmann, J.L.; Ackermann, H.; Naguib, N.N.N. Evaluation of microwave ablation of liver malignancy with enabled constant spatial energy control to achieve a predictable spherical ablation zone. *Int. J. Hyperth.* **2018**, *34*, 492–500. [\[CrossRef\]](#)
- Radjenović, B.; Sabo, M.; Šoltes, L.; Prnova, M.; Čičak, P.; Radmilović-Radjenović, M. On Efficacy of Microwave Ablation in the Thermal Treatment of an Early-Stage Hepatocellular Carcinoma. *Cancers* **2021**, *13*, 5784. [\[CrossRef\]](#)
- Tehrani, M.H.H.; Soltani, M.; Kashkooli, F.M.; Raahemifar, K. Use of microwave ablation for thermal treatment of solid tumors with different shapes and sizes—A computational approach. *PLoS ONE* **2020**, *15*, e0233219. [\[CrossRef\]](#)
- Radmilović-Radjenović, M.; Bošković, N.; Radjenović, B. Computational Modeling of Microwave Tumor Ablation. *Bioengineering* **2022**, *9*, 656. [\[CrossRef\]](#) [\[PubMed\]](#)
- Radmilović-Radjenović, M.; Sabo, M.; Prnova, M.; Šoltes, L.; Radjenović, B. Finite Element Analysis of the Microwave Ablation Method for Enhanced Lung Cancer Treatment. *Cancers* **2021**, *13*, 3500. [\[CrossRef\]](#)
- Radmilović-Radjenović, M.; Bošković, N.; Sabo, M.; Radjenović, B. An Analysis of Microwave Ablation Parameters for Treatment of Liver Tumors from the 3D-IRCADb-01 Database. *Biomedicines* **2022**, *10*, 1569. [\[CrossRef\]](#)
- Ji, Z.; Brace, C.L. Expanded modeling of temperature-dependent dielectric properties for microwave thermal ablation. *Phys. Med. Biol.* **2011**, *56*, 5249. [\[CrossRef\]](#) [\[PubMed\]](#)
- Rossmann, C.; Haemmerich, D. Review of temperature dependence of thermal properties, dielectric properties, and perfusion of biological tissues at hyperthermic and ablation temperatures. *Crit. Rev. Biomed. Eng.* **2014**, *42*, 467–492. [\[CrossRef\]](#) [\[PubMed\]](#)
- Taeprasartsit, P.; Pathompatai, C.; Jusomjai, K.; Wibowo, H.; Sebek, J.; Prakash, P. A personalized approach for microwave ablation treatment planning fusing radiomics and bioheat transfer modeling. *Proc. SPIE* **2020**, *11315*, 780–795. [\[CrossRef\]](#)

21. Hossan, M.R.; Dutta, P. Effects of temperature dependent properties in electromagnetic heating. *Int. J. Heat. Mass. Transf.* **2012**, *55*, 3412–3422. [CrossRef]
22. O'Rourke, A.P.; Lazebnik, M.; Bertram, J.M.; Converse, M.C.; Hagness, S.C.; Webster, J.G.; Mahvi, D.M. Dielectric properties of human normal, malignant and cirrhotic liver tissue: In vivo and ex vivo measurements from 0.5 to 20 GHz using a precision open-ended coaxial probe. *Phys. Med. Biol.* **2007**, *52*, 4707–4719. [CrossRef]
23. Andreozzi, A.; Iasiello, M.; Tucci, C. An overview of mathematical models and modulated-heating protocols for thermal ablation. *Adv. Heat Transf.* **2020**, *52*, 489–541. [CrossRef]
24. Heat Transfer Modeling Software for Analyzing Thermal Effects. Available online: <https://www.comsol.com/heat-transfer-module/> (accessed on 6 February 2023).
25. COMSOL—Software for Multiphysics Simulation. Available online: <https://www.comsol.com/> (accessed on 6 February 2023).
26. 3D-IRCADb. Available online: <https://www.ircad.fr/research/3dircadb/> (accessed on 6 February 2023).
27. Kiah, M.L.M.; Haiqi, A.; Zaidan, B.B.; Zaidan, A.A. Open source EMR software: Profiling, insights and hands-on analysis. *Comput. Methods Programs Biomed.* **2014**, *117*, 360–382. [CrossRef]
28. Delp, S.L.; Anderson, F.C.; Arnold, A.S.; Loan, P.; Habib, A.; John, C.T.; Guendelman, E.; Thelen, D.G. OpenSim: Open-source software to create and analyze dynamic simulations of movement. *IEEE Trans. Biomed. Eng.* **2007**, *54*, 1940–1950. [CrossRef]
29. Cross, D.E.; Bauer, T.M.; Tchantchaleishvili, V. 3D organ modeling with open-source software. *Artif. Organs* **2019**, *43*, 596–598. [CrossRef] [PubMed]
30. Schmitz, A.; Piovesan, D. Development of an Open-Source, Discrete Element Knee Model. *IEEE Trans. Biomed. Eng.* **2016**, *63*, 2056–2067. [CrossRef] [PubMed]
31. Jian-Ming, J. *Theory and Computation of Electromagnetic Fields*, 2nd ed.; John Wiley & Sons, Inc.: Hoboken, NJ, USA, 2015.
32. Frey, P.J.; George, P.-L. *Mesh Generation: Application to Finite Elements*, 2nd ed.; John Wiley & Sons, Inc.: Hoboken, NJ, USA, 2008.
33. Geuzaine, C.; Remacle, J.-F. Gmsh: A three-dimensional finite element mesh generator with built-in pre- and post-processing facilities. *Int. J. Numer. Meth. Eng.* **2009**, *79*, 1309–1331. [CrossRef]
34. Remacle, J.-F.; Geuzaine, C.; Compère, G.; Marchandise, E. High-quality surface remeshing using harmonic maps. *Int. J. Numer. Meth. Eng.* **2010**, *83*, 403–425. [CrossRef]
35. Marchandise, E.; de Wiart, C.C.; Vos, W.G.; Geuzaine, C.; Remacle, J.-F. High-quality surface remeshing using harmonic maps—Part II: Surfaces with high genus and of large aspect ratio. *Int. J. Numer. Meth. Eng.* **2011**, *86*, 1303–1321. [CrossRef]
36. Marchandise, E.; Remacle, J.-F.; Geuzaine, C. Optimal parametrizations for surface remeshing. *Eng. Comput.* **2014**, *30*, 383–402. [CrossRef]
37. Remacle, J.-F.; Lambrechts, J.; Seny, B.; Marchandise, E.; Johnen, A.; Geuzainet, C. Blossom-Quad: A non-uniform quadrilateral mesh generator using a minimum-cost perfect-matching algorithm. *Int. J. Numer. Meth. Eng.* **2012**, *89*, 1102–1119. [CrossRef]
38. Remacle, J.-F.; Henrotte, F.; Carrier-Baudouin, T.; Béchet, E.; Marchandise, E.; Geuzaine, C.; Mouton, T. A frontal Delaunay quad mesh generator using the L_∞ norm. *Int. J. Numer. Meth. Eng.* **2013**, *94*, 494–512. [CrossRef]
39. Johnen, A.; Remacle, J.-F.; Geuzaine, C. Geometric validity of curvilinear finite elements. *J. Comput. Phys.* **2013**, *233*, 359–372. [CrossRef]
40. Johnen, A.; Remacle, J.-F.; Geuzaine, C. Geometric validity of high-Order triangular finite elements. *Eng. Comput.* **2014**, *30*, 375–382. [CrossRef]
41. Toulorge, T.; Geuzaine, C.; Remacle, J.-F.; Lambrechts, J. Robust untangling of curvilinear meshes. *J. Comput. Phys.* **2013**, *254*, 8–26. [CrossRef]
42. Remacle, J.-F.; Chevaugnon, N.; Marchandise, E.; Geuzaine, C. Efficient visualization of high-order finite elements. *Int. J. Numer. Meth. Eng.* **2006**, *69*, 750–771. [CrossRef]
43. Geuzaine, C.; Remacle, J.-F. Gmsh Reference Manual, A Three-Dimensional Finite Element Mesh Generator with Built-in Pre- and Post-Processing Facilities. Available online: <https://gmsh.info/> (accessed on 6 February 2023).
44. Open CASCADE Technology. Available online: <https://dev.opencascade.org/> (accessed on 6 February 2023).
45. Dular, P.; Geuzaine, C. GetDP Reference Manual: The Documentation for GetDP, A General Environment for the Treatment of Discrete Problems. Available online: <https://getdp.info/> (accessed on 6 February 2023).
46. Dular, P.; Geuzaine, C.; Henrotte, F.; Legros, W. A general environment for the treatment of discrete problems and its application to the finite element method. *IEEE Trans. Magn.* **1998**, *34*, 3395–3398. [CrossRef]
47. ONELAB: Open Numerical Engineering Laboratory. Available online: <https://onelab.info/> (accessed on 6 February 2023).
48. Pennes, H.H. Analysis of tissue and arterial blood temperatures in the resting human forearm. *J. Appl. Physiol.* **1948**, *1*, 93–122. [CrossRef]
49. Gillies, R.J.; Schornack, P.A.; Secomb, T.W.; Raghunand, N. Causes and effects of heterogeneous perfusion in tumors. *Neoplasia* **1999**, *1*, 197–207. [CrossRef]
50. Sweeney, P.W.; d'Esposito, A.; Walker-Samuel, S.; Shipley, R.J. Modelling the transport of fluid through heterogeneous, whole tumours in silico. *PLoS Comput. Biol.* **2019**, *15*, e1006751. [CrossRef] [PubMed]
51. Chartampilas, E.; Rafailidis, V.; Georgopoulou, V.; Kalarakis, G.; Hatzidakis, A.; Prassopoulos, P. Current Imaging Diagnosis of Hepatocellular Carcinoma. *Cancers* **2022**, *14*, 3997. [CrossRef]
52. Kim, S.H.; Kamaya, A.; Willmann, J.K. CT Perfusion of the Liver: Principles and Applications in Oncology. *Radiology* **2014**, *272*, 322–344. [CrossRef] [PubMed]

53. Cavagnaro, M.; Pinto, R.; Lopresto, V. Numerical models to evaluate the temperature increase induced by ex vivo microwave thermal ablation. *Phys. Med. Biol.* **2015**, *60*, 3287–3311. [[CrossRef](#)] [[PubMed](#)]
54. Yang, D.; Converse, M.C.; Mahvi, D.M.; Webster, J.G. Expanding the Bioheat Equation to Include Tissue Internal Water Evaporation during Heating. *IEEE Trans. Biomed. Eng.* **2007**, *54*, 1382–1388. [[CrossRef](#)]
55. Berjano, E.J. Theoretical modeling for radiofrequency ablation: State-of-the-art and challenges for the future. *BioMed Eng. Online* **2006**, *5*, 24. [[CrossRef](#)]
56. Selmi, M.; Bin Dukhyil, A.A.; Belmabrouk, H. Numerical Analysis of Human Cancer Therapy Using Microwave Ablation. *Appl. Sci.* **2020**, *10*, 211. [[CrossRef](#)]
57. Gartling, D.K.; Reddy, J.N. *The Finite Element Method in Heat Transfer and Fluid Dynamics*, 3rd ed.; CRC Press: Boca Raton, FL, USA; Taylor & Francis Group: Abingdon, UK, 2010.
58. Zhang, J.; Chauhan, S. Real-time computation of bio-heat transfer in the fast explicit dynamics finite element algorithm (FED-FEM) framework. *Numer. Heat Transf. Part B Fundam.* **2019**, *75*, 217–238. [[CrossRef](#)]
59. Rong, X.; Niu, R.; Liu, J. Stability analysis of smoothed finite element methods with explicit method for transient heat transfer problems. *Int. J. Comput. Methods* **2018**, *17*, 1845005. [[CrossRef](#)]
60. Singh, M.; Singh, T.; Soni, S. Pre-operative Assessment of Ablation Margins for Variable Blood Perfusion Metrics in a Magnetic Resonance Imaging Based Complex Breast Tumour Anatomy: Simulation Paradigms in Thermal Therapies. *Comput. Methods Programs Biomed.* **2021**, *198*, 105781. [[CrossRef](#)]
61. Singh, M.; Gu, Q.; Ma, R.; Zhu, L. Heating Protocol Design Affected by Nanoparticle Redistribution and Thermal Damage Model in Magnetic Nanoparticle Hyperthermia for Cancer Treatment. *ASME J. Heat Transfer*. **2020**, *142*, 072501. [[CrossRef](#)]
62. Pearce, J.A. Comparative analysis of mathematical models of cell death and thermal damage processes. *Int. J. Hyperth.* **2013**, *29*, 262–280. [[CrossRef](#)] [[PubMed](#)]
63. LeBrun, A.; Ma, R.; Zhu, L. MicroCT image based simulation to design heating protocols in magnetic nanoparticle hyperthermia for cancer treatment. *J. Therm. Biol.* **2016**, *62*, 129–137. [[CrossRef](#)]
64. Zhang, B.; Moser, M.A.J.; Zhang, E.M.; Luo, Y.; Zhang, H.; Zhang, W. Study of the relationship between the target tissue necrosis volume and the target tissue size in liver tumours using two-compartment finite element RFA modelling. *Int. J. Hyperth.* **2014**, *30*, 593–602. [[CrossRef](#)] [[PubMed](#)]
65. Manuchehrabadi, N.; Zhu, L. Development of a computational simulation tool to design a protocol for treating prostate tumours using transurethral laser photothermal therapy. *Int. J. Hyperth.* **2014**, *30*, 349–361. [[CrossRef](#)] [[PubMed](#)]
66. Lodewick, T.M.; Arnoldussen, C.W.; Lahaye, M.J.; van Mierlo, K.M.; Neumann, U.P.; Beets-Tan, R.G.; Dejong, C.H.; van Dam, R.M. Fast and accurate liver volumetry prior to hepatectomy. *HPB (Oxford)* **2016**, *18*, 764–772. [[CrossRef](#)]
67. Singh, M.; Ma, R.; Zhu, L. Quantitative evaluation of effects of coupled temperature elevation, thermal damage, and enlarged porosity on nanoparticle migration in tumors during magnetic nanoparticle hyperthermia. *Int. Commun. Heat Mass Transf.* **2021**, *126*, 105393. [[CrossRef](#)]

Disclaimer/Publisher's Note: The statements, opinions and data contained in all publications are solely those of the individual author(s) and contributor(s) and not of MDPI and/or the editor(s). MDPI and/or the editor(s) disclaim responsibility for any injury to people or property resulting from any ideas, methods, instructions or products referred to in the content.

Article

An Analysis of Microwave Ablation Parameters for Treatment of Liver Tumors from the 3D-IRCAdB-01 Database

Marija Radmilović-Radjenović ^{1,*} , Nikola Bošković ¹ , Martin Sabo ² and Branislav Radjenović ¹¹ Institute of Physics, University of Belgrade, Pregrevica 118, 11080 Belgrade, Serbia; nikolab@ipb.ac.rs (N.B.); bradjeno@ipb.ac.rs (B.R.)² Faculty of Informatics and Information Technologies, Slovak University of Technology in Bratislava, Ilkovicova 2, 84216 Bratislava, Slovakia; martin.sabo@stuba.sk

* Correspondence: marija@ipb.ac.rs

Abstract: Simulation techniques are powerful tools for determining the optimal conditions necessary for microwave ablation to be efficient and safe for treating liver tumors. Owing to the complexity and computational resource consumption, most of the existing numerical models are two-dimensional axisymmetric models that emulate actual three-dimensional cancers and the surrounding tissue, which is often far from reality. Different tumor shapes and sizes require different input powers and ablation times to ensure the preservation of healthy tissues that can be determined only by the full three-dimensional simulations. This study aimed to tailor microwave ablation therapeutic conditions for complete tumor ablation with an adequate safety margin, while avoiding injury to the surrounding healthy tissue. Three-dimensional simulations were performed for a multi-slot microwave antenna immersed in two tumors obtained from the 3D-IRCAdB-01 liver tumors database. The temperature dependence of the dielectric and thermal properties of healthy and tumoral liver tissues, blood perfusion, and water content are crucial for calculating the correct ablation time and, thereby, the correct ablation process. The developed three-dimensional simulation model may help practitioners in planning patient-individual procedures by determining the optimal input power and duration of the ablation process for the actual shape of the tumor. With proper input power, necrotic tissue is placed mainly in the tumor, and only a small amount of surrounding tissue is damaged.

Keywords: liver tumor; microwave ablation; ablation zone; necrotic tissue



Citation: Radmilović-Radjenović, M.; Bošković, N.; Sabo, M.; Radjenović, B. An Analysis of Microwave Ablation Parameters for Treatment of Liver Tumors from the 3D-IRCAdB-01 Database. *Biomedicines* **2022**, *10*, 1569. <https://doi.org/10.3390/biomedicines10071569>

Academic Editor: Young-Kwon Seo

Received: 31 May 2022

Accepted: 17 June 2022

Published: 1 July 2022

Publisher's Note: MDPI stays neutral with regard to jurisdictional claims in published maps and institutional affiliations.



Copyright: © 2022 by the authors. Licensee MDPI, Basel, Switzerland. This article is an open access article distributed under the terms and conditions of the Creative Commons Attribution (CC BY) license (<https://creativecommons.org/licenses/by/4.0/>).

1. Introduction

Liver cancer, also known as hepatic cancer, arises because of the abnormal growth of cells inside the liver [1–5]. It may originate in the liver from hepatocytes, bile duct epithelium, or mesenchymal tissue (primary) or spread to the liver from primary cancer developed elsewhere in the body (secondary) [6–10]. The most prevalent type of liver cancer is Hepatocellular carcinoma (HCC) or hepatoma with a median survival time of fewer than six months if untreated, and a five-year survival rate of only 5–9% from the time of diagnosis [11,12]. Since HCC is the sixth most common cancer and the second most common cause of cancer mortality worldwide, establishing an efficient treatment for this type of cancer has never been more urgent [13–18].

Treatments for liver cancer are strongly dictated by the tumor stage and the extent of the underlying liver disease, in addition to the patient's overall age and health [19–22]. Despite recent advances in therapeutic options for liver cancer, it remains one of the most difficult cancers to treat [23]. Among the various applicable procedures, microwave ablation has proven to be an effective minimally invasive procedure for curing liver malignancies [24–28]. HCC ablation is defined by the Barcelona Clinic Liver Cancer (BCLC) algorithm that should be applied to each patient individually [29]. The success rate for eliminating small liver tumors in patients treated with MWA is greater than 85% [30]. MWA is also used for the treatment of liver metastases from colorectal cancer [31].

MWA is a widely used thermal ablation modality for eradicating malignant cells with minimal damage to the surrounding tissues [32–34]. It consists in focusing an energy source in the target zone (the tumoral tissue) causing tumor destruction. Some benefits of MWA include a large zone of treated tissue, short treatment duration, and less susceptibility to the heat sink effect generated by the cooling effect of blood flow. One of the main problems with ablation therapy is tumor recurrence and the exact prediction of tissue temperature requiring ablation zone monitoring. CT thermography allows the measurement of temperature non-invasively during ablation and is crucial to achieving a successful ablation with completely devitalized tumors [35]. MWA destroys tumors using one or more antennae as the source of the microwave fields, which leads to the frictional heating of water molecules in the soft tissues around the field source. A key element in MWA treatments is the microwave antenna (MW), which delivers energy and provides lethal temperature rise, resulting in cell death in the ablation zone [36]. Advanced antenna designs are based on three different mechanisms: thermal, field, and wavelength control [37]. Recently, a compact, multi-slot coaxial antenna was developed to achieve the required ablation zone and suitable impedance matching to the target tumoral tissue without damaging the surrounding healthy tissues [38].

Nowadays, thermal therapy has evolved into a very important topic in medicine, and many studies on the application of heat transfer to living tissues have been carried out in the last few decades, including cancer tumor treatment, drug delivery [39], or pain relief [40]. Numerical studies may have a great impact on patient care by creating predictive models from procedural planning to execution [41–43]. Moreover, the lack of experimentation in this field underlines mathematical models even more significantly. In this context, understanding the physics behind thermal therapy has a key role in modeling heat transfer in thermal therapies, to develop more and more accurate tissue and process models. Every mathematical model for the simulation of MWA must contain three fundamental components: the antenna probe, heat distribution in the tissue, and the effect of heat on tumor cells and their destruction. All these components depend on a diversity of material parameters, which, in turn, depend on the various states of the tissue characteristics of the individual patient.

Recently, MWA has been analyzed using a more complex heat transfer model based on the porosity concept that leads to two bioheat equations for tissue and blood temperatures [44]. The shape of the tumor is supposed to be spherical. Although it seems to be more realistic, the problem is that such an approach introduces a new set of parameters, whose values are very difficult to determine precisely. In an earlier reference [45], an effort to include the effects of tissue deformation during MWA was made, but only for an *in vitro* experiment with the liver (without tumor) under specific mechanical conditions, far from realistic MWA procedures. Both references present 2D axisymmetric calculations only. Most of the existing numerical models of MWA are mainly two-dimensional (2D) axis-symmetric, assuming a homogeneous medium and reducing the problem from three-dimensional (3D) to 2D [43,46,47].

Considering that each liver tumor is different, treatment options must be chosen on an individualized basis, depending on the tumor size and shape. The primary goal of this study was to demonstrate that 3D simulation is an ideal technique for MWA planning adjusted for each patient. For this purpose, we used a full 3D model of the MWA developed and tested using the COMSOL Multiphysics simulation platform [48–50]. Simulations were performed for a compact 10-slot coaxial antenna operating at 2.45 GHz inserted into realistic models of two tumors labeled as 1.07 and 1.03 in the 3D-IRCAdb-01 liver tumors database [51]. The optimal input power and duration of the ablation process were individually determined for each tumor, based on the time evolution of the iso-contours, temperature distribution, and degree of tissue destruction.

2. Materials and Methods

For this study, calculations were performed for a compact 10-slot microwave antenna, schematically shown in Figure 1 and described in detail in Ref. [48]. A compact 10-slot microwave antenna with an impedance π -matching network was designed to create predictable, optimal heating patterns with shorter ablation times and lower input powers, compared to previously developed antennae [52–54]. The required ablation shape was achieved by adopting the distance between the adjacent slots and the number of the slots. The finely tuned impedance π -matching network provides optimal ablation zones with minimal damage to surrounding healthy tissues. The disadvantage of such an antenna could be a relatively complicated construction, although it is compensated by its excellent features—optimal heating pattern and low overheating of healthy tissue.

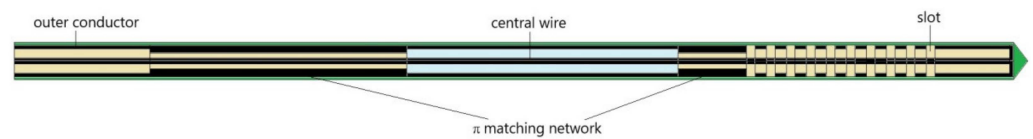


Figure 1. Schematic view of the 10-slot microwave antenna with an impedance π -matching network. The conducting material, Teflon, air, and dielectric are represented by black, green, light blue, and light brown, respectively. The width of the slot is 0.6 mm with a spacing of 0.8 mm between adjacent slots.

To demonstrate the importance of finding the optimal conditions for each patient individually, simulations were performed for two real tumors taken from the 3D-IRCAdB-01 database [51]. This database includes several sets of CT scans of patients manually segmented by clinical experts [55]. In this study, simulations were carried out for tumors denoted by 1.07 (1.74 cm \times 1.53 cm \times 2.10 cm) and 1.03 (1.78 cm \times 1.97 cm \times 2.27 cm) in the 3D-IRCAdB-01 liver tumors database [51]. The sizes and shapes of both cancers are shown in Figure 2.

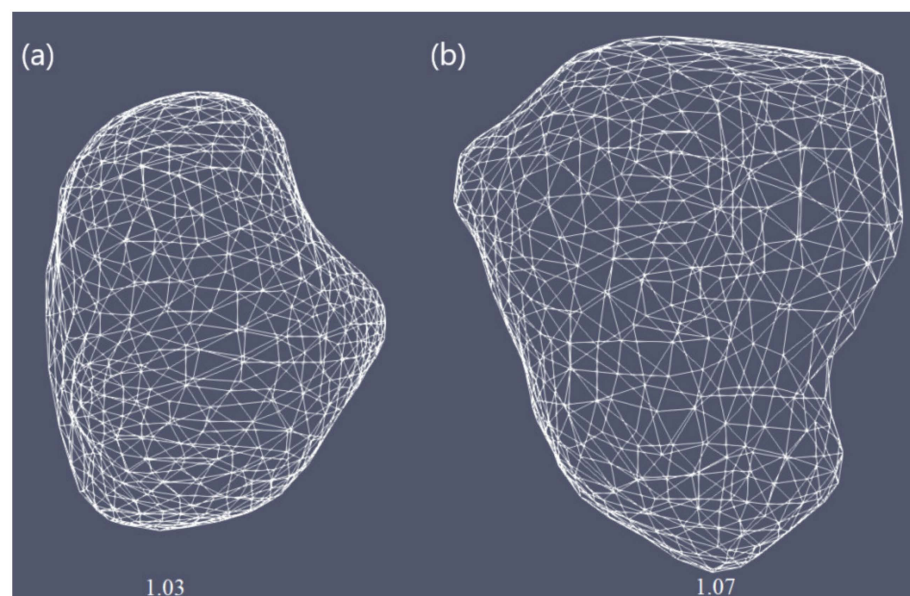


Figure 2. Three-dimensional simulation models corresponding to two liver tumors (triangulated surfaces) labeled as (a) 1.07 and (b) 1.03 in the 3D-IRCAdB-01 database that contains several sets of CT scans of the patients [51].

The simulation model was composed of the coupled electromagnetic field and heat-transfer equations solved by the 3D finite elements method (FEM), with all details of multi-slot antenna design and properties of healthy and tumoral tissues. Our 3D model was generated using the COMSOL Multiphysics FEM-based simulation platform [45]. Since the developed 3D model was completely described in a previous paper [48], we shall not attempt to repeat it here, except for the governing equations. The propagation of microwaves in the tissue by an antenna is expressed as [48,56]:

$$\nabla^2 E - \mu_r k_0^2 \left(\epsilon_r - \frac{j\sigma}{\omega \epsilon_0} \right) E = 0, \quad (1)$$

where E is the vector of the electric field and ω is the angular frequency. The value $k_0 = \omega/c_0$ is the vacuum propagation constant, and ϵ_0 is the vacuum dielectric constant. The electrical conductivity, relative permittivity, and permeability of the tissue are denoted by σ , ϵ_r , and μ_r , respectively. The electric field was calculated in the dielectric, healthy tissue, and tumor regions, with appropriate boundary conditions. On conducting surfaces, PEC conditions were imposed (the tangential component of the field was set to zero). On the computational zone boundaries (outer cylinder surfaces) the first order absorbing boundary conditions were used. The input power is connected to the antenna through the coaxial port on its top.

The Pennes bioheat equation describes the heat transfer during MWA [57]:

$$\rho c_{\text{eff}} \frac{\partial T}{\partial t} = \nabla \cdot (k \nabla T) + \rho_b W_b c_b (T_b - T) + Q_{\text{ext}} + Q_m, \quad (2)$$

where t is the time, ρ and T are the density and temperature of the tissue, respectively. Values ρ_b , c_b , T_b , and W_b are the density, heat capacity, temperature, and perfusion rate of the blood, respectively. Although the heat source from metabolism Q_m was neglected in our calculations, the external heat source Q_{ext} was related to coupling with the electromagnetic field. The effect of internal water evaporation in the bioheat Equation (2) was included by replacing specific heat c with an effective value, as described in ref. [48]:

$$c_{\text{eff}} = c - \frac{\alpha}{\rho} \frac{\partial W}{\partial T} \quad (3)$$

where α is the water latent heat constant equal to 2260 (kJ/kg), whereas $W(T)$ is the water content. The temperature was calculated only in healthy and tumor regions. Initial temperature was set to 37 °C. On the outer antenna surface and computational zone, boundaries zero flux (thermal insulation) boundary conditions were used.

The water content of liver tissue is approximately 78% water by mass; therefore, the thermal properties of the tissue are similar to those of water [58,59]. For temperatures above 100 °C, the water content of the tissue may decrease by mass owing to evaporation, causing substantial changes in tissue dielectric parameters and considerable penetration of microwaves [58]. The decrease in the dielectric properties of the tissue with increasing temperature due to evaporation was incorporated into our model according to the description in [48,60].

Tissue damage processes are regularly modeled via Arrhenius formalism defining an arbitrary function of tissue injury Ω as [61,62]:

$$\Omega(t) = \int_0^t A \exp\left(-\frac{\Delta E}{RT}\right) dt, \quad (4)$$

where A is the frequency factor, ΔE is the activation energy for the irreversible damage reaction, T is the temperature determined at each point in the model region, and R is the gas constant.

The proper choice of the input power and treatment time required to achieve the optimal ablation zones strongly depends on the size and the shape of the tumor. In this study, we performed realistic modeling of the effect of MWA operating at 2.45 GHz on two liver tumors of different sizes and shapes, denoted by 1.03 and 1.07 in the 3D-IRCADb-01 database [46]. The optimal input power and duration of the ablation process were individually estimated for each tumor. The simulation conditions included the density, dielectric properties, thermal conductivity, and heat capacity of the liver tissues (healthy and tumoral), as well as the density, thermal conductivity, and heat capacity of the blood listed in Table 1. The temperature dependence of the dielectric and thermal properties of both healthy and malignant liver tissues, blood perfusion, and water content were implemented in the simulation model [48,56].

Table 1. The parameters that characterize the liver tissue (healthy and tumoral) and the blood collected from the literature [48,56] and used in the numerical simulations.

Parameter	Value
<i>Healthy tissue</i>	
Density	1079 kg/m ³
Relative permittivity	44.3
Electric conductivity	1.8 S/m
Thermal conductivity	0.52 W/m °C
Specific heat	3540 J/kg °C
<i>Tumoral tissue</i>	
Density	1040 kg/m ³
Relative permittivity	54.8
Electric conductivity	2 S/m
Thermal conductivity	0.57 W/m °C
Specific heat	3960 J/kg °C
<i>Blood</i>	
Density	1060 kg/m ³
Thermal conductivity	0.5 W/m °C
Specific heat	3600 J/kg °C
Temperature	37 °C

3. Results and Discussions

For both tumors, the optimal value of the input power was chosen such that a very small area of healthy tissue around the tumor was damaged, based on the iso-contours shown in Figure 3. Since tumors do not have regular shapes on both sides, the front (left) and back (right) of tumors are displayed. For tumor 1.07 [51] (see Figure 3a), if 9 W was applied, tumoral tissue (backside) was not entirely removed. When the input power was 11 W, the ablation zone enclosed the entire tumor as well as a large amount of healthy tissue. The iso-contour that best fit the necrotic tissue was obtained for an input power of 10 W, leading to a treated tumor with minimal damage to the healthy surrounding tissue. However, the application of 11 W in the case of tumor 1.03 [51] (see Figure 3b) did not ensure complete malignancy (both sides). Although the entire tumor was eliminated using an input power of 13 W, the healthy tissue was significantly damaged. Therefore, the best choice of input power, for tumor 1.03 [51] was 12 W, because the whole tumor was destroyed while healthy tissue was preserved.

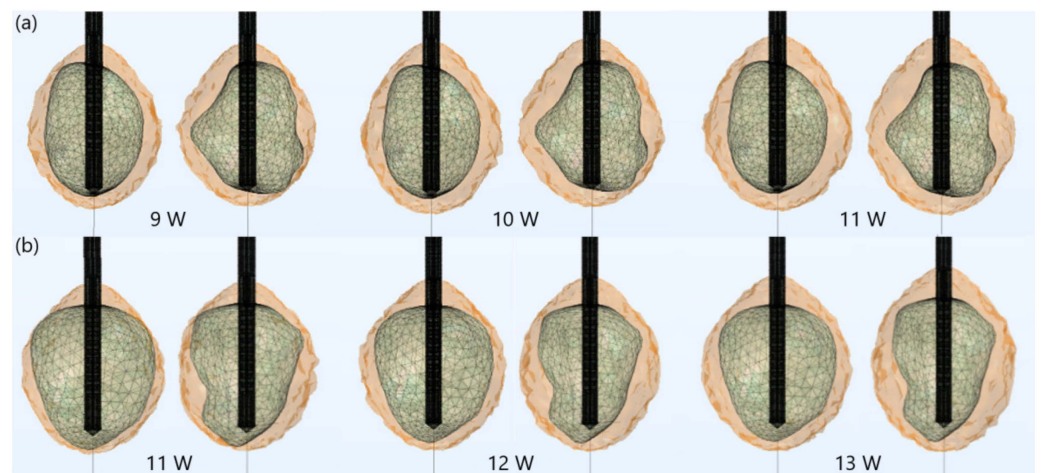


Figure 3. Iso-contours representing the ablated regions (solid light brown surface) after 600 s of MWA at 2.45 GHz around tumors (triangulated surface) (a) 1.07 [51] (for input powers of 9 W, 10 W, and 11 W) and (b) 1.03 [51] (for input powers of 11 W, 12 W, and 13 W).

The importance of proper determination of the input power and ablation time is illustrated in Figure 4. If a power of 15 W or 17 W was applied for MWA of the tumor 1.07 [51] (Figure 4a), the ablation time should be shortened from 600 s to 340 s or 300 s, respectively. If tumor 1.03 [46] (Figure 4b) was treated with an input power of 15 W or 17 W, the ablation time required for complete removal of tumoral tissue should be 440 s or 380 s, respectively. Damages to healthy surrounding tissue by applying 15 W or 17 W during a shorter ablation time were similar to those obtained for 10 W (for tumor 1.07 [51]) and 12 W (for tumor 1.07 [51]) after 600 s. However, this did not necessarily mean that higher input power and shorter ablation time corresponded to the most efficient and safe MWA procedure. As can be observed from Figure 5, higher input power increased damage to surrounding healthy tissue, due to undesirable shapes of ablation zones, even if the ablation time was shorter. For powers of 20 W (for tumor 1.07 [51]) and 25 W (for tumor 1.03 [46]) the ablation zones formed were neither spherical nor predictable. They appeared to be elongated, with a greater length along the shaft of the antenna than the transverse diameter. Elongated shapes were undesirable ablation patterns that caused unavoidable damage to normal tissues, even if the ablation time was shorter.

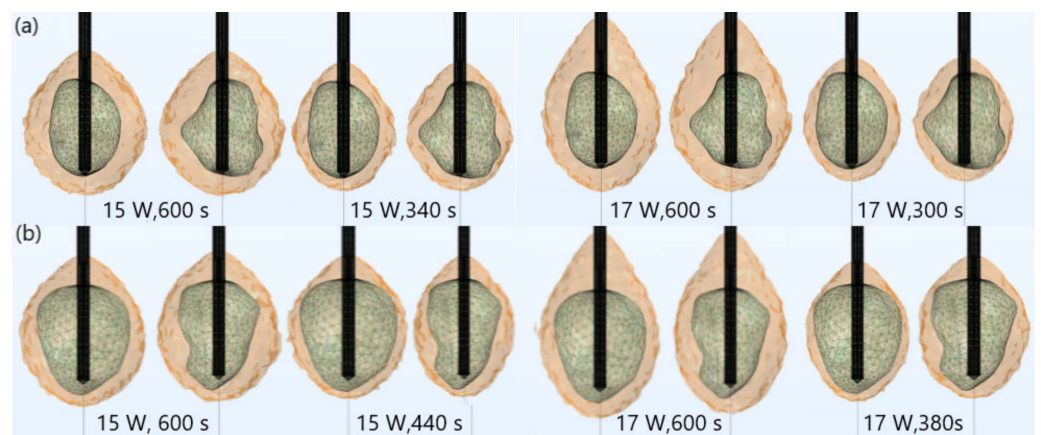


Figure 4. Iso-contours consisting of totally ablated regions (solid light brown surface) and tumors (triangulated surface) (a) 1.07 [51] and (b) 1.03 [51] exposed to a frequency of 2.45 GHz, an input power of 15 W and 17 W for various ablation times.

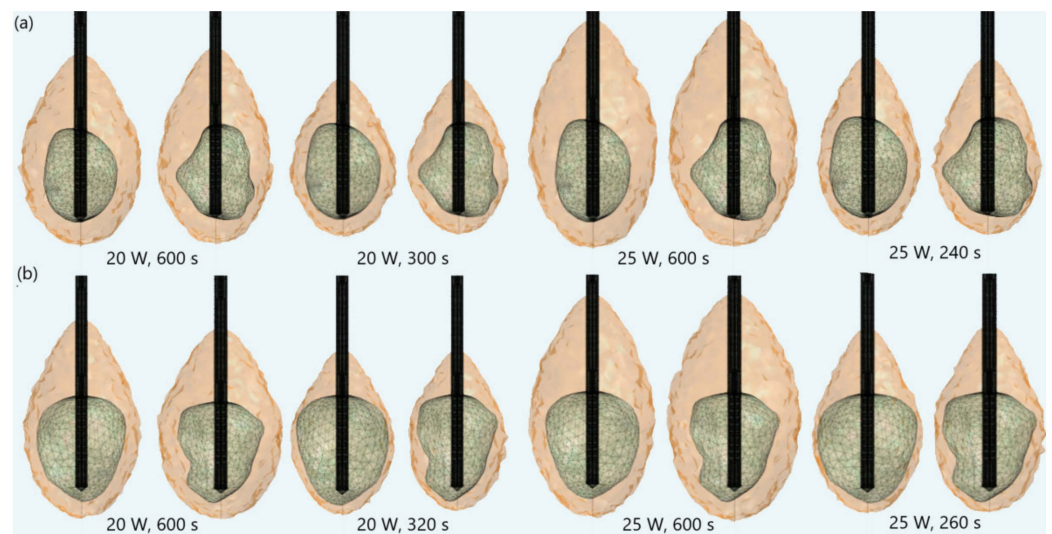


Figure 5. Iso-contours that include the ablated regions (solid light brown surface) around the liver tumor (triangulated surface) (a) 1.07 [51] and (b) 1.03 [51] when an input power of 20 W or 25 W is applied during various ablation times.

The ablation times as a function of the input power for tumors 1.03 [51] and 1.07 [51] are plotted in Figure 6a. Although the ablation time decreased with increasing power for both tumors, the ablation time of tumor 1.03 [51] was systematically higher, owing to its larger size. The difference between ablation times of tumors 1.03 [51] and 1.07 [51] was approximately 25% for the power of 12 W and approximately 8% for 25 W. Controlling the power/time values allowed for changes in ablation sizes. The optimal choice of the input power and the ablation time should be made by the surgeon since it depends on medical factors. The time dependence of the temperature on the input power calculated at the point in the center of the heating zone is shown in Figure 6b. The antenna immersed in the tissue radiated energy that was absorbed and converted into thermal energy, causing an increase in the tissue temperature. Despite the input power, the temperature first rapidly increased with increasing time, and then steeply rose and reached saturation when the diffusion and heat conduction, due to blood perfusion, became significant. The obtained simulation results had similar trends as the results of measurements for liver tissue provided in Ref. [63].

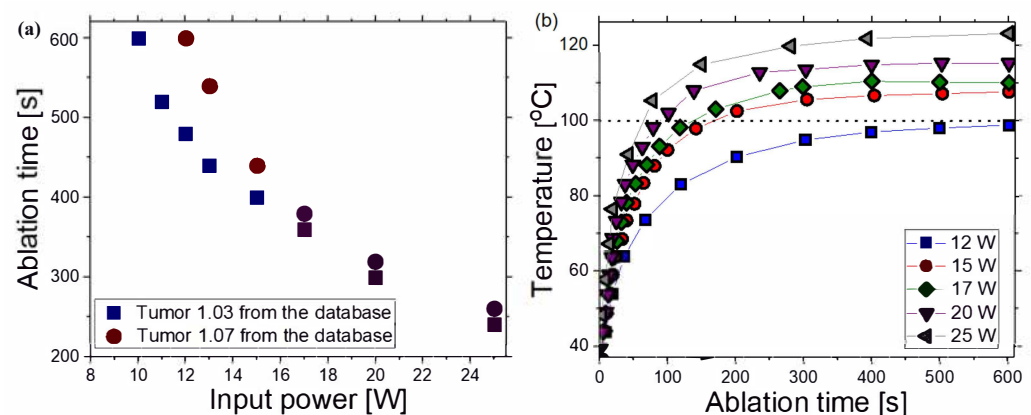


Figure 6. (a) Dependence of the ablation time on the input power for tumor 1.03 [51] (blue squares) and tumor 1.07 [51] (red circles). (b) Temperature as a function of the ablation time for various input power values calculated in the center of the heating zone.

Figure 7 displays iso-contours of the temperature distribution in the tissue at $t = 600$ s for the optimal input power of 10 W and 12 W for tumors (a) 1.07 [51] and (b) 1.03 [51], respectively, chosen to affect a very small area of surrounding healthy tissue. For both tumors, iso-contours had similar near-spherical shapes. The temperature was the highest in the vicinity of the antenna slot, while it noticeably dropped as the distance from the antenna increased. The maximum values of the temperature were achieved inside the tumor regions where cancer cells were destroyed. It was reported that temperatures above 60°C instantly destroyed all cancer cells [62], so the 60°C isothermal contour was related to the lesion size and shape of the ablated tissue. According to previous studies [48,56], a multi-slot antenna structure enabled more localized and optimal heating distributions.

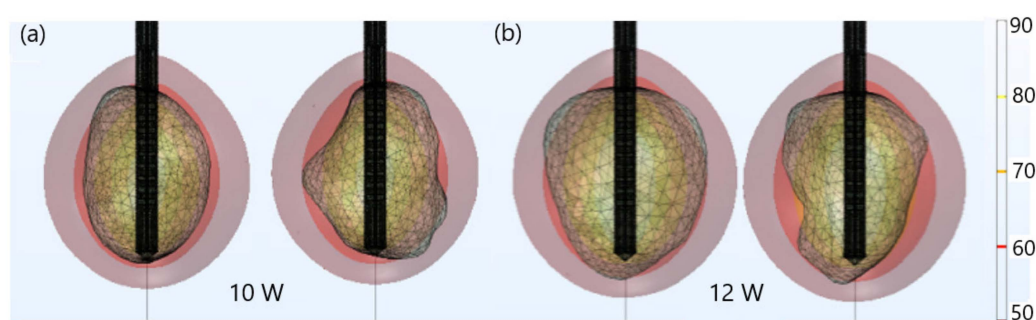


Figure 7. Iso-contours associated with various temperatures (solid colored surface) around tumors (triangulated surface) (a) 1.07 [51] (for an input power of 10 W) and (b) 1.03 [51] (for an input power of 12 W).

The absorbed energy was converted into thermal energy, resulting in an increase in tissue temperature. Temperature changes in tissues during MWA for tumors (a) 1.07 [51] and (b) 1.03 [51] are shown in Figure 8. The black line represents the boundary of the tumoral tissue. The temperature value was the highest close to the antenna and decreased with distance from the antenna, where the heat source became weaker. Blood perfusion restricted the extent of the heated area. The temperature increased with the ablation time and after 600 s reached a value of approximately 92°C for tumor 1.07 [51] and 98°C for tumor 1.03 [51]. When the temperature approached 100°C , a boiling effect could occur in the tissues [64].

The thermal damage fraction and the time required for complete necrosis of tumors (a) 1.07 [51] and (b) 1.03 [51] are presented in Figure 9. The upper figures are obtained in the cut plane ($x = 0$), where the black line shows the boundary of the tumoral tissue. Regardless of the time, ablation zones were concentrated around the tip and slots of the antenna with small backward heating. The active ablation zone closest to the antenna encompassed the volume of tissue that was subjected to sufficiently high energy absorption to ensure thermal tissue. In contrast, the passive ablation zone surrounded the active zone involving the volume of tissue, which experienced a lower intensity of energy absorption [43,48]. However, the ablation zones shown in the upper figures (in the cut plane) may not accurately reflect the ablated tissue. Based on the upper figures, for example, one might conclude that the entire tumoral tissue was removed after 400 s, which was far from reality. As can be seen from the lower figures, the front and back sides of both tumors were not completely ablated after 400 s. The lower figures indicated the entire tumors would not be removed before 600 s, implying the importance of performing full 3D simulations for each tumor individually, due to tumor geometric complexity. Figure 9 indicates that correct ablation time can be determined only if calculations are performed for actual shapes of tumors.

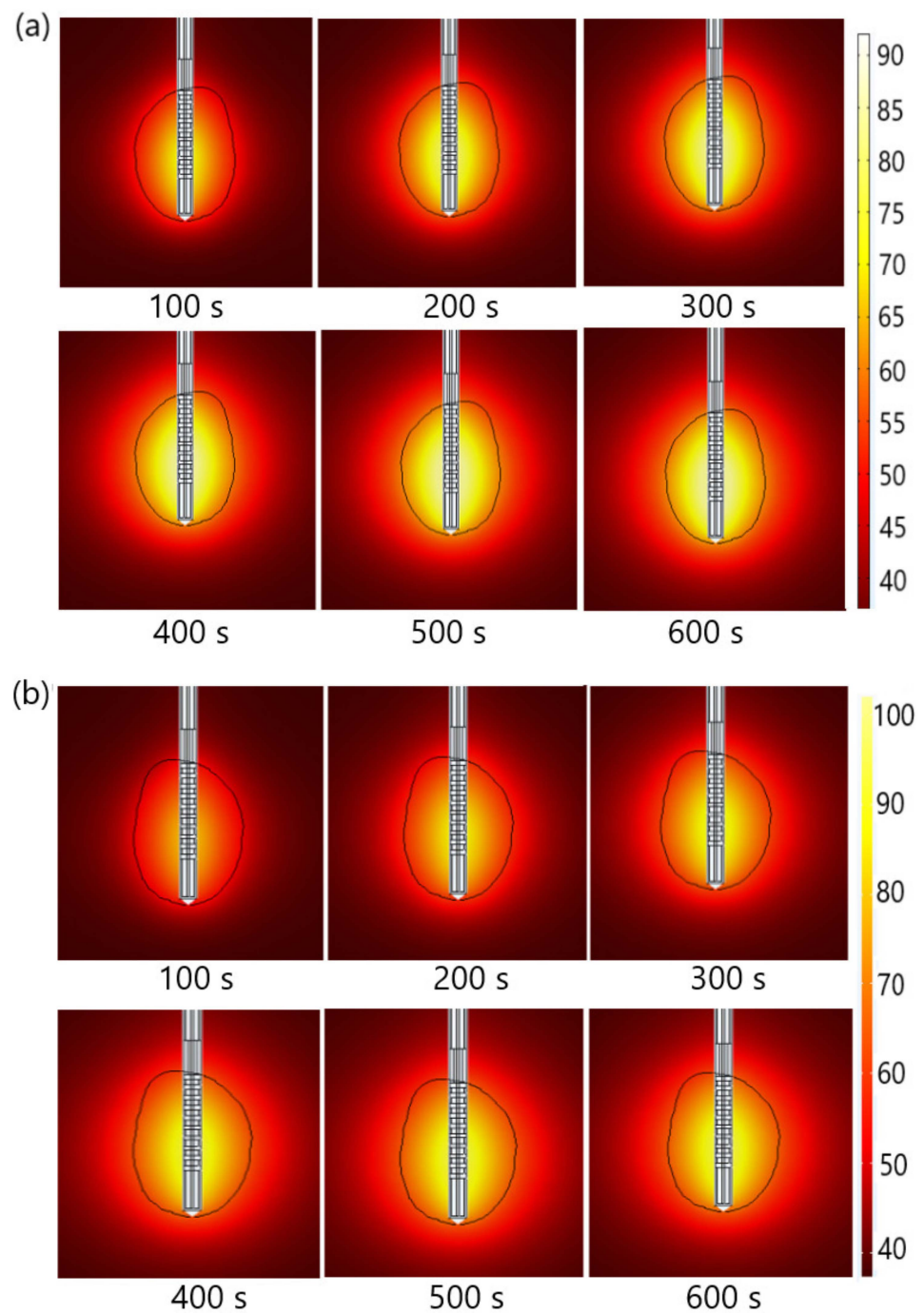


Figure 8. Time evolution of the temperature distribution (in °C) for tumors (a) 1.07 [51] and (b) 1.03 [51] treated by MWA at a frequency of 2.45 GHz. The boundary of the tumor tissue is marked by a black line.

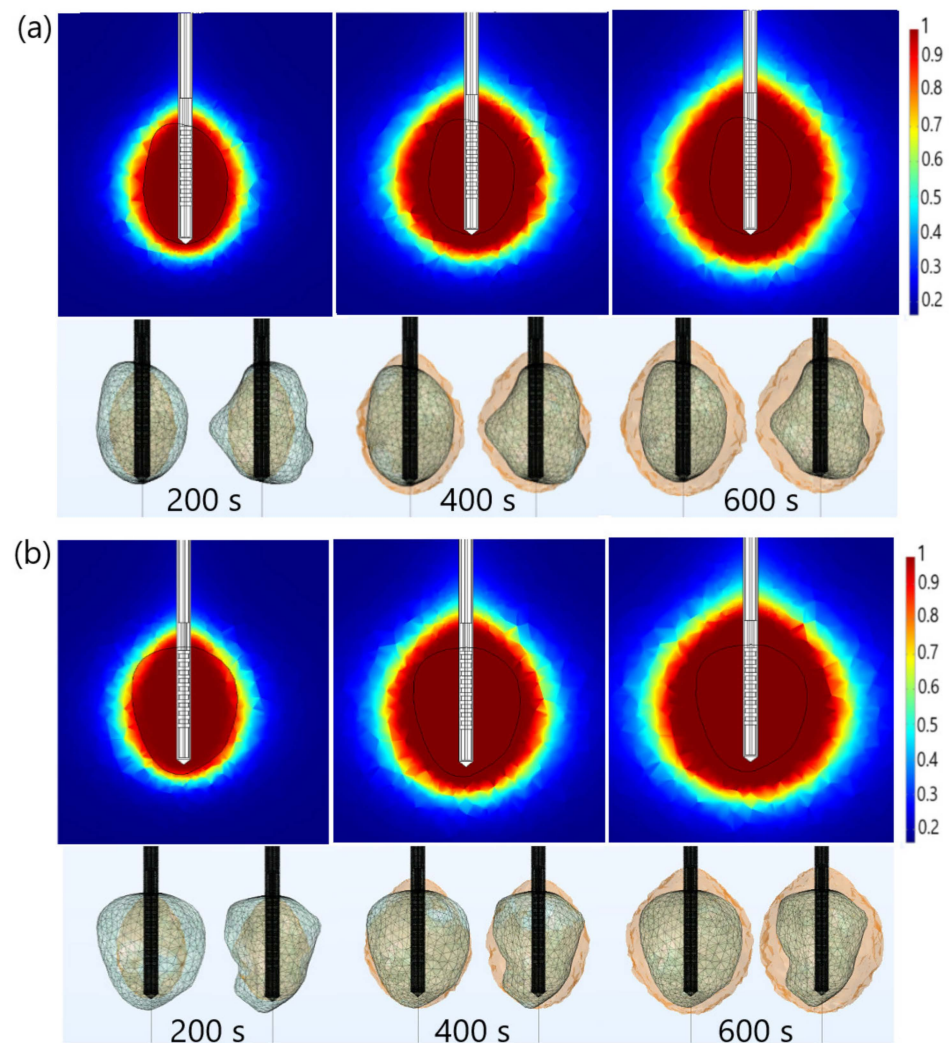


Figure 9. The time evolution of the necrotic tissue of tumors (a) 1.07 [51] and (b) 1.03 [51], after 200 s, 400 s, and 600 s MWA at a frequency of 2.45GHz. The upper figures show the necrotic tissue in the cut plane ($x = 0$). The lower figures show the front and back sides of the tumors (triangulated surfaces).

4. Conclusions

This study aimed to determine the most influential parameters (input power and ablation time) for successful tumor ablation with an adequate safety margin, while avoiding injury to the surrounding healthy tissue. To achieve this goal, full three-dimensional simulations developed within the COMSOL simulation package were used. Calculations were performed for a 10-slots antenna operating at 2.45 GHz immersed in liver tumors labeled as 1.07 and 1.03 in the database 3D-ICRADb-01 [51]. The density, thermal conductivity, and heat capacity of the liver tissues (healthy and tumoral) and blood were collected from the literature [48,56]. The temperature dependence of the dielectric and thermal properties of both healthy and malignant liver tissues, blood perfusion, and water content were included because of the importance of establishing a correct ablation process.

The size of the ablative zone was determined by the amount of energy delivered from the microwave generator to the antenna. Higher input power than the optimal value led to significant damage to surrounding healthy tissue, due to undesirable shapes of ablation zones. The optimal values of the input power for tumors 1.07 [51] and 1.03 [51] were 10 W and 12 W, respectively, enabling optimal ablation zones concentrated around the tip and slots of the antenna, resulting in successful ablation of the tumors with minimal damage to healthy tissues. As expected, a higher power would increase temperatures and reduce the overall time to necrose tumoral tissue. For tumor 1.07 [51], the ablation times for 25 W

and 10 W differed by approximately 60%. For tumor 1.03 [51], the application of 25 W would reduce the ablation time by approximately 57%, compared to that for 12 W. However, higher values of input power and shorter ablation time sometimes led to the formation of elongated ablation zones, causing significant damage to healthy tissue around the tumor. In addition, it was reported that delivery of high-power, short-duration ablation is not commonly used because of the increased risk of steam pop and thrombus formation [65]. The temperature increased with the ablation time, reaching the maximum value near the microwave antenna slots. The maximal temperature for 25 W differed by approximately 21%, 15%, 9%, and 8.5% from those calculated for 12 W, 15 W, 17 W, and 20 W, respectively. It was also demonstrated that axisymmetric calculations are not sufficient to estimate the optimal input power and ablation time. Thus, full 3D simulations, that take into account details of the tumor geometry, are needed [48,66].

The obtained results can be used to determine the optimal conditions for microwave ablation to be as effective as possible for treating liver tumors with minimal invasiveness and collateral damage. The developed three-dimensional predictive model of the microwave ablation procedure with all details of the tissue antenna design is a prerequisite, not only for further ablation studies but also for planning the MWA procedure for each patient individually. Regarding the limitations of the simulation model, it has to be pointed out that macroscale models of biological tissues are either based on the mixture theory of continuum mechanics or on the porous-media theory [67]. Simply put, Pennes' bioheat equation belongs to the first group, reducing the complete tissue model to a single heat transport equation with an additional term describing heat removal by blood perfusion. Models based on porous-media theory [67–69] are more complex, usually containing at least two equations: one for tissue and one for blood temperature. Of course, more subtle aspects can be included (thermo-mechanical, microscopic, etc.), but in this paper, we concentrated on problems connected with full 3D modeling of antennae used in MWA procedures and realistic tumor shapes of actual patients. Finally, it has to be pointed out that before any applications, experimental validation is mandatory to verify the reliability of predictive models.

Author Contributions: Conceptualization, M.R.-R. and B.R.; methodology, M.R.-R., B.R., N.B. and M.S.; software, B.R., M.R.-R. and N.B.; investigation and data interpretation, M.R.-R., B.R., N.B. and M.S.; original draft preparation, M.R.-R. and B.R.; writing—review, and editing, all of the authors; supervision, B.R. and M.R.-R. All authors have read and agreed to the published version of the manuscript.

Funding: Authors M.R.-R., N.B. and B.R. acknowledge that this research was supported by the Science Fund of the Republic of Serbia, The Program IDEAS, GRANT No. 7739583, SimSurgery. M.S. acknowledges support of the Operational Programme Integrated Infrastructure for the projects: International Center of Excellence for Research on Intelligent and Secure Information and Communication Technologies and Systems (ITMS code: 313021W404) and Research in the SANET network and possibilities of its further use and development (ITMS code: 313011W988), co-funded by the European Regional Development Fund (ERDF).

Institutional Review Board Statement: Not applicable.

Informed Consent Statement: Not applicable.

Data Availability Statement: Data is contained within the article.

Conflicts of Interest: The authors declare no conflict of interest.

References

1. Yamashita, T.; Wang, X.W. Cancer stem cells in the development of liver cancer. *J. Clin. Investig.* **2013**, *123*, 1911–1918. [CrossRef] [PubMed]
2. Sia, D.; Villanueva, A.; Friedman, S.L.; Llovet, J.M. Liver Cancer Cell of Origin, Molecular Class, and Effects on Patient Prognosis. *Gastroenterology* **2017**, *152*, 745–761. [CrossRef] [PubMed]
3. Willacy, H. Primary Liver Cancer. 2018. Available online: <https://patient.info/cancer/primary-liver-cancer-leaflet> (accessed on 8 February 2022).

4. Pichard, G. Understanding Liver Cancer—The Basics. 2019. Available online: <https://www.webmd.com/cancer/understanding-liver-cancer-basic-information> (accessed on 10 February 2022).
5. Crespo, M.; Leiva, M.; Sabio, G. Circadian Clock and Liver Cancer. *Cancers* **2021**, *13*, 3631. [CrossRef] [PubMed]
6. Liu, H.; Zhang, W.; Jia, Y.; Yu, Q.; Grau, G.E.; Peng, L.; Ran, Y.; Yang, Z.; Deng, H.; Lou, J. Single-cell clones of liver cancer stem cells have the potential of differentiating into different types of tumor cells. *Cell Death Dis.* **2013**, *4*, e857. [CrossRef] [PubMed]
7. Gaba, R.C.; Zivin, S.P.; Dikopf, M.S.; Parvinian, A.; Casadaban, L.C.; Lu, Y.; Bui, J.T. Characteristics of Primary and Secondary Hepatic Malignancies Associated with Hepatopulmonary Shunting. *Radiology* **2014**, *271*, 602–612. [CrossRef] [PubMed]
8. Watson, J.; Hydon, K.; Lodge, P. Primary and secondary liver tumours. *InnovAiT* **2016**, *9*, 477–482. [CrossRef]
9. Heinrich, S.; Lang, H. Hepatic resection for primary and secondary liver malignancies. *Innov. Surg. Sci.* **2017**, *2*, 1–8. [CrossRef]
10. Markman, M. Liver Cancer Types. 2021. Available online: <https://www.cancercenter.com/cancer-types/liver-cancer/types> (accessed on 13 February 2022).
11. Vogl, T.J.; Nour-Eldin, N.A.A.; Hammerstingl, R.M.; Panahi, B.; Naguib, N.N.N. Microwave Ablation (MWA): Basics, Technique and Results in Primary and Metastatic Liver Neoplasms—Review Article. *Fortschr. Röntgenstr.* **2017**, *189*, 1055–1066. [CrossRef]
12. Llovet, J.M.; Kelley, R.K.; Villanueva, A.; Singal, A.G.; Pikarsky, E.; Roayaie, S.; Lencioni, R.; Koike, K.; Zucman-Rossi, J.; Finn, R.S. Hepatocellular carcinoma. *Nat. Rev. Dis. Prim.* **2021**, *7*, 6. [CrossRef]
13. Hui, T.C.; Kwan, J.; Pua, U. Advanced Techniques in the Percutaneous Ablation of Liver Tumours. *Diagnostics* **2021**, *11*, 585. [CrossRef]
14. Shira, K.; Ebata, T.; Oda, K.; Nishio, X.; Nagasaka, T.; Nimura, Y.; Nagino, M. Perineural Invasion Is a Prognostic Factor in Intrahepatic Cholangiocarcinoma. *World J. Surg.* **2008**, *32*, 2395–2402. [CrossRef] [PubMed]
15. Chen, J.G.; Chen, H.Z.; Zhu, J.; Yang, Y.L.; Zhang, Y.H.; Huang, P.X.; Chen, Y.S.; Zhu, C.Y.; Yang, L.P.; Shen, K.; et al. Cancer survival in patients from a hospital-based cancer registry, China. *J. Cancer* **2018**, *9*, 851–860. [CrossRef] [PubMed]
16. Chen, J.; Zhu, J.; Zhang, Y.; Chen, Y.; Lu, J.; Zhu, Y.; Chen, H.; Shen, A.; Wang, G.; Groopman, J.D.; et al. Liver cancer mortality over six decades in an epidemic area: What we have learned. *PeerJ* **2021**, *9*, e10600. [CrossRef] [PubMed]
17. Linn, Y.L.; Chee, M.Y.; Koh, Y.X.; Teo, J.T.; Cheow, P.C.; Chow, P.K.H.; Chan, C.Y.; Chung, A.Y.F.; Ooi, L.L.P.; Jgoh, B.K.P. Actual 10-year survivors and 10-year recurrence free survivors after primary liver resection for hepatocellular carcinoma in the 21st century: A single institution contemporary experience. *J. Surg. Oncol.* **2021**, *123*, 214–221. [CrossRef]
18. Chen, J.G.; Zhu, J.; Zhang, Y.H.; Chen, Y.S.; Ding, L.L.; Chen, H.Z.; Shen, A.G.; Wang, G.R. Liver Cancer Survival: A Real World Observation of 45 Years with 32,556 Cases. *J. Hepatocell. Carcinoma* **2021**, *8*, 1023–1034. [CrossRef]
19. Chen, J.G.; Zhang, Y.H.; Zhu, J.; Lu, J.H.; Wang, J.B.; Sun, Y.; Xue, X.F.; Lu, L.L.; Chen, Y.S.; Wu, Y.; et al. Early diagnosis and early treatment for liver cancer in Qidong: Survival of patients and effectiveness of screening. *Chin. J. Oncol.* **2017**, *39*, 946–951. [CrossRef]
20. Hassanipour, S.; Mohammadzadeh, M.; Mansour-Ghanaei, F.; Fathalipour, M.; Joukar, F.; Salehiniya, H.; Abdzadeh, E.; Samadani, A.A.; Nikbakht, H.A.; Arab-Zozani, M. The Incidence of Hepatocellular Carcinoma in Iran from 1996 to 2016: A Systematic Review and Meta-analysis. *J. Gastrointest. Cancer* **2019**, *50*, 193–200. [CrossRef]
21. Chen, J.G.; Zhang, Y.H.; Lu, L.L.; Chen, H.Z.; Shen, A.G.; Zhu, Y.R. Liver cancer screening in China: Practices and its extended questions. *Hepatoma. Res.* **2019**, *5*, 2. [CrossRef]
22. Chong, C.C.N.; Lee, K.F.; Chu, C.M.; Chan, A.W.H.; Wong, J.; Chan, S.L.; Lok, H.T.; Fung, A.K.Y.; Fong, A.K.Y.; Cheung, Y.S.; et al. Microwave ablation provides better survival than liver resection for hepatocellular carcinoma in patients with borderline liver function: Application of ALBI score to patient selection. *HPB* **2018**, *20*, 546–554. [CrossRef]
23. Liu, C.Y.; Chen, K.F.; Chen, P.J. Treatment of Liver Cancer. *Cold Spring Harb. Perspect. Med.* **2015**, *5*, a021535. [CrossRef]
24. Ong, S.L.; Gravante, G.; Metcalfe, M.S.; Strickland, A.D.; Dennison, A.R.; Lloyd, D.M. Efficacy and safety of microwave ablation for primary and secondary liver malignancies: A systematic review. *Eur. J. Gastroenterol. Hepatol.* **2009**, *21*, 599–605. [CrossRef] [PubMed]
25. Facciorusso, A.; Di Maso, M.; Muscatiello, N. Microwave ablation versus radiofrequency ablation for the treatment of hepatocellular carcinoma: A systematic review and meta-analysis. *Int. J. Hyperth.* **2016**, *32*, 339–344. [CrossRef] [PubMed]
26. Glassberg, M.B.; Ghosh, S.; Clymer, J.W.; Wright, G.W.J.; Ferko, N.; Amaral, J.F. Microwave ablation compared with hepatic resection for the treatment of hepatocellular carcinoma and liver metastases: A systematic review and meta-analysis. *World J. Surg. Oncol.* **2019**, *17*, 98. [CrossRef] [PubMed]
27. Suresh, D.; Srinivas, A.N.; Kumar, D.P. Etiology of Hepatocellular Carcinoma: Special Focus on Fatty Liver Disease. *Front. Oncol.* **2020**, *10*, 601710. [CrossRef]
28. Koulouris, A.; Tsagkaris, C.; Spyrou, V.; Pappa, E.; Troullinou, A.; Nikolaou, M. Hepatocellular Carcinoma: An Overview of the Changing Landscape of Treatment Options. *J. Hepatocell. Carcinoma* **2021**, *8*, 387–401. [CrossRef]
29. Reig, M.; Forner, A.; Rimola, J.; Ferrer-Fàbrega, J.; Burre, M.; Garcia-Criado, A.; Kelley, R.K.; Galle, P.R.; Mazzaferro, V.; Salem, R.; et al. BCLC strategy for prognosis prediction and treatment recommendation: The 2022 update. *J. Hepatol.* **2022**, *76*, 681–693. [CrossRef]
30. Radiofrequency Ablation (RFA)/Microwave Ablation (MWA) of Liver Tumors. 2021. Available online: <https://www.radiologyinfo.org/en/info/rfaliver> (accessed on 14 February 2022).

31. Ausania, F.; Borin, A.; Melendez, R.; del Rio, P.S.; Iglesias, A.; Bodenlle, P.; Paniagua, M.; Arias, M. Microwave ablation of colorectal liver metastases: Impact of a 10-mm safety margin on local recurrence in a tertiary care hospital. *Ann. Hepatobiliary Pancreat. Surg.* **2021**, *25*, 366–370. [\[CrossRef\]](#)
32. Inchingolo, R.; Posa, A.; Mariappan, M.; Spiliopoulos, S. Locoregional treatments for hepatocellular carcinoma: Current evidence and future directions. *World J. Gastroenterol.* **2019**, *25*, 4614–4628. [\[CrossRef\]](#)
33. Yau, T.; Kang, Y.K.; Kim, T.Y.; El-Khoueiry, A.B.; Santoro, A.; Sangro, B.; Melero, I.; Kudo, M.; Hou, M.M.; Matilla, A.; et al. Nivolumab (NIVO) + ipilimumab (IPI) combination therapy in patients (pts) with advanced hepatocellular carcinoma (aHCC): Results from CheckMate 040. *J. Clin. Oncol.* **2019**, *37*, 4012. [\[CrossRef\]](#)
34. Crocetti, L.; Scalise, P.; Bozzi, E.; Campani, D.; Rossi, P.; Cervelli, R.; Bargellini, I.; Ghinolfi, D.; De Simone, P.; Cioni, R. Microwave Ablation of Very-Early- and Early-Stage HCC: Efficacy Evaluation by Correlation with Histology after Liver Transplantation. *Cancers* **2021**, *13*, 3420. [\[CrossRef\]](#)
35. Primavesi, F.; Swierczynski, S.; Klier, E.; Kiesslich, T.; Jäger, T.; Urbas, R.; Hutter, J.; Neureiter, D.; Öfner, D.; Stättner, S. Thermographic real-time-monitoring of surgical radiofrequency and microwave ablation in a perfused porcine liver model. *Oncol. Lett.* **2018**, *15*, 2913–2920. [\[CrossRef\]](#) [\[PubMed\]](#)
36. Huang, H.; Zhang, L.; Moser, M.A.J.; Zhang, W.; Zhang, B. A review of antenna designs for percutaneous microwave ablation. *Phys. Med.* **2021**, *84*, 254–264. [\[CrossRef\]](#) [\[PubMed\]](#)
37. Kuroda, H.; Nagasawa, T.; Fujiwara, Y.; Sato, H.; Abe, T.; Kooka, Y.; Endo, K.; Oikawa, T.; Sawara, K.; Takikawa, Y. Comparing the Safety and Efficacy of Microwave Ablation Using Thermosphere™ Technology versus Radiofrequency Ablation for Hepatocellular Carcinoma: A Propensity Score-Matched Analysis. *Cancers* **2021**, *13*, 1295. [\[CrossRef\]](#) [\[PubMed\]](#)
38. Ge, M.; Jiang, H.; Huang, X.; Zhou, Y.; Zhi, D.; Zhao, G.; Chen, Y.; Wang, L.; Qiu, B. A multi-slot coaxial microwave antenna for liver tumor ablation. *Phys. Med. Biol.* **2018**, *6*, 175011. [\[CrossRef\]](#)
39. Andreozzi, A.; Iasiello, M.; Netti, P.A. A thermoporoelectric model for fluid transport in tumour tissues. *J. R. Soc. Interface* **2019**, *16*, 20190030. [\[CrossRef\]](#)
40. Singh, S.; Melnik, R. Domain heterogeneity in radiofrequency therapies for pain relief: A computational study with coupled models. *Bioengineering* **2020**, *7*, 35. [\[CrossRef\]](#)
41. Rubio, M.F.; López, G.D.; Perezgasga, F.V.; García, F.F.; Hernández, A.V.; Salas, L.L. Computer Modeling for Microwave Ablation in Breast Cancer Using a Coaxial Slot Antenna. *Int. J. Thermophys.* **2015**, *36*, 2687–2704. [\[CrossRef\]](#)
42. Reinhardt, M.; Brandmaier, P.; Seider, D.; Kolesnik, M.; Jenniskens, S.; Sequeiros, R.B.; Eibisberger, M.; Voglreiter, P.; Ronan Flanagan, R.; Mariappan, P.; et al. A prospective development study of software-guided radio-frequency ablation of primary and secondary liver tumors: Clinical intervention modelling, planning and proof for ablation cancer treatment (ClinicIMPACT). *Contemp. Clin. Trials Commun.* **2017**, *8*, 25–32. [\[CrossRef\]](#)
43. Radmilović-Radjenović, M.; Radjenović, D.; Radjenović, B. Finite element analysis of the effect of microwave ablation on the liver, lung, kidney, and bone malignant tissues. *Europhys. Lett.* **2021**, *135*, 3500. [\[CrossRef\]](#)
44. Tucci, C.; Trujillo, M.; Berjano, E.; Iasiello, M.; Andreozzi, A.; Vanoli, G.P. Mathematical modeling of microwave liver ablation with a variable-porosity medium approach. *Comput. Methods Progr. Biomed.* **2022**, *214*, 106569. [\[CrossRef\]](#)
45. Keangin, P.; Wessapan, T.; Rattanadecho, P. Analysis of heat transfer in deformed liver cancer modeling treated using a microwave coaxial antenna. *Appl. Therm. Eng.* **2011**, *31*, 3243–3254. [\[CrossRef\]](#)
46. Wang, X.; Gao, H.; Wu, S.; Jiang, T.; Zhou, Z.; Bai, Y. Numerical evaluation of ablation zone under different tip temperatures during radiofrequency ablation. *Math. Biosci. Eng.* **2019**, *16*, 2514–2531. [\[CrossRef\]](#)
47. Radmilović-Radjenović, M.; Sabo, M.; Prnova, M.; Šoltes, L.; Radjenović, B. Finite Element Analysis of the Microwave Ablation Method for Enhanced Lung Cancer Treatment. *Cancers* **2021**, *13*, 3500. [\[CrossRef\]](#) [\[PubMed\]](#)
48. Radjenović, B.; Sabo, M.; Šoltes, L.; Prnova, M.; Čičak, P.; Radmilović-Radjenović, M. On Efficacy of Microwave Ablation in the Thermal Treatment of an Early-Stage Hepatocellular Carcinoma. *Cancers* **2021**, *13*, 5784. [\[CrossRef\]](#)
49. Comsol Multiphysics. 1986–2020. Burlington (MA): COMSOL, Inc. Available online: <https://www.comsol.com/comsol-multiphysics> (accessed on 7 March 2022).
50. Heat Transfer Modeling Software for Analyzing Thermal Effects. Burlington (MA): COMSOL, Inc. Available online: <https://www.comsol.com/heat-transfer-module> (accessed on 7 March 2022).
51. 3D-IRCADb. Strasbourg (F): IrcadFrance. Available online: <https://www.ircad.fr/research/data-sets/liver-segmentation-3d-ircadb-01/> (accessed on 7 March 2022).
52. Ibitoye, A.Z.; Nwoye, E.O.; Aweda, A.M.; Oremosu, A.A.; Anunobi, C.C.; Akanmu, N.O. Microwave ablation of ex vivo bovine tissues using a dual slot antenna with a floating metallic sleeve. *Int. J. Hypertherm.* **2016**, *32*, 923–930. [\[CrossRef\]](#) [\[PubMed\]](#)
53. Yang, D.S.; Bertram, J.M.; Converse, M.C.; O'Rourke, A.P.; Webster, J.G.; Hagness, S.C.; Will, J.A.; Mahvi, D.M. A floating sleeve antenna yields localized hepatic microwave ablation. *IEEE Trans. Bio-Med. Eng.* **2006**, *53*, 533–537. [\[CrossRef\]](#)
54. Luyen, H.; Hagness, S.C.; Behdad, N. Reduced-Diameter Designs of Coax-Fed Microwave Ablation Antennas Equipped with Baluns. *IEEE Antennas Wirel. Propag. Lett.* **2017**, *16*, 1385–1388. [\[CrossRef\]](#)
55. Cazacu, D.I. Modeling and Simulation of Microwave Ablation of Liver Tumors. Ph.D. Thesis, Jacobs University, Bremen, Germany, 2019. Available online: <https://opus.jacobs-university.de/frontdoor/index/index/docId/887> (accessed on 25 February 2022).
56. Tehrani, M.H.H.; Soltani, M.; Kashkooli, F.M.; Raahemifar, K. Use of microwave ablation for thermal treatment of solid tumors with different shapes and sizes—A computational approach. *PLoS ONE* **2020**, *15*, e0233219. [\[CrossRef\]](#)

-
57. Pennes, H.H. Analysis of tissue and arterial blood temperatures in the resting human forearm. *J. Appl. Physiol.* **1948**, *1*, 93–122. [[CrossRef](#)]
 58. Cavagnaro, M.; Pinto, R.; Lopresto, V. Numerical models to evaluate the temperature increase induced by ex vivo microwave thermal ablation. *Phys. Med. Biol.* **2015**, *60*, 3287–3311. [[CrossRef](#)]
 59. Stauffer, P.R.; Rossetto, F.; Prakash, M.; Neuman, D.G.; Lee, T. Phantom and animal tissues for modelling the electrical properties of human liver. *Int. J. Hyperth.* **2003**, *19*, 89–101. [[CrossRef](#)] [[PubMed](#)]
 60. Prakash, P. Theoretical Modeling for Hepatic Microwave Ablation. *Open Biomed. Eng. J.* **2010**, *4*, 27–38. [[CrossRef](#)] [[PubMed](#)]
 61. Diller, K.R.; Pearce, J.A. Issues in modeling thermal alterations in tissues. *Ann. N. Y. Acad. Sci.* **1999**, *888*, 153–164. [[CrossRef](#)] [[PubMed](#)]
 62. Berjano, E.J. Theoretical modeling for radiofrequency ablation: State-of-the-art and challenges for the future. *BioMed. Eng. OnLine* **2006**, *5*, 24. [[CrossRef](#)] [[PubMed](#)]
 63. Yang, D.; Converse, C.M.; Mahvi, D.M.; Webster, J.G. Expanding the Bioheat Equation to Include Tissue Internal Water Evaporation During Heating. *IEEE Trans. Biomed. Eng.* **2007**, *54*, 1382–1388. [[CrossRef](#)]
 64. Selmi, M.; Bajazhar, A.; Belmabrouk, H. Effects of target temperature on thermal damage during temperature-controlled MWA of liver tumor. *Case Stud. Therm. Eng.* **2022**, *31*, 101821. [[CrossRef](#)]
 65. Rozen, G.; Ptaszek, L.M.; Zilberman, I.; Douglas, V.; Heist, E.K.; Beeckler, C.; Altmann, A.; Ruskin, J.N.; Govari, A.; Mansour, M. Safety and efficacy of delivering high-power short-duration radiofrequency ablation lesions utilizing a novel temperature sensing technology. *Europace* **2018**, *20*, f444–f450. [[CrossRef](#)]
 66. Gorman, J.; Tan, W.; Abraham, J. Numerical Simulation of Microwave Ablation in the Human Liver. *Processes* **2022**, *10*, 361. [[CrossRef](#)]
 67. Wang, L.; Fan, J. Modeling bioheat transport at macroscale. *J. Heat Transf.* **2011**, *133*, 011010. [[CrossRef](#)]
 68. Andreozzi, A.; Iasiello, M.; Tucci, C. An overview of mathematical models and modulated-heating protocols for thermal ablation. *Adv. Heat Transf.* **2020**, *52*, 489–541. [[CrossRef](#)]
 69. Hristov, J. Bio-Heat Models Revisited—Concepts, Derivations, Nondimensionalization and Fractionalization Approaches. *Front. Phys.* **2019**, *7*, 189. [[CrossRef](#)]

Article

Safety and Effectiveness of Triple-Antenna Hepatic Microwave Ablation

Nikola Bošković ¹, Srdjan Nikolić ^{2,3}, Branislav Radjenović ¹ and Marija Radmilović-Radjenović ^{1,*}¹ Institute of Physics, University of Belgrade, Pregrevica 118, 11080 Belgrade, Serbia; nikolab@ipb.ac.rs (N.B.); bradjeno@ipb.ac.rs (B.R.)² Department of Surgery, Institute of Oncology and Radiology of Serbia, Pasterova 14, 11000 Belgrade, Serbia; onkosurge1@yahoo.com³ Faculty of Medicine, University of Belgrade, Dr Subotica 8, 11000 Belgrade, Serbia

* Correspondence: marija@ipb.ac.rs

Abstract: Microwave ablation is becoming a standard procedure for treating tumors based on heat generation, causing an elevation in the tissue temperature level from 50 to 60 °C, causing tissue death. Microwave ablation is associated with uniform cell killing within ablation zones, multiple-antenna capability, low complication rates, and long-term survival. Several reports have demonstrated that multiple-antenna microwave ablation is a promising strategy for safely, rapidly, and effectively treating large tumors. The key advantage of multi-antenna tumor microwave ablation is the creation of a large, well-defined ablation zone without excessively long treatment times or high power that can damage healthy tissue. The strategic positioning of multiple probes provides a fully ablated volume, even in regions where individual probe damage is incomplete. Accurate modeling of the complex thermal and electromagnetic behaviors of tissue is critical for optimizing microwave ablation because material parameters and tissue responses can change significantly during the procedure. In the case of multi-antenna microwave ablation, the calculation complexity increases significantly, requiring significant computational resources and time. This study aimed to evaluate the efficacy and safety of liver percutaneous microwave ablation using the simultaneous activation of three antennas for the treatment of lesions larger than 3 cm. Based on the known results from a single-probe setup, researchers can estimate and evaluate various spatial configurations of the three-probe array to identify the optimal arrangement. Due to the synergistic effects of the combined radiation from the three antennas, the resulting ablation zone can be significantly larger, leading to better outcomes in terms of treatment time and effectiveness. The obtained results revealed that volumetric damage and the amount of damaged healthy tissue are smaller for a three-antenna configuration than for microwave ablation using a single-antenna and two-antenna configurations.

Keywords: computational physics; microwave ablation; necrotic tissue; open-source software



Citation: Bošković, N.; Nikolić, S.; Radjenović, B.; Radmilović-Radjenović, M. Safety and Effectiveness of Triple-Antenna Hepatic Microwave Ablation. *Bioengineering* **2024**, *11*, 1133. <https://doi.org/10.3390/bioengineering11111133>

Academic Editors: Aili Zhang and Kai Yue

Received: 30 September 2024

Revised: 5 November 2024

Accepted: 7 November 2024

Published: 11 November 2024



Copyright: © 2024 by the authors. Licensee MDPI, Basel, Switzerland. This article is an open access article distributed under the terms and conditions of the Creative Commons Attribution (CC BY) license (<https://creativecommons.org/licenses/by/4.0/>).

1. Introduction

Microwave ablation (MWA) is a minimally invasive thermal ablation modality for treating various types of tumors [1–5]. MWA is based on tumor cell destruction via hyperthermia caused by microwave radiation emitted by a small probe inserted into the tumor [6]. The success of MWA relies on carefully balancing various technical parameters to achieve efficient tumor destruction while sparing the healthy surrounding tissue. The key parameters affecting tissue damage are the input power, treatment duration, geometry, position of the probe, and radiation propagation characteristics of the antenna [7–9].

Single-antenna and multi-antenna MWA's showed similar effectiveness for local treatment of liver tumors. Nevertheless, synchronous multi-antenna MWA exhibited better local tumor progression-free survival as compared to other MWA approaches, particularly for larger liver tumors [10–12]. For large tumors, the use of a single probe is not

recommended, requiring extreme power and/or treatment duration, thus causing excessive damage to healthy tissues [13]. There are two main approaches for the treatment of large tumors [14,15]. The simplest method is to use a single probe at multiple points, creating overlapping smaller ablation zones to form one large ablation zone that lasts longer than standard MWA. The second approach uses multiple probes simultaneously, creating a larger, more uniform, and symmetrical ablation zone compared to the sequential single-probe approach. The procedure duration was the same as single-probe MWA, but the overlapping radiation zones achieved with multiple probes result in a much higher density of the electromagnetic field [16].

The choice of the radiating antenna is critical for providing efficient radiation in high-density tissue media [17,18]. Coaxial slot antennas are commonly used, with multi-slot antennas typically exhibiting better radiation patterns to create more predictable spherical ablation zones [19,20]. In a real-time multi-probe setup, the probes are generally placed in one of two configurations in a straight line with identical probe separation, for elongated tumors, or in an equilateral geometric shape like a triangle or square, for large irregular tumors [21]. The focus is on understanding the development of the ablation zone in a multi-probe setup.

Computer modeling plays a critical role in improving the precision and effectiveness of MWA by providing a deeper understanding of thermal spread, which is crucial for successful clinical outcomes [22–25]. It was demonstrated that two-dimensional (2D) calculations are not sufficient to estimate the optimal input power and ablation time [20,25]. Thus, it is necessary to perform three-dimensional (3D) simulations, taking into account not only the tumor geometry and the antenna design but also properties of healthy and tumoral tissues [20,25].

In this study, we used the SimSurgery simulation environment based on open-source scientific computing libraries to determine the optimal parameters required for efficient microwave ablation [26,27]. The finite element method (FEM) was used to calculate the processes during MWA. The FEM involves segmenting the entire domain into small finite elements, and the number and quality of these elements directly affect the duration and accuracy of the FEM numerical method [28–30]. Calculations were performed for the triple-antenna MWA of a real liver tumor (from the database [31]). For complex simulations involving a probe, real-life tumor, and part of the liver, the required computational resources can be high. With a multi-probe setup, there are many possible combinations, and as the number of probes increases, the number of finite elements increases significantly, making the full FEM simulation of each setup unacceptably long. The critical challenge seems to be the high computational cost and time required to perform detailed FEM simulations for all the possible multi-probe configurations, given the complexity of the real-life tumor and the geometry involved.

2. Methodology

2.1. Theoretical Background

The material parameters of the tissue dictate the propagation of electromagnetic waves. Liver tissue has a high water content of approximately 70%. As the heating water content decreased, the material parameters change drastically [32]. Blood perfusion is another major factor affecting tissue heating. The blood flow behaved as a coolant, significantly affecting the temperature distribution. There are differences between the material parameters of healthy tissue and tumor, and these parameters change drastically with temperature [33,34]. Instantaneous cell death occurs at temperatures greater than 60 °C, and blood flow stops due to coagulation. Exposure to temperatures above 50 °C for a moderate duration can cause cell death, whereas prolonged exposure to temperatures above 42 °C can cause permanent tissue damage. Determining tissue damage as a function of temperature is a complex task. The calculation of the MWA process can be divided into three stages: calculation of the propagating electromagnetic field inside the tissue, calculation of the temperature, and estimation of thermal damage [35].

The electric field distribution inside the domain can be determined by solving Maxwell's equations [35]:

$$\nabla^2 \vec{E} - \mu_r k_0^2 \left(\epsilon_r - \frac{j\sigma}{\omega \epsilon_0} \right) \vec{E} = 0, \quad (1)$$

where μ_r is the relative permeability, \vec{E} is the electric field vector, σ is the electric conductivity, ϵ_0 is the permittivity of vacuum, $\omega = 2\pi f$ is the angular frequency, and k_0 is the vacuum propagation constant.

Pennes' bio-heat equation describes temperature changes due to microwave radiation [35,36]:

$$\rho \left(c - \frac{\alpha}{\rho} \frac{\partial W}{\partial T} \right) \frac{\partial T}{\partial t} = \nabla \cdot (k \nabla T) + \rho_b \omega_b c_b (T_b - T) + Q_{ext} + Q_{met}, \quad (2)$$

where α , W , ρ , c , T , t , and k are the water latent heat constant, change in water content with temperature, density, specific heat capacity, temperature of the tissue, time, and thermal conductivity of the tissue, respectively. ρ_b , ω_b , and c_b represent the density, perfusion rate, and specific heat capacity of the blood, respectively. $T_b = 37^\circ\text{C}$ is the arterial blood temperature, and Q_{met} is the metabolic heat, which is much lower than Q_{ext} , which represents the external heat source; hence, it can be neglected.

The specific absorption rate (SAR) is defined as the energy of the EM field divided by mass density, representing a measure of the radiation absorbed by the tissue [35]:

$$SAR = \frac{\sigma}{2\rho} \left| \vec{E} \right|^2. \quad (3)$$

where \vec{E} is the electric field vector, σ is electric conductivity, and ρ is the density of the observed domain. The SAR can identify the tissue that is most affected by radiation and how the electric field propagation interacts with the tissue.

Tissue damage accumulates over time and is a function of both temperature and duration of exposure and can be estimated according to the Arrhenius form [37]:

$$\frac{\partial \Omega}{\partial t} = A e^{\left(-\frac{\Delta E}{RT} \right)}, \quad (4)$$

where R and T are the gas constant and temperature, respectively. A is the frequency factor, while ΔE is the activation energy of the irreversible damage reaction.

Two expressions were used to estimate damage to healthy tissue. The volumetric damage (VD) was calculated as the ratio of the volume of the damaged healthy tissue ($V_{DAMAGED}$) and tumor tissue (V_{TUMOR}) [38,39]:

$$VD = \frac{V_{DAMAGED}}{V_{TUMOR}} \cdot 100\%. \quad (5)$$

The amount of damaged healthy tissue (DT) was calculated as the ratio of the volume of the damaged healthy tissue to the total volume of the liver (V_{LIVER}) without tumor tissue (V_{TUMOR}) [38,39]:

$$DT = \frac{V_{DAMAGED}}{V_{LIVER} - V_{TUMOR}} \cdot 100\%. \quad (6)$$

2.2. Simulation Conditions

In this study, we compared the efficacy of single-probe vs. multi-probe MWA of a large liver tumor in a female patient born in 1987 (from the IRCADb-01 liver tumor database [31]). The tumor was irregularly shaped and large (31.6 mm \times 35.4 mm \times 33.9 mm) with the position and shape shown in Figure 1. The probes were oriented along the z-axis. With a fixed duration of MWA of 600 s with a single probe, the only modality that changed the

ablation size was the input power change. We performed a simulation for a three 10-slot antenna configuration placed inside the probe as the source of radiation. The 10-slot antenna (Figure 2a) for microwave ablation represents an advancement in minimally invasive cancer treatment, providing precise and effective tissue destruction with the potential for improved patient outcomes [35]. The multi-slot antenna contains several periodic elements equal to a linear uniform antenna array. Each periodic element includes a slot with a width of 0.6 mm, and there is a conductor spacing of 0.8 mm between neighboring slots. The antennas operate at a frequency of 2.45 GHz, belonging to the ISM bands (Industrial, Scientific, and Medical bands), which is the most commonly used frequency in MWA procedures. Power generators operating at 2.45 GHz are easily available, small antennas with a few millimeters in diameter can be made, and electromagnetic waves at 2.45 GHz can penetrate deep into tissue [40].

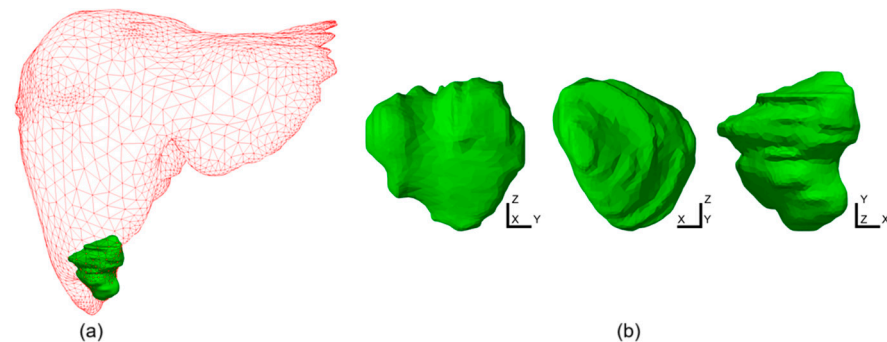


Figure 1. (a) Liver (red triangular surface) and tumor (solid green surface). (b) Tumor STL (stereolithography) representation obtained from the patient in different planes. The dimensions of the tumor are 31.6 mm × 35.4 mm × 33.9 mm [31].

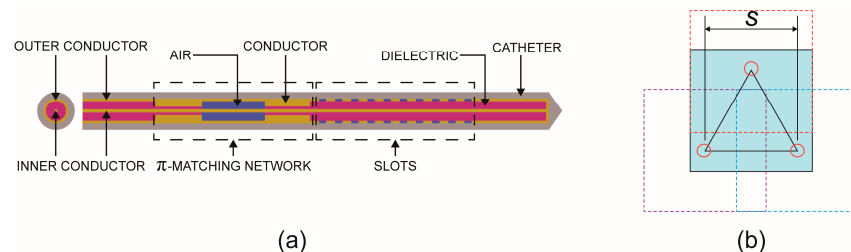


Figure 2. (a) Schematic views of the 10-slot microwave antenna; (b) The three-antenna configuration (blue surface) represents the cross-section of the domain in the xy -plane, red circles represent probes, and dashed lines illustrate domains around the probes.

If we calculate a single probe in the entire domain, multiply this domain, and spatially translate all finite elements around the probe to the positions of the probes in the multi-probe setup, we can obtain a large virtual computational domain consisting of n subdomains and n probes. We can then sum all fractions of tissue damage in the n subdomains and create a large computational domain with the solid first estimation of ablation in a specific multi-probe setup. This of course would never be identical to a complete FEM simulation with a multi-probe setup due to the existing mutual coupling of the probes. Calculations of this type can be performed almost instantaneously for any number of spatial combinations as they do not require costly FEM simulation but simple numerical post-processing of the existing results. Hence, we can identify the best possible combination for the full FEM simulation.

The computational domain size was 60 mm × 60 mm × 90 mm and has the shape of a hexahedron. From the simulation of necrosis with a single probe, we obtained the distribution of the fraction of necrotic tissue in the simulation domain (blue square in Figure 2b). Each finite element in the domain is assigned a corresponding fraction of

necrotic tissue. If we position the center of the system at the position of (0, 0) in the xy -plane, the centers of the probes in the equilateral triangular configuration would be $(-s/2, -s/6 \times \sqrt{3})$, $(0, s/3 \times \sqrt{3})$, and $(s/2, -s/6 \times \sqrt{3})$. Here, s represents the separation between the probes. From the fraction of necrotic tissue in the case with a single probe, we can create three identical domains and position the centers of these domains at the positions of the probes in the multi-probe configuration and create a new domain, which is again positioned and has the same dimensions as the starting domain (blue square), whose value for the fraction of necrotic tissue is the sum of the values of all domains composing the new domain.

Full 3D calculations of the electromagnetic field were calculated and available at each time step. The distribution of the electric field vector by volume is sufficient for the complete calculation of the MWA. All effects, including losses and tissue interaction, are included in the volumetric electric field vector distribution. The temperature was calculated for each time step during the MWA, and consequently, the temperature-dependent material parameters changed with time/temperature. For each time step, the electric field was recalculated with new material parameters.

3. Results

Figure 3a shows that a 10 W power input resulted in a small, spherical ablation zone with a diameter of approximately 15 mm. An input power of 15 W produced a highly spherical ablation zone with a diameter of approximately 26 mm, thereby increasing the ablation volume by 5.7 times compared with the 10 W case. A 20 W input led to a greater increase in ablation volume, which was 2.23 times larger than that for a 15 W input. However, the growth was more focused on the power source in the longitudinal direction, reaching a length of 46.6 mm, while the maximum diameter in the transverse plane was around 30 mm. An input power of 30 W resulted in an ablation volume that was 2.37 times larger than that of the 20 W case, whereas a 40 W power resulted in a total volume of 1.65 times larger than that of the 30 W case. In 30 W ablation, the tumor was not entirely contained, and small transverse plane parts appeared. On the other hand, for 40 W, the entire tumor can be easily ablated; however, the volume of ablation is 5.3 times larger than the tumor volume; hence, there is a particularly large amount of damaged and healthy tissue. As power increases, the ablation effect tends to extend primarily in the longitudinal direction around the probe, leading to significant damage to the healthy tissue.

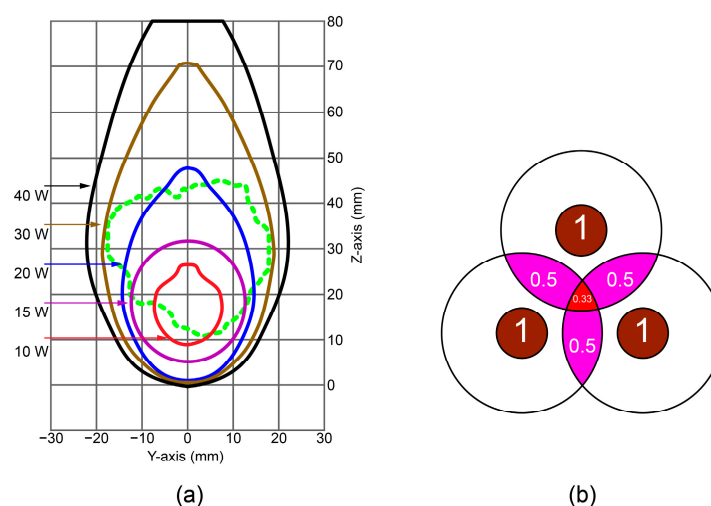


Figure 3. (a) Ablation zones created around the tumor (green dashed line) after 600 s of MWA for different input powers. The green dashed curve represents the tumor. (b) Diagram representing the overlapped ablation zones from three individual probes with designed zones of different fractions of necrotic tissue.

Based on the nearly triangular shape of the tumor in the xy -plane (Figure 1b), using three probes in a triangular configuration appears to be an optimal choice. Figure 3b shows the ideal circular distribution of the ablation zones originating from the three individual probes, which allowed us to estimate total necrosis, including overlapping areas and combined ablation zones. The probe is in the center of each circle, and the proximity of the probe radiation causes it to have the highest intensity, and ablation will occur rapidly. Small red circles with fractions of tissue damage close to 1 represent these zones. Moving away from this zone, we would have zones with a fraction of tissue damage ranging from 1 to 0. In the multiple-probe configuration, the key element is the overlap of the ablation zones. For example, if two overlapping zones each have a necrotic tissue fraction of approximately 0.5, the combined necrotic tissue fraction would be approximately 1. At the same time, if we have three probes, we would only need to have a fraction of the necrotic tissue of approximately 0.33 in the overlapping zones to reach full tissue necrosis.

Figure 4a shows the estimated ablation shapes in different planes for 10 W per antenna and separations of 10–25 mm. In all cases, the tumor was larger than the ablation zone. For 10 mm separation, the ablation was highly spherical and unified, and there was no differentiation between the ablation zones originating from the individual probes. With increasing separation, the unity is broken, especially for separations larger than 20 mm, which is undesirable because it can leave large central parts of the tumors untouched. For 15 W per antenna, the entire tumor in the xy -plane was within the ablation zone, as shown in Figure 4b. In the zy -plane for separation equal to or larger than 20 mm, the created ablation zones are non-unified compared with the large spherical ablation zone created for 10 mm. Based on the analysis of these results, we proceed with the full 3D FEM simulation of the model with three probes, 15 W per antenna, and separations of 10 and 15 mm.

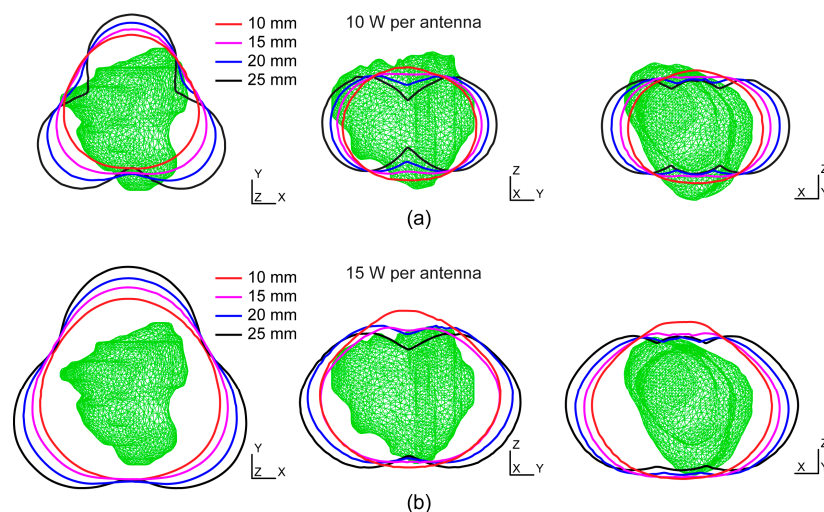


Figure 4. Overlapping ablation zones from three individual probes estimated from single-probe simulations with different separations and input powers of (a) 10 W and (b) 15 W for each probe. The green triangular surfaces represent tumors from the database [31].

The full 3D FEM simulation results of the SAR for the three simultaneous probes in a triangular configuration with 15 W for each probe and two separations are shown in Figure 5. The SAR represents the interaction of electromagnetic radiation with living tissue and closely follows the temperature and ablation distribution. Tissue within zones with levels of at least 25 dBW/kg are practically guaranteed to be ablated. We can see that with a 10 mm separation, the SAR shape is spherical, while with a 15 mm separation, it is triangular, and there is significant concentration of the high-level SAR in the zones between the probes and at the intersections.

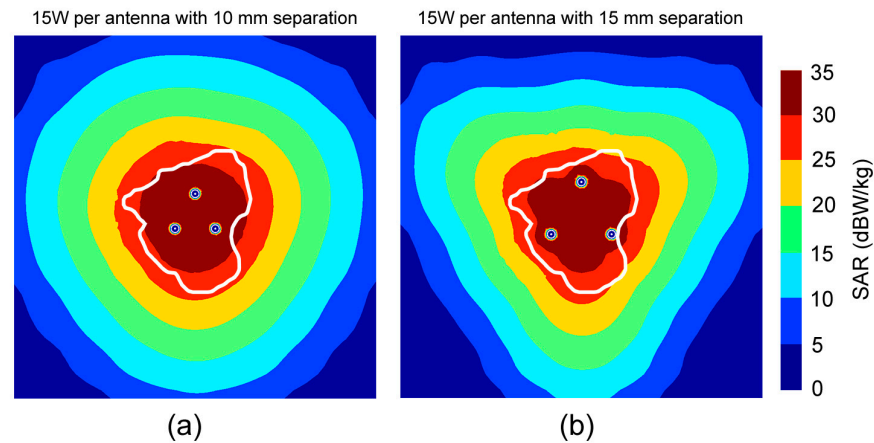


Figure 5. SAR patterns for three probes in a triangular configuration in the xy -plane with 15 W per probe and separations of (a) 10 mm and (b) 15 mm. The white line indicates the tumor from the database [31].

The absorbed energy converted into thermal energy causes an increase in the tissue temperature. The temperature distribution after 600 s of MWA with an input power of 15 W and the antenna separation of (a) 10 mm and (b) 15 mm is shown in Figure 6. For both separations, the entire tumor was within the region at temperatures higher than 60 °C, which guarantees instantaneous cell death. The highest temperature is near the antenna slots and decreases as the distance from the antenna increases.

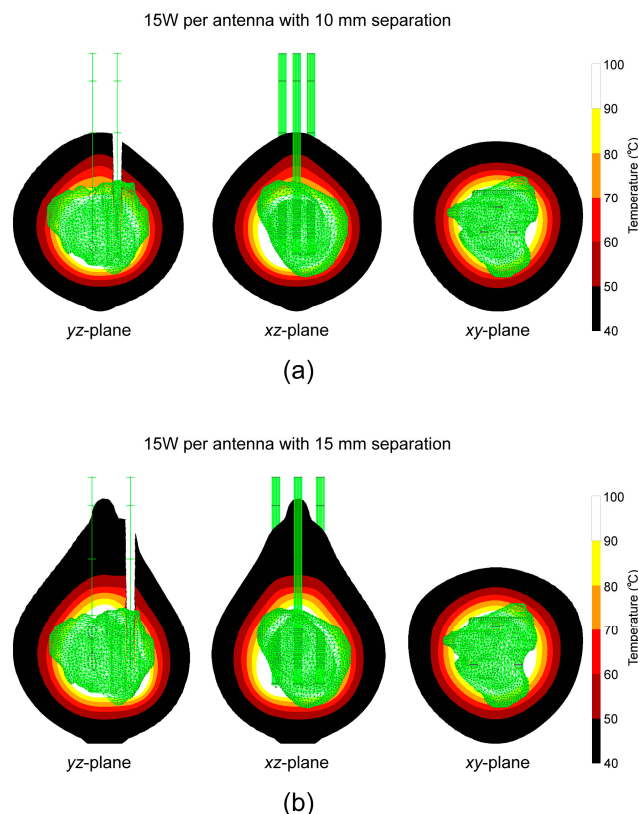


Figure 6. Temperature distribution for 15 W per probe and separation of (a) 10 mm and (b) 15 mm after 600 s in the yz -plane, xz -plane, and xy -plane. The green triangular surface represents the tumor (from the database [31]).

Figure 7a shows that the fraction of tissue necrosis followed the temperature distribution with time, starting with the Y-area between the probes after 60 s, expanding to

areas around the probes after 120 s, creating a large triangular formation after 180 s, which changed to a spherical shape later. As can be seen from Figure 7b–d, the entire tumor is inside the ablation zone. The total ablation volume was 34.6 cm³.

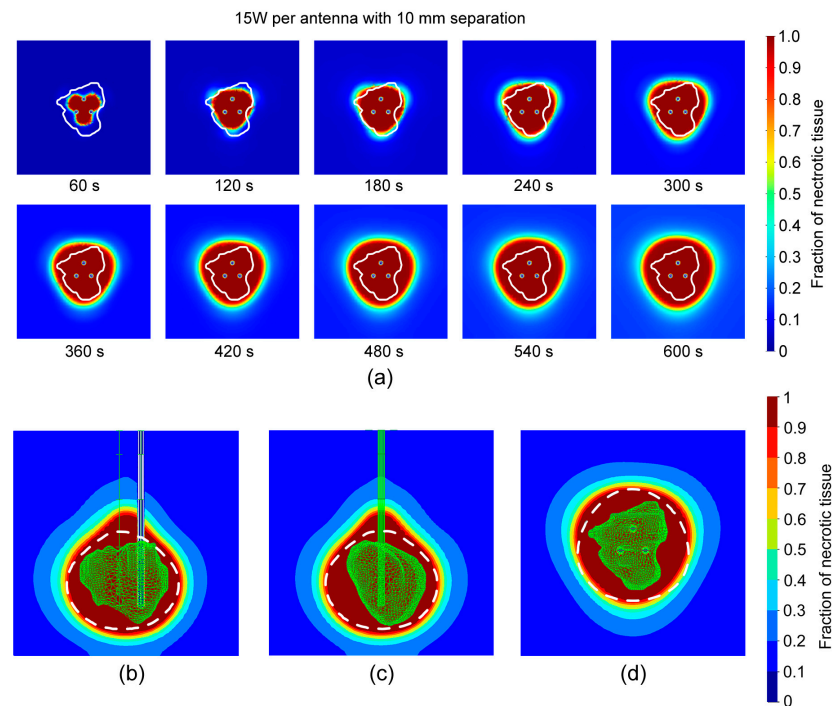


Figure 7. (a) Change in the fraction of necrotic tissue with time for 15 W per probe and separation of 10 mm during 600 s in the *xy*-plane. The white line indicates the tumor [31]. A fraction of necrotic tissue distribution after 600 s in the (b) *yz*, (c) *xz*-plane, and (d) *xy*-plane. The white dashed lines show predictions from Figure 4b.

Observing tissue necrosis in Figure 8a, we can see that during ablation, the triangle shape between the probes later expands with the area around the probes, forming a hexagonal shape that later expands to a more spherical shape. From Figure 8b–d, we can see that the entire tumor was ablated with a larger ablation size of 38.9 cm³ compared with the case with a 10 mm separation. Figures 7 and 8 show a comparison of the ablation results and the rough estimation based on a single probe (black dashed lines). In both cases, the lateral dimensions were reasonably estimated, whereas the longitudinal size of the ablation was larger in the full FEM simulation, especially in the case with the 15 mm separation.

The parameters that characterize the tissue damage *VD* and *DT* were calculated using Equations (5) and (6). The values for single-antenna, two-antenna, and three-antenna configurations are shown in Table 1. The greatest damage to healthy tissue occurs with a single-antenna configuration. The use of two- and three-antenna configurations causes less damage to the healthy tissue. When three antennas are used, the amount of damaged healthy tissue was less than 2%. As compared with other results, Cazzato and co-workers reported volumetric damage around 237.5% and 337.5% that corresponds to two- and three-antenna liver tumor ablation [10]. For two-antenna ablation, Andresciani et al. found 246% volumetric damage. Manuchehrabadi and Zhu obtained an amount of damaged healthy tissue less than 5% with 100% tumor volume damage [39].

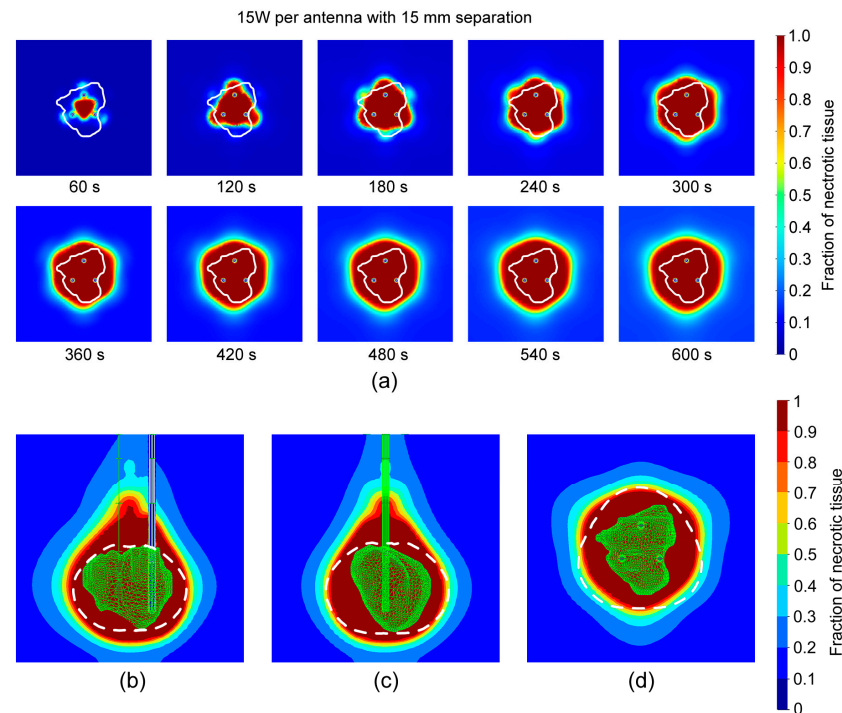


Figure 8. (a) Change in the fraction of necrotic tissue with time for 15 W per probe and separation of 15 mm during 600 s in the xy -plane. The white line shows the tumor [31]. A fraction of necrotic tissue distribution after 600 s at (b) yz , (c) xz -plane, and (d) xy -plane. The white dashed lines represent predictions from Figure 4b.

Table 1. VD and DT after MWA performed using single-antenna, two-antenna, and three-antenna configurations.

Configuration	VD	DT
Single antenna (40 W)	452.3%	3.4%
Two antennas (15 mm separation and 20 W per probe)	213.1%	1.6%
Three antennas (15 mm separation and 15 W per probe)	194.6%	1.4%
Three antennas (10 mm separation and 15 W per probe)	161.6%	1.2%

4. Conclusions

In this study, we investigated several treatment scenarios for real large elongated tumors (from the database [31]) using three identical parallel-positioned probes with multi-slot coaxial antennas. Three-dimensional simulations with both tumoral and healthy tissue and antenna design were performed using a software framework based on open-source components [26,27]. We assumed that, for large tumors, MWA achieved the best results when multiple probes were used simultaneously to exploit the synergistic effects of the overlapping radiation fields and create an efficient, targeted ablation zone. The 10-slot design helps focus energy on a specific area while minimizing damage to surrounding healthy tissues.

For a fixed duration of the MWA procedure with a single fixed probe, an increase in the input power alone was sufficient to increase the ablation size. Using multiple probes enables the spatial distribution of total power and the ability to customize the ablation shape based on tumor shape and orientation. The main issue when using multiple probes is to find the optimal number of probes, power, and spatial distribution. The number of potential combinations can be quite overwhelming. The accurate shape of the ablation can also be assessed using the numerical FEM approach in the same manner as in the case with a single probe, but with each probe's numerical complexity increasing

considerably; hence, blindly checking multiple combinations is highly inefficient. The number of possible array configuration of different spatial and power distributions is extremely large. We used the SAR results obtained from the single probe to estimate the optimal array configuration and confirmed the validation of the approach by running a full 3D simulation with selected configurations.

Moving away from the radiation source, the fraction of tissue damage decreases; however, in a multi-probe setup, the overlap of lower-damage zones can still cause complete tissue necrosis. For example, if n overlapping zones each have a fraction of tissue damage of $1/n$, the sum of the fractions will be 1, indicating complete tissue ablation. In summary, the results indicate that higher-power inputs (30 W and 40 W) are more likely to provide complete tumor coverage than lower-power inputs (10 W, 15 W, and 20 W).

In a multi-probe setup, each probe generates a separate ablation zone. The goal is to unite these individual ablation zones into a single, large, unified, and uninterrupted ablation zone that covers the entire tumor. Therefore, the individual ablation zones created by each probe should be near each other. The combined ablation zone can be significantly larger than the simple sum of the volumes obtained from the individual probes. These results can be attributed to the synergistic effects of the combined radiation from multiple probes. Our results showed that volumetric damage and the amount of damaged healthy tissue were greatest with microwave ablation using a single antenna. The damage to healthy tissue decreases for two and three antennas. For the three-antenna ablation, the amount of damaged healthy tissue was less than 2%. Presented results indicate that triple-antenna MWA provides complete ablation of a large tumor with a small risk of unnecessary damage and predictable ablation zones.

Author Contributions: Conceptualization, N.B. and M.R.-R.; methodology, N.B. and B.R.; software, N.B. and B.R.; investigation and data interpretation, N.B. and S.N.; original draft preparation, N.B. and M.R.-R.; writing—review, and editing, all of the authors; supervision, S.N. and M.R.-R. All authors have read and agreed to the published version of the manuscript.

Funding: N.B., B.R. and M.R.-R. acknowledge that this research was supported by the Science Fund of the Republic of Serbia, the program IDEAS, grant No. 7739583, SimSurgery.

Institutional Review Board Statement: Not applicable.

Informed Consent Statement: Not applicable.

Data Availability Statement: The data are available from the corresponding authors upon reasonable request.

Conflicts of Interest: The authors declare no conflicts of interest.

References

1. Ong, S.L.; Gravante, G.; Metcalfe, M.S.; Strickland, A.D.; Dennison, A.R.; Lloyd, D.M. Efficacy and safety of microwave ablation for primary and secondary liver malignancies: A systematic review. *Eur. J. Gastroenterol. Hepatol.* **2009**, *21*, 599–605. [[CrossRef](#)] [[PubMed](#)]
2. Brace, C.L. Microwave ablation technology: What every user should know. *Curr. Probl. Diagn. Radiol.* **2009**, *38*, 61–67. [[CrossRef](#)] [[PubMed](#)]
3. Izzo, F.; Granata, V.; Grassi, R.; Fusco, R.; Palaia, R.; Delrio, P.; Carrafiello, G.; Azoulay, D.; Petrillo, A.; Curley, S.A. Radiofrequency Ablation and Microwave Ablation in Liver Tumors: An Update. *Oncologist* **2019**, *24*, e990–e1005. [[CrossRef](#)] [[PubMed](#)]
4. Lobascio, F.; Di Modugno, R.; Fiore, M.; Di Modugno, N.; Bruno, C.; De Nicolo, T.; Barberis, R.V.; Cabiale, K.; Radoiu, M. Microwave and Radiofrequency Ablation: A Comparative Study between Technologies in Ex Vivo Tissues. *Drugs Drug Candidates* **2024**, *3*, 550–565. [[CrossRef](#)]
5. Yao, L.J.; Zhu, X.D.; Zhou, L.M.; Zhang, L.L.; Liu, N.N.; Chen, M.; Wang, J.Y.; Hu, S.J. Short-term efficacy of microwave ablation in the treatment of liver cancer and its effect on immune function. *World J. Clin. Cases* **2024**, *12*, 3395–3402. [[CrossRef](#)]
6. Vogl, T.J.; Nour-Eldin, N.A.A.; Hammerstingl, R.M.; Panahi, B.; Naguib, N.N.N. Microwave Ablation (MWA): Basics, Technique and Results in Primary and Metastatic Liver Neoplasms—Review Article. *Fortschr. Röntgenstr.* **2017**, *89*, 1055–1066. [[CrossRef](#)]
7. Bachetta, A.; Cheung, S.; Moore, E.R.; Nguyen, D.; Kiely, M.J.; Whiteley, M.S. Defining the Parameters for Endovenous Microwave Ablation to Achieve Equivalence with Endovenous Laser Ablation, Using the Porcine Liver Model. *Vasc. Endovasc. Surg.* **2024**, *58*, 491–497. [[CrossRef](#)]

8. Ashour, A.S.; Asran, M.; Fotiadis, D.I. Optimal Power for Microwave Slotted Probes in Ablating Different Hepatocellular Carcinoma Sizes. *Comput. Biol. Med.* **2020**, *127*, 104101. [\[CrossRef\]](#)
9. Hui, T.; Brace, C.L.; Hinshaw, J.L.; Quek, L.H.H.; Huang, I.K.H.; Kwan, J.; Lim, G.H.T.; Lee, F.T., Jr.; Pua, U. Microwave ablation of the liver in a live porcine model: The impact of power, time and total energy on ablation zone size and shape. *Int. J. Hyperther.* **2020**, *37*, 668–676. [\[CrossRef\]](#)
10. Cazzato, R.L.; De Marini, P.; Leclerc, L.; Dalili, D.; Koch, G.; Rao, P.; Auloge, P.; Garnon, J.; Gangi, A. Large nearly spherical ablation zones are achieved with simultaneous multi-antenna microwave ablation applied to treat liver tumours. *Eur. Radiol.* **2020**, *30*, 971–975. [\[CrossRef\]](#)
11. Garnon, J.; Delmas, L.; De Marini, P.; Leclerc, L.; Dalili, D.; Koch, G.; Auloge, P.; Cazzato, R.L.; Gangi, A. Triple-Antenna Microwave Ablation with Repositioning for the Creation of a Reliable 6-cm Ablation Zone in the Liver. *Cardiovasc. Intervent Radiol.* **2021**, *44*, 1291–1295. [\[CrossRef\]](#) [\[PubMed\]](#)
12. Keangin, P.; Rattanadecho, P.; Wessapan, T. An analysis of heat transfer in liver tissue during microwave ablation using single and double slot antenna. *Int. Commun. Heat Mass Transf.* **2011**, *38*, 757–766. [\[CrossRef\]](#)
13. Han, Y.; Zhao, W.; Wu, M.; Qian, Y. Efficacy and safety of single- and multiple-antenna microwave ablation for the treatment of hepatocellular carcinoma and liver metastases: A systematic review and network meta-analysis. *Medicine* **2022**, *101*, e32304. [\[CrossRef\]](#) [\[PubMed\]](#)
14. Andresciani, F.; Pacella, G.; Vertulli, D.; Altomare, C.; Bitonti, M.T.; Bruno, A.; Cea, L.; Faiella, E.; Beomonte Zobel, B.; Grasso, R.F. Microwave ablation using two simultaneous antennas for the treatment of liver malignant lesions: A 3 year single-Centre experience. *Int. J. Hyperther.* **2023**, *40*, 2163309. [\[CrossRef\]](#)
15. Zhang, T.Q.; Huang, S.M.; Gu, Y.K.; Jiang, X.Y.; Huang, Z.M.; Deng, H.X.; Huang, J.H. Sequential and Simultaneous 4-Antenna Microwave Ablation in an Ex Vivo Bovine Liver Model. *Cardiovasc. Interv. Radiol.* **2019**, *42*, 1466–1474. [\[CrossRef\]](#) [\[PubMed\]](#)
16. Wright, A.S.; Lee, F.T., Jr.; Mahvi, D.M. Hepatic microwave ablation with multiple antennae results in synergistically larger zones of coagulation necrosis. *Ann. Surg. Oncol.* **2003**, *10*, 275–283. [\[CrossRef\]](#)
17. Fallahi, H.; Prakash, P. Antenna designs for microwave tissue ablation. *Crit. Rev. Biomed. Eng.* **2018**, *46*, 495–521. [\[CrossRef\]](#)
18. Huang, H.; Zhang, L.; Moser, M.A.J.; Zhang, W.; Zhang, B. A review of antenna designs for percutaneous microwave ablation. *Phys. Med.* **2021**, *84*, 254–264. [\[CrossRef\]](#)
19. Ge, M.; Jiang, H.; Huang, X.; Zhou, Y.; Zhi, D.; Zhao, G.; Chen, Y.; Wang, L.; Qiu, B. A multi-slot coaxial microwave antenna for liver tumor ablation. *Phys. Med. Biol.* **2018**, *63*, 175011. [\[CrossRef\]](#)
20. Radjenović, B.; Sabo, M.; Šoltes, L.; Prnova, M.; Čičak, P.; Radmilović-Radjenović, M. On Efficacy of Microwave Ablation in the Thermal Treatment of an Early-Stage Hepatocellular Carcinoma. *Cancers* **2021**, *13*, 5784. [\[CrossRef\]](#)
21. Harari, C.M.; Magagna, M.; Bedoya, M.; Lee, F.T., Jr.; Lubner, M.G.; Hinshaw, J.L.; Ziemlewicz, T.; Brace, C.L. Microwave Ablation: Comparison of Simultaneous and Sequential Activation of Multiple Antennas in Liver Model Systems. *Radiology* **2016**, *278*, 95–103. [\[CrossRef\]](#) [\[PubMed\]](#)
22. Selmi, M.; Bin Dukhyil, A.A.; Belmabrouk, H. Numerical Analysis of Human Cancer Therapy Using Microwave Ablation. *Appl. Sci.* **2020**, *10*, 211. [\[CrossRef\]](#)
23. Tehrani, M.H.H.; Soltani, M.; Kashkooli, F.M.; Raahemifar, K. Use of microwave ablation for thermal treatment of solid tumors with different shapes and sizes—A computational approach. *PLoS ONE* **2020**, *15*, e0233219. [\[CrossRef\]](#)
24. Wang, J.; Huang, S.; Gao, H.; Liu, J.; Zhang, Y.; Wu, S. Computer Simulations of Dual-Antenna Microwave Ablation and Comparison to Experimental Measurements. *Appl. Sci.* **2023**, *13*, 26. [\[CrossRef\]](#)
25. Cafarchio, A.; Iasiello, M.; Brunese, M.C.; Francica, G.; Rocca, A.; Andreozzi, A. Emprint Microwave Thermoablation System: Bridging Thermal Ablation Efficacy between Human Patients and Porcine Models through Mathematical Correlation. *Bioengineering* **2023**, *10*, 1057. [\[CrossRef\]](#) [\[PubMed\]](#)
26. Bošković, N.; Radmilović-Radjenović, M.; Radjenović, B. Finite Element Analysis of Microwave Tumor Ablation Based on Open-Source Software Components. *Mathematics* **2023**, *11*, 2654. [\[CrossRef\]](#)
27. Bošković, N.; Radjenović, B.; Nikolić, S.; Radmilović-Radjenović, M. Effectiveness of microwave ablation using two simultaneous antennas for liver malignancy treatment. *Open Phys.* **2024**, *22*, 20240079. [\[CrossRef\]](#)
28. Chang, I. Finite Element Analysis of Hepatic Radiofrequency Ablation Probes using Temperature-Dependent Electrical Conductivity. *Biomed. Eng. OnLine* **2003**, *2*, 12. [\[CrossRef\]](#)
29. Phasukkit, P.; Tungjitsulmun, S.; Sangworasil, M. Finite element analysis and in vitro experiments of placement configurations using triple antennas in microwave hepatic ablation. *IEEE Trans. Biomed. Eng.* **2009**, *56*, 2564–2572. [\[CrossRef\]](#)
30. Gangadhara, B.; Mariappan, P. A vector finite element approach to temperature dependent parameters of microwave ablation for liver cancer. *Int. J. Numer. Method. Biomed. Eng.* **2023**, *39*, e3661. [\[CrossRef\]](#)
31. Soler, L.; Hostettler, A.; Agnus, V.; Charnoz, A.; Fasquel, J.B.; Moreau, J.; Osswald, A.-B.; Bouhadjar, M.; Marescaux, J. 3D image reconstruction for comparison of algorithm database: A patient-specific anatomical and medical image database. IRCAD, Strasbourg, France. *Tech. Rep.* **2010**, *1*, 1. Available online: <https://www.ircad.fr/research/data-sets/liver-segmentation-3d-ircadb-01/> (accessed on 15 September 2024).
32. Rossmann, C.; Haemmerich, D. Review of temperature dependence of thermal properties, dielectric properties, and perfusion of biological tissues at hyperthermic and ablation temperatures. *Crit. Rev. Biomed. Eng.* **2014**, *42*, 467–492. [\[CrossRef\]](#) [\[PubMed\]](#)

33. O'Rourke, A.P.; Lazebnik, M.; Bertram, J.M.; Converse, M.C.; Hagness, S.C.; Webster, J.G.; Mahvi, D.M. Dielectric properties of human normal, malignant and cirrhotic liver tissue: In vivo and ex vivo measurements from 0.5 to 20 GHz using a precision open-ended coaxial probe. *Phys. Med. Biol.* **2007**, *52*, 4707–4719. [[CrossRef](#)] [[PubMed](#)]
34. Ji, Z.; Brace, C.L. Expanded modeling of temperature-dependent dielectric properties for microwave thermal ablation. *Phys. Med. Biol.* **2011**, *56*, 5249–5264. [[CrossRef](#)]
35. Radmilović-Radjenović, M.; Bošković, N.; Radjenović, B. Computational modeling of microwave tumor ablation. *Bioengineering* **2022**, *9*, 656. [[CrossRef](#)] [[PubMed](#)]
36. Pennes, H.H. Analysis of tissue and arterial blood temperatures in the resting human forearm. *J. Appl. Physiol.* **1998**, *85*, 5–34. [[CrossRef](#)]
37. Diller, K.R.; Pearce, J.A. Issues in modeling thermal alterations in tissues. *Ann. N. Y. Acad. Sci.* **1999**, *888*, 153–164. [[CrossRef](#)]
38. Zhang, B.; Moser, M.A.; Zhang, E.M.; Luo, Y.; Zhang, H.; Zhang, W. Study of the relationship between the target tissue necrosis volume and the target tissue size in liver tumours using two-compartment finite element RFA modelling. *Int. J. Hyperth.* **2014**, *30*, 593–602. [[CrossRef](#)]
39. Manuchehrabadi, N.; Zhu, L. Development of a computational simulation tool to design a protocol for treating prostate tumours using transurethral laser photothermal therapy. *Int. J. Hyperth.* **2014**, *30*, 349–361. [[CrossRef](#)]
40. Aliqab, K.; Nadeem, I.; Khan, S.R. A Comprehensive Review of In-Body Biomedical Antennas: Design, Challenges and Applications. *Micromachines* **2023**, *14*, 1472. [[CrossRef](#)]

Disclaimer/Publisher's Note: The statements, opinions and data contained in all publications are solely those of the individual author(s) and contributor(s) and not of MDPI and/or the editor(s). MDPI and/or the editor(s) disclaim responsibility for any injury to people or property resulting from any ideas, methods, instructions or products referred to in the content.

Computational Modeling of Microwave Tumor Ablation

Marija Radmilović-Radjenović , Nikola Bošković  and Branislav Radjenović

Institute of Physics, University of Belgrade, Pregrevica 118, 11080 Belgrade, Serbia

* Correspondence: marija@ipb.ac.rs

Abstract: Microwave ablation is recognized as a minimally invasive, fast-recovery treatment for destroying cancer cells using the heat generated by microwave energy. Despite the unquestionable benefits of microwave ablation, the interaction of the microwave applicator with the tissue may result in localized heating and damage to the surrounding tissue. The majority of the tissue damage can be removed by clarifying the conditions for their development. In addition to experimental methods, computer modeling has proven to be an effective tool for optimizing the performance of microwave ablation. Furthermore, because the thermal spread in biological tissue is difficult to measure, developing a predictive model from procedural planning to execution may have a substantial influence on patient care. The comprehension of heat transport in biological tissues plays a significant role in gaining insight into the mechanisms underlying microwave ablation. Numerical methods that enable ablation size control are required to guarantee tumor destruction and minimize damage to healthy tissues. Various values of input power and ablation time correspond to different tumor shapes ensuring the preservation of healthy tissues. The optimal conditions can be estimated by performing full three-dimensional simulations. This topical review recapitulates numerous computational studies on microwave tumor ablation. Novel areas emerging in treatment planning that exploit the advantages of numerical methods are also discussed. As an illustration, the results of the three-dimensional simulations of real liver tumors in the 3D-IRCADb-01 database are presented and analyzed. The simulation results confirm that numerical methods are very useful tools for modeling microwave tumor ablation with minimal invasiveness and collateral damage.

Keywords: finite element method; microwave ablation; heat transport; tissue damage



Citation: Radmilović-Radjenović, M.; Bošković, N.; Radjenović, B. Computational Modeling of Microwave Tumor Ablation. *Bioengineering* **2022**, *9*, 656. <https://doi.org/10.3390/bioengineering9110656>

Academic Editors: Kwong Ming Tse and Riccardo Colella

Received: 8 October 2022

Accepted: 31 October 2022

Published: 5 November 2022

Publisher's Note: MDPI stays neutral with regard to jurisdictional claims in published maps and institutional affiliations.



Copyright: © 2022 by the authors. Licensee MDPI, Basel, Switzerland. This article is an open access article distributed under the terms and conditions of the Creative Commons Attribution (CC BY) license (<https://creativecommons.org/licenses/by/4.0/>).

1. Introduction

Microwave ablation (MWA) is the most widely used ablation method for a broad spectrum of cellular pathologies and malignancies [1–5]. MWA is a thermal modality based on tissue destruction by localized heat, which increases the temperature to exceed the physiological threshold to kill cancer cells. Compared with other thermal technologies, MWA offers unique advantages such as an improved convection profile, higher intratumoral temperatures, larger ablation zones especially when using multiple antennas simultaneously, and reduced treatment times [6–12]. In particular, MWA at 2.45 GHz has become the highly recommended treatment for primary and secondary liver malignancies with both curative and palliative intent. According to the literature, MWA treatment completely eliminates small liver tumors, with a success rate greater than 85% [13]. During MWA, ablation can be accomplished by either implicitly controlling the power or temperature, resulting in a modulating heat procedure [14].

Microwave (MW) antennas that operate at microwave frequencies (915–2450 MHz) and radiate microwave energy are strategically placed in biological tissues [15,16]. The MW field causes the rotation of polar molecules, therefore, part of the electromagnetic (EM) energy is absorbed and converted into heat. Water molecules are polar, and therefore, the electric charges on these molecules are asymmetric. Hydrogen atoms are positively charged, whereas oxygen atoms have a negative charge, represented by red and blue,

respectively (see Figure 1a). The electric charge of electromagnetic radiation flips between the positive and negative values. The MW field oscillates rapidly, causing water molecules to spin and change orientation 2–5 billion times per second depending on the frequency of the MW energy, as shown in Figure 1b [17]. The vigorous molecular movement of water molecules significantly raises the temperature of the water, heating the target tissue and causing cancer cell death via coagulation necrosis [18].

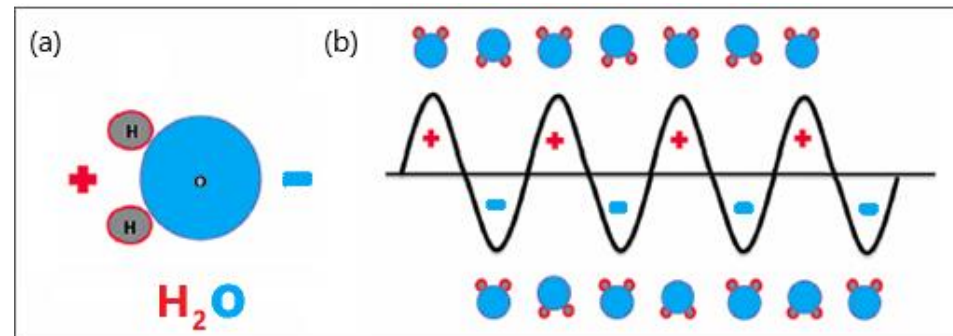


Figure 1. Schematic illustration of (a) polar water molecules and (b) interaction between an oscillating electromagnetic microwave waveform and water molecules.

Understanding the dielectric properties of tissues is particularly important for the application of MWA [19–21]. Electrical conductivity σ is the current density per unit electric field, with units of $\text{kg}^{-1}\text{n}^{-3}\text{s}^3\text{A}^2$. Current density is related to ion mobility, which is velocity per unit electric field. The physical characteristic that determines MW penetration in tissues is related to permittivity ϵ and it is given by the relation $\epsilon = \epsilon' - j\epsilon'' = \epsilon_r - j\sigma/\omega\epsilon_0$, where ω is the angular frequency, ϵ_r is the static relative permittivity, and ϵ_0 is the vacuum permittivity [22]. It has been reported that the dielectric properties of tumoral tissues are 10–20% greater than those of healthy tissues [23,24].

Another factor that strongly affects the efficiency of MWA is the antenna design, which is responsible for the formation of ablation zones that extend radially from the antenna. Over the past few decades, various antenna designs have been developed to minimize thermal damage to healthy tissue [25–28]. Early-generation MWA antennas created elongated ablation zones with the so-called ‘comet tail’, which invades the healthy surrounding tissue [29]. Recent antenna designs have produced shorter ablation zones centered on the antenna tip, which is useful for treating small tumors. [30,31]. Some commercial MWA systems based on “thermosphere technology” can produce spherical ablation patterns by adding small saline irrigation channels to the antennas [32,33]. Novel compact multislot coaxial antennas ensure the formation of spherical ablation zones that are suitable for the interstitial MWA process [34,35].

In addition to experimental methods, computer modeling is a powerful tool for improving the performance of MWA devices and procedures. Moreover, numerical models of the antenna-tissue system are essential for investigating thermal spread through the tissue [36–39]. Several numerical studies have predicted the temperature profile and accompanying tissue damage caused by the MWA applicator [40,41]. The Arrhenius model is widely employed to estimate the degree of tissue destruction [42,43]. Owing to the complexity of the models and computational resource consumption, the majority of actual numerical studies are based on two-dimensional (2D) axisymmetric models to reproduce realistic tumor shapes, which are usually non-axisymmetric [44–48]. Several 3D simulations have recently been performed to determine the fraction of damage during MWA of tumoral tissues [49–53]. The higher the level of predictability achieved in simulations, the easier it is to plan a treatment procedure that is safer, more effective, and less time-consuming.

In this topical review article, we focus primarily on numerical methods useful in modeling the MWA treatment of tumors. Although computational modeling has experienced unprecedented growth in recent years owing to the availability of high-performance

low-cost computers, attention needs to be paid to the actual capabilities and limitations of current simulation techniques. This article is organized as follows. The introduction describes the fundamentals of the MWA procedure. The advances and limitations of various mathematical models of tissue and heat transport through tissues are discussed in Section 2. Special attention will be paid to progress in the development of heat-transfer equations in biological tissues. Section 3 describes the modeling of the electromagnetic field generated by an antenna immersed in a tissue. Certain simulation results regarding the modeling of the MWA of hepatocellular carcinoma will be highlighted in Section 4 helping us to understand the application of numerical methods in biomedicine in more detail. Section 5 reflects the author's point of view regarding computer modeling of microwave tumor ablation. We conclude this article in Section 6, indicating perspectives on new studies and methodology directions that have begun to appear as numerical models have been developed more completely.

2. Mathematical Models of Tissue and Heat Transport

In recent years, numerical models of ablation procedures have undergone continuous refinement and have been adopted to simulate the effects of current flow through biological tissue [54–57]. Furthermore, thermal spread in biological tissues is difficult to measure; hence, a predictive model of the MWA procedure can significantly improve the efficiency of this thermal modality. Mathematical models of MWA procedures consist of three fundamental components. The first is the modeling of tissue and heat transport in tissues. The second is related to the modeling of the microwave EM field generated by ablation probes (antennas). The third component is associated with modeling the effect of heating on tumor cells.

Kenyon [58] applied the mixture theory to biological tissues, while experimental investigations of biological tissues within a theoretical framework began in earnest in a series of papers [59–63]. One of the main challenges in using mixture theory as a modeling framework for biological tissues is the apparent complexity. Cowin [64] concluded that most studies related to the mixture theory have an unusually large number of equations. As the structure of biological tissues is porous and consists of different cells and a microvascular bed, the theory of porous media for heat transfer in tissues is more appropriate than that of a homogenous model [65,66]. Most previous models of heat transport have focused on single-layer porous media biomaterials [67–69]. According to porous media theory, the entire biological medium can be divided into distinct tissue and blood phases. The governing equations for bioheat transfer and blood flow were averaged over the control volume.

In studies that used porous media models for heat transfer in biomaterials, various parameters, such as tumor diameter, tumor porosity, and input MW power were not considered. However, in practice, these parameters may intensify the absorption process in the target tissue. Hence, to represent the actual process of MW ablation, it is crucial to take into account complete modeling based on the porous media theory in porous tissue.

2.1. Tissue Model

Biological tissue is a complex heterogeneous system consisting of dispersed cells segregated by voids. Blood flows through a network of vessels, known as the circulatory system, which is composed of arteries, veins, and capillaries. The primary function of capillaries, the smallest and most numerous blood vessels, is the exchange of materials between blood and tissue cells. Figure 2 shows a schematic plot of the tissue consisting of blood vessels, cells, and interstitium, which can be further divided into the extracellular matrix and interstitial fluid [70,71]. However, for simplicity, biological tissue can be divided into two distinct regions: The vascular and extravascular regions (cells and interstitium). The extravascular region is considered to be a solid matrix, albeit with extravascular fluid. Thus, the tissue can be treated as a fluid-saturated porous medium through which the blood infiltrates.

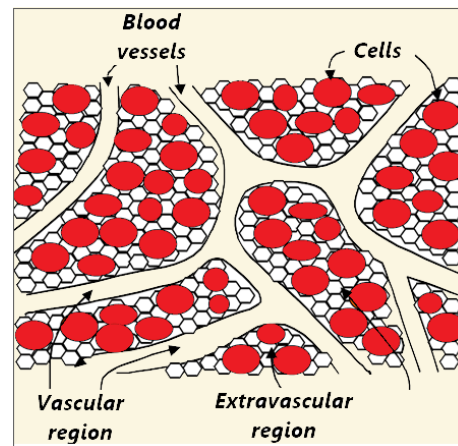


Figure 2. Schematic illustration of three compartments (blood vessels, cells, and interstitium) of the porous biological tissue. The interstitial space is split into the extracellular matrix and interstitial fluid.

The modeling of heat transport in biological tissues must include tissue heat exchange, blood-tissue convection, blood perfusion, and metabolic heat production [72]. Heat transport in tissues can be considered from different viewpoints: Molecular, microscopic, or macroscopic [73]. Moreover, heating may lead to vaporization (phase changes) and ionization of the water content and, in some cases, vapor expansion and tissue fragmentation. Therefore, microscopic modeling is practically impossible, and macroscopic modeling must be used for heat transport in tissues.

The macroscale is a phenomenological scale that is far larger than the microscale of cells and voids, but substantially smaller than the system length scale. Macroscale considerations are important because of the possible complications caused by a large number of particles at the molecular scale or the complex microscale structure of biological tissues [74,75]. Good separation of the length scales is pivotal for establishing a macroscale representation identical to the microscale behavior [76,77]. There are two approaches to the development of macroscopic thermal models for blood-perfused tissues. The first is scaling down based on the mixture theory of continuum mechanics. The second one is recognized as scaling up from the microscale based on the porous media theory [78].

2.1.1. Top-Down Approach

The top-down approach does not involve microscale system representation or microscale quantities. The phase properties were determined at a macroscale level. The shortcomings of this approach are the failure to link microscale and macroscale properties and the extension of multiphase systems with different features of interfaces and common curves. Full balance equations are established in terms of macroscale properties, with additional terms related to the blood–tissue interaction. The energy conservation equation is expressed as [78,79]:

$$\frac{\partial(\rho c \epsilon T)_{mac}^t}{\partial t} = -\nabla \cdot (\epsilon \mathbf{q})_{mac}^t + (\rho \epsilon q_m)_{mac}^t + (\rho \epsilon q_c)_{mac}^t + (\rho \epsilon q_p)_{mac}^t + (\rho \epsilon q_e)_{mac}^t, \quad (1)$$

where t is the time, T is the temperature, ρ is the density, ϵ is the volume fraction, and c is the specific heat. Subscript “ mac ” denotes the macroscale properties, while the superscript t designates the tissue properties. The volumetric rates of heat due to metabolic heating, blood interfacial convective heat transfer, and blood perfusion are labeled by q_m , q_c , and q_p , respectively. q_e is the volumetric rate related to the external heat supply. For the heat flux density vector \mathbf{q} , three constitutive relations can be used: The Fourier law, Cattaneo–Vernotte (CV) relation, and dual-phase-lagging (DPL) relation (more details can be found in Ref. [78]).

Combining Fourier's law ($\mathbf{q}(\mathbf{r}, t) = -k\nabla T(\mathbf{r}, t)$, where \mathbf{r} denotes the material point and k is the thermal conductivity of the material) and Equation (1) leads to a group of thermal models for biological tissues (bioheat equations) [78]:

$$\begin{aligned} \frac{\partial(\rho c \epsilon T)_{mac}^t}{\partial t} &= \nabla \cdot (\epsilon k \nabla T)_{mac}^t + (\rho \epsilon q_m)_{mac}^t \\ &+ (\rho \epsilon q_c)_{mac}^t + (\rho \epsilon q_p)_{mac}^t + (\rho \epsilon q_e)_{mac}^t. \end{aligned} \quad (2)$$

Using the CV constitutive relation ($\mathbf{q}(\mathbf{r}, t) + \tau_q \partial \mathbf{q}(\mathbf{r}, t) / \partial t = -k \nabla T(\mathbf{r}, t)$) and Equation (1) yields the following expression [78]:

$$\begin{aligned} \frac{\partial(\rho c \epsilon T)_{mac}^t}{\partial t} + \tau_q \frac{\partial^2(\rho c \epsilon T)_{mac}^t}{\partial t^2} &= \nabla \cdot (\epsilon k \nabla T)_{mac}^t \\ &+ \left(1 + \tau_q \frac{\partial}{\partial t}\right) (\rho \epsilon q_m + \rho \epsilon q_c + \rho \epsilon q_p + \rho \epsilon q_e)_{mac}^t. \end{aligned} \quad (3)$$

Finally, by combining the DPL constitutive relation ($\mathbf{q}(\mathbf{r}, t + \tau_q) = -k \nabla T(\mathbf{r}, t + \tau_q)$) with Equation (1), a hyperbolic bioheat equation is obtained [78]:

$$\begin{aligned} \frac{\partial(\rho c \epsilon T)_{mac}^t}{\partial t} + \tau_q \frac{\partial^2(\rho c \epsilon T)_{mac}^t}{\partial t^2} &= \nabla \cdot \left[(\epsilon k)_{mac}^t \nabla T_{mac}^t \right] + \tau_T \frac{\partial}{\partial t} \left\{ \nabla \cdot \left[(\epsilon k)_{mac}^t \nabla T_{mac}^t \right] \right\} \\ &+ \left(1 + \tau_q \frac{\partial}{\partial t}\right) (\rho \epsilon q_m + \rho \epsilon q_c + \rho \epsilon q_p + \rho \epsilon q_e)_{mac}^t. \end{aligned} \quad (4)$$

Equation (4) predicts that the temperatures and thermal tissue damage differ significantly from those obtained by the Pennes model [80–82].

2.1.2. Bottom-Up Approach

The basic idea behind the porous media theory is that the entire biological medium can be divided into two distinct phases corresponding to tissue and blood (see Figure 3a). The tissue phase is solid, involving cells and interstitial spaces. The blood phase is the fluid part considered as the blood, which flows through the solid phase [83]. The blood volume fraction in the whole biological medium is represented by porosity, which is very important for tissues with high vascularization (e.g., the kidney, liver, and tumors).

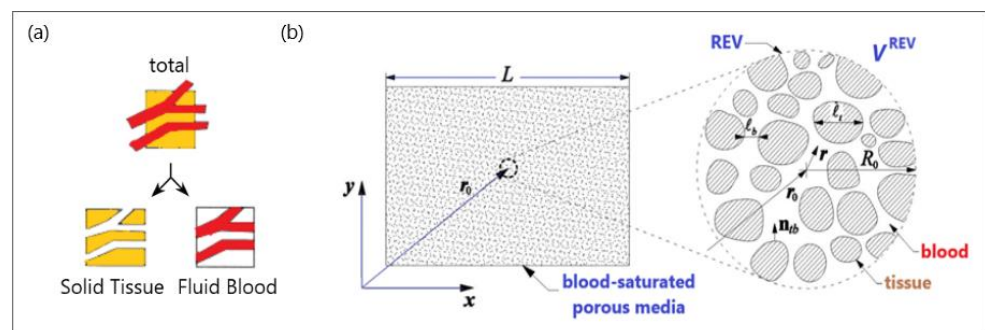


Figure 3. A schematic diagram of (a) a biological medium split into solid and blood phases and (b) a blood-saturated porous matrix encompassing cells and interstices and representative elementary volume (REV).

To establish the macroscale equations governing blood flow and bioheat transfer, biological tissue is simplified to a blood-saturated porous matrix comprising cells and interstices, as displayed in Figure 3b [84]. The resulting microscale field equations were then averaged over a representative elementary volume V^{REV} [78,85]:

$$\frac{1}{V^{\text{REV}}} \int_{V^b} \nabla \cdot \mathbf{v}_{mic}^b dV = 0, \quad (5)$$

$$\begin{aligned} & \frac{1}{V_{REV}} \int_{V^b} (\rho c)_{mic}^b \frac{\partial T_{mic}^b}{\partial t} dV + \frac{1}{V_{REV}} \int_{V^b} (\rho c)_{mic}^b \mathbf{v}_{mic}^b \cdot \nabla T_{mic}^b dV \\ &= \frac{1}{V_{REV}} \int_{V^b} \nabla \cdot (k_{mic}^b \nabla T_{mic}^b) dV. \end{aligned} \quad (6)$$

$$\begin{aligned} & \frac{1}{V_{REV}} \int_{V^t} (\rho c)_{mic}^t \frac{\partial T_{mic}^t}{\partial t} dV = \frac{1}{V_{REV}} \int_{V^t} \nabla \cdot (k_{mic}^t \nabla T_{mic}^t) \\ &+ \frac{1}{V_{REV}} \int_{V^t} (q_m)_{mic}^t dV. \end{aligned} \quad (7)$$

where V_b and V_t are the blood (denoted by superscript b) and tissue (denoted by superscript t), respectively, in the REV. The subscript “mic” refers to microscale properties, \mathbf{v} is the velocity, and T is the temperature. ρ , μ , c , and k are the density, viscosity, specific heat, and thermal conductivity, respectively. The volumetric rate of heat generated by the metabolic reaction is q_m .

2.2. Heat Transport in Tissues

MWA uses heat from microwave energy to kill cancer cells. The energy from the MW frequency waves emitted by the microwave coaxial antenna (MCA) creates heat in cancerous tissue without damaging the surrounding healthy tissue. As previously mentioned, the applied MW energy causes water molecules to vibrate and rotate, resulting in a temperature sufficiently high to cause cell death. An exact representation of heat transport through biological tissues plays a key role not only in the fundamental understanding of the process but also in many medical therapeutic options.

The bioheat transfer mechanism is illustrated in Figure 4 [86]. MW antenna immersed in tissue generates heat through the deposition of electromagnetic (EM) energy. Thermal diffusion of heat within the tissue leads to thermal conduction. Tissue fluid convection is unimportant for heat transfer inside the tissue because tissue fluid is either intracellular and cannot pass through the cell membrane or is extracellular with movement constrained by neighboring cells and the tissue matrix. Metabolic heat and blood perfusion are two mechanisms specific to biological tissues. Metabolic heat is generated by the metabolic activities of cells [87]. Blood perfusion causes the cooling of any tissue above the physiological temperature and, in many cases, represents a dominant mechanism affecting the tissue temperature during electromagnetic-energy-based thermal therapies [88].

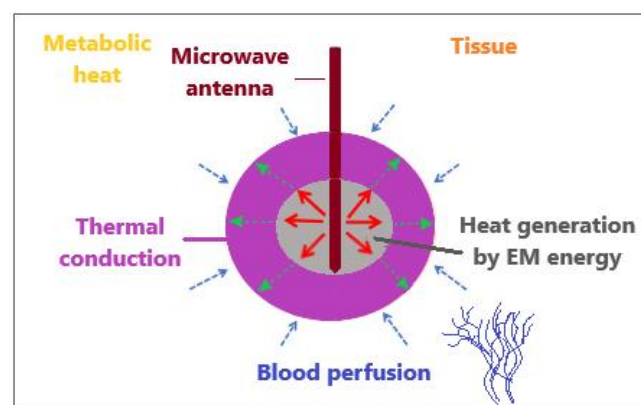


Figure 4. An illustrative overview of heat transfer mechanisms when an MW antenna is inserted into tissue to generate heat by the deposition of electromagnetic energy.

Most studies devoted to MWA have dealt with Pennes’ bioheat equation for modeling the heat transport of biological tissues because of its simplicity despite certain shortcomings. [83]. This model was developed under the assumption of a uniform perfusion rate without considering the blood flow direction and artery–vein countercurrent arrangement. In Pennes’ bioheat model, all heat exchange between the tissue and vasculature occurs in the capillaries, and the temperature of the vasculature within the capillaries is equivalent

to the core temperature of the human body. The assumptions also include that the venous blood is in thermal equilibrium with the tissue and that the arterial blood remains at a constant temperature of 37 °C. To overcome these simplifications and limitations, Pennes' bioheat model has been extended, modified, or coupled with other models [83]. Some researchers have attempted to overcome the simplifications and limitations of this model in order to obtain more accurate results. Pennes' theory has been extended in numerous papers [89–92]. An extensive review of the different bioheat models can be found in Andreozzi et al. [14].

2.2.1. Pennes Model

Heat transfer is often governed by the Pennes bio-heat equation [80,83]:

$$(\rho c)_t \frac{\partial T_t}{\partial t} = \nabla \times (k_t \nabla T_t) + \beta \rho_b \omega_b c_b (T_b - T_t) + Q_{\text{ext}} + Q_m, \quad (8)$$

where t is time. ρ_t , c_t , and T_t are the density, heat capacity, and temperature of the tissue, respectively, and ρ_b , T_b , c_b , and w_b are the density, temperature, heat capacity, and blood perfusion rate, respectively. The thermal damage affects values β between 0 and 1. The external heat source Q_{ext} refers to coupling with the electromagnetic field, whereas Q_m is related to metabolic heating [83].

Vaporization is embedded into Pennes' equation via the enthalpy method, and the term $(\rho c)_t$ in Equation (8) is given by the relation [83]

$$(\rho c)_t = \begin{cases} (\rho_l c_l)_t & 0^\circ\text{C} < T_t \leq 99^\circ\text{C} \\ \frac{h_{fg} C_{w,t}}{\Delta T_{b,t}} & 99^\circ\text{C} < T_t \leq 100^\circ\text{C} \\ \rho_g c_g & T_t > 100^\circ\text{C} \end{cases} \quad (9)$$

where ρ_l and c_l are the density and specific heat of tissue at a temperature below 100 °C (liquid phase). At temperatures above 100 °C (gas phase), the density and specific heat of the tissue are denoted by ρ_g and c_g , respectively. The product of the latent heat of vaporization and the water density at 100 °C is h_{fg} , whereas $C_{w,t}$ is the water content inside the liver tissue.

2.2.2. Modified Local Thermal Non-Equilibrium (LTNE) Model

The basic concept of the LTNE model is that the entire biological medium is divided into the tissue and blood phases. Thus, there are two energy equations for the LTNE model corresponding to the tissue temperature (T_t) and blood temperature (T_b) [83,93]:

$$(1 - \varepsilon)(\rho c)_t \frac{\partial \langle T_t \rangle}{\partial t} = (1 - \varepsilon)k_t \nabla^2 \langle T_t \rangle - h_c a (\langle T_t \rangle - \langle T_b \rangle) + \beta \rho_b \omega_b c_b (\langle T_b \rangle - \langle T_t \rangle) + (1 - \varepsilon)Q_{\text{ext}}, \quad (10)$$

$$\varepsilon(\rho c)_b \left(\frac{\partial \langle T_b \rangle}{\partial t} + \beta \langle \mathbf{u} \rangle \cdot \nabla \langle T_b \rangle \right) = \varepsilon k_b \nabla^2 \langle T_b \rangle + h_c a (\langle T_t \rangle - \langle T_b \rangle) + \beta \rho_b \omega_b c_b (\langle T_t \rangle - \langle T_b \rangle) + \varepsilon Q_{\text{ext}}, \quad (11)$$

where ε is the ratio of the blood volume to the total volume, \mathbf{u} is the vector of the blood velocity, and β is a coefficient whose value depends on the thermal damage function. h_c is the interfacial heat transfer coefficient and is the volumetric heat transfer area between the tissue and blood phases. Vaporization is included for the tissue phase, whereas for the blood phase, the following relation can be used [83]:

$$(\rho c)_b = \begin{cases} (\rho_l c_l)_b & 0^\circ\text{C} < T_b \leq 99^\circ\text{C} \\ \frac{h_{fg} C_{w,b}}{(100^\circ\text{C} - 99^\circ\text{C})} & 99^\circ\text{C} < T_b \leq 100^\circ\text{C} \\ \rho_g c_g & T_b > 100^\circ\text{C} \end{cases} \quad (12)$$

where $C_{w,b}$ represents the water content in blood.

2.2.3. Modified Local Thermal Equilibrium (LTE) Model

The LTNE model also describes blood and tissue phases at two distinct temperatures (i.e., $T_t \neq T_b$). However, under the local thermal equilibrium hypothesis, the tissue and blood are at the same temperature ($T_t = T_b = T$); thus, Equations (10) and (11) can be combined into a single equation [83]:

$$\begin{aligned} & [(1 - \varepsilon)(\rho c)_t + \varepsilon(\rho c)_b] \frac{\partial T}{\partial t} + \varepsilon(\rho c)_b \beta \cdot \mathbf{u} \cdot \nabla T \\ & = [(1 - \varepsilon)k_t + \varepsilon k_b](1 - \varepsilon) \nabla^2 T + Q_{\text{ext}}. \end{aligned} \quad (13)$$

Although local thermal equilibrium is a good approximation for temperature distributions in small vessels, it is not valid for larger vessels.

Dissimilarities between Pennes' model and the two porous media-based models (the LTNE and the LTE equations) can be observed in Figure 5 [83]. In the LTE and LTNE models, the Pennes' equation perfusion term is divided into a modified perfusion term and a convective term. Both models were modified to account for two-phase water vaporization (tissue and blood).

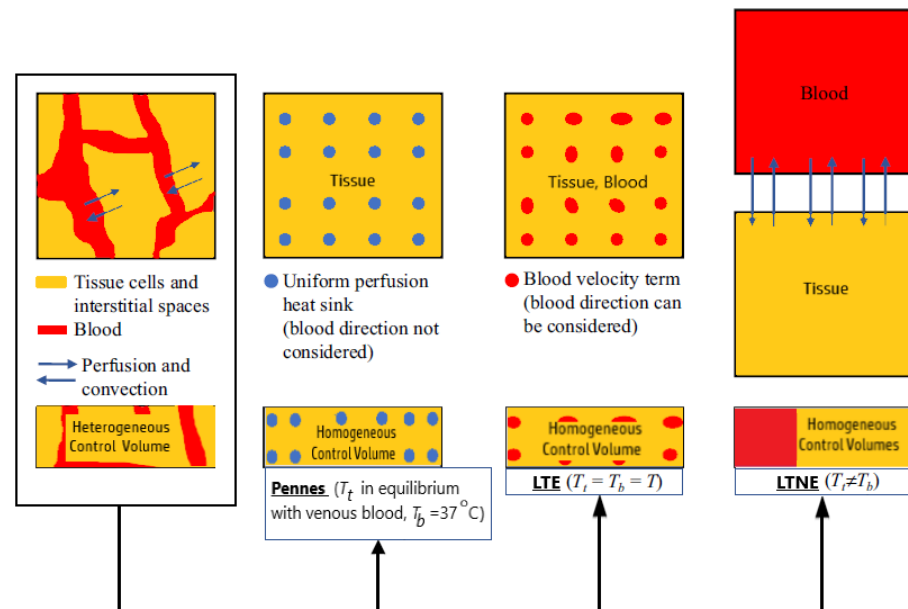


Figure 5. A comparison between Pennes' model and two porous-media-based models (the Local Thermal Non-Equilibrium and the Local Thermal Equilibrium equations).

3. Modeling of the Electromagnetic Field Generated by the Antenna

Another component that is indispensable in any mathematical model of MWA is the modeling of the microwave EM field generated by ablation probes (antennas). The efficiency of the MWA procedure strongly depends on the structure of the MW antenna. The MW antenna delivers energy to the tumor and surrounding area, resulting in an increase in temperature to a lethal level and cell death in the ablation zone. To enhance the performance of the MWA procedure, various antenna designs have been developed including choke [94], cap-choke [95], floating sleeve [96,97], and water-cooled [98] antennas (Figure 6). The factors that may lead to a temperature increase along the antenna shaft and, thus, to the formation of elongated heating patterns (see Figure 7a) are the impedance mismatch between the antenna and tissues and the leakage current along the outer conductor of the antenna. Recently, small microwave antennas capable of creating larger spherical ablation volumes in the liver have been developed [95,99,100]. With its simple construction, compact size, and low cost, the coaxial antenna with several slots became a promising

antenna design due to its simple construction, compact size, and low cost [99]. In their theoretical work, Wang et al. proposed a multi-slot coaxial antenna with periodic slots [99]. The desired shape of ablation zones can be attained by regulating the distance between adjacent slots and the number of slots. Compared with other antenna designs (see [101] and references therein), a multi-slot coaxial antenna has a better ability to produce an optimal shape of the ablation zone pattern (see Figure 7b) [101]. Recent simulation results have confirmed that a compact 10-slot antenna consisting of several periodic elements equivalent to a linear uniform antenna array creates near-spherical ablation zones [50,53]. Finely tuned impedance matching minimizes damage to the surrounding healthy tissues. In one of the most sophisticated antenna designs, the required ablation zones are achieved using three different mechanisms: Thermal, field, and wavelength controls [32,33].

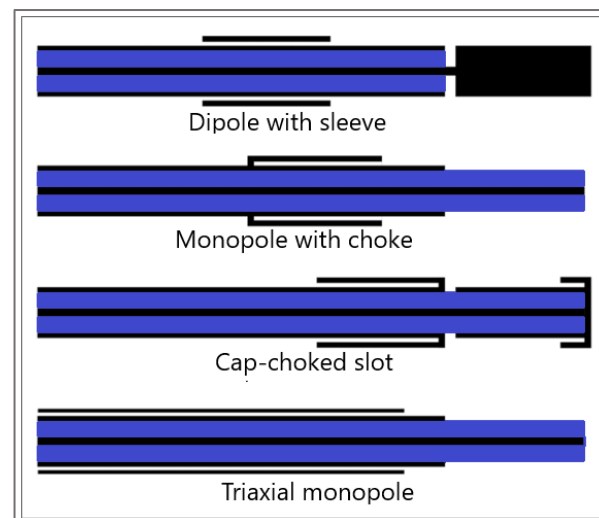


Figure 6. Sketches of antenna designs with sleeve, choke, cap-choked, and monopole in triaxial configuration. The metal and the dielectric are shown in black and blue, respectively.

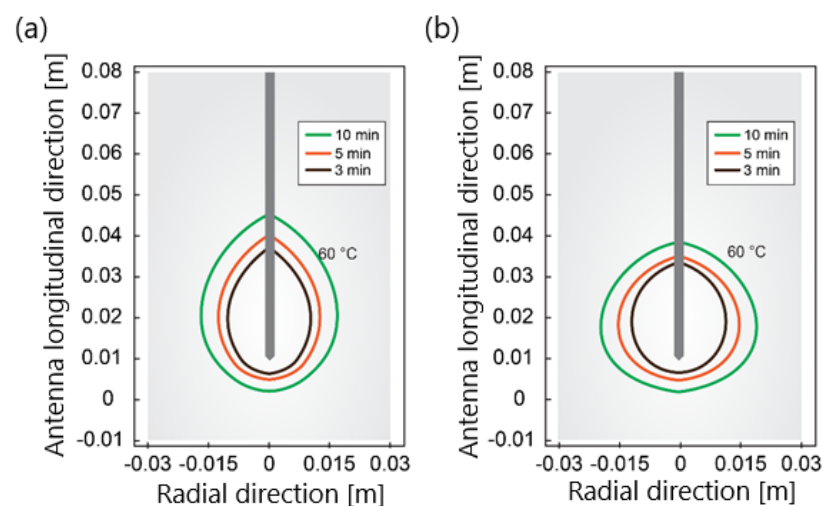


Figure 7. The isotherm corresponds to 60 °C for (a) a single-slot antenna and (b) 10-slot antenna with impedance matching after ablation times of 180 s, 300 s, and 600 s for an input power of 30 W.

Tissue heating is directly related to the ratio of absorbed heat power to tissue density, that is, the so-called specific absorption rate (SAR). In the tumor region, the values of the SAR are maximal. As shown in Figure 8, a 10-slot antenna has the highest SAR value among antennas with various numbers of slots.

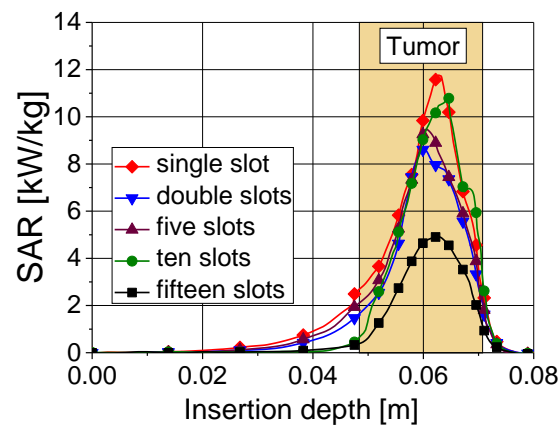


Figure 8. Specific absorption rate versus insertion depth for five antennas with different numbers of slots. The results were obtained for an input power of 45 W and ablation time of 600 s.

Owing to its mechanical and geometrical complexity, antenna modeling is strongly affected by electromagnetic material and tissue properties. The antenna probe (or applicator) immersed in the tissue generates a microwave field governed by equations [50,102]:

$$\nabla^2 \mathbf{E} - \mu_r k_0^2 \left(\epsilon_r - \frac{j\sigma}{\omega \epsilon_0} \right) \mathbf{E} = 0, \quad (14)$$

where ω is the angular frequency, \mathbf{E} is the electric field vector, $k_0 = \omega/c_0$ is the vacuum propagation constant, and ϵ_0 is the vacuum dielectric constant. σ , ϵ_r , and μ_r denote tissue electrical conductivity, relative permittivity, and tissue permeability, respectively.

During MWA, an increase in the temperature may result in structural modifications of the treated tissue, leading to changes in the dielectric and thermal properties, thus affecting the electromagnetic power distribution [103]. The conductivity and permittivity depend on the temperature. The temperature dependence of tissue dielectric properties arises primarily because of the significant water concentration in organ tissue [104]. During MWA, tissue heating causes the evaporation of water molecules, which irreversibly changes the protein structures, causing changes in the conductivity and permittivity of the tissue [50,102].

$$\epsilon_r(T) = s_1 \left[1 - \frac{1}{1 + \exp(s_2 - s_3 T)} \right], \quad (15)$$

$$\sigma(T) = r_1 \left[1 - \frac{1}{1 + \exp(r_2 - r_3 T)} \right], \quad (16)$$

where the coefficients can be found elsewhere (e.g., in [102]). The sigmoidal temperature-dependent model of (a) relative permittivity and (b) electric conductivity of healthy and tumoral liver tissues are plotted in Figure 9. Tumors have an approximately 24% higher relative permittivity and 11% higher conductivity than healthy tissue [105]. During MWA, as the temperature increases, water evaporation leads to a decrease in dielectric properties [102,106]. The time dependence of the water content $W(T)$ is expressed as [40]:

$$W(T) = \begin{cases} 0.778 \cdot \left(1 - e^{\frac{T-106}{3.42}} \right), & 70^\circ \text{C} \leq T < 100^\circ \text{C} \\ 7.053 - 0.064096 \cdot T, & 100^\circ \text{C} \leq T < 104^\circ \text{C} \\ 0.778 \cdot e^{-\frac{T-80}{34.37}}, & T \geq 104^\circ \text{C} \end{cases} \quad (17)$$

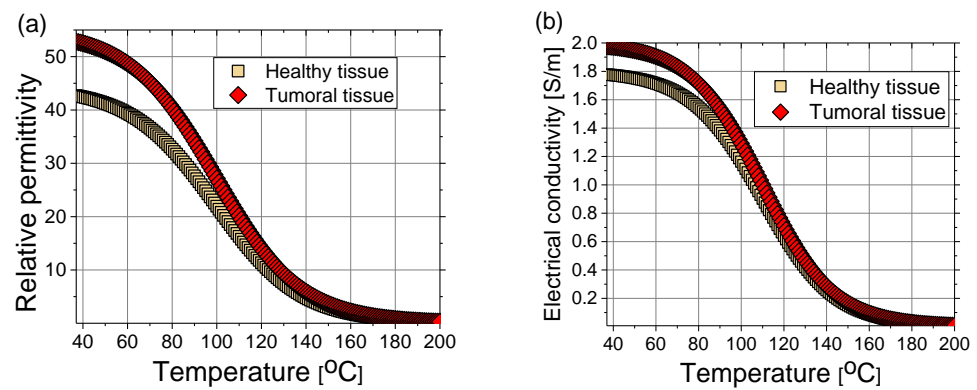


Figure 9. (a) Relative permittivity and (b) electrical conductivity of healthy (squares) and tumoral (diamonds) liver tissue as a function of time according to Equations (15) and (16) with coefficients from Ref. [102].

In a steady state, the liver tissue contains approximately 78% water by mass (Figure 10a). Therefore, its thermal properties are similar to those of water [40]. As a result of evaporation at temperatures above 100 °C, the water content of the tissue may decrease to less than 20% by mass, leading to drastic changes in the dielectric properties of the tissue and the significant penetration of microwaves. The effect of water evaporation can be included in the bio-heat Equation (8) by replacing specific heat c with an effective value c' :

$$c' = c - \frac{\alpha}{\rho} \frac{\partial W}{\partial T}, \quad (18)$$

where the derivative of $W(T)$ is plotted in Figure 10b, and $\alpha = 2260$ (kJ/kg) is the latent heat constant [40].

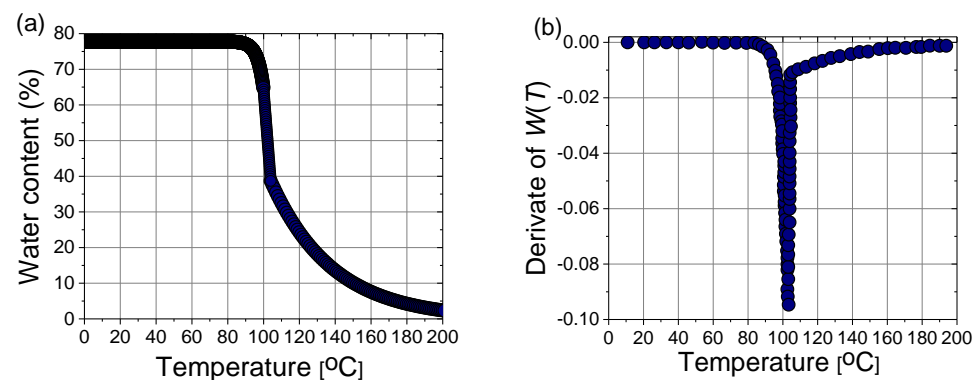


Figure 10. (a) Variation of the water content with the temperature $W(T)$ according to (17) and (b) the first derivative of $W(T)$ necessary for the calculation of the effective specific heat (18).

Damage to biological tissues depends on both temperature and time. The most well-known expression for determining tissue injury Ω is the Arrhenius form [107]:

$$\Omega(t) = \int_0^t A \exp\left(-\frac{\Delta E}{RT}\right) dt, \quad (19)$$

with the frequency factor A , temperature T , and activation energy for irreversible damage reaction ΔE . R is the gas constant.

4. Modeling of Microwave Ablation in the Treatment of Hepatocellular Carcinoma

Hepatocellular carcinoma (HCC) is the most common form of liver cancer, constituting > 90% of primary liver malignancy [108–110]. In terms of HCC mortality, the 3-year survival rate is only 12.7% [111,112]. Although HCC is the fourth most common cause of cancer-related deaths worldwide, therapeutic options remain insufficient. One of the most promising therapies for HCC is MWA at 2.45 GHz as a rapid treatment with a short recovery [9,113]. The development of mathematical models enables the determination of the optimal conditions necessary for planning patient-specific MWA procedures to be as effective as possible for treating HCC [50,53].

The 3D models of the MW applicator (antenna) and the tumor without homogeneity assumptions are the most realistic representations of the physical problem. However, the complexity and computational resource consumption limit the number of 3D models. Hence, most numerical studies are 2D models rotated around an axis to emulate 3D models that are often far from reality. To overcome the limitations and deficiencies of the 2D models, a full 3D model was developed by considering all the details described in the previous sections. The 3D finite element method (FEM) within COMSOL Multiphysics [114] was applied to solve the system of coupled equations corresponding to the electromagnetic field and heat transfer. In the model, Pennes' bio-heat equation is used, taking into account the temperature dependence of thermal conductivity and effective specific heat. The temperature dependence of electrical conductivity and permittivity of healthy and tumoral tissues is included in the calculation of the electromagnetic field. A compact 10-slot antenna with several periodic elements (Figure 11) was immersed in tissue [50,53].

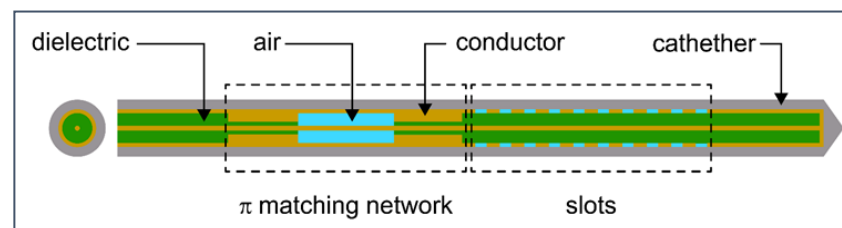


Figure 11. Schematic of 10-slot microwave antenna. The width of a single slot is 0.6 mm, whereas the distance between two slots is 0.8 mm. Finely tuned impedance matching preserves the surrounding tissues.

To make the model as realistic as possible, we did not use a spherical tumor geometry, as was typically performed. Instead, we used realistic tumor geometry based on data from the 3D-IRCAdb-01 database, which comprises several sets of patients' CT scans manually segmented by clinical experts [115]. The simulation parameters characteristics for healthy liver, malignancy, and blood are listed in Table 1 [50,53,102].

4.1. Results

4.1.1. Hepatocellular Carcinoma of Patient 16 in the 3D-IRCAdb-01 Database

Figure 12 shows the liver (triangular surface) with early-stage HCC (1.64 cm × 1.71 cm × 3.81 cm) (solid red surface) of patient 16 (male, born in 1950) in the 3D-IRCAdb-01 database [115]. The optimal value of the input power is the value required for treating the entire tumor with minimal damage to the healthy surrounding tissue. In the case of HCC in patient 16 [115], the optimal input power can be evaluated from the isocontours associated with the fraction of damage equal to 1, as shown in Figure 13. When a power of 10 W was applied, the tumor was not completely ablated. At 15 W, the ablation zone encompasses not only the whole tumor but also significant damage to healthy tissue. The application of 13 W provides treatment for the entire tumor with minimal damage to the surrounding tissue [50]. Because the shape and size of the tumor significantly affect the proper choice of input power, it should be estimated before the procedure begins to attain the desired ablation zone.

Table 1. Parameters of biological materials (healthy liver tissue, liver tumor lesions, and blood) used in the simulations [50,53,102].

Parameter	Value
Healthy liver tissue	
Density	1079 kg/m ³
Thermal conductivity	0.52 W/m °C
Specific heat	3540 J/kg °C
Tumoral liver tissue	
Density	1040 kg/m ³
Thermal conductivity	0.57 W/m °C
Specific heat	3960 J/kg °C
Blood	
Density	1060 kg/m ³
Thermal conductivity	0.5 W/m °C
Specific heat	3600 J/kg °C
Temperature	37 °C

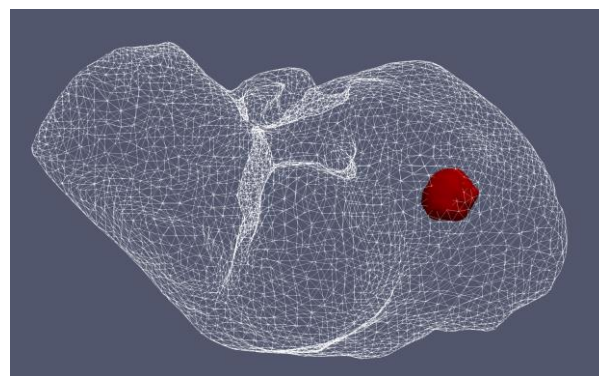


Figure 12. Three-dimensional simulation model of HCC (solid red surface), which belonged to patient 16 in the 3D-IRCADb-01 database [115], and its position in the liver (triangulated surface).

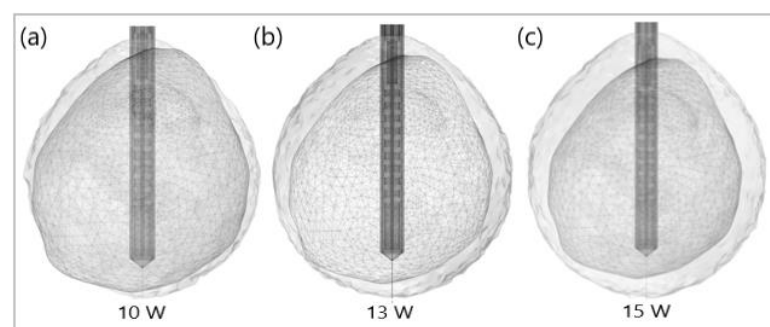


Figure 13. Isocontours that are related to ablated regions (solid gray surfaces) around the HCC (triangulated surface) after 600 s of microwave ablation at 2.45 GHz with an input power of (a) 10 W, (b) 13 W, and (c) 15 W.

Energy radiated by the MW antenna is absorbed and converted into thermal energy. The temporal evolution of the temperature distribution during MWA is shown in Figure 14. Black and white lines mark the boundary of the tumor and the lethal isotherm at 60 °C,

respectively. The 60 °C isothermal contours are correlated to the lesion size and shape of the ablated tissue [50]. Blood perfusion limits the extent of the heating.

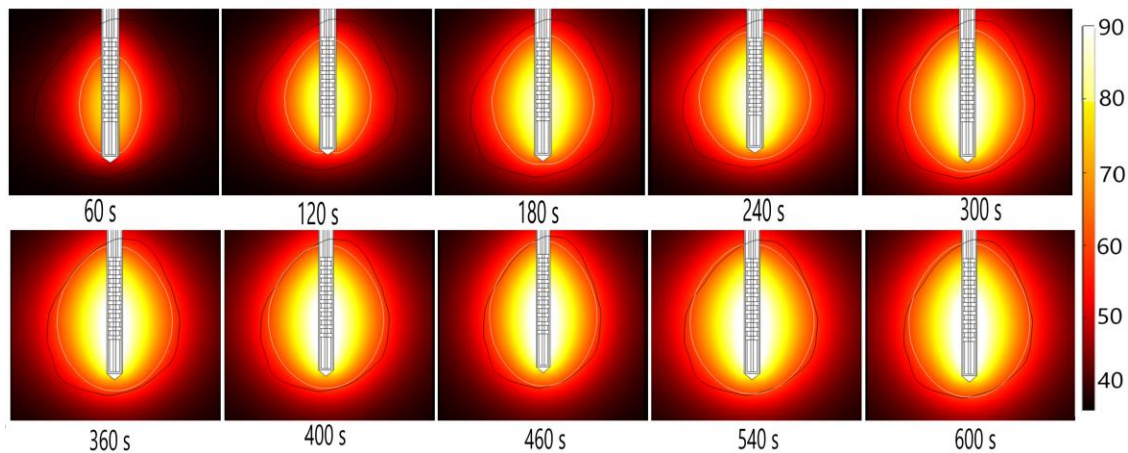


Figure 14. The temperature distribution during microwave ablation (in °C) when an early-stage HCC [115] is exposed to a frequency of 2.45 GHz and an input power of 13 W. The boundary of the tumor tissue is represented by a black line.

The fraction of necrotic tissue during MWA at 2.45 GHz and a power of 13 W is shown in Figure 15. A multislot antenna produces near-spherical ablation zones with damage concentrated around the tip and slots of the antenna [50]. The 10-slot antenna produces localized near-spherical heating distributions. Two distinct heating zones can be distinguished [8]. The active heating zone is located inside the tumor close to the antenna where the intensity of energy is high and its absorption by tissue is fast. The passive zone is far from the antenna in the region with low energy intensity.

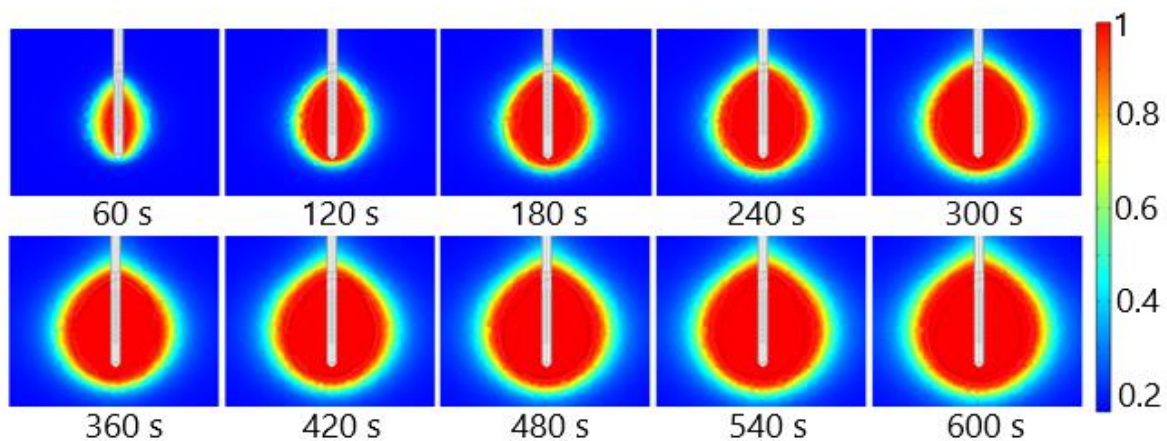


Figure 15. The fraction of tissue damage during microwave ablation of HCC [115] at a frequency of 2.45 GHz and an input power of 13 W. The black line denotes the boundary of the tumor.

It is evident from the isocontours related to different temperatures (Figure 16a) that, when approaching the antenna, the heat source is stronger, and the temperature is higher. Isocontours associated with different fractions of damage (Figure 16b) illustrate that complete ablation of the tumor was achieved for a fraction of damage of 1 [50].

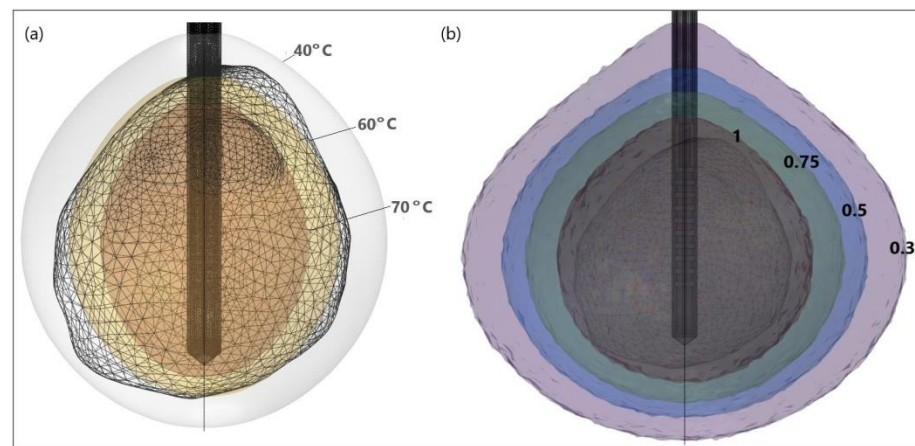


Figure 16. HCC (triangulated surface) [115] and isocontours that correspond to (a) temperatures of 40 °C, 60 °C, and 70 °C, and (b) fractions of damage of 0.3, 0.5, 0.75, and 1.

4.1.2. Hepatocellular Carcinomas of Patient 1 in the 3D-IRCAdB-01 Database

Figure 17 shows the liver and severe HCCs of patient 1 (female born in 1940) in the 3D-IRCAdB-01 database [115]. Simulations were carried out for two of them (solid red surfaces) labeled as 1.07 (1.74 cm × 1.53 cm × 2.10 cm) and 1.03 (1.78 cm × 1.97 cm × 2.27 cm). First, the optimal values of the input power were determined for both HCCs. Because of the irregular shapes of the tumors, both sides—the front (left) and back (right)—of the tumors are shown. For tumor 1.07 [115] (Figure 18a), an input power of 9 W did not ensure complete ablation of the tumor (backside). When 11 W was applied, the ablation zone enclosed the entire tumor, and a large amount of healthy tissue was damaged. The isocontour that ensures necrosis of the entire tumor preserving healthy tissue was achieved for an input power of 10 W [53]. By using a similar procedure, it was found that the optimal input power for HCC 1.03 [115] is 12 W (Figure 18b).

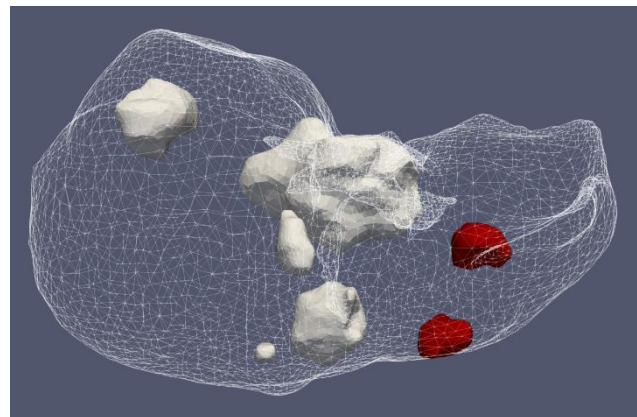


Figure 17. Positions of seven HCCs (solid surfaces) in the liver (triangulated surface) of patient 1 in the 3D-IRCAdB-01 database [115].

The significance of the proper choice of optimal values of the input power and ablation time is demonstrated in Figure 19. The ablation time decreased with an increase in the input power. Damage to healthy tissue around tumors applying a power of 15 W or 17 W during a shorter ablation time is similar to those obtained for 10 W (for tumor 1.07 [115]) and 12 W (for tumor 1.07 [115]) after 600 s [53]. However, higher input power and shorter ablation time are not always related to the safest MWA treatment. Further increases in the input power cause significant damage to healthy tissue despite the shorter ablation time, as shown in Figure 20. For higher input power, ablation zones became more elongated with a

greater length along the shaft of the antenna causing unavoidable damage to the healthy tissue [53].

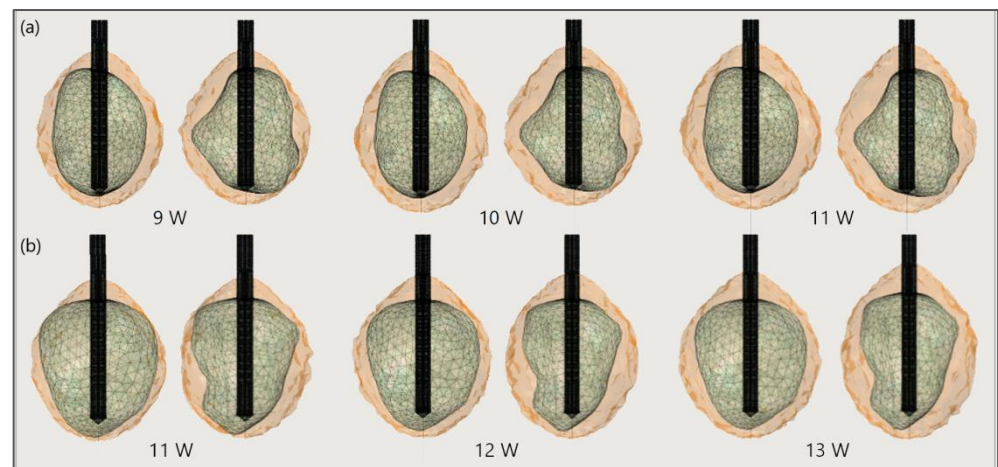


Figure 18. The ablated regions (solid light brown surface) around the front (left) and back (right) sides of tumors (triangulated surface) (a) 1.07 [115] and (b) 1.03 [115] after 600 s of microwave ablation at 2.45 GHz and different values of the input power.

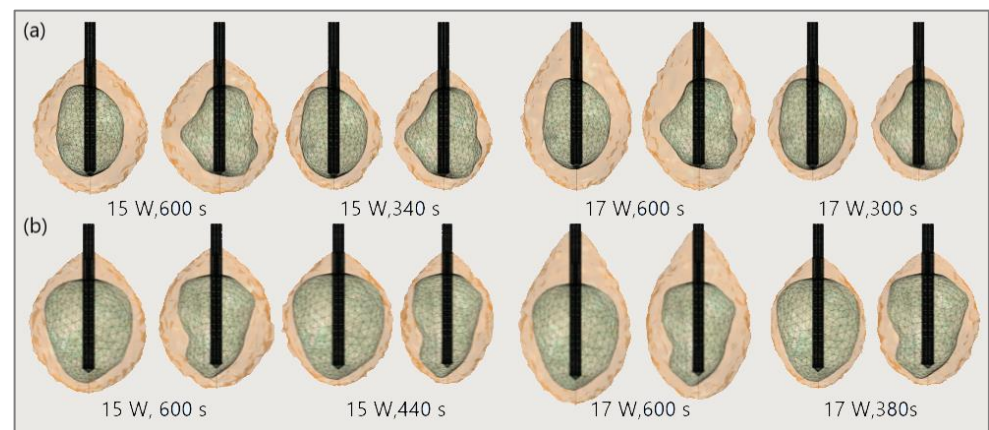


Figure 19. Isocounturs representing the ablated regions (solid light brown surface) around the front (left) and back (right) sides of tumors (triangulated surface) (a) 1.07 [115] and (b) 1.03 [115] for input powers of 15 W and 17 W and various duration of microwave ablation.

Finally, to demonstrate the necessity of performing 3D simulations, Figure 21 shows the necrotic tissue and time required for the complete ablation of tumors (a) 1.07 [115] and (b) 1.03 [115]. The ablation zones plotted in the upper figures (in the cut plane $x = 0$) may not precisely represent tissue necrosis. The upper figures indicate that the entire tumor was ablated after 400 s. However, both sides of the tumor (lower figures) suggest that they were completely ablated after 600 s [53].

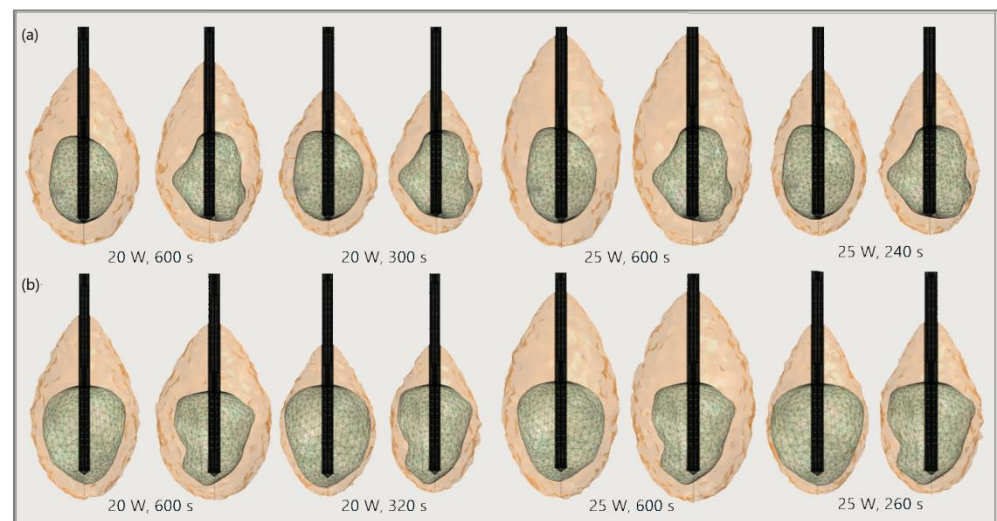


Figure 20. The ablated regions (solid light brown surface) around the front (left) and back (right) sides of tumors (triangulated surface) (a) 1.07 [115] and (b) 1.03 [115] for input powers of 20 W and 25 W and various ablation times.

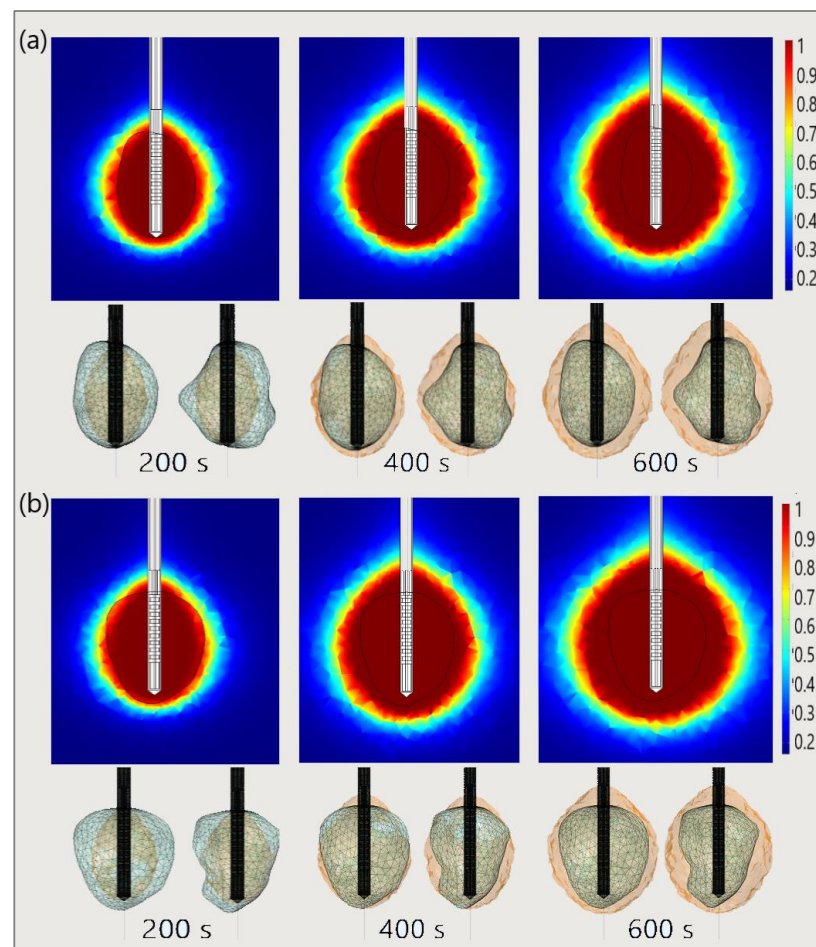


Figure 21. The time evolution of the necrotic tissue tumors (a) 1.07 [115] and (b) 1.03 [115], after ablation times of 200 s, 400 s, and 600 s. Necrotic tissue in the cut plane ($x = 0$) (upper figures) and the front and back sides of the tumors (triangulated surfaces) (lower figures).

5. Discussion

Since the thermal spread in biological tissue is difficult to measure, the development of predictive models is essential. For studying heat transport in complex heterogeneous systems such as biological tissues, macroscale models must be used. The macroscopic point of view is important foremost to overcome possible complications due to a large number of particles at the molecular scale or the compound microscale structure of tissues. Proper separation of the length scales represents a crucial step in establishing a macroscale representation that is identical to the microscale behavior. Beyond macroscopic models, some researchers have attempted to provide a link between microscopic processes and the overall dynamics of tissues. Based on the mixture theory and poroelasticity concepts, tissues are represented as a mixture of interacting solid and fluid phases, which enable investigation of the biological tissues at a fundamental level. Micromechanical effects at the cellular level also must be included for determining the heat transport and thermal damages for which satisfactory models still do not exist. However, researchers must have the disposal of novel computer approaches directed toward the development of more sophisticated tissue models.

Computer modeling is proven to be an effective tool to improve the performance of MWA. Most of the existing numerical models of MWA are 2D axis-symmetric based on the assumption of a homogeneous medium reducing the problem from 3D to 2D. Taking into account that each tumor has a different shape and size, the development of 3D predictive models of the MWA procedure including all details of the targeted tissue characteristics and the antenna design is a prerequisite for further ablation studies with a promising possibility of application in the treatment planning adjusted for each patient.

6. Conclusions and Perspectives

Microwave ablation therapy has become an important topic in medicine, and numerous investigations on the applications of heat transfer to biological tissues have been conducted in the last few decades. Numerical methods may significantly influence patient care by creating predictive models from procedural planning to execution. Furthermore, the lack of experimental results in this field emphasizes the need for mathematical models. Understanding the science underlying ablation therapy is crucial for developing accurate models of tissue and heat processes. For microwave ablation simulations, every mathematical model must contain three fundamental components that depend on the tissue characteristics of an individual patient. Currently, complex heat transfer models rely on the porosity concept, leading to two “bioheat” equations for the tissue and blood temperatures.

In this article, we review the current status of numerical methods for modeling microwave ablation procedures. We reviewed different models and theories proposed to describe tissue and heat transport. We compare them to highlight their differences and identify important trends. We have also summarized numerous microwave antenna designs developed over the last few decades including a recent multi-slot antenna that offers the best performance and provides near-spherical ablation zone patterns. To illustrate the application of the reviewed numerical methods, we present the results of three-dimensional simulations of real Hepatocellular Carcinomas from the 3D-IRCAdb-01 database. The primary aim was to create a realistic simulation model that could predict ablation results. The final goal is to transform the treatment plan based on the simulation outputs into a minimally invasive and safe microwave ablation procedure. Therefore, several questions and challenges remain. The main reason for this is whether and how antenna design alters the dielectric and other properties of the tissue during microwave ablation. Finally, this work focused on microwave ablation, but with numerous other operating modes, these concepts and theories need to be expanded. All these challenges may lead to exponential progress in the computational modeling of microwave tissue ablation.

Author Contributions: Conceptualization, M.R.-R. and B.R.; methodology, M.R.-R., N.B. and B.R.; validation, M.R.-R.; formal analysis, M.R.-R., N.B. and B.R.; writing—original draft preparation, M.R.-

R.; writing—review and editing, B.R.; visualization, M.R.-R.; supervision, B.R.; project administration, M.R.-R. All authors have read and agreed to the published version of the manuscript.

Funding: All authors acknowledge that this research was supported by the Science Fund of the Republic of Serbia, The Program IDEAS, GRANT No. 7739583, SimSurgery.

Institutional Review Board Statement: Not applicable.

Informed Consent Statement: Not applicable.

Data Availability Statement: Data are contained within the article.

Acknowledgments: Authors acknowledge the support of the Institute of Physics Belgrade through the grant by the Ministry of Education, Science, and Technological Development of the Republic of Serbia.

Conflicts of Interest: The authors declare no conflict of interest.

References

- Ong, S.L.; Gravante, G.; Metcalfe, M.S.; Strickland, A.D.; Dennison, A.; Lloyd, D.M. Efficacy and safety of microwave ablation for primary and secondary liver malignancies: A systematic review. *Eur. J. Gastroenterol. Hepatol.* **2009**, *21*, 599–605. [\[CrossRef\]](#) [\[PubMed\]](#)
- Poggi, G.; Tosoratti, N.; Montagna, B.; Picchi, C. Microwave ablation of hepatocellular carcinoma. *World J. Hepatol.* **2015**, *7*, 2578–2589. [\[CrossRef\]](#) [\[PubMed\]](#)
- Crocetti, L.; Scalise, P.; Bozzi, E.; Campani, D.; Rossi, P.; Cervelli, R.; Bargellini, I.; Ghinolfi, D.; De Simone, P.; Cioni, R. Microwave Ablation of Very-Early- and Early-Stage HCC: Efficacy Evaluation by Correlation with Histology after Liver Transplantation. *Cancers* **2021**, *13*, 3420. [\[CrossRef\]](#) [\[PubMed\]](#)
- Ausania, F.; Borin, A.; Melendez, R.; del Rio, P.S.; Iglesias, A.; Bodenlle, P.; Paniagua, M.; Arias, M. Microwave ablation of colorectal liver metastases: Impact of a 10-mm safety margin on local recurrence in a tertiary care hospital. *Ann. Hepato-Biliary-Pancreatic Surg.* **2021**, *25*, 366–370. [\[CrossRef\]](#)
- Lee, S.K.; Chung, D.J.; Cho, S.H. A Real-World Comparative Study of Microwave and Radiofrequency Ablation in Treatment-Naïve and Recurrent Hepatocellular Carcinoma. *J. Clin. Med.* **2022**, *11*, 302. [\[CrossRef\]](#)
- Facciorusso, A.; Di Maso, M.; Muscatiello, N. Microwave ablation versus radiofrequency ablation for the treatment of hepatocellular carcinoma: A systematic review and meta-analysis. *Int. J. Hypertherm.* **2016**, *32*, 339–344. [\[CrossRef\]](#)
- Violi, N.V.; Duran, R.; Guiu, B.; Cercueil, J.-P.; Aubé, C.; Digkila, A.; Pache, I.; Deltenre, P.; Knebel, J.-F.; Denys, A. Efficacy of microwave ablation versus radiofrequency ablation for the treatment of hepatocellular carcinoma in patients with chronic liver disease: A randomised controlled phase 2 trial. *Lancet Gastroenterol. Hepatol.* **2018**, *3*, 317–325. [\[CrossRef\]](#)
- Izzo, F.; Granata, V.; Grassi, R.; Fusco, R.; Palaia, R.; Delrio, P.; Carrafiello, G.; Azoulay, D.; Petrillo, A.; A Curley, S. Radiofrequency Ablation and Microwave Ablation in Liver Tumors: An Update. *Oncol.* **2019**, *24*, e990–e1005. [\[CrossRef\]](#)
- Glassberg, M.B.; Ghosh, S.; Clymer, J.W.; Wright, G.W.J.; Ferko, N.; Amaral, J.F. Microwave ablation compared with hepatic resection for the treatment of hepatocellular carcinoma and liver metastases: A systematic review and meta-analysis. *World J. Surg. Oncol.* **2019**, *17*, 98. [\[CrossRef\]](#)
- Facciorusso, A.; El Aziz, M.A.A.; Tartaglia, N.; Ramai, D.; Mohan, B.P.; Cotsoglou, C.; Pusceddu, S.; Giacomelli, L.; Ambrosi, A.; Sacco, R. Microwave Ablation Versus Radiofrequency Ablation for Treatment of Hepatocellular Carcinoma: A Meta-Analysis of Randomized Controlled Trials. *Cancers* **2020**, *12*, 3796. [\[CrossRef\]](#)
- Chong, C.C.; Lee, K.F.; Cheung, S.Y.; Chu, C.C.; Fong, A.K.; Wong, J.; Hui, J.W.; Fung, A.K.; Lok, H.T.; Lo, E.Y.; et al. Prospective double-blinded randomized controlled trial of Microwave versus RadioFrequency Ablation for hepatocellular carcinoma (McRFA trial). *HPB* **2020**, *22*, 1121–1127. [\[CrossRef\]](#) [\[PubMed\]](#)
- Suwa, K.; Seki, T.; Aoi, K.; Yamashina, M.; Murata, M.; Yamashiki, N.; Nishio, A.; Shimatani, M.; Naganuma, M. Efficacy of microwave ablation versus radiofrequency ablation for hepatocellular carcinoma: A propensity score analysis. *Abdom. Radiol.* **2021**, *46*, 3790–3797. [\[CrossRef\]](#) [\[PubMed\]](#)
- Sun, Q.; Shi, J.; Ren, C.; Du, Z.; Shu, G.; Wang, Y. Survival analysis following microwave ablation or surgical resection in patients with hepatocellular carcinoma conforming to the Milan criteria. *Oncol. Lett.* **2020**, *19*, 4066–4076. [\[CrossRef\]](#) [\[PubMed\]](#)
- Andreozzi, A.; Iasiello, M.; Tucci, C. Chapter Six—An overview of mathematical models and modulated-heating protocols for thermal ablation. *Adv. Heat Transf.* **2020**, *52*, 489–541.
- Lubner, M.G.; Brace, C.L.; Hinshaw, J.L.; Lee, F.T. Microwave Tumor Ablation: Mechanism of Action, Clinical Results, and Devices. *J. Vasc. Interv. Radiol.* **2010**, *21*, S192–S203. [\[CrossRef\]](#) [\[PubMed\]](#)
- Curto, S.; Taj-Eldin, M.; Fairchild, D.; Prakash, P. Microwave ablation at 915 MHz vs. 2.45 GHz: A theoretical and experimental investigation. *Med. Phys.* **2015**, *42*, 6152–6161. [\[CrossRef\]](#)
- Simon, C.J.; Dupuy, D.; Mayo-Smith, W.W. Microwave Ablation: Principles and Applications. *RadioGraphics* **2005**, *25*, S69–S83. [\[CrossRef\]](#)

18. Kim, H.J.; Rhim, H.; Lee, M.W.; Jeong, W.K. Measurement of Intrahepatic Pressure during Microwave Ablation in an Ex Vivo Bovine Liver Model. *Gut Liver* **2015**, *9*, 784–790. [[CrossRef](#)]
19. Wang, H.; He, Y.; Yang, M.; Yan, Q.; You, F.; Fu, F.; Wang, T.; Huo, X.; Dong, X.; Shi, X. Dielectric properties of human liver from 10Hz to 100MHz: Normal liver, hepatocellular carcinoma, hepatic fibrosis and liver hemangioma. *Bio-Medical Mater. Eng.* **2014**, *24*, 2725–2732. [[CrossRef](#)]
20. Zhekov, S.S.; Franek, O.; Pedersen, G.F. Dielectric Properties of Human Hand Tissue for Handheld Devices Testing. *IEEE Access* **2019**, *7*, 61949–61959. [[CrossRef](#)]
21. Bottiglieri, A.; Ruvio, G.; O'Halloran, M.; Farina, L. Exploiting Tissue Dielectric Properties to Shape Microwave Thermal Ablation Zones. *Sensors* **2020**, *20*, 3960. [[CrossRef](#)] [[PubMed](#)]
22. Baker-Jarvis, J.; Kim, S. The Interaction of Radio-Frequency Fields with Dielectric Materials at Macroscopic to Mesoscopic Scales. *J. Res. Natl. Inst. Stand. Technol.* **2012**, *117*, 1–60. [[CrossRef](#)] [[PubMed](#)]
23. Farsaci, F.; Russo, A.; Ficarra, S.; Tellone, E. Dielectric Properties of Human Normal and Malignant Liver Tissue: A Non-Equilibrium Thermodynamics Approach. *Open Access Libr. J.* **2015**, *2*, e1395. [[CrossRef](#)]
24. Fahmy, H.M.; Hamad, A.M.; Sayed, F.A.; Abdelaziz, Y.S.; Abu Serea, E.S.; Mustafa, A.B.E.; Mohammed, M.A.; Saadeldin, A.M. Dielectric spectroscopy signature for cancer diagnosis: A review. *Microw. Opt. Technol. Lett.* **2020**, *62*, 3739–3753. [[CrossRef](#)]
25. Stauffer, P.R. Evolving technology for thermal therapy of cancer. *Int. J. Hyperth.* **2005**, *21*, 731–744. [[CrossRef](#)] [[PubMed](#)]
26. Kuang, M.; Lu, M.D.; Xie, X.Y.; Xu, H.X.; Mo, L.Q.; Liu, G.J.; Xu, Z.F.; Zheng, Y.L.; Liang, J.Y. Liver Cancer: Increased Microwave Delivery to Ablation Zone with Cooled-Shaft Antenna—Experimental and Clinical Studies. *Radiology* **2007**, *242*, 914–924. [[CrossRef](#)]
27. Simon, C.J.; Dupuy, D.E.; Iannitti, D.A.; Lu, D.S.K.; Yu, N.C.; Aswad, B.I.; Busuttil, R.W.; Lassman, C. Intraoperative Triple Antenna Hepatic Microwave Ablation. *Am. J. Roentgenol.* **2006**, *187*, W333–W340. [[CrossRef](#)]
28. Hojjatollah, F.; Punit, P. Antenna Designs for Microwave Tissue Ablation. *Crit. Rev. Biomed. Eng.* **2018**, *46*, 495–521.
29. Kapoor, H.; Nisiewicz, M.J.; Jayavarapu, R.; Gedaly, R.; Raissi, D. Early Outcomes with Single-antenna High-powered Percutaneous Microwave Ablation for Primary and Secondary Hepatic Malignancies: Safety, Effectiveness, and Predictors of Ablative Failure. *J. Clin. Imaging Sci.* **2020**, *10*, 10. [[CrossRef](#)]
30. Hendriks, P.; Berkhout, W.E.M.; Kaanen, C.I.; Sluijter, J.H.; Visser, I.J.; Dobbela, J.J.V.D.; de Geus-Oei, L.F.; Webb, A.G.; Burgmans, M.C. Performance of the Emprint and Amica Microwave Ablation Systems in ex vivo Porcine Livers: Sphericity and Reproducibility Versus Size. *Cardiovasc. Interv. Radiol.* **2021**, *44*, 952–958. [[CrossRef](#)]
31. Trujillo-Romero, C.; Leija-Salas, L.; Vera-Hernández, A.; Rico-Martínez, G.; Gutiérrez-Martínez, J. Double Slot Antenna for Microwave Thermal Ablation to Treat Bone Tumors: Modeling and Experimental Evaluation. *Electronics* **2021**, *10*, 761. [[CrossRef](#)]
32. Alonzo, M.; Bos, A.; Bennett, S.; Ferral, H. The Emprint™ Ablation System with Thermosphere™ Technology: One of the Newer Next-Generation Microwave Ablation Technologies. *Semin. Interv. Radiol.* **2015**, *32*, 335–338.
33. Kuroda, H.; Nagasawa, T.; Fujiwara, Y.; Sato, H.; Abe, T.; Kooka, Y.; Endo, K.; Oikawa, T.; Sawara, K.; Takikawa, Y. Comparing the Safety and Efficacy of Microwave Ablation Using Thermosphere™ Technology versus Radiofrequency Ablation for Hepatocellular Carcinoma: A Propensity Score-Matched Analysis. *Cancers* **2021**, *13*, 1295. [[CrossRef](#)]
34. Acikgoz, H.; Turer, I. A Novel Microwave Coaxial Slot Antenna for Liver Tumor Ablation. *Adv. Electromagn.* **2014**, *3*, 20–25. [[CrossRef](#)]
35. Towoju, O.; Ishola, F.; Sanni, T.; Olatunji, O. Investigation of Influence of Coaxial Antenna Slot Positioning on Thermal Efficiency in Microwave Ablation using COMSOL. *J. Phys. Conf. Ser.* **2019**, *1378*, 32066. [[CrossRef](#)]
36. Liu, D.; Brace, C. Numerical simulation of microwave ablation incorporating tissue contraction based on thermal dose. *Phys. Med. Boil.* **2017**, *62*, 2070–2086. [[CrossRef](#)] [[PubMed](#)]
37. Rattanadecho, P.; Keangin, P. Numerical study of heat transfer and blood flow in two-layered porous liver tissue during microwave ablation process using single and double slot antenna. *Int. J. Heat Mass Transf.* **2013**, *58*, 457–470. [[CrossRef](#)]
38. Maini, S.; Marwaha, A. Modeling and simulation of novel antenna for the treatment of hepatocellular carcinoma using finite element method. *Electromagn. Biol. Med.* **2013**, *32*, 373–381. [[CrossRef](#)]
39. Reinhardt, M.; Brandmaier, P.; Seider, D.; Kolesnik, M.; Jenniskens, S.; Sequeiros, R.B.; Eibisberger, M.; Voglreiter, P.; Flanagan, R.; Mariappan, P.; et al. A prospective development study of software-guided radio-frequency ablation of primary and secondary liver tumors: Clinical intervention modelling, planning and proof for ablation cancer treatment (ClinicIMPACT). *Contemp. Clin. Trials Commun.* **2017**, *8*, 25–32. [[CrossRef](#)]
40. Cavagnaro, M.; Pinto, R.; Lopresto, V. Numerical models to evaluate the temperature increase induced by ex vivo microwave thermal ablation. *Phys. Med. Biol.* **2015**, *60*, 3287–3311. [[CrossRef](#)]
41. Selmi, M.; Bajahzar, A.; Belmabrouk, H. Effects of target temperature on thermal damage during temperature-controlled MWA of liver tumor. *Case Stud. Therm. Eng.* **2022**, *31*, 101821. [[CrossRef](#)]
42. Simanovskii, D.M.; Mackanos, M.A.; Irani, A.R.; O'Connell-Rodwell, C.E.; Contag, C.H.; Schwettman, H.A.; Palanker, D.V. Cellular tolerance to pulsed hyperthermia. *Phys. Rev. E* **2006**, *74*, 011915. [[CrossRef](#)] [[PubMed](#)]
43. Liljemalm, R.; Nyberg, T. Quantification of a thermal damage threshold for astrocytes using infrared laser generated heat gradients. *Ann. Biomed. Eng.* **2014**, *42*, 822–832. [[CrossRef](#)] [[PubMed](#)]
44. Chiang, J.; Wang, P.; Brace, C.L. Computational modelling of microwave tumour ablations. *Int. J. Hyperth.* **2013**, *29*, 308–317. [[CrossRef](#)] [[PubMed](#)]

45. Keangin, P.; Rattanadecho, P. A numerical investigation of microwave ablation on porous liver tissue. *Adv. Mech. Eng.* **2018**, *10*, 1–13. [[CrossRef](#)]
46. Radmilović-Radjenović, M.; Radjenović, D. Finite element analysis of the effect of microwave ablation on the liver, lung, kidney, and bone malignant tissues. *Eur. Lett.* **2021**, *136*, 28001. [[CrossRef](#)]
47. Chen, C.; Yu, M.-A.; Qiu, L.; Chen, H.-Y.; Zhao, Z.-L.; Wu, J.; Peng, L.-L.; Wang, Z.-L.; Xiao, R.-X. Theoretical Evaluation of Microwave Ablation Applied on Muscle, Fat and Bone: A Numerical Study. *Appl. Sci.* **2021**, *11*, 8271. [[CrossRef](#)]
48. Radmilović-Radjenović, M.; Sabo, M.; Prnova, M.; Šoltes, L.; Radjenović, B. Finite Element Analysis of the Microwave Ablation Method for Enhanced Lung Cancer Treatment. *Cancers* **2021**, *13*, 3500. [[CrossRef](#)]
49. An, C.; Li, X.; Zhang, M.; Yang, J.; Cheng, Z.; Yu, X.; Han, Z.; Liu, F.; Dong, L.; Yu, J.; et al. 3D visualization ablation planning system assisted microwave ablation for hepatocellular carcinoma (Diameter >3): A precise clinical application. *BMC Cancer* **2020**, *20*, 44. [[CrossRef](#)]
50. Radjenović, B.; Sabo, M.; Šoltes, L.; Prnova, M.; Čičak, P.; Radmilović-Radjenović, M. On Efficacy of Microwave Ablation in the Thermal Treatment of an Early-Stage Hepatocellular Carcinoma. *Cancers* **2021**, *13*, 5784. [[CrossRef](#)]
51. Loya, R.R.; Jutte, P.C.; Kwee, T.C.; van Ooijen, P.M.A. Computer 3D modeling of radiofrequency ablation of atypical cartilaginous tumours in long bones using finite element methods and real patient anatomy. *Eur. Radiol. Exp.* **2022**, *6*, 21. [[CrossRef](#)]
52. Gorman, J.; Tan, W.; Abraham, J. Numerical Simulation of Microwave Ablation in the Human Liver. *Processes* **2022**, *10*, 361. [[CrossRef](#)]
53. Radmilović-Radjenović, M.; Bošković, N.; Sabo, M.; Radjenović, B. An Analysis of Microwave Ablation Parameters for Treatment of Liver Tumors from the 3D-IRCADb-01 Database. *Biomedicines* **2022**, *10*, 1569. [[CrossRef](#)] [[PubMed](#)]
54. Trujillo, M.; Berjano, E. Review of the mathematical functions used to model the temperature dependence of electrical and thermal conductivities of biological tissue in radiofrequency ablation. *Int. J. Hyperth.* **2013**, *29*, 590–597. [[CrossRef](#)] [[PubMed](#)]
55. Pearce, J.A. Comparative analysis of mathematical models of cell death and thermal damage processes. *Int. J. Hyperth.* **2013**, *29*, 262–280. [[CrossRef](#)]
56. Andreozzi, A.; Brunese, L.; Iasiello, M.; Tucci, C.; Vanoli, G.P. Modeling Heat Transfer in Tumors: A Review of Thermal Therapies. *Ann. Biomed. Eng.* **2018**, *47*, 676–693. [[CrossRef](#)]
57. Tucci, C.; Trujillo, M.; Berjano, E.; Iasiello, M.; Andreozzi, A.; Vanoli, G.P. Mathematical modeling of microwave liver ablation with a variable-porosity medium approach. *Comput. Methods Programs Biomed.* **2021**, *214*, 106569. [[CrossRef](#)]
58. Kenyon, D.E. Transient Filtration in a Porous Elastic Cylinder. *J. Appl. Mech.* **1976**, *43*, 594–598. [[CrossRef](#)]
59. Mow, V.C.; Lai, W.M. Recent Developments in Synovial Joint Biomechanics. *SIAM Rev.* **1980**, *22*, 275–317. [[CrossRef](#)]
60. Mow, V.C.; Kuei, S.C.; Lai, W.M.; Armstrong, C.G. Biphasic Creep and Stress Relaxation of Articular Cartilage in Compression: Theory and Experiments. *J. Biomech. Eng.* **1980**, *102*, 73–84. [[CrossRef](#)]
61. Lai, W.M.; Mow, V.C.; Roth, V. Effects of Nonlinear Strain-Dependent Permeability and Rate of Compression on the Stress Behavior of Articular Cartilage. *J. Biomech. Eng.* **1981**, *103*, 61–66. [[CrossRef](#)] [[PubMed](#)]
62. Armstrong, C.G.; Lai, W.M.; Mow, V.C. An Analysis of the Unconfined Compression of Articular Cartilage. *J. Biomech. Eng.* **1984**, *106*, 165–173. [[CrossRef](#)] [[PubMed](#)]
63. Mak, A.F.; Lai, W.M.; Mow, V.C. Biphasic indentation of articular cartilage-I. *Theor. Anal. J. Biomech.* **1987**, *20*, 703–714. [[CrossRef](#)]
64. Cowin, S.C. The Specific Growth Rates of Tissues: A Review and a Re-Evaluation. *J. Biomech. Eng.* **2011**, *133*, 041001. [[CrossRef](#)]
65. Khaled, A.-R.A.; Vafai, K. The role of porous media in modeling flow and heat transfer in biological tissues. *Int. J. Heat Mass Transf.* **2003**, *46*, 4989–5003. [[CrossRef](#)]
66. Kosari, E.; Vafai, K. Synthesis of Flow and Thermal Transport in Porous Media as Applied to Biological Applications. *J. Heat Transf.* **2021**, *143*, 062701. [[CrossRef](#)]
67. Allan, F.; Hamdan, M. Fluid mechanics of the interface region between two porous layers. *Appl. Math. Comput.* **2002**, *128*, 37–43. [[CrossRef](#)]
68. Mahjoob, S.; Vafai, K. Analysis of Bioheat Transport Through a Dual Layer Biological Media. *J. Heat Transf.* **2009**, *132*, 031101. [[CrossRef](#)]
69. Yang, K.; Huang, W.; Li, X.; Wang, J. Analytical Analysis of Heat Transfer and Entropy Generation in a Tube Filled with Double-Layer Porous Media. *Entropy* **2020**, *22*, 1214. [[CrossRef](#)]
70. Li, L.; Liang, M.; Yu, B.; Yang, S. Analysis of thermal conductivity in living biological tissue with vascular network and convection. *Int. J. Therm. Sci.* **2014**, *86*, 219–226. [[CrossRef](#)]
71. Li, X.; Qin, Q.-H.; Tian, X. Thermomechanical response of porous biological tissue based on local thermal non-equilibrium. *J. Therm. Stress.* **2019**, *42*, 1481–1498. [[CrossRef](#)]
72. Ragab, M.; Abouelregal, A.E.; AlShaibi, H.F.; Mansouri, R.A. Heat Transfer in Biological Spherical Tissues during Hyperthermia of Magnetoma. *Biology* **2021**, *10*, 1259. [[CrossRef](#)] [[PubMed](#)]
73. Liu, L.; Zheng, L.; Liu, F. Research on macroscopic and microscopic heat transfer mechanisms based on non-Fourier constitutive model. *Int. J. Heat Mass Transf.* **2018**, *127*, 165–172. [[CrossRef](#)]
74. Wang, L.Q.; Xu, M.T.; Wei, X.H. Multiscale Theorems. *Adv. Chem. Eng.* **2008**, *34*, 175–468.
75. Miller, C.T.; Gray, W.G.; Schrefler, B.A. A continuum mechanical framework for modeling tumor growth and treatment in two- and three-phase systems. *Ingenieur-Archiv* **2021**, *92*, 461–489. [[CrossRef](#)] [[PubMed](#)]

76. Rahman, M.M.; Feng, Y.; Yankeelov, T.E.; Oden, J.T. A fully coupled space–time multiscale modeling framework for predicting tumor growth. *Comput. Methods Appl. Mech. Eng.* **2017**, *320*, 261–286. [\[CrossRef\]](#)
77. Goyal, H.; Vlachos, D.G. Multiscale modeling of microwave-heated multiphase systems. *Chem. Eng. J.* **2020**, *397*, 125262. [\[CrossRef\]](#)
78. Wang, L.; Fan, J. Modeling Bioheat Transport at Macroscale. *J. Heat Transf.* **2010**, *133*, 011010. [\[CrossRef\]](#)
79. Eringen, A.; Ingram, J.D. A Continuum theory of chemically reacting media—I. *Int. J. Eng. Sci.* **1965**, *3*, 197–212. [\[CrossRef\]](#)
80. Pennes, H.H. Analysis of tissue and arterial blood temperatures in the resting human forearm. *J. Appl. Physiol.* **1948**, *1*, 93–122. [\[CrossRef\]](#)
81. Zhou, J.; Chen, J.; Zhang, Y. Dual-phase lag effects on thermal damage to biological tissues caused by laser irradiation. *Comput. Biol. Med.* **2009**, *39*, 286–293. [\[CrossRef\]](#)
82. Zhou, J.; Zhang, Y.W.; Chen, J.K. An Axisymmetric Dual-PhaseLag Bioheat Model for Laser Heating of Living Tissues. *Int. J. Therm. Sci.* **2009**, *48*, 1477–1485. [\[CrossRef\]](#)
83. Tucci, C.; Trujillo, M.; Berjano, E.; Iasiello, M.; Andreozzi, A.; Vanoli, G.P. Pennes’ bioheat equation vs. porous media approach in computer modeling of radiofrequency tumor ablation. *Sci. Rep.* **2021**, *11*, 5272. [\[CrossRef\]](#) [\[PubMed\]](#)
84. Habibishandiz, M.; Saghir, M. A critical review of heat transfer enhancement methods in the presence of porous media, nanofluids, and microorganisms. *Therm. Sci. Eng. Prog.* **2022**, *30*, 101267. [\[CrossRef\]](#)
85. Nakayama, A.; Kuwahara, F. A general bioheat transfer model based on the theory of porous media. *Int. J. Heat Mass Transf.* **2008**, *51*, 3190–3199. [\[CrossRef\]](#)
86. Prakash, P. Microwave ablation: Physical principles and technology. In *Principles and Technologies for Electromagnetic Energy Based Therapies*, 1st ed.; Editor Prakash, P., Srimathveeravalli, G., Eds.; Elsevier: Amsterdam, The Netherlands, 2022; pp. 139–167.
87. Singh, S.; Kumar, S. A Study on the Effect of Metabolic Heat Generation on Biological Tissue Freezing. *Sci. World J.* **2013**, *2013*, 398386. [\[CrossRef\]](#)
88. Kalsi, K.K.; Chiesa, S.T.; Trangmar, S.J.; Ali, L.; Lotlikar, M.D.; González-Alonso, J. Mechanisms for the control of local tissue blood flow during thermal interventions: Influence of temperature-dependent ATP release from human blood and endothelial cells. *Exp. Physiol.* **2017**, *102*, 228–244. [\[CrossRef\]](#)
89. Ingram, J.D.; Eringen, A.C. A continuum theory of chemically reacting media—II Constitutive equations of reacting fluid mixtures. *Int. J. Eng. Sci.* **1967**, *5*, 289–322. [\[CrossRef\]](#)
90. Bedford, A.; Drumheller, D.S. Theories of immiscible and structured mixtures. *Int. J. Eng. Sci.* **1983**, *21*, 863–960. [\[CrossRef\]](#)
91. Lakhsassi, A.; Kengne, E.; Semmaoui, H. Modified pennes’ equation modelling bio-heat transfer in living tissues: Analytical and numerical analysis. *Nat. Sci.* **2010**, *2*, 1375–1385. [\[CrossRef\]](#)
92. Hristov, J. Bio-Heat Models Revisited: Concepts, Derivations, Nondimensionalization and Fractionalization Approaches. *Front. Phys.* **2019**, *7*, 189. [\[CrossRef\]](#)
93. Roetzel, W.; Xuan, Y. Bioheat equation of the human thermal system. *Chem. Eng. Technol.* **1997**, *20*, 268–276.
94. Prakash, P.; Converse, M.C.; Webster, J.G.; Mahvi, D.M. An optimal sliding choke antenna for hepatic microwave ablation. *IEEE Trans. Bio-Med. Eng.* **2009**, *56*, 2470–2476.
95. Cavagnaro, M.; Amabile, C.; Bernardi, P.; Pisa, S.; Tosoratti, N. A Minimally Invasive Antenna for Microwave Ablation Therapies: Design, Performances, and Experimental Assessment. *IEEE Trans. Biomed. Eng.* **2010**, *58*, 949–959. [\[CrossRef\]](#)
96. Yang, D.S.; Bertram, J.M.; Converse, M.C.; O’Rourke, A.P.; Webster, J.G.; Hagness, S.C.; Will, J.A.; Mahvi, D.M. A floating sleeve antenna yields localized hepatic microwave ablation. *IEEE Trans. Bio-Med. Eng.* **2006**, *53*, 533–537. [\[CrossRef\]](#) [\[PubMed\]](#)
97. Maini, S. FEM simulation of tapered cap floating sleeve antenna for hepatocellular carcinoma therapy. *Electromagn. Biol. Med.* **2015**, *35*, 152–160. [\[CrossRef\]](#)
98. Sun, Y.Y.; Cheng, Z.G.; Dong, L.; Zhang, G.M.; Wang, Y.; Liang, P. Comparison of temperature curve and ablation zone between 915-and 2450 MHz cooled-shaft microwave antenna: Results in ex vivo porcine livers. *Eur. J. Radiol.* **2015**, *81*, 553–557. [\[CrossRef\]](#)
99. Wang, T.; Zhao, G.; Qiu, B.S. Theoretical evaluation of the treatment effectiveness of a novel coaxial multi-slot antenna for conformal microwave ablation of tumors. *Int. J. Heat Mass Transf.* **2015**, *90*, 81–91. [\[CrossRef\]](#)
100. Luyen, H.; Hagness, S.C.; Behdad, N. Reduced-diameter designs of coax-fed microwave ablation antennas equipped with baluns. *IEEE Antennas Wirel. Propag.* **2017**, *16*, 1385–1388.
101. Ge, M.; Jiang, H.; Huang, X.; Zhou, Y.; Zhi, D.; Zhao, G.; Chen, Y.; Wang, L.; Qiu, B. A multi-slot coaxial microwave antenna for liver tumor ablation. *Phys. Med. Biol.* **2018**, *63*, 175011. [\[CrossRef\]](#)
102. Tehrani, M.H.H.; Soltani, M.; Kashkooli, F.M.; Raahemifar, K. Use of microwave ablation for thermal treatment of solid tumors with different shapes and sizes—A computational approach. *PLoS ONE* **2020**, *15*, e0233219. [\[CrossRef\]](#) [\[PubMed\]](#)
103. Lopresto, V.; Pinto, R.; Lovisolo, G.A.; Cavagnaro, M. Changes in the dielectric properties of ex vivo bovine liver during microwave thermal ablation at 2.45 GHz. *Phys. Med. Biol.* **2012**, *57*, 2309–2327. [\[CrossRef\]](#) [\[PubMed\]](#)
104. Prakash, P. Theoretical Modeling for Hepatic Microwave Ablation. *Open Biomed. Eng. J.* **2010**, *4*, 27–38. [\[CrossRef\]](#)
105. O’Rourke, A.P.; Lazebnik, M.; Bertram, J.M.; Converse, M.C.; Hagness, S.C.; Webster, J.G.; Mahvi, D.M. Dielectric properties of human normal, malignant and cirrhotic liver tissue: In vivo and ex vivo measurements from 0.5 to 20 GHz using a precision open-ended coaxial probe. *Phys. Med. Biol.* **2007**, *52*, 4707–4719. [\[CrossRef\]](#) [\[PubMed\]](#)
106. Rossmanna, C.; Haemmerich, D. Review of Temperature Dependence of Thermal Properties, Dielectric Properties, and Perfusion of Biological Tissues at Hyperthermic and Ablation Temperatures. *Crit. Rev. Biomed. Eng.* **2014**, *42*, 467–492. [\[CrossRef\]](#) [\[PubMed\]](#)

107. Berjano, E.J. Theoretical modeling for radiofrequency ablation: State-of-the-art and challenges for the future. *Biomed. Eng. Online* **2006**, *5*, 24. [[CrossRef](#)] [[PubMed](#)]
108. Balogh, J.; Victor, D.; Asham, E.H.; Burroughs, S.G.; Boktour, M.; Saharia, A.; Li, X.; Ghobrial, R.M.; Monsour, H.P., Jr. Hepatocellular carcinoma: A review. *J. Hepatocell. Carcinoma* **2016**, *3*, 41–53. [[CrossRef](#)]
109. Villanueva, A. Hepatocellular Carcinoma. *N. Engl. J. Med.* **2019**, *380*, 1450–1462. [[CrossRef](#)]
110. Llovet, J.M.; Kelley, R.K.; Villanueva, A.; Singal, A.G.; Pikarsky, E.; Roayaie, S.; Lencioni, R.; Koike, K.; Zucman-Rossi, J.; Finn, R.S. Hepatocellular carcinoma. *Nat. Rev. Dis. Primers* **2021**, *7*, 6. [[CrossRef](#)]
111. Wang, S.; Yang, D.; Kong, W. Prediction of Overall Survival Rate in Patients With Hepatocellular Carcinoma Using an Integrated Model Based on Autophagy Gene Marker. *Front. Genet.* **2021**, *12*, 1–10. [[CrossRef](#)]
112. Chen, Z.H.; Hong, Y.F.; Chen, X.; Chen, J.; Lin, Q.; Lin, J.; Li, X.; Wen, J.Y.; Ruan, D.Y.; Dong, M.; et al. Comparison of five staging systems in predicting the survival rate of patients with hepatocellular carcinoma undergoing trans-arterial chemoembolization therapy. *Oncology Letters* **2018**, *15*, 855–862. [[CrossRef](#)] [[PubMed](#)]
113. Hui, T.; Kwan, J.; Pua, U. Advanced Techniques in the Percutaneous Ablation of Liver Tumours. *Diagnostics* **2021**, *11*, 585. [[CrossRef](#)] [[PubMed](#)]
114. Comsol Multiphysics. 1986–2020. Burlington (MA): COMSOL, Inc. Available online: <https://www.comsol.com/comsol-multiphysics> (accessed on 7 March 2022).
115. D-IRCADb. Strasbourg (F): IrcadFrance. Available online: <https://www.ircad.fr/research/data-sets/liver-segmentation-3d-ircadb-01> (accessed on 7 March 2022).

Research Article

Nikola Bošković, Branislav Radjenović, Srdjan Nikolić, and Marija Radmilović-Radjenović*

Effectiveness of microwave ablation using two simultaneous antennas for liver malignancy treatment

<https://doi.org/10.1515/phys-2024-0079>

received April 17, 2024; accepted August 01, 2024

Abstract: Microwave ablation is becoming an increasingly important minimally invasive procedure that uses dielectric hysteresis to generate heat and destroy cancer cells. Tissue damage depends on the input power, procedure duration, and antenna position. Therefore, one of the essential problems is determining parameters that ensure the destruction of the tumor with the desired margins and minimal damage to the healthy tissue. In addition to experimental methods, computer modeling has been proven to be an effective approach for improving the performance of microwave ablation (MWA). Moreover, since the thermal spread in biological tissue is difficult to measure, the development of a predictive model from procedural planning to execution may have a great impact on patient care. This study focuses on determining the optimal parameters for MWA treatment of liver tumors using two identical parallel-positioned multi-slot coaxial antennas. The simulation results suggest that an input power of 20 W or 15 W per antenna suffices for complete tumor ablation with a sufficient safety margin for 600 and 900 s, respectively. In both cases, the created ablation zones were similar. The ablation zones for 15 W per antenna were more spherical, invading a smaller amount of healthy tissue than those for 20 W per antenna. This study may represent a step forward in planning MWA treatment for individual patients.

Keywords: microwave radiation, microwave ablation, necrotic tissue

1 Introduction

Liver cancer is one of the most common causes of cancer-related deaths worldwide, accounting for over 700,000 deaths annually [1–4]. Among the various therapeutic options used to treat liver cancer [5–8], microwave ablation (MWA) is a minimally invasive modality based on the destruction of cancer cells by microwave radiation-induced hyperthermia [9–12]. MWA can operate at different frequencies, but the most common frequency is 2.45 GHz, which allows the use of compact antennas and good radiation penetration into tissues [13]. In terms of efficiency and safety, high-temperature, short-duration MWA is the standard of care [14]. Assessing the distribution of heating damage is the most challenging task in MWA because it highly depends on the time, tissue type, and blood vessel distribution [15–17].

The antenna design responsible for the formation of ablation zones strongly affects the MWA efficiency. Over the years, various antenna designs have been developed to minimize thermal damage to healthy tissue [18–20]. A specially designed AngioDynamic Solero MWA system can rapidly ablate soft tissue, improving procedural outcomes [21]. MWA systems based on “thermosphere technology” create spherical ablation zones by adding small saline irrigation channels to the antennas [22]. However, the cooling system significantly increased the complexity and size of the probe. Novel compact multi-slot coaxial antennas are specially designed to work inside tissues without requiring a cooling system [23].

There are differences between ablation performed using a single probe and ablation performed using multiple probes simultaneously. In spite of some disadvantages, such as complication rates, multiple antenna configurations have been proposed for efficient ablation of large tumors [24,25]. This can be achieved by placing the same probe sequentially at multiple points or using multiple probes placed at multiple points simultaneously. Ablation performed using multiple probes is larger, more symmetrical and requires less treatment time [26,27]. In a multi-antenna configuration, the

* **Corresponding author: Marija Radmilović-Radjenović**, Institute of Physics, University of Belgrade, Pregrevica 118, 11080 Belgrade, Serbia, e-mail: marija@ipb.ac.rs

Nikola Bošković, Branislav Radjenović: Institute of Physics, University of Belgrade, Pregrevica 118, 11080 Belgrade, Serbia

Srdjan Nikolić: Department of Surgery, Institute of Oncology and Radiology of Serbia, Pasterova 14, Belgrade, Serbia; Faculty of Medicine, University of Belgrade, Dr Subotica 8, 11000 Belgrade, Serbia

antennas usually have a parallel orientation; however, it is possible to change the ablation shape to a non-parallel orientation. The two-antenna configuration is the simplest, cheapest, and easiest to implement, producing more uniform thermal profiles and causing less damage to healthy tissues [28–30].

In addition to clinical studies, computational models have played a significant role in predicting MWA outcomes, especially three-dimensional (3D) models of an antenna and targeted tissue without assumptions of homogeneity [31–33]. This study aimed to provide optimal parameters for treating a real large tumor (from a database [34]) using two identical 10-slot coaxial antennas [17,23,35]. The simulations presented in this article were realized using an in-house developed SimSurgery simulation environment based on several open-source libraries widely used in scientific computing [35]. The obtained simulation results revealed that MWA treatment of large tumors using a two-antenna configuration causes less damage to the healthy tissue compared with using a single antenna. Furthermore, the two-antenna configurations produce more uniform thermal profiles and peripheral tissue temperatures.

2 Methodology

2.1 Physics of the MWA procedure

The equations governing the calculation of the electric-field distribution through the tissue and heat generated by the electromagnetic field during the MWA procedure have already been described in previous publications [11,33,35], so only the main equations are listed here. The first part is the wave equation for the electric field in the frequency domain:

$$\nabla^2 \vec{E} - \mu_r k_0^2 \left(\epsilon_r - \frac{j\sigma}{\omega \epsilon_0} \right) \vec{E} = 0, \quad (1)$$

where μ_r is the relative permeability (its value is 1 for a non-magnetic environment), $\omega = 2\pi f$ is the angular frequency, \vec{E} is the electric field vector generated by the antenna, σ is the electric conductivity, ϵ_0 is the permittivity of the vacuum, and k_0 is the vacuum propagation constant.

The change in temperature over time can be calculated using Pennes' bio-heat equation [33,36,37]:

$$\rho c \frac{\partial T}{\partial t} = \nabla \cdot (k \nabla T) + \rho_b \omega_b c_b (T_b - T) + Q_{\text{ext}} + Q_{\text{met}}, \quad (2)$$

where t is the time, ρ , c , and T are the density, specific heat capacity, and temperature of tissue, respectively. ρ_b , c_b ,

and ω_b are the density, specific heat capacity, and perfusion rate of blood, respectively. $T_b = 37^\circ\text{C}$ denotes the arterial blood temperature, Q_{met} is the metabolic heat, and Q_{ext} represents the external heat source generated from MWA, and $Q_{\text{ext}} \gg Q_{\text{met}}$, Q_{met} can be neglected. The bio-heat equation must be solved in the time domain.

Soft tissues, such as the liver, have a very high water concentration. At steady state, the water content of liver tissue is ~78% water by mass, whereas at temperatures $>100^\circ\text{C}$, the tissue water content may decrease to 20% by mass due to evaporation. An increase in temperature leads to a significant change in water content, affecting tissue parameters [15]. The temperature dependence of the water content can be mathematically expressed as follows [33,35,38]:

$$W(T) = \begin{cases} 0.778 \cdot \left(1 - e^{\frac{T-106}{3.42}} \right), & 70^\circ\text{C} \leq T \leq 100^\circ\text{C} \\ 7.053 - 0.064096 \cdot T, & 100^\circ\text{C} \leq T \leq 104^\circ\text{C} \\ 0.778 \cdot e^{-\frac{T-80}{34.37}}, & T > 104^\circ\text{C}. \end{cases} \quad (3)$$

This function can be implemented into the specific heat capacity c in Eq. (2) as effective specific heat capacity $c' = c - \frac{\partial W}{\partial T}$ [36]. The material parameters of the tissues used in this study are summarized in Table 1.

The dielectric constant of the tissue ϵ_r and electrical conductivity σ are considered temperature-dependent functions [17,33,35]:

$$\epsilon_r = a_1 \cdot \left(1 - \frac{1}{1 + e^{(a_2 - a_3 T)}} \right), \quad (4)$$

$$\sigma = b_1 \cdot \left(1 - \frac{1}{1 + e^{(b_2 - b_3 T)}} \right), \quad (5)$$

with coefficients listed in Table 2.

The blood perfusion ω_b also depends on the temperature T [17]:

$$\omega_b = 2.1 \times 10^{-5} T + 3.5 \times 10^{-3}. \quad (6)$$

The difference in temperature between blood and tissue results in convective heat transfer.

Table 1: Thermophysiological parameters corresponding to tumor tissues, healthy tissues, and blood used in this study

Parameter	Tissue		
	Liver	Tumor	Blood
Density (kg/m ³)	1,079	1,040	1,060
Specific heat (J/kg/°C)	3,540	3,960	3,600
Thermal conductivity (W/m/°C)	0.52	0.57	0.5

Table 2: Values of the coefficients used in the calculation of ε_r and σ for the liver tissue and tumors

Coefficients	Tissue	
	Liver	Tumor
a_1	44.3	54.8
a_2	5.223	5.223
a_3	0.0524	0.0524
b_1	1.69	2
b_2	6.583	6.583
b_3	0.0598	0.0598

The specific absorption rate (SAR) is a measure of the radiation absorbed by the tissue [33,35]:

$$\text{SAR} = \frac{\sigma}{2\rho} |\vec{E}|^2, \quad (7)$$

where \vec{E} is the electric field vector, σ is the electric conductivity, and ρ is the density of the observed domain. It can identify the tissue that is most affected by radiation and how the electric field propagation interacts with the tissue. The total power loss in the targeted tissue can be estimated from the SAR as follows [39]:

$$P_{\text{LOSS}} = \int_V \rho \text{SAR} \, dV = \frac{1}{2} \int_V \sigma |\vec{E}|^2 \, dV. \quad (8)$$

The relative to the input power ratio (in %) is $(P_{\text{LOSS}}/P_{\text{IN}}) \cdot 100\%$.

Estimation of the temperature damage Ω as a function of time can be performed using the Arrhenius equation [33,40]:

$$\frac{\partial \Omega}{\partial t} = A e^{\left(-\frac{\Delta E}{RT}\right)}, \quad (9)$$

where $A = 7.39 \times 10^{39} \, 1/s$ and $\Delta E = 2.577 \times 10^5 \, \text{J/mol}$ represent the frequency factor and activation energy for the irreversible damage reaction, respectively, T is the temperature, and R is the universal gas constant. The most common parameter for the expression of tissue necrosis caused by MWA is the fraction of necrotic tissue [33,35]:

$$\theta_d = 1 - e^{-\Omega}, \quad (10)$$

ranging from 0 (no damage) to 1 (total tissue necrosis). Numerical values of $\theta_d > 0.99$ are acceptable as the total tissue necrosis.

The extent of damage to healthy tissue during MWA should be minimal relative to tumor size. Volumetric damage (VD) is defined as the ratio of the volume of damaged healthy tissue (V_{DAMAGED}) to that of tumor tissue [41]:

$$\text{VD} = \frac{V_{\text{DAMAGED}}}{V_{\text{TUMOR}}} \cdot 100\%. \quad (11)$$

The amount of damaged healthy tissue (DT) was calculated as the ratio of the volume of the damaged healthy tissue to the total volume of the liver (V_{LIVER}) without tumor tissue (V_{TUMOR}) [42,43]. The mean volume of the human liver is approximately $1,750 \, \text{cm}^3$ [44]. $V_{\text{TUMOR}} = 13 \, \text{cm}^3$.

$$\text{DT} = \frac{V_{\text{DAMAGED}}}{V_{\text{LIVER}} - V_{\text{TUMOR}}} \cdot 100\%. \quad (12)$$

The total delivered energy (TDE) is associated with the input power and duration of the MWA: $\text{TDE} = \text{Time} \cdot P_{\text{in}}$ [45]. A higher TDE can result in higher temperatures and ablation zones.

2.2 Geometric model

As the first step in modeling, it is necessary to determine the optimal number and position of antennas, depending on the tumor shape. The use of a single antenna in MWA is recommended for the treatment of tumors up to 3 cm in diameter, whereas multiple antenna designs are more useful for larger tumors. Figure 1 illustrates two identical parallel antennas that create spherical ablation zones approximately 3 cm in diameter with a mutual spacing of 3 cm, leading to complete tumor ablation. Although the part of the tumor between the red circles is outside the ablation zones, with

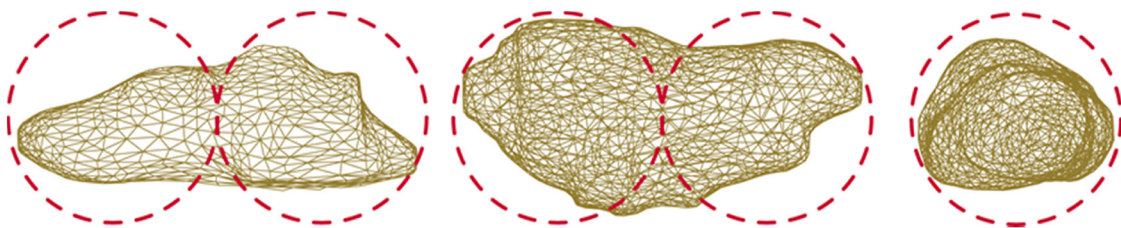


Figure 1: Stereolithography (STL) representation of the liver tumor (taken from a database [34]) from different perspectives. The dimensions of the tumor were $56.8 \, \text{mm} \times 27.6 \, \text{mm} \times 22.4 \, \text{mm}$, with a total volume of approximately $13 \, \text{cm}^3$. Red circles denote 30 mm in diameter.

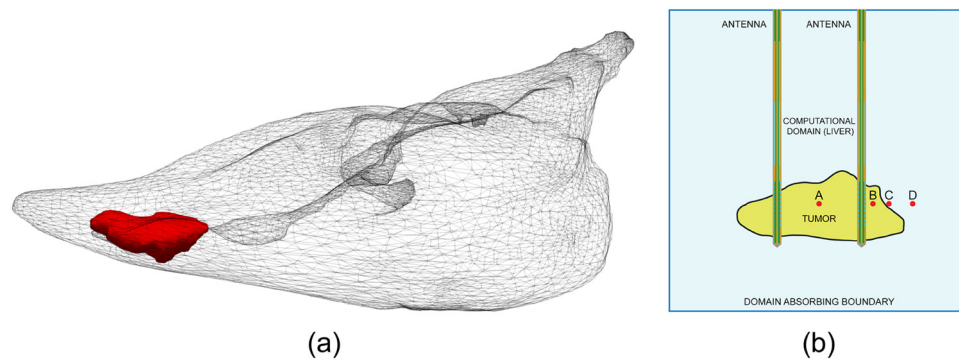


Figure 2: A schematic view of (a) 3D model of the liver (gray surface) and tumor (red surface) [34] and (b) planar cross-section of the 3D geometry of the problem with two multi-slot antennas with control points.

the simultaneous use of multiple antennas, closely spaced ablation zones tend to merge, making the overall combined ablation larger than a simple combination of the two ablation zones.

Figure 2a shows a 3D simulation model of the tumor (56.8 mm × 27.6 mm × 22.4 mm) (red surface), which was acquired from a 54-year-old male [34], and its position in the liver (gray surface). The 3D-IRCADb-01 database [34] contains enhanced 3D CT images of 10 women and 10

men with hepatic tumors in 75% of cases. The 3D medical images and masks of the segmented structures of interest are available as DICOM files, and the representation of segmented zones is provided as surface meshes in the VTK format, which can be converted to the STL format. The STL surface representation of the tumor was then used to co-create the solid geometry volume in STEP format, which could be directly used in our 3D finite-element method (FEM) simulation. In this study, a configuration of

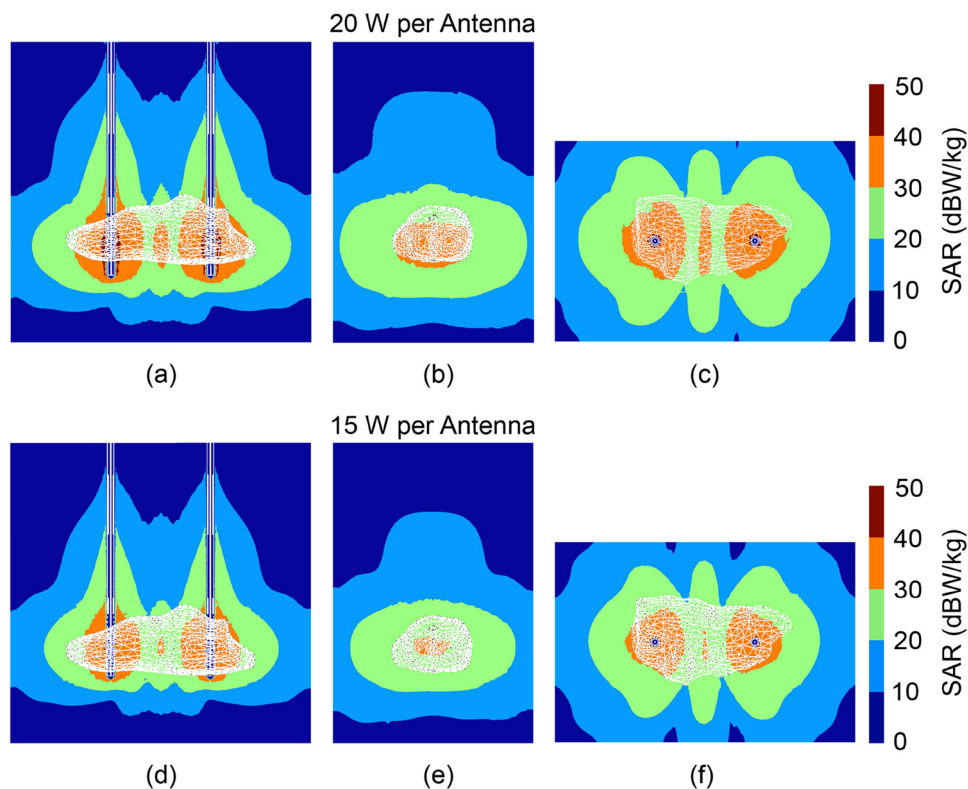


Figure 3: SAR calculation for two 10-slot antennas with 30-mm separation and power of 20 W per antenna (a) x - z cut plane, (b) y - z cut plane, (c) x - y cut plane, and 15 W per antenna (d) x - z cut plane, (e) y - z cut plane, and (f) x - y cut plane. White curves represent the tumors.

two coaxial antennas with 10 slots was used. As mentioned in previous publications, a 10-slot antenna offers higher heating efficiency for tissues and more near-spherical ablation zones than a 1-slot antenna [11,23].

The liver is typically much larger than the tumor and antenna setup. Modeling and simulation of the entire liver create an extremely large computational model. Using a portion of the liver as a computational domain in a given setup can create a suitable model that is much faster to compute [33,35]. This domain is composed of material parameters corresponding to the liver, and it is limited by the absorbing boundary, which prevents wave reflection, thus imitating a much larger volume (Figure 2b). The number, quality, and size of the finite elements are the second factors after domain size, and they have a large influence on the overall simulation. To capture the behavior of electromagnetic waves, the general rule is that the size of the element should be within a $1/10$ of a guided wavelength at 2.45 GHz, which is approximately 2 mm for liver tissue. Some parameters were calculated at control points A, B, C,

and D. Point A was in the center of the tumor 15 mm from each antenna, whereas point D was located 15 mm from the first antenna. Therefore, these points can be used to determine the radiation contribution of a single antenna relative to the combined contribution of two antennas. Point B was located 10 mm from the first antenna, and point C was located 13.2 mm from the first antenna, away from the tumor.

Our study focused on the creation and analysis of a complete MWA model using an in-house developed SimSurgery simulation framework. The graphic user interface and 3D visualizations of the framework are based on the Qt [46] and VTK [47] libraries, which are currently the standard for scientific calculations. The geometry module, which can create and manipulate complex model geometries, is based on the OpenCASCADE computer-aided design engine [48]. Meshing operations are performed using the Gmsh package [49]. The details of our strategy of using Gmsh to generate meshes for MWA analysis can be found in Bošković *et al.* [35]. In this study, we used mixed meshing for the geometry segmentation. The tumor has an irregular geometry and is

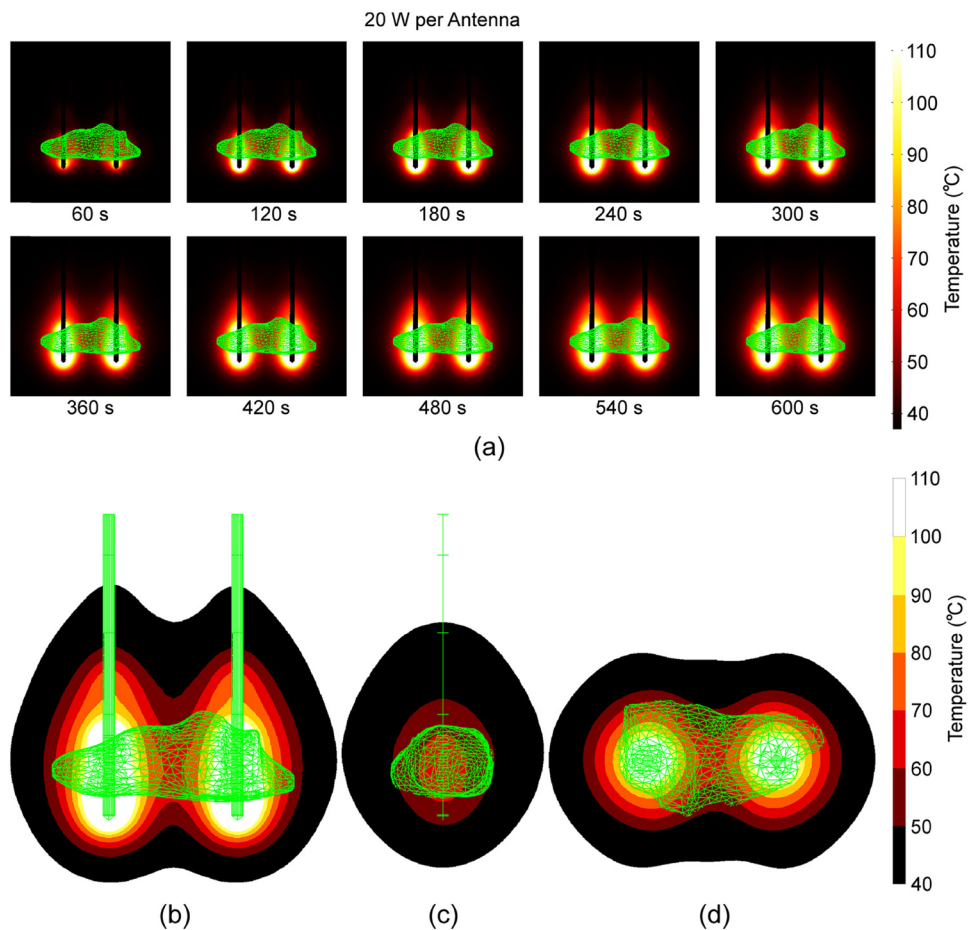


Figure 4: Temperature distribution for two 10-slot antennas with 30-mm separation and 20 W per antenna: (a) x-z cut plane during 600 s; at 600 s for (b) x-z cut plane, (c) y-z cut plane, and (d) x-y cut planes. The tumor is plotted on a green surface.

meshed with unstructured meshing using tetrahedrons. The mesh of the probe with the antenna and computational domain is composed of standard geometric cylinders and hexahedrons, which can be easily represented by structured meshing with hexahedrons. The transition between structured and unstructured meshing was made using the pyramid layer. There is a great advantage in using hexahedrons in FEM simulations, as regular structures can be represented with substantially smaller numbers of elements compared with standard unstructured representations, and the equilateral hexahedron (cube) is the perfect element for FEM analyses, providing the most accurate results. The maximum size of the FEM element is 1/10 of the guided wavelength, and smaller sizes yield negligible differences in the results. The time step size check is incorporated into the time loop. There

are four control points in the proposed domain. If the temperature difference between successive time steps is greater than 1°C at any point, the time loop is repeated with a smaller time step, thus ensuring the stability of the results. The model equations were solved using the FEM implemented in the open-source package GetDP [50–52]. The GetDP function in SimSurgery is optional, and other FEM solvers can also be used.

3 Results and discussions

The SAR radiation at a power of 20 W per antenna is shown in Figures 3a–c. The highest level (above 40 dBW/kg) was

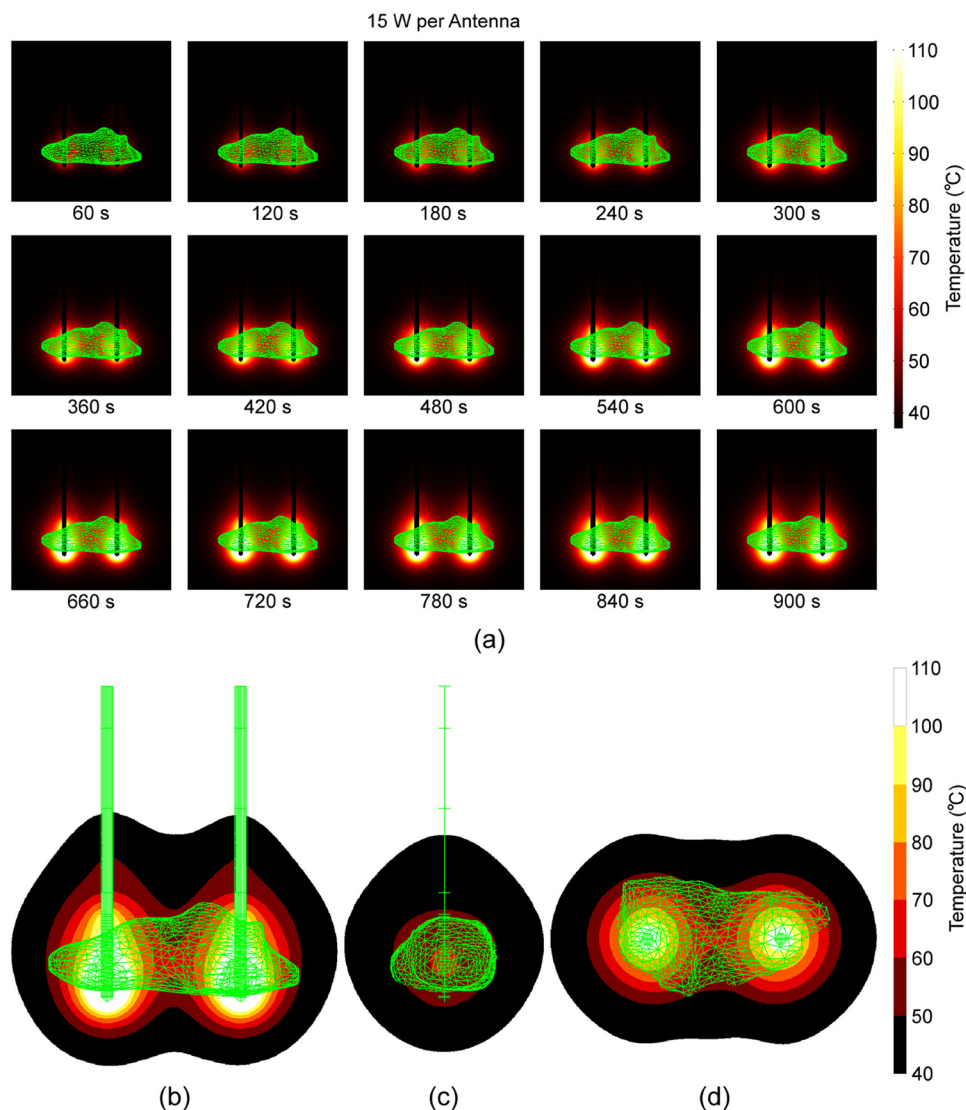


Figure 5: Temperature distribution for two 10-slot antennas with 30-mm separation and 15 W per antenna: (a) x-z cut plane during 900 s; at 900 s for (b) x-z cut plane, (c) y-z cut plane, and (d) x-y cut planes. The tumor is plotted on a green triangulated surface.

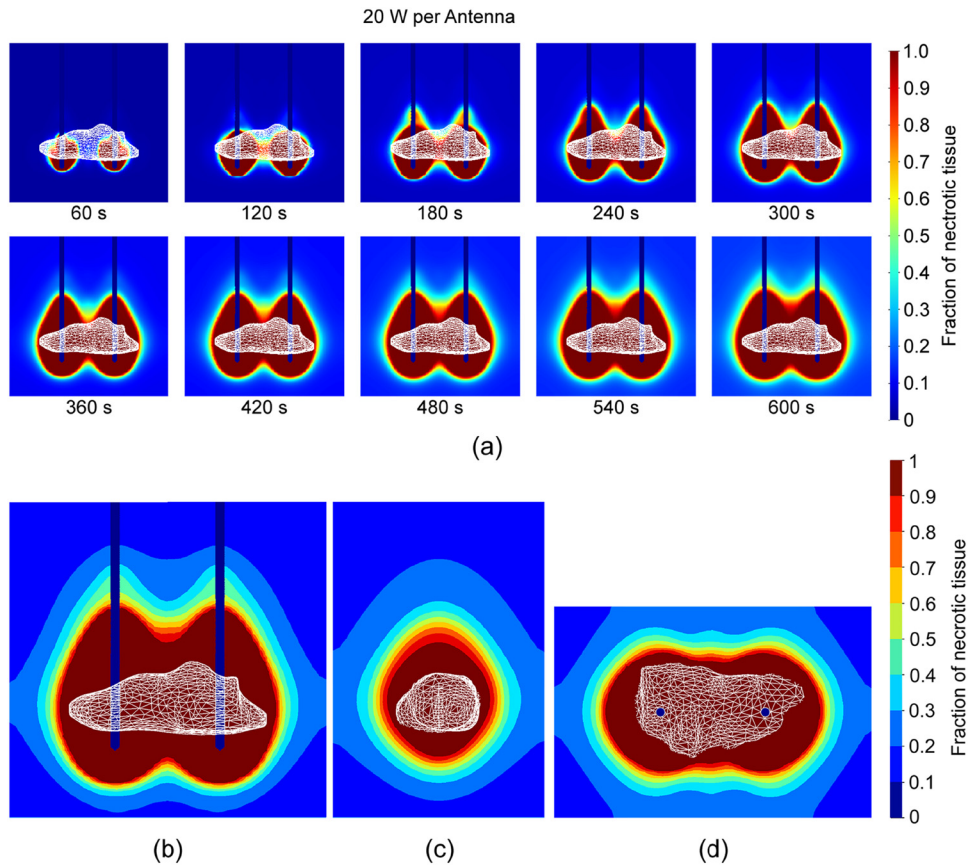


Figure 6: Fraction of necrotic tissue for two 10-slot antennas with 30-mm separation and 20 W per antenna: (a) x-z cut plane during 600 s; at 60 s for (b) x-z cut plane, (c) y-z cut plane, and (d) x-y cut planes. The white surface represents the tumor.

observed around the antenna slots. Zones >30 dBW/kg are practically guaranteed to be ablated within a short period, whereas zones <30 dBW/kg indicate MWA progression over a longer period. The tumor mass was positioned along the x-axis; therefore, the ablation zone grew in the direction of the x-axis (Figure 3a). There is also an ablation zone along the z-axis in the form of a comet tail along the probe structure toward the power source. Figures 3d–f show SAR radiation at a power of 15 W for each antenna. As expected, high-intensity zones above 30 dBW/kg were smaller. The zone between the antennas can be problematic because the x-z plane radiation intensity may not necessarily be sufficient to encompass the entire tumor. Based on the presented spatial and power distributions, we can conclude that a power of 20 W per antenna can provide complete tumor ablation, whereas a power of 15 W per antenna would require an extended duration of MWA.

Temperature-dependent material parameters influence the temperature distribution of the MWA [16]. The locations with the highest temperatures were always near the antenna slot. Moving away from the slots, the electromagnetic wave travels through the tissue, and the effect of radiation on the

temperature strongly depends on the material parameters. Blood perfusion dictates bio-heat transfer in tissues. Below 60°C , blood perfusion has a significant effect on the temperature distribution [17,23,35]. Above 60°C , the tissue is completely ablated, and there is no more blood perfusion in the ablated tissue [17,23,35]. Lower conductivity and permittivity of the tissue affect the electromagnetic wave passing through the ablated tissue. With a certain power, the temperature increases to a certain level and then saturates.

The temperature distribution with time for two 10-slot antennas with 30-mm separation and 20 W per antenna is displayed in Figure 4a. Evidently, high temperatures are near the antenna slots and decrease as the antennas move away from the antennas. The temperature rapidly rose until 120 s, after which it became much subtler. As observed from Figures 4b–d (temperature distribution at 600 s at different cross-sections), the bulk of the tumor was inside the area with temperatures of and above 60°C , which ensured instantaneous cell death. Figure 4b clearly shows that a region with a temperature greater than 60°C has a comet-like shape, implying the destruction of a substantial amount of healthy tissue.

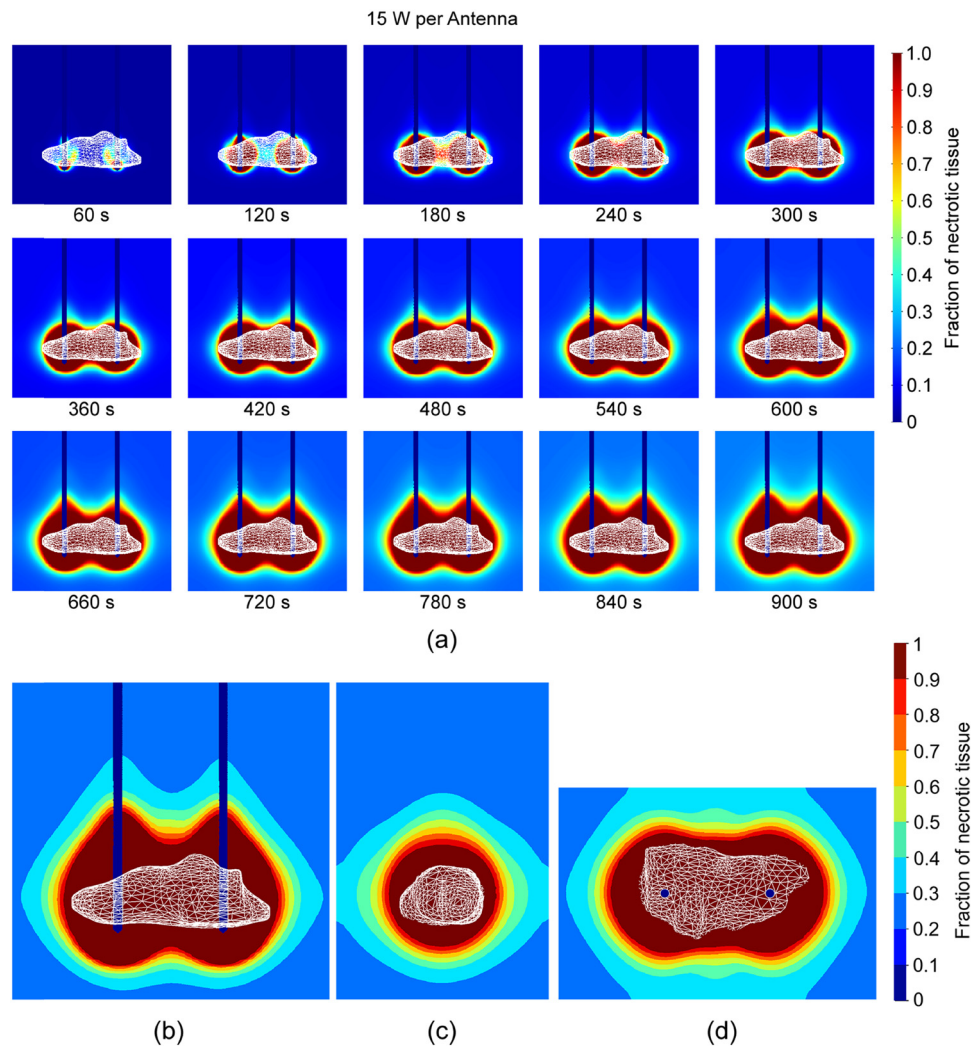


Figure 7: Fraction of necrotic tissue for two 10-slot antennas with 30-mm separation and 15 W per antenna: (a) x - z cut plane during 900 s; at 900 s for (b) x - z cut plane, (c) y - z cut plane, and (d) x - y cut planes. The tumor is plotted on a white surface.

For 15 W of the antenna, a similar effect was achieved over a longer time than 600 s, as shown in Figure 5. During the entire 900 s period, the temperature rises slowly (Figure 5a). At 900 s, the larger part of the tumor was practically inside the zones at temperatures of 60°C or higher (Figures 5b–d), thereby guaranteeing immediate cell death, but the shape of the zones was much more spherical.

Figure 6 illustrates the tumor's complete ablation after 600 s using a total power of 20 W per antenna. Both antennas form ablation zones that merge into a single zone. Until 180 s, the necrotic zones were spherical, but after that, they became the shape of a comet with the tail oriented toward the power source. Figure 6 indicates that 20 W per antenna for 600 s is sufficient for complete tumor necrosis with the desired ablation margin. For 15 W per antenna (Figure 7a), however, the ablation zone encompasses

two highly spherical zones for up to 600 s. Practically, no margins are observed, so additional time is needed. After 900 s, the necrotic zone became larger, encompassing not only the tumor but also the proper ablation margin. Figures 7b–d show that the damage caused to the healthy tissue was much smaller than that caused by the use of 20 W per antenna for 600 s.

Figure 8 depicts the temporal evolution of (a) the temperature and (b) the fraction of necrotic tissue calculated at the control points plotted in Figure 2b. As seen in Figure 8a, at point A, for 20 W per antenna, the temperature rises rapidly at approximately 120 s and then remains almost constant for up to 300 s. At 450 s, there was an abrupt change in the slope owing to the cessation of blood perfusion. For 15 W per antenna, the temperature first increased and then reached saturation at around 62°C after 540 s. At

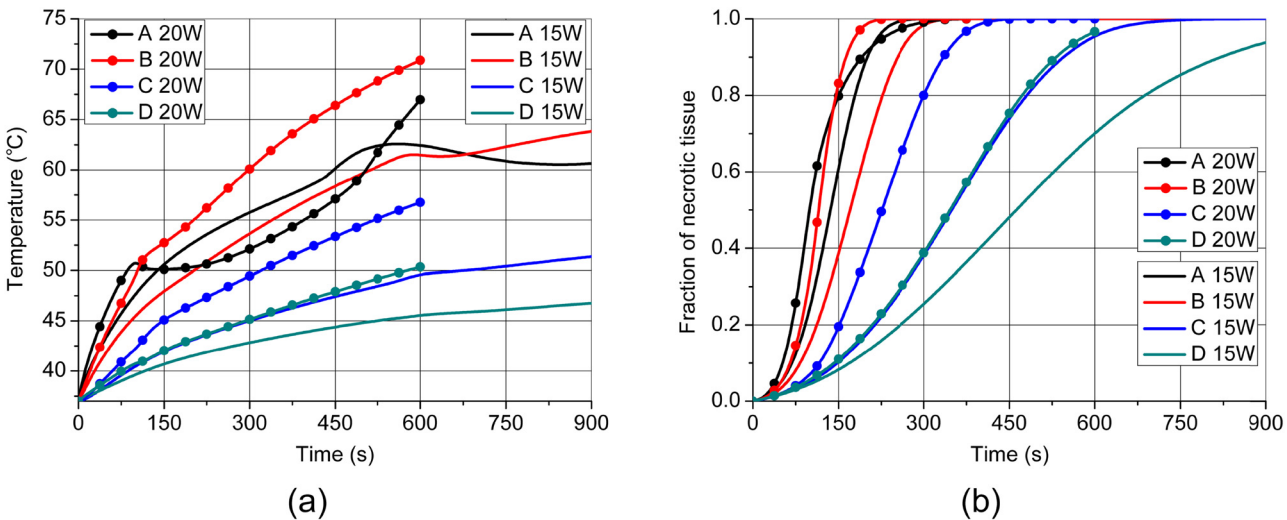


Figure 8: The time dependence of (a) the temperature distribution and (b) the fraction of necrotic tissue at the points shown in Figure 2b for antennas with 15 or 20 W.

point B, for 20 W per antenna, the temperature dependence is similar to that observed at point A. For 15 W per antenna, saturation occurs at approximately 61°C after 570 s. At point C, for 20 W per antenna, the temperature exhibited a small change in the slope around 150 s and reached 56.8°C after 600 s. Similarly, for 15 W per antenna, the temperature reached 51.3°C after 900 s. For 20 and 15 W per antenna, the temperature recorded at point D exhibits a very stable change over time, with a maximum value of 50.5°C at 600 s and 46.8°C at 900 s. Figure 8b shows that, during the observation period, 100% of the fraction of necrotic tissue was not achieved only at point D, which can be attributed to the fact that this point is outside the tumor. Complete ablation was achieved at points B, A, and

Table 3: VD, DT, and TDE after MWA for 15 and 20 W per antenna

MWA	V_{DAMAGED} (cm ³)	VD (%)	DT (%)	TDE (kJ)
15 W after 600 s	7.5	46.9	0.4	18
15 W after 900 s	18.1	113.1	1.0	27
20 W after 600 s	26.6	166.2	1.5	24

C after 150, 200, and 450 s, respectively, using 20 W per antenna and after 300, 320, and 750 s, respectively, using 15 W per antenna.

In Figure 9, the difference between the use of a single antenna and two identical antennas under the same conditions is shown. We can see that with the same input

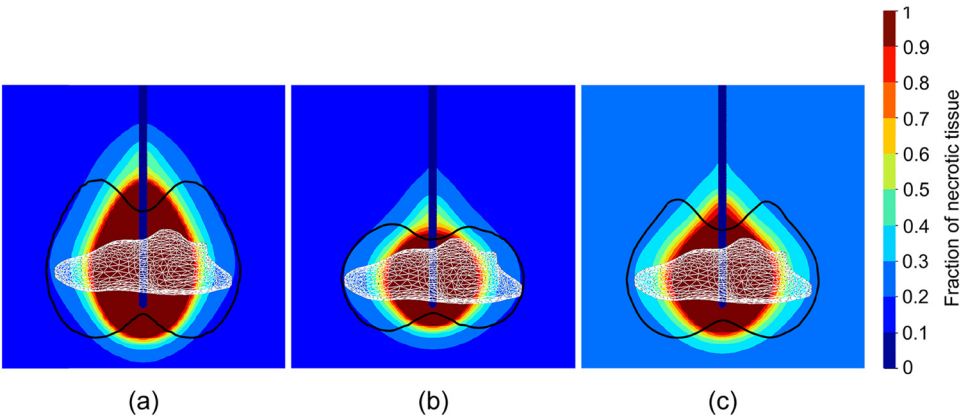


Figure 9: Fraction of necrotic tissue for a single 10-slot antenna at x-z plane: (a) 20 W after 600 s, (b) 15 s after 600 s, and (c) 15 W after 900 s. The triangulated surface represents the tumor. The black curves represent the shape of the ablation for the cases with the two antennas shown in Figures 6b and 7b under the same parameters.

power and duration of the MWA, in the case of the two antennas, there are two connected ablation zones that are slightly larger than the simple sum of the ablation zones originating from the single antennas. This is in accordance with the conclusions of [24].

VD and DT can be calculated using Eqs. (11) and (12). Both increase with time and power (Table 3). The least damage to the healthy tissue was observed after 600 s at 15 W, with a VD of 46.9% and a DT of 0.4%. After 900 s, the volume of damaged healthy tissue increased more than twice, with a VD of 113.1% and a DT of 1%. The highest damage occurred for the case with 20 W after 600 s, with a VD of 166.2% and a DT of 1.5%. Higher power and longer durations of MWA increase TDE, but tissue necrosis is not a simple linear function. Depending on the radiation pattern of the MWA system and system configuration, the power distribution among multiple antennas can produce a targeted ablation shape, thereby minimizing unwanted damage to healthy tissue [32]. The largest TDE was observed for the case with 15 W per antenna after 900 s; however, due to more spherical ablation zones, the damage was confined in the area around the tumor, thus producing a lower amount of damage to healthy tissue compared with the case with 20 W per antenna after 600 s.

4 Conclusion

In this study, we simulated MWA treatment of a real large elongated tumor from the database [34] using two identical parallel-positioned multi-slot coaxial antennas. The obtained simulation results show that the fastest temperature rise occurs near the radiating slots. For 20 W per antenna, tumor ablation was completed in 600 s, the temperature rapidly increased, and the two connected comet-shaped ablation zones led to excessive damage to the healthy tissue. Ablation can also be achieved using 15 W per antenna for 600 s without margins between the healthy tissue and tumor. Prolonging MWA to 900 s resulted in larger spherical ablation zones with significantly less damage to the healthy tissue. Our results indicate that using a two-antenna configuration with lower power and longer MWA duration provides complete ablation of large tumors with a sufficient safety margin. A comparison of the ablation created with 20 W per antenna during 600 s and 15 W per antenna during 900 s showed that volumetric damage was significantly higher in the first case (166.2 vs 113.1%). On the other hand, the total delivered power was larger in the second case as a direct consequence of the more spherical ablation zones. The calculation results showed that 25.7 and 24.8% of the input energy was converted into

thermal energy for heating the tumor tissue for the 15 and 20 W per antenna, respectively. The remaining energy is converted into thermal energy for heating the liver tissue and losses in the device itself. These results agree well with those published in [53].

Funding information: N.B., B.R., and M.R.-R. acknowledge that this research was supported by the Science Fund of the Republic of Serbia, The Program IDEAS, GRANT No. 7739583, SimSurgery.

Author contributions: Conceptualization: N.B., S.N., and M.R.-R.; methodology: B.R., N.B., and M.R.-R.; software: N.B. and B.R.; investigation and data interpretation: all of the authors; original draft preparation: N.B. and M.R.-R.; writing – review, and editing: all of the authors; supervision: B.R., S.N., and M.R.-R. All authors have accepted responsibility for the entire content of this manuscript and approved its submission.

Conflict of interest: The authors state no conflict of interest.

Data availability statement: The datasets generated and/or analyzed during the current study are available from the corresponding author on reasonable request.

References

- [1] Villanueva A. Hepatocellular carcinoma. *N Engl J Med*. 2019;380(15):1450–62. doi: 10.1056/NEJMra1713263.
- [2] Yao Z, Dai C, Yang J, Xu M, Meng H, Hu X, et al. Time-trends in liver cancer incidence and mortality rates in the U.S. from 1975 to 2017: a study based on the Surveillance, Epidemiology, and End Results database. *J Gastrointest Oncol*. 2023;14(1):312–24. doi: 10.21037/jgo-23-25.
- [3] Li Y, Ou Z, Yu D, He H, Zheng L, Chen J, et al. The trends in death of primary liver cancer caused by specific etiologies worldwide: results from the Global Burden of Disease Study 2019 and implications for liver cancer management. *BMC Cancer*. 2023;23(1):598. doi: 10.1186/s12885-023-11038-3.
- [4] Bray F, Laversanne M, Sung H, Ferlay J, Siegel RL, Soerjomataram I, et al. Global cancer statistics 2022: GLOBOCAN estimates of incidence and mortality worldwide for 36 cancers in 185 countries. *CA Cancer J Clin*. 2024;74(3):229–63. doi: 10.3322/caac.21834.
- [5] Li W, Ni CF. Current status of the combination therapy of transarterial chemoembolization and local ablation for hepatocellular carcinoma. *Abdom Radiol*. 2019;44(6):2268–75. doi: 10.1007/s00261-019-01943-2.
- [6] Glassberg MB, Ghosh S, Clymer JW, Qadeer RA, Ferko NC, Sadeghirad B, et al. Microwave ablation compared with radiofrequency ablation for treatment of hepatocellular carcinoma and liver metastases: a systematic review and meta-analysis. *Oncotargets Ther*. 2019;12:6407–38. doi: 10.2147/OTT.S204340.

- [7] Kudo M. Targeted and immune therapies for hepatocellular carcinoma: Predictions for 2019 and beyond. *World J Gastroenterol*. 2019;25(7):789–807. doi: 10.3748/wjg.v25.i7.789.
- [8] Wang Z, Liu M, Zhang DZ, Wu SS, Hong ZX, He GB, et al. Microwave ablation versus laparoscopic resection as first-line therapy for solitary 3-5-cm HCC. *Hepatology*. 2022;76(1):66–77. doi: 10.1002/hep.32323.
- [9] Itoh S, Ikeda Y, Kawanaka H, Okuyama T, Kawasaki K, Eguchi D, et al. Efficacy of surgical microwave therapy in patients with unresectable hepatocellular carcinoma. *Ann Surg Oncol*. 2011;18(13):3650–6. doi: 10.1245/s10434-011-1831-z.
- [10] Facciurusso A, Di Maso M, Muscatiello N. Microwave ablation versus radiofrequency ablation for the treatment of hepatocellular carcinoma: A systematic review and meta-analysis. *Int J Hyperth*. 2016;32(3):339–44. doi: 10.3109/02656736.2015.1127434.
- [11] Radjenović B, Sabo M, Šoltes L, Prnova M, Čičak P, Radmilović-Radjenić M. On efficacy of microwave ablation in the thermal treatment of an early-stage hepatocellular carcinoma. *Cancers*. 2021;13(22):5784. doi: 10.3390/cancers13225784.
- [12] Yao LJ, Zhu XD, Zhou LM, Zhang LL, Liu NN, Chen M, et al. Short-term efficacy of microwave ablation in the treatment of liver cancer and its effect on immune function. *World J Clin Cases*. 2024;12(18):3395–402. doi: 10.12998/wjcc.v12.i18.3395.
- [13] Izzo F, Granata V, Grassi R, Fusco R, Palaia R, Delrio P, et al. Radiofrequency ablation and microwave ablation in liver tumors: an update. *Oncologist*. 2019;24(10):e990–1005. doi: 10.1634/theoncologist.2018-0337.
- [14] De Vita E, Lo Presti D, Massaroni C, Iadicicco A, Schena E, Campopiano S. A review on radiofrequency, laser, and microwave ablations and their thermal monitoring through fiber Bragg gratings. *iScience*. 2023;26(11):108260. doi: 10.1016/j.isci.2023.108260.
- [15] Rossmann C, Haemmerich D. Review of temperature dependence of thermal properties, dielectric properties, and perfusion of biological tissues at hyperthermic and ablation temperatures. *Crit Rev Biomed Eng*. 2014;42(6):467–92. doi: 10.1615/critrevbiomedeng.2015012486.
- [16] Sawicki JF, Luyen H, Mohtashami Y, Shea JD, Behdad N, Hagness SC. The performance of higher frequency microwave ablation in the presence of perfusion. *IEEE Trans Biomed Eng*. 2019;66(1):257–62. doi: 10.1109/TBME.2018.2836317.
- [17] Tehrani MHH, Soltani M, Kashkooli FM, Raahemifar K. Use of microwave ablation for thermal treatment of solid tumors with different shapes and sizes-A computational approach. *PLoS One*. 2020;15(6):e0233219. doi: 10.1371/journal.pone.0233219.
- [18] Fallahi H, Prakash P. Antenna designs for microwave tissue ablation. *Crit Rev Biomed Eng*. 2018;46(6):495–521. doi: 10.1615/CritRevBiomedEng.2018028554.
- [19] Huang H, Zhang L, Moser MAJ, Zhang W, Zhang B. A review of antenna designs for percutaneous microwave ablation. *Phys Med*. 2021;84:254–64. doi: 10.1016/j.ejmp.2021.03.010.
- [20] Radmilović-Radjenić M, Bošković N, Radjenović B. Computational modeling of microwave tumor ablation. *Bioengineering*. 2022;9(11):656. doi: 10.3390/bioengineering9110656.
- [21] Solero Microwave Tissue Ablation System | AngioDynamics [Internet]; 2024 [cited 2024 Mar 6]. Available from: <https://www.angiodynamics.com/product/solero-microwave-tissue-ablation-system>.
- [22] Kuroda H, Nagasawa T, Fujiwara Y, Sato H, Abe T, Kooka Y, et al. Comparing the safety and efficacy of microwave ablation using thermosphere™ technology versus radiofrequency ablation for hepatocellular carcinoma: a propensity score-matched analysis. *Cancers*. 2021;13(6):1295. doi: 10.3390/cancers13061295.
- [23] Ge M, Jiang H, Huang X, Zhou Y, Zhi D, Zhao G, et al. A multi-slot coaxial microwave antenna for liver tumor ablation. *Phys Med Biol*. 2018;63(17):175011. doi: 10.1088/1361-6560/aad9c5.
- [24] Harari CM, Magagna M, Bedoya M, Lee Jr FT, Lubner MG, Hinshaw JL, et al. Microwave ablation: comparison of simultaneous and sequential activation of multiple antennas in liver model systems. *Radiology*. 2016;278(1):95–103. doi: 10.1148/radiol.2015142151.
- [25] Zhang D, Liang W, Zhang M, Liang P, Gu Y, Kuang M, et al. Multiple antenna placement in microwave ablation assisted by a three-dimensional fusion image navigation system for hepatocellular carcinoma. *Int J Hyperth*. 2019;35(1):122–32. doi: 10.1080/02656736.2018.1484183.
- [26] Cazzato RL, De Marini P, Leclerc L, Dalili D, Koch G, Rao P, et al. Large nearly spherical ablation zones are achieved with simultaneous multi-antenna microwave ablation applied to treat liver tumours. *Eur Radiol*. 2020;30(2):971–5. doi: 10.1007/s00330-019-06431-1.
- [27] Trujillo-Romero CJ, Leija-Salas L, Vera-Hernández A, Rico-Martínez G, Gutiérrez-Martínez J. Double slot antenna for microwave thermal ablation to treat bone tumors: modeling and experimental evaluation. *Electronics*. 2021;10(7):761. doi: 10.3390/electronics10070761.
- [28] Trujillo-Romero CJ, Dionisio Merida J, Ramírez-Guzmán TJ, Martínez-Valdez R, Leija-Salas L, Vera-Hernández A, et al. Thermal evaluation of multi-antenna systems proposed to treat bone tumors: finite element analysis. *Sensors*. 2022;22(19):7604. doi: 10.3390/s22197604.
- [29] Wang J, Huang S, Gao H, Liu J, Zhang Y, Wu S. Computer simulations of dual-antenna microwave ablation and comparison to experimental measurements. *Appl Sci*. 2023;13(1):26. doi: 10.3390/app13010026.
- [30] Andresiani F, Pacella G, Vertulli D, Altomare C, Bitonti MT, Bruno A, et al. Microwave ablation using two simultaneous antennas for the treatment of liver malignant lesions: a 3 year single-Centre experience. *Int J Hyperth*. 2023;40(1):2163309. doi: 10.1080/02656736.2022.2163309.
- [31] Radmilović-Radjenić M, Radjenović D, Radjenović B. Finite element analysis of the effect of microwave ablation on the liver, lung, kidney, and bone malignant tissues. *Europhys Lett*. 2021;136(2):28001. doi: 10.1209/0295-5075/ac2719.
- [32] Andreozzi A, Brunese L, Iasiello M, Tucci C, Vanoli GP. Numerical analysis of the pulsating heat source effects in a tumor tissue. *Comput Methods Prog Biomed*. 2021;200:105887. doi: 10.1016/j.cmpb.2020.105887.
- [33] Radmilović-Radjenić M, Bošković N, Sabo M, Radjenović B. An analysis of microwave ablation parameters for treatment of liver tumors from the 3D-IRCADb-01 database. *Biomedicines*. 2022;10(7):1569. doi: 10.3390/biomedicines10071569.
- [34] Soler L, Hostettler A, Agnus V, Charnoz A, Fasquel JB, Moreau J, et al. 3D image reconstruction for comparison of algorithm database: A patient-specific anatomical and medical image database. *IRCAD, Strasbourg, France, Tech Rep*. 2010;1(1):1 [cited 2024 Mar 6]. <https://www.ircad.fr/research/data-sets/liver-segmentation-3d-ircadb-01/>.
- [35] Bošković N, Radmilović-Radjenić M, Radjenović B. Finite element analysis of microwave tumor ablation based on open-source software components. *Mathematics*. 2023;11(12):2654. doi: 10.3390/math11122654.

- [36] Yang D, Converse MC, Mahvi DM, Webster JG. Expanding the bio-heat equation to include tissue internal water evaporation during heating. *IEEE Trans Biomed Eng.* 2007;54(8):1382–8. doi: 10.1109/TBME.2007.890740.
- [37] Pennes HH. Analysis of tissue and arterial blood temperatures in the resting human forearm. *J Appl Physiol.* 1998;85(1):5–34. doi: 10.1152/jappl.1998.85.1.5.
- [38] Cavagnaro M, Pinto R, Lopresto V. Numerical models to evaluate the temperature increase induced by ex vivo microwave thermal ablation. *Phys Med Biol.* 2015;60(8):3287–311. doi: 10.1088/0031-9155/60/8/3287.
- [39] Miaskowski A, Gas P. Numerical estimation of SAR and temperature distributions inside differently shaped female breast tumors during radio-frequency ablation. *Materials.* 2023;16(1):223. doi: 10.3390/ma16010223.
- [40] Selmi M, Bin Dukhyil AA, Belmabrouk H. Numerical analysis of human cancer therapy using microwave ablation. *Appl Sci.* 2020;10(1):211. doi: 10.3390/app10010211.
- [41] LeBrun A, Ma R, Zhu L. MicroCT image based simulation to design heating protocols in magnetic nanoparticle hyperthermia for cancer treatment. *J Therm Biol.* 2016;62(Pt B):129–37. doi: 10.1016/j.jtherbio.2016.06.025.
- [42] Zhang B, Moser MA, Zhang EM, Luo Y, Zhang H, Zhang W. Study of the relationship between the target tissue necrosis volume and the target tissue size in liver tumours using two-compartment finite element RFA modelling. *Int J Hyperth.* 2014;30(8):593–602. doi: 10.3109/02656736.2014.984000.
- [43] Manuchehrabadi N, Zhu L. Development of a computational simulation tool to design a protocol for treating prostate tumours using transurethral laser photothermal therapy. *Int J Hyperth.* 2014;30(6):349–61. doi: 10.3109/02656736.2014.948497.
- [44] Lodewick TM, Arnoldussen CW, Lahaye MJ, van Mierlo KM, Neumann UP, Beets-Tan RG, et al. Fast and accurate liver volumetry prior to hepatectomy. *HPB (Oxford).* 2016;18(9):764–72. doi: 10.1016/j.hpb.2016.06.009.
- [45] Hui TCH, Brace CL, Hinshaw JL, Quek LHH, Huang IKH, Kwan J, et al. Microwave ablation of the liver in a live porcine model: the impact of power, time and total energy on ablation zone size and shape. *Int J Hyperth.* 2020;37(1):668–76. doi: 10.1080/02656736.2020.1774083.
- [46] Qt | Development framework for cross-platform applications [Internet]; 2024 [cited 2024 Mar 6]. Available from: <https://www.qt.io/product/framework>.
- [47] The visualization toolkit [Internet]; 2024 [cited 2024 Mar 6]. Available from: <https://vtk.org>.
- [48] Open CASCADE Technology | Collaborative development portal [Internet]; 2024 [cited 2024 Mar 6]. Available from: <https://dev.opencascade.org>.
- [49] Geuzaine C, Remacle JF. Gmsh: a three-dimensional finite element mesh generator with built-in pre- and post-processing facilities [Internet]. 2024 [cited 2024 Mar 6]. Available from: <https://gmsh.info>.
- [50] Dular P, Geuzaine C. GetDP: a general environment for the treatment of discrete problems [Internet]; 2024 [cited 2024 Mar 6]. Available from: <https://getdp.info>.
- [51] Dular P, Geuzaine C, Henrotte F, Legros W. A general environment for the treatment of discrete problems and its application to the finite element method. *IEEE Trans Magn.* 1998;34(5):3395–8. doi: 10.1109/20.717799.
- [52] Geuzaine C. ONELAB: Open numerical engineering laboratory [Internet]; 2024 [cited 2024 Mar 6]. Available from: <https://onelab.info>.
- [53] Gorman J, Tan W, Abraham J. Numerical simulation of microwave ablation in the human liver. *Processes.* 2022;10(2):361. doi: 10.3390/pr10020361.



Optimal parameters for the efficient microwave ablation of liver tumor from the 3D-IRCAdB-01 database

NIKOLA BOŠKOVIĆ, BRANISLAV RADJENOVIC, MARIJA RADMILOVIĆ-RADJENOVIC*

Institute of Physics, University of Belgrade, Serbia.

Purpose: Microwave ablation is a minimally invasive thermal modality for cancer treatment with high survival and low recurrence rates. Despite the unquestionable benefits of microwave ablation, the interaction between the medical instruments and the tissue may cause damage to the healthy tissue around the tumor. Such damages can be removed by clarifying the conditions for their development. In addition to clinical methods, computer simulations have become very effective tools for optimizing microwave ablation performance. **Methods:** The study was focused on the determination of the optimal input power for complete microwave tumor ablation with an adequate safety margin avoiding injury to the surrounding healthy tissue. In three-dimensional simulations, the liver tumor model was based on a real tumor (1.74 cm × 2.40 cm × 1.43 cm) from the 3D-IRCAdB-01 database. Calculations were performed for a 10-slot antenna proven to achieve a higher degree of ablation zone localization than a standard single-slot antenna. The temperature-dependent dielectric and thermal properties of healthy and tumoral liver tissue, blood perfusion, and water content were included in the model. **Results:** The obtained simulation results revealed that the proper choice of input power ensures that necrotic tissue is mainly located in the tumor with minimal damage to the surrounding healthy tissue. **Conclusions:** This study may represent a step forward in the planning of individual microwave ablation treatment for each patient.

Key words: microwave ablation, optimal conditions, tumoral tissue, necrotic tissue, three-dimensional simulation

1. Introduction

Liver cancer is one of the most common types of cancer worldwide and poses a significant health challenge because of its high mortality rate [1]–[5]. Treatment options for liver cancer may include surgery, liver transplantation, ablation therapy (such as radiofrequency or microwave ablation), embolization, chemotherapy, targeted therapy or immunotherapy. The choice of treatment depends on various factors such as tumor size and location, extent of liver damage, and overall health of the patient [6], [7].

The advantages of microwave ablation (MWA) in treating liver tumors include its ability to create larger ablation zones compared with other ablation techniques such as radiofrequency ablation, potentially improving treatment outcomes [8]–[10]. In addition, MWA may be

more efficient in heating tissue, resulting in shorter procedure times. Although the effectiveness rate of MWA in removing small liver tumors is more than 85% for large tumors, completion rates are slightly lower [11], [12].

The mechanism underlying MWA is associated with an increase in temperature above the normal physiological threshold to kill cancer cells. A microwave antenna (MW) radiates an electromagnetic field, leading to frictional heating of water molecules in soft tissues [13]. The MW antenna design strongly affects the efficacy of MWA treatment [14]. Over the years, various antenna designs have been developed, including choke, cap-choke [15], floating sleeve [16], and water-cooled [17]. Recently developed compact multi-slot coaxial antennas ensure faster heating rates in the heating center and more localized heating distribution without damaging the surrounding healthy tissues than single-slot antennas [18].

* Corresponding author: Marija Radmilović-Radjenović, Institute of Physics, University of Belgrade, Pregrevica 118, 11080 Belgrade, Serbia. E-mail: marija@ipb.ac.rs

Received: February 24th, 2024

Accepted for publication: April 22nd, 2024

The role of computational models in predicting medical treatment outcomes has significantly increased [19]–[23]. In most numerical studies, the degree of biological tissue destruction is determined by using the Arrhenius model [24]. Although three-dimensional (3D) simulations of radiofrequency ablation (RFA) exist [25], most simulations devoted to MWA are performed under the assumption of a homogeneous medium that reduces the problem from 3D to 2D, which often does not adequately represent reality [26]–[29].

In this study, simulations were performed using a three-dimensional simulation model [29]. A realistic model of the tumor was based on a real tumor denoted by 1.04 in the 3D-IRCAdb-01 liver tumor database [30]. The primary goal of this study was to determine the optimal input power for complete tumor ablation with minimal damage to the surrounding healthy tissue. Estimation of the optimal power guarantees the best ratio of necrotic tissue to healthy tissue.

2. Numerical method

Modeling MWA as a multiphysics problem involves modeling multiple physical phenomena, such as electromagnetic wave propagation, heat transfer, and tissue damage, that occur during the procedure. The equation governing the electric field distribution through the tissue [29], [31] is as follows:

$$\nabla^2 \mathbf{E} - \mu_r k_0^2 \left(\varepsilon_r - \frac{j\sigma}{\omega \varepsilon_0} \right) \mathbf{E} = 0, \quad (1)$$

where ω is the angular frequency, \mathbf{E} is the electric field vector, σ is the electrical conductivity of the tissue, and $k_0 = \omega/c_0$ is the vacuum propagation constant. ε_0 , ε_r , and μ_r are the vacuum dielectric constant, relative permittivity, and permeability of the tissue, respectively.

The heat transfer is described by Pennes' bio-heat [29], [31]:

$$\rho c \frac{\partial T}{\partial t} = \nabla \cdot (k \nabla T) + \rho_b W_b c_b (T_b - T) + Q_{ext} + Q_m, \quad (2)$$

where t is the time. The parameters that characterize the tissue are density ρ , heat capacity c , and temperature T . Parameters associated with blood are density ρ_b , heat capacity c_b , temperature T_b , and perfusion rate W_b . In our calculations, the heat source from metabolism Q_m was neglected, whereas coupling with the electromagnetic field was included in the external heat source Q_{ext} .

During MWA, the tissue temperature increases leading to structural modifications of the treated tissue and causing changes in dielectric and thermal properties that affect the electromagnetic power distribution. The temperature dependence of the dielectric properties of the tissue is expressed by the following equations [29], [31]:

$$\varepsilon_r(T) = s_1 \left[1 - \frac{1}{1 + \exp(s_2 - s_3 T)} \right], \quad (3)$$

$$\sigma(T) = r_1 \left[1 - \frac{1}{1 + \exp(r_2 - r_3 T)} \right], \quad (4)$$

with the coefficients listed in [28]. It has been reported that the relative permittivity and conductivity of tumors are approximately by 24 and 11% higher than those of healthy tissue, respectively [29], [31]. The dielectric properties of both tumoral and healthy tissues decrease with increasing temperature because of water evaporation during MWA. Since liver tissue contains approximately 78% water, an increase in temperature above 100 °C may result in a decrease in tissue water content by approximately 20% by mass.

Tissue damage depends on both temperature and time according to the following Arrhenius form [29], [31]:

$$\Omega(t) = \int_0^t A \exp\left(-\frac{\Delta E}{RT}\right) dt, \quad (5)$$

where R and T are the gas constant and temperature, respectively. A is the frequency factor, while ΔE is the activation energy of the irreversible damage reaction. From the degree of tissue injury, the fraction of necrotic tissue θ_d can be calculated as follows [29], [31]:

$$\theta_d = 1 - \exp(-\Omega). \quad (6)$$

In this study, calculations were performed for a compact 10-slot antenna composed of several periodic elements, as shown in Fig. 1 [29]. Optimal ablation zones were achieved by adjusting the number of slots and the distance between them. Each periodic element complied with a slot and width of 0.6 mm and a spacing conductor of 0.8 mm between the two slots. Finely tuned impedance matching allows near-spherical ablation zones without damaging the surrounding healthy tissues. In contrast to the frequently used spherical tumor geometry, our simulation model is based on a real tumor labeled as 1.04 in the database 3D-IRCAdb-01, which contains CT scans of several patients [30]. This tumor, which belonged to a female born in 1944 is relatively large (1.74 cm × 2.40 cm × 1.43 cm) with a volume

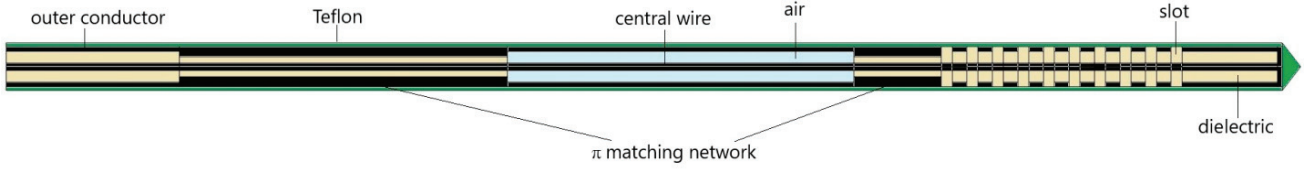


Fig. 1. Schematic representation of a 10-slot antenna with a finely tuned impedance π -matching network to preserve surrounding healthy tissues. The distance between the two slots is 0.8 mm, while the width of the single slot is 0.6 mm

of 2.38 cm^3 and an irregular shape, as displayed in Fig. 2. One of the most critical steps in finite element calculations is meshing, which involves volume separation into many smaller elements. The mesh should be sufficiently fine to obtain accurate results, convergence and stability, but sufficiently coarse to avoid long computer time consumption. Our developed software [31] uses hybrid meshing with the combination of tetrahedrons, hexahedrons, pyramids and provides a highly accurate solution with much smaller number of elements compared to commercial softwares [19]–[23]. Unstructured meshing with only tetrahedrons would typically require millions of finite elements, and multiple refinement steps, to achieve sufficient quality and convergence. Most of the computational domain can be represented with regular geometries, which can easily be represented with structured meshing (hexahedrons) of superior quality, while complex geometry such as tumor can be represented with tetrahedrons and connected with the hexahedrons via a pyramidal layer. For these calculations, the mesh was composed of 78 469 tetrahedrons, 50 220 hexahedrons and 2233 pyramids.

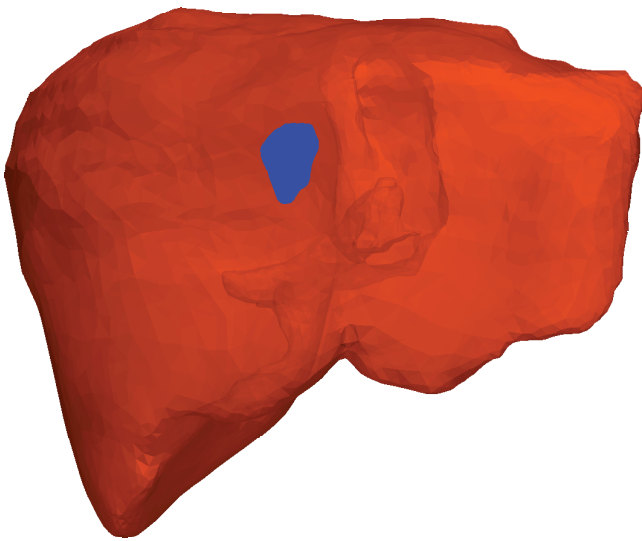


Fig. 2. Three-dimensional view of the liver (red solid surface) with the real position of tumor 1.04 taken from the database [30] (solid blue surface). Dimensions of tumor are $(1.74 \text{ cm} \times 2.40 \text{ cm} \times 1.43 \text{ cm})$

To determine the optimal input power, numerical simulations were performed for tumor 1.04 from the database [30] exposed to a frequency of 2.45 GHz and input power in the range of 10–30 W. The parameters of the biological materials used in the numerical simulations are described in the literature [28], [29]. For the healthy liver, tumor, and blood samples, the density values (expressed in $[\text{kg}/\text{m}^3]$) were 1079, 1040, and 1060, respectively. The thermal conductivities in units $\text{W}/\text{m}^\circ\text{C}$ corresponding to healthy tissue, tumor tissue, and blood were 0.52, 0.57, and 0.5, respectively. Before treatment, the *tissue temperature* was assumed to be 37°C .

3. Results

In Figure 3, the tumor (triangulated surface) and ablation zones (solid surfaces) are shown for an input power in the range of 10–30 W. The optimal value of the input power corresponded to total tumor ablation with minimal damage to healthy tissues. At an input power of

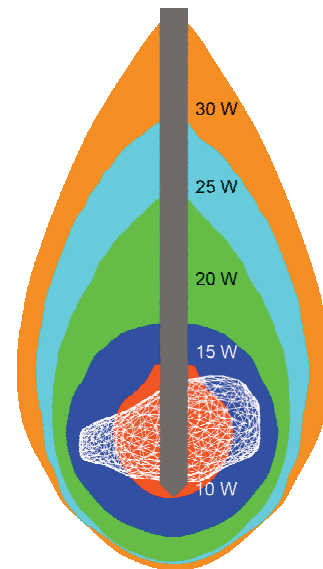


Fig. 3. Isocontours composed of the totally ablated region (solid surface) after 600 s of MWA of tumor 1.04 [30] (triangulated surface) for input power from 10 to 30 W

10 or 15 W, although the ablation zones were spherical, they did not ensure complete ablation of the tumor. With increasing the input power (25 or 30 W), ablation zones became more elongated, resulting in significant damage to healthy tissue around the tumor. Elongated shapes are undesirable ablation patterns that damage healthy tissues even if the ablation time is shorter. The ablation zone that best fit the necrotic tissue was achieved for an input power of 20 W, while the healthy tissue was preserved.

The fraction of necrosis around liver tumor 1.04 [30] (triangulated surface) during MWA at 20 W is shown in Fig. 4. The formed ablation zones are elongated with a greater length along the shaft of the antenna. The ablation zones are concentrated around the tip and slots of the antenna with two distinct heating zones [32]. The active heating zone appears within the tissue nearest to the antenna, where the intensity of energy is high and its absorption by the tissue is fast. The passive zone is far from the antenna, where the energy intensity is lower.

In Figure 5, the time evolution of the specific absorption rate (SAR), defined as the ratio of the absorbed heat power to tissue density, is presented [33]. The black lines represent tumor. The SAR increased along the axis and decreased after reaching a peak around the antenna slot. Although the maximal value of the SAR corresponds to the tumor area, the absorbed energy also invades the healthy surrounding tissue.

The time dependence of the temperature distribution around the tumor (triangulated surface) calculated for the estimated optimal power of 20 W is presented in Fig 6a. As the absorbed energy is converted into thermal energy, tissue temperature increases. In the vicinity of the antenna, the heat source is strong and the temperatures were higher. The temperature increased with ablation time and reached a maximum value inside the tumor region. The extent of heating is limited by the blood perfusion. Different cross sections of the temperature distribution at the end of the MWA at 600 s are illustrated in Fig. 6b.

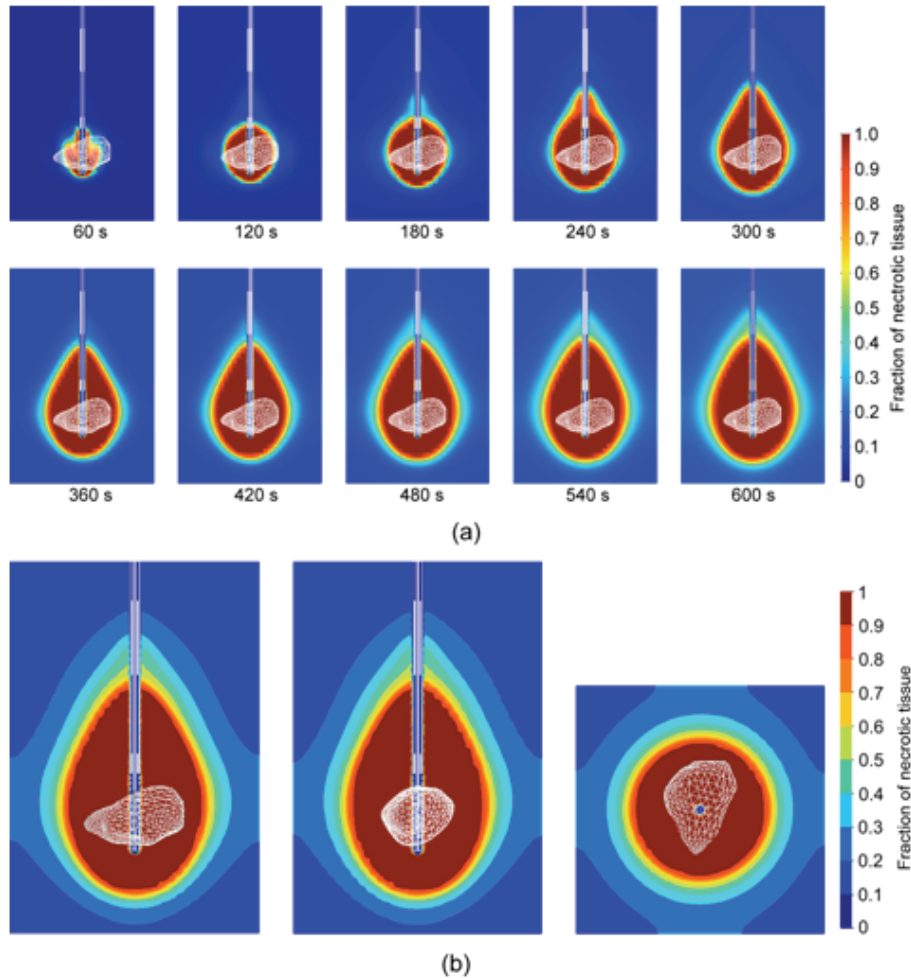


Fig. 4. (a) Time evolution of the fraction of necrosis from 60 s to 600 s, (b) fraction of necrotic tissue at different cross-sections at 600 s, around liver tumor 1.04 [30] (triangulated surface) during MWA at 2.45 GHz and input power of 20 W

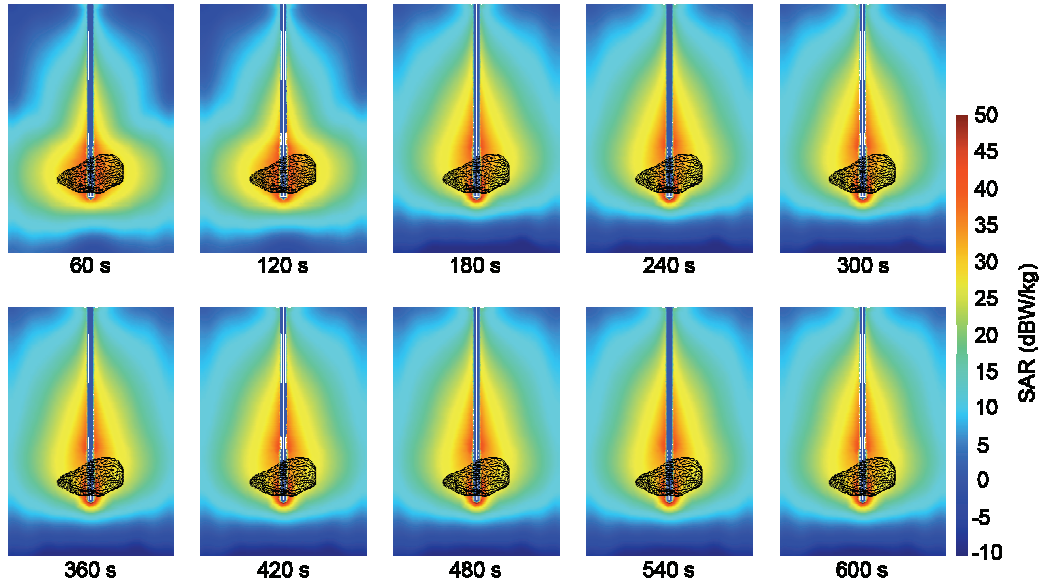


Fig. 5. (a) Time evolution of SAR distribution from 60 s to 600 s, (b) SAR distribution at different cross-sections at 600 s, around liver tumor 1.04 [30] (triangulated surface) during MWA at 2.45 GHz and input power of 20 W

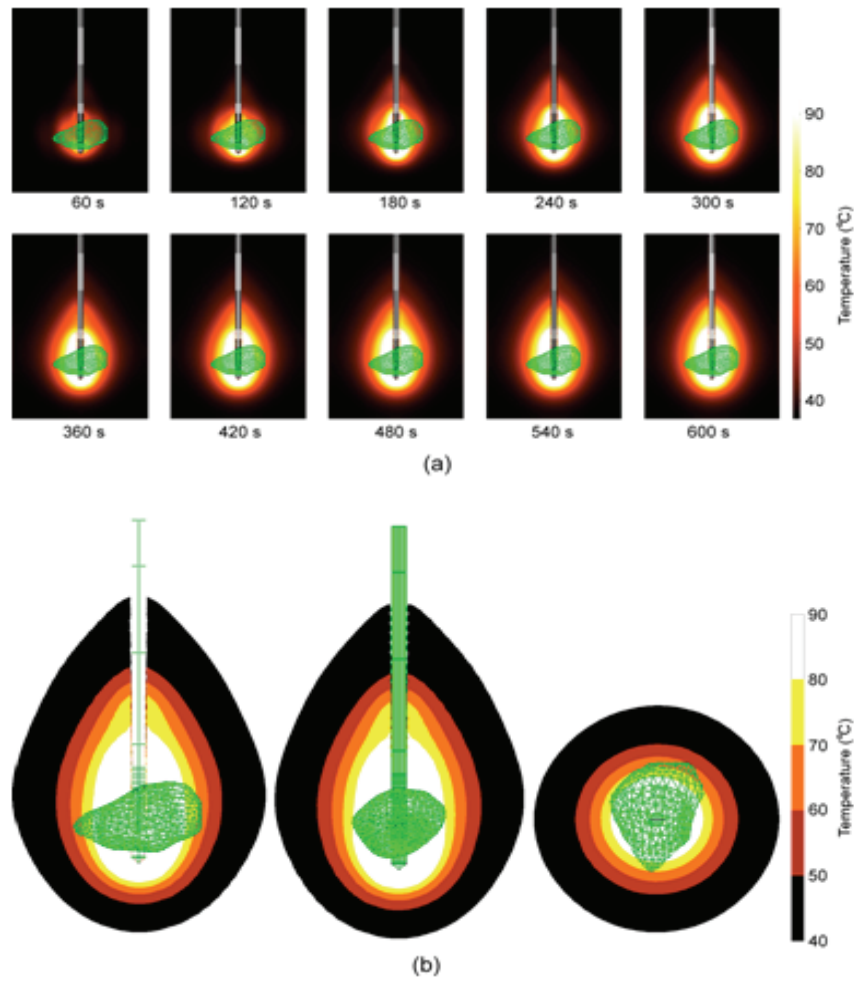


Fig. 6. (a) The time evolution of temperature distribution from 60 s to 600 s, (b) temperature distribution at different cross-sections at 600 s, around liver tumor 1.04 [30] (triangulated surface) during MWA at 2.45 GHz and the input power of 20 W

4. Discussion

The size of the ablative zones depends on the amount of energy delivered from the microwave generator to the antenna. The fraction of damage increased as the ablation time increased. Even though the absorbed power density is high close to the antenna, the absorbed energy may also affect the healthy surrounding tissue. In our study, for an input power of 10 W, the ablation was small, located around the radiating slots. At 15 W, the ablation zone has a spherical shape. For higher input powers, ablation expansions are mostly focused in the longitudinal direction around the probe. The estimated optimal value of the input power of 20 W ensures complete tumor necrosis and sufficient safety margins. Ablation time decreased with increasing input power. However, even if the ablation time is shorter, higher input power values may result in the formation of elongated undesirable ablation zones, causing significant damage to healthy tissue around the tumor. Furthermore, delivery of high-power, short-duration ablation is not commonly used because of the increased risk of steam pop and thrombus formation [34].

The time evolution of the ablation shows that up to 120 s, the ablation remains highly spherical, after which it grows and elongates. In addition, the high-intensity SAR zones follow the ablation shape. Any tissue in the zone with a SAR of approximately 25 dBW/kg or more can be considered ablated. The temperature also increases with increasing ablation time and reaches a maximum value near the microwave antenna slots. Any tissue within the zone with a temperature above 60 °C is instantly ablated. The tissue inside the zone above 50 °C would typically be ablated after approximately 10 min, whereas prolonged exposure to temperatures above 42 °C can also cause irreversible tissue damage. The distribution of high temperature with time follows the form of necrosis. The entire tumor is located within the zone with a temperature of 60 °C and above, ensuring that MWA is successful.

In contrast to our simulation model, the 3D model of MWA implemented in the commercial ANSYS software includes parts of liver tissue, bones, skin and fat [23]. However, it does not include any tumor that affects the accuracy of the calculations because of different material parameters corresponding to tumoral and healthy tissue [23]. In addition, the duration of the simulation presented in [23] ranges between 15 and 20 days, whereas our simulations usually last around 100 minutes. Our 3D FEM simulation results obtained for a real tumor provide a much more accurate representation of the MWA process compared

with simplified tumor geometry and 2D-axial symmetric simulations [26], [27]. Significant differences between results obtained using the 2D axisymmetric FEM model of the MWA and experimental results clearly indicate the importance of performing full 3D simulations [26]. When a 1-slot antenna is used [27], the tail of the so-called “comet-shaped” ablation zones obtained for sphere-like tumors unavoidably damages the healthy tissue along the shaft of the antenna as opposed to minimal surrounding tissue damage obtained in our results. Regarding antenna design, our results agree well with the 3D simulation results presented in [28], revealing that a 10-slot antenna offers higher heating efficiency of tissue and more near-spherical ablation zones than a 1-slot antenna.

Determining the optimal ratio of necrotic tissue to healthy tissue is important for improving MWA treatment to remove the maximal part of the tumor while preserving healthy surrounding tissue. Although a multi-slot coaxial antenna produces a more localized heating pattern for spherical tumors; for realistic tumor shapes, the ablation zones are usually elongated. In some cases, to treat larger tumors, two or three antenna systems are recommended.

5. Conclusions

In this study, we determined the optimal input power for efficient and safe microwave liver tumor ablation. For this purpose, full three-dimensional simulations based on a finite element method have been developed and tested [28], [30]. Calculations were performed for a model of a real liver tumor denoted by 1.04 in the database 3D-ICRADb-01 (3D-IRCADb) [29] exposed to radiation from a 10-slot antenna operating at a frequency of 2.45 GHz. Parameters characterizing healthy and tumoral tissues are included in the model. Since blood flow acts as cooling fluid, if not taken into account, the ablation estimation can be severely wrong. We assumed that there is no perfusion in necrotic tissue, hence blood perfusion increases with temperature until tissue necrosis, when it becomes zero. Since ablation processes follow the Arrhenius model, we used it to estimate tissue damage as a function of time.

The optimal value of the input power of 20 W was estimated so that the whole tumor was completely ablated with minimal damage to the healthy tissue. The presented results clearly show the importance of three-dimensional modeling in determining the optimal conditions MWA which may be incorporated into medical procedure planning for each tumor. Recent

advancements in simulation models of tissue damage may play a crucial role in the development of medical devices and the improvement of surgical therapeutic procedures.

Acknowledgements

Authors acknowledge that this research was supported by the Science Fund of the Republic of Serbia, The Program IDEAS, GRANT No. 7739583, SimSurgery.

References

- [1] ANANTHAKRISHNAN A., GOGINENI V., SAEIAN K., *Epidemiology of Primary and Secondary Liver Cancers*, Semin. Intervent. Radiol., 2006, 23 (1), 47–63.
- [2] BALOGH J., VICTOR D., ASHAM E.H., BURROUGHS S.G., BOKTOUR M., SAHARIA A., LI X., GHOBRIAL R.M., MONSOUR H.P. Jr., *Hepatocellular carcinoma: A review*, J. Hepatocell. Carcinoma, 2016, 3, 41–53.
- [3] VILLANUEVA A., *Hepatocellular Carcinoma*, N. Engl. J. Med., 2019, 380, 1450–1462.
- [4] LINN Y.L., CHEE M.Y., KOH Y.X., TEO J.Y., CHEOW P.C., CHOW P.K.H., CHAN C.Y., CHUNG A.Y.F., OOI L.L.P.J., GOH B.K.P., *Actual 10-year survivors and 10-year recurrence free survivors after primary liver resection for hepatocellular carcinoma in the 21st century: a single institution contemporary experience*, J. Surg. Oncol., 2021, 123 (1), 214–221.
- [5] CHEN J.G., ZHU J., ZHANG Y.H., CHEN Y.S., DING L.L., CHEN H.Z., SHEN A.G., WANG G.R., *Liver Cancer Survival: A Real World Observation of 45 Years with 32,556 Cases*, Journal of Hepatocellular Carcinoma, 2021, 8, 1023–1034.
- [6] LI Y., ZHANG R., XU Z., WANG Z., *Advances in Nanoliposomes for the Diagnosis and Treatment of Liver Cancer*, Int. J. Nanomedicine, 2022, 17, 909–925.
- [7] KOULOURIS A., TSAGKARIS C., SPYROU V., PAPPAS E., TROULLINO A., NIKOLAOU M., *Hepatocellular Carcinoma: An Overview of the Changing Landscape of Treatment Options*, J. Hepatocell. Carcinom., 2021, 8, 387–401.
- [8] XU X.L., LIU X.D., LIANG M., LUO B.M., *Radiofrequency ablation versus hepatic resection for small hepatocellular carcinoma: systematic review of randomized controlled trials with meta-analysis and trial sequential analysis*, Radiology, 2018, 287 (2), 461–472.
- [9] GLASSBERG M.B., GHOSH S., CLYMER J.W., WRIGHT G.W.J., FERKO N., AMARAL J.F., *Microwave ablation compared with hepatic resection for the treatment of hepatocellular carcinoma and liver metastases: A systematic review and meta-analysis*, World J. Surg. Oncol., 2019, 17 (1), 98.
- [10] REIG M., FORNER A., RIMOLA J., FERRER-FÀBREGA J., BURRELL M., GARCIA-CRIADO Á., KELLEY R.K., GALLE P.R., MAZZAFERRO V., SALEM R., SANGRO B., SINGAL A.G., VOGEL A., FUSTER J., AYUSO C., BRUIX J., *BCLC strategy for prognosis prediction and treatment recommendation: The 2022 update*, J. Hepatol., 2022, 76 (3), 681–683.
- [11] XU H., ZHANG Q., TAN Y.L., ZHANG Y., WEI J.Z., WANG L.L., XIE B., *Efficacy of microwave ablation and entecavir as a combination treatment for primary liver cancer and their effects on hepatitis B virus and liver function*, All Life, 2020, 13 (1), 524–531.
- [12] HUMPHREY S., NEWCOMER J.B., RAISSI D., GABRIEL G., *Percutaneous microwave ablation for early-stage intrahepatic cholangiocarcinoma: A single-institutional cohort*, J. Clin. Imaging Sci., 2024, 13, 4.
- [13] CURTO S., TAJ-ELDIN M., FAIRCHILD D., PRAKASH P., *Microwave ablation at 915 MHz vs 2.45 GHz: A theoretical and experimental investigation*, Med. Phys., 2015, 42 (11), 6152–6161.
- [14] KARAMPATZAKIS A., KÜHN S., TSANIDIS G., NEUFELD E., SAMARAS T., KUSTER N., *Antenna design and tissue parameters considerations for an improved modelling of microwave ablation in the liver*, Phys. Med. Biol., 2013, 58 (10), 3191–3206.
- [15] PRAKASH P., CONVERSE M.C., WEBSTER J.G., MAHVI D.M., *An optimal sliding choke antenna for hepatic microwave ablation*, IEEE Trans. Bio-Med. Eng., 2009, 56 (10), 2470–2476.
- [16] YANG D., BERTRAM J.M., CONVERSE M.C., O’ROURKE A.P., WEBSTER J.G., HAGNESS S.C., WILL J.A., MAHVI D.M., *A floating sleeve antenna yields localized hepatic microwave ablation*, IEEE Trans. Bio-Med. Eng., 2006, 53 (5), 533–537.
- [17] SUN Y.Y., CHENG Z.G., DONG L., ZHANG G.M., WANG Y., LIANG P., *Comparison of temperature curve and ablation zone between 915-and 2450 MHz cooled-shaft microwave antenna: Results in ex vivo porcine livers*, Eur. J. Radiol., 2012, 81 (3), 553–557.
- [18] GE M., JIANG H., HUANG X., ZHOU Y., ZHI D., ZHAO G., CHEN Y., WANG L., QIU B., *A multi-slot coaxial microwave antenna for liver tumor ablation*, Phys. Med. Biol., 2018, 63 (17), 175011.
- [19] WANG Q., YAN H., GUO M., MENG L., LONG Z., LONG Y., YANG H., *Three-dimensional finite element analysis of a novel interzygapophyseal fusion device for lower cervical spine*, Acta Bioeng. Biomech., 2022, 24 (2), 187–193.
- [20] LIU P., WAN J., LIU W., ZHAO Y., YAN S., JIANG W., LIU H., *Numerical analysis of the effects of canal wall-up and canal wall-down mastoidectomy on the sound transmission characteristics of human ears*, Acta of Bioengineering and Biomechanics, 2023, 25 (2), 132–145.
- [21] SU P., YANG Y., ZHANG L., HUANG L., *Biomechanical simulation of needle insertion into cornea based on distortion energy failure criterion*, Acta Bioeng. Biomech., 2016, 18 (1), 65–75.
- [22] SERVIN F., COLLINS J.A., HEISELMAN J.S., FREDERICK-DYER K.C., PLANZ V.B., GEEVARGHESE S.K., BROWN D.B., JARNAGIN W.R., MIGA M.I., *Simulation of Image-Guided Microwave Ablation Therapy Using a Digital Twin Computational Model*, IEEE Open Journal of Engineering in Medicine and Biology, 2024, 5, 107–124.
- [23] GORMAN J., TAN W., ABRAHAM J., *Numerical Simulation of Microwave Ablation in the Human Liver*, Processes, 2022, 10 (2), 361.
- [24] QIN Z., BALASUBRAMANIAN S.K., WOLKERS W.F., PEARCE J.A., BISCHOF J.C., *Correlated parameter fit of arrhenius model for thermal denaturation of proteins and cells*, Ann. Biomed. Eng., 2014, 42 (12), 2392–2404.
- [25] SHEU T.W., CHOU C.W., TSAI S.F., LIANG P.C., *Three-dimensional analysis for radio-frequency ablation of liver tumor with blood perfusion effect*, Computer Methods in Biomechanics and Biomedical Engineering, 2005, 8 (4), 229–240.
- [26] ORTEGA-PALACIOS R., TRUJILLO-ROMERO C.J., CEPEDA-RUBIO M.F.J., LEJA L., VERA HERNÁNDEZ A., *Heat Transfer Study in Breast Tumor Phantom during Microwave Ablation: Modeling and Experimental Results for Three Different Antennas*, Electronics, 2020, 9 (3), 535.

- [27] SELMI M., BIN DUKHYIL A.A., BELMABROUK H., *Numerical Analysis of Human Cancer Therapy Using Microwave Ablation*, Appl. Sci., 2020, 10 (1), 211.
- [28] TEHRANI M.H.H., SOLTANI M., KASHKOOLY F.M., RAAHEMIFAR K., *Use of microwave ablation for thermal treatment of solid tumors with different shapes and sizes – A computational approach*, PLoS ONE, 2020, 15 (6), e0233219.
- [29] RADMILOVIĆ-RADJENOVIĆ M., BOŠKOVIĆ N., SABO M., RADJENOVIĆ B., *An Analysis of Microwave Ablation Parameters for Treatment of Liver Tumors from the 3D-IRCAdB-01 Database*, Biomedicines, 2022, 10 (7), 1569.
- [30] 3D-IRCAdB database, <https://www.ircad.fr/research/3dircadb/> [Accessed: 25 January 2024].
- [31] BOŠKOVIĆ N., RADMILOVIĆ-RADJENOVIĆ M., RADJENOVIĆ B., *Finite Element Analysis of Microwave Tumor Ablation Based on Open-Source Software Components*, Mathematics, 2023, 11 (12), 2654.
- [32] RADMILOVIĆ-RADJENOVIĆ M., RADJENOVIĆ D., RADJENOVIĆ B., *Finite element analysis of the effect of microwave ablation on the liver, lung, kidney, and bone malignant tissues*, Europhys. Lett., 2021, 136, 1363500.
- [33] MIASKOWSKI A., GAS P., *Numerical Estimation of SAR and Temperature Distributions inside Differently Shaped Female Breast Tumors during Radio-Frequency Ablation*, Materials, 2023, 16 (1), 223.
- [34] MERCADO MONTOYA M., GOMEZ BUSTAMANTE T., BERJANO E., MICKELSEN S.R., DANIELS J.D., HERNANDEZ ARANGO P., SCHIEBER J., KULSTAD E., *Proactive esophageal cooling protects against thermal insults during high-power short-duration radiofrequency cardiac ablation*, International Journal of Hyperthermia, 2022, 39 (1), 1202–1212.

Dual-Antenna Microwave Ablation of Liver Tumor from the 3D-IRCAdB-01 Database

Nikola Bošković, Branislav Radjenović, Marija Radmilović-Radjenović*

Institute of Physics, University of Belgrade, Belgrade, Serbia

Abstract

Microwave ablation (MWA) is a minimally invasive energy-based thermal ablative technique designed to destroy tumor cells using microwave energy. Each tumor indeed has unique characteristics, including size, shape, and location, which significantly influence treatment options. The primary goal is to eliminate malignant cells while preserving as much surrounding healthy tissue as possible. The tissue damage depends on the input power, procedure duration, and the spatial position of the radiator. Thus, it is crucial to determine optimal parameters for maximizing efficacy while minimizing side effects. The ability to adjust the placement and power output of each antenna can lead to more precise treatment, enabling clinicians to tailor the procedure to the specific tumor characteristics. Recent advancements in numerical modeling have enhanced the understanding of ablation procedures. These models simulate the effects of microwave energy on biological tissue, leading to improved procedural efficiency. This study focuses on the destruction of a real large-elongated tumor with maximum dimensions of 56.8 mm × 27.6 mm × 22.4 mm. The investigation employs two identically parallel-positioned probes equipped with multi-slot coaxial antennas. The dual-antenna configuration allows for a more concentrated energy delivery to the tumor, enhancing the effectiveness of the ablation process. The simulation model includes the geometry of the tumor, antenna configuration design, and characteristics of both tumoral and healthy tissues. The findings indicate that utilizing a dual-antenna setup with a power output of 16 W per antenna effectively ablates tumors of interest while sparing healthy tissue. (International Journal of Biomedicine. 2024;14(4):583-586.)

Keywords: computational physics • microwave ablation • necrotic tissue • open-source software

For citation: Bošković N, Radjenović B, Radmilović-Radjenović M. Dual-Antenna Microwave Ablation of Liver Tumor from the 3D-IRCAdB-01 Database. International Journal of Biomedicine. 2024;14(4):583-586. doi:10.21103/Article14(4)_OA7

Introduction

Hepatocellular carcinoma (HCC) is a primary hepatic cancer ranking among the top causes of cancer-related mortality worldwide.¹⁻³ The appropriate treatment options can significantly enhance survival outcomes,^{4,5} but surgical options can pose significant risks, particularly concerning major blood loss, especially in surgeries involving larger tumors or those located in challenging anatomical positions. These risks are amplified in elderly patients, who may have comorbidities that complicate surgical intervention.⁶ MWA is a minimally invasive technique that effectively treats various cancers, including HCC, by utilizing microwave radiation to generate hyperthermia, leading to the destruction of cancer cells.^{7,8}

MWA is indeed a promising technique for treating tumors, particularly HCC. It is less invasive than traditional surgical methods, allowing quicker recovery times and reducing the risk of complications. MWA uses a thin needle to transmit microwaves into tumors to destroy cancer cells with heat. By carefully controlling the placement of the antenna, the input power, and the duration of treatment, clinicians can enhance the efficacy of MWA while minimizing risks to surrounding healthy tissues. Cell death is immediate when temperatures exceed 60°C, and prolonged exposure to temperatures exceeding 42°C permanently damages cell function. Assessing the distribution of heating damage caused by temperatures between 42°C and 60°C is the most challenging task in MWA because it is a function of time and highly depends on tissue type and blood vessel distribution.

In addition to clinical studies, computational models have emerged as important for predicting MWA outcomes.^{9,10} For example, the design of antennas for MWA relies heavily on computer models, which offer a quick, convenient, and accurate

*Corresponding author: Dr. Marija Radmilović-Radjenović, Institute of Physics, University of Belgrade, Belgrade, Pregrevica 118, Belgrade 11080, Serbia. E-mail: marija@ipb.ac.rs

method of estimating antenna performance. A numerical model of the antenna-tissue system plays an important role in providing vital information on the thermal behavior of the tissue during MWA.¹¹

It has been found that two-antenna configurations are less invasive than single-antenna configurations. Ablation zones created using two antennas are smaller, resulting in less damage to the healthy tissue than zones created using a single antenna. Two-antenna configurations produce more uniform thermal profiles and higher peripheral tissue temperatures.^{12,13}

To emphasize the importance of determining optimal conditions for each patient individually, we used the developed and tested simulation software SimSurgery open-source software components.¹⁴ Simulations were performed for a real large liver tumor from a database¹⁵ using two identical 10-slot coaxial antennas operating at 2.45 GHz. It is crucial to evaluate tissue damage during MWA, as it significantly impacts treatment outcomes. Understanding the correlation between temperature, exposure time, and tissue properties is vital for optimizing MWA.¹⁶ As temperature increases, tissue properties change, influencing how microwaves interact with the tissue. The water content in tissue affects both thermal and dielectric properties. Higher water content enhances the tissue’s ability to absorb microwave energy, leading to more effective heating. Blood flow acts as a cooler and strongly influences the temperature distribution, especially near large blood vessels. Tissue ablation reduces blood flow, altering temperature distribution and, consequently, the material properties of the tissue.

Methodology

The equations governing the calculation of the electric-field distribution through the tissue and the heat generated by the electromagnetic field during the MWA procedure have been described in detail in previous publications.^{9,13,14} The change in temperature over time can be calculated using Pennes’ bio-heat equation, where electromagnetic radiation is an external heat source. As the first step in modeling, it is necessary to determine the optimal number and position of antennas, depending on the tumor shape. A single antenna in the MWA is recommended for treating tumors up to 3 cm in diameter, whereas multiple antenna designs are more useful for larger tumors. Figure 1 shows a 3D simulation model of the tumor (56.8 mm × 27.6 mm × 22.4 mm) (red solid surface), which belonged to a 54-year-old male,¹⁵ and its position in the liver (gray surface). The liver is typically much larger than the tumor and antenna setup. The center of the tumor was located between the antennas and in the zone of maximum radiation. Both antennas contributed to the formation of ablation zones. Simulations were performed using the developed and optimized software package SimSurgery.¹⁴ In the simulation model, both the specific heat capacity and thermal conductivity were significantly larger in tumor tissue, whereas the blood perfusion rate was a linear function of temperature up to 60°C, when coagulation occurred and blood flow stopped. The relative permittivity and electric conductivity directly affect the electric-field distribution.¹⁴ Parameters describing tumoral tissues, healthy tissues, and blood are listed in Table 1.

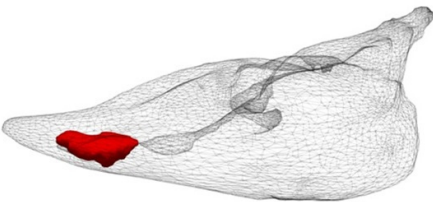


Fig. 1. Schematic view: 3D model of the liver (gray surface) and tumor with dimensions 56.8 mm × 27.6 mm × 22.4 mm (red solid surface) taken from a database.¹⁵

Table 1.
The thermophysiological parameters used in this study.

Parameter	Tissue		
	Liver	Tumor	Blood
Density [kg/m³]	1079	1040	1060
Specific heat [J/kg·°C]	3540	3960	3600
Thermal conductivity [W/m·°C]	0.52	0.57	0.5

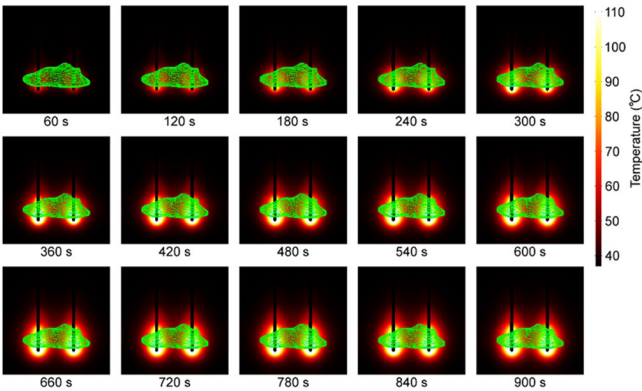


Fig. 2. Temporal temperature evolution (in °C) during two 10-slot antennas microwave ablation. The separation is 30 mm, while the input power is 16 W per antenna. The green triangular surface represents the tumor.¹⁵

The absorbed energy is transformed into thermal energy, leading to an increase in the tissue temperature. Figure 2 shows the temperature evolution during MWA using two 10-slot antennas separated by 30 mm with an initial power of 16 W. With the multi-slot antenna structure, a more localized near-spherical heating distribution can be achieved. The temperature rises as the ablation time reaches a maximal value at approximately 600 s. After 600 s of MWA, a large part of the tumor remained in the zone at 60°C, and the entire tumor was inside the zone at 50°C or higher. On the other hand, after an ablation time of 900 s, most parts of the tumor were in the zone at a temperature of 60°C or higher.

Figure 3 illustrates the ablation of a tumor during 900 s of MWA using dual-antenna configurations. With increasing time, two highly spherical ablation zones from each antenna merge into a comet-like zone. The shape of the temperature

distribution followed the shape of the calculated distribution of the fraction of necrotic tissue. The center of the tumor is located between the antennas and in the zone of maximum radiation. During the 900 s ablation, the ablation zone expands very slowly and remains stable.

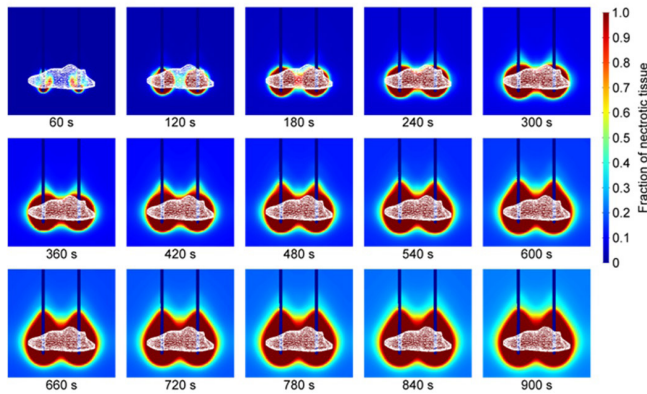


Fig. 3. Fraction of necrotic tissue during MWA using two 10-slot antennas with 30-mm separation and an input power of 16 W for 900 s. The white triangular surface corresponds to the tumor.¹⁵

Figure 4 shows the comparison of necrotic tissue fractions during MWA using different configurations of 10-slot antennas, revealing important insights into the effectiveness of treatment. When a single 10-slot antenna is used, the ablation zone is limited to the area directly surrounding that antenna. In contrast, employing two 10-slot antennas simultaneously leads to forming two connected ablation zones. The combined area of the ablation zones from the two antennas is slightly larger than the simple sum of the individual zones created by each antenna when operated separately. This indicates a synergistic effect when using multiple antennas, which can enhance the overall treatment efficacy.

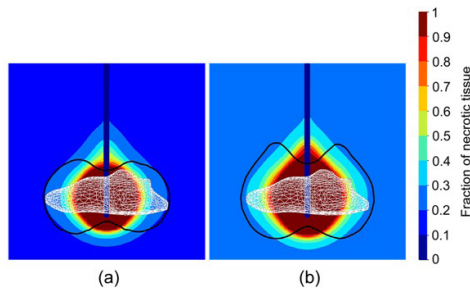


Fig. 4. Fraction of necrotic tissue during MWA using a single 10-slot antenna powered by 16 W after (a) 600 s and (b) 900 s. Black curves represent the shape of the ablation when a two 10-slot antenna (16 W per antenna) configuration is used. The tumor ¹⁵ is represented by the white surface.

The damage to the healthy tissue during MWA should be minimal compared with the reduction in tumor size. Volumetric damage (VD) is the ratio of the volume of damaged healthy tissue to tumor tissue¹²:

$$VD = \frac{V_{DAMAGED}}{V_{TUMOR}} \cdot 100\%$$

To quantify the amount of damaged healthy tissue (DT) during MWA, we can use the following formula¹²:

$$DT = \frac{V_{DAMAGED}}{V_{LIVER} - V_{TUMOR}} \cdot 100\%$$

The mean volume of the human liver is around 1750 cm³, whereas V_{TUMOR} was 13 cm³. Table 2 shows results for VD and DT after 600 s and 900 s of MWA. Both VD and DT increased with time. After 600 s, the VD and DT were 77.5% and 0.7%, respectively. After 900s, VD =143.7% and DT =1.3%.

Table 2.

VD and DT after 600 s and 900 s of dual-antenna MWA (3 cm separation and 16 W per antenna).

MWA	$V_{DAMAGED}$ (cm ³)	VD (%)	DT (%)
16 W after 600 s	12.4	77.5	0.7
16 W after 900 s	23	143.7	1.3

Discussion

This study focused on the effect of the dual-antenna MWA on the liver tumor (56.8 mm × 27.6 mm × 22.4 mm) (taken from a database¹⁵). All simulations were performed using the developed and tested software SimSurgery¹⁴ for two identical parallel-positioned probes with 10-slot coaxial antennas separated by 3 cm and powered by 16 W for each antenna. The temperature distribution, necrotic tissue fraction, and estimated amount of damaged healthy tissue during MWA are presented and analyzed. The fastest temperature rise occurs near the radiating slots. Due to the combined radiation, the area between the probes can reach a much higher temperature than that achieved with a single probe. The conclusion is that by using lower power and longer duration of the MWA, it is possible to target the same tumors, but with a much smaller risk of unnecessary damage and more predictable ablation zones. The obtained simulation results indicate that the ablation zones at 16 W per antenna are sufficient for complete tumor necrosis encompassing a small amount of healthy tissue. The results presented here align with those presented in a study by Gorman et al.¹⁸ Based on our study, we may conclude that the dual-antenna technique represents a promising advancement in tumor ablation therapies, highlighting the importance of innovation in medical technology for improving patient care. The ability to create a larger and more effective ablation zone is significant for ensuring comprehensive treatment of tumors, potentially improving patient outcomes. Understanding these dynamics is crucial for optimizing configurations in MWA clinical applications.

Sources of Funding

The authors acknowledge that this research was supported by the Science Fund of the Republic of Serbia (GRANT No. 7739583, SimSurgery).

Conflicts of Interest

The authors declare no conflict of interest.

References

- Villanueva A. Hepatocellular Carcinoma. *N Engl J Med*. 2019 Apr 11;380(15):1450-1462. doi: 10.1056/NEJMr1713263. PMID: 30970190.
- Arnold M, Abnet CC, Neale RE, Vignat J, Giovannucci EL, McGlynn KA, Bray F. Global Burden of 5 Major Types of Gastrointestinal Cancer. *Gastroenterology*. 2020 Jul;159(1):335-349.e15. doi: 10.1053/j.gastro.2020.02.068. Epub 2020 Apr 2. PMID: 32247694; PMCID: PMC8630546.
- Llovet JM, Kelley RK, Villanueva A, Singal AG, Pikarsky E, Roayaie S, Lencioni R, Koike K, Zucman-Rossi J, Finn RS. Hepatocellular carcinoma. *Nat Rev Dis Primers*. 2021 Jan 21;7(1):6. doi: 10.1038/s41572-020-00240-3. Erratum in: *Nat Rev Dis Primers*. 2024 Feb 12;10(1):10. doi: 10.1038/s41572-024-00500-6. PMID: 33479224.
- Itoh S, Ikeda Y, Kawanaka H, Okuyama T, Kawasaki K, Eguchi D, Korenaga D, Takenaka K. Efficacy of surgical microwave therapy in patients with unresectable hepatocellular carcinoma. *Ann Surg Oncol*. 2011 Dec;18(13):3650-6. doi: 10.1245/s10434-011-1831-z. Epub 2011 Jun 15. PMID: 21674268.
- Pucci C, Martinelli C, Ciofani G. Innovative approaches for cancer treatment: current perspectives and new challenges. *Ecancermedicalscience*. 2019;13:961. doi: 10.3332/ecancer.2019.961. PMID: 31537986; PMCID: PMC6753017.
- Phan K, An VV, Ha H, Phan S, Lam V, Pleass H. Hepatic resection for malignant liver tumours in the elderly: a systematic review and meta-analysis. *ANZ J Surg*. 2015 Nov;85(11):815-22. doi: 10.1111/ans.13211. Epub 2015 Jun 15. PMID: 26073054.
- Tan W, Deng Q, Lin S, Wang Y, Xu G. Comparison of microwave ablation and radiofrequency ablation for hepatocellular carcinoma: a systematic review and meta-analysis. *Int J Hyperthermia*. 2019;36(1):264-272. doi: 10.1080/02656736.2018.1562571. Epub 2019 Jan 24. PMID: 30676100.
- Facciorusso A, Abd El Aziz MA, Tartaglia N, Ramai D, Mohan BP, Cotsoglou C, Pusceddu S, Giacomelli L, Ambrosi A, Sacco R. Microwave Ablation Versus Radiofrequency Ablation for Treatment of Hepatocellular Carcinoma: A Meta-Analysis of Randomized Controlled Trials. *Cancers (Basel)*. 2020 Dec 16;12(12):3796. doi: 10.3390/cancers12123796. PMID: 33339274; PMCID: PMC7766963.
- Bošković N, Radjenović B, Radmilović-Radjenović M. Optimal parameters for the efficient microwave ablation of liver tumor from the 3D-IRCAdB-01 database. *Acta Bioeng Biomech*. 2024 Apr 22;26(1):47-54. doi: 10.37190/abb-02406-2024-04. PMID: 39219087.
- Tehrani MHH, Soltani M, Kashkooli FM, Raahemifar K. Use of microwave ablation for thermal treatment of solid tumors with different shapes and sizes-A computational approach. *PLoS One*. 2020 Jun 15;15(6):e0233219. doi: 10.1371/journal.pone.0233219. PMID: 32542034; PMCID: PMC7295236.
- Wang J, Huang S, Gao H, Liu J, Zhang Y, Wu S. Computer Simulations of Dual-Antenna Microwave Ablation and Comparison to Experimental Measurements. *Applied Sciences*. 2023;13(1):26. doi: 10.3390/app13010026
- Ge M, Jiang H, Huang X, Zhou Y, Zhi D, Zhao G, Chen Y, Wang L, Qiu B. A multi-slot coaxial microwave antenna for liver tumor ablation. *Phys Med Biol*. 2018 Sep 6;63(17):175011. doi: 10.1088/1361-6560/aad9c5. PMID: 30102247.
- Bošković N, Radjenović B, Nikolić S, Radmilović-Radjenović M. Effectiveness of microwave ablation using two simultaneous antennas for liver malignancy treatment. *Open Physics*. 2024;22(1):20240079. doi: 10.1515/phys-2024-0079
- Bošković N, Radmilović-Radjenović M, Radjenović B. Finite Element Analysis of Microwave Tumor Ablation Based on Open-Source Software Components. *Mathematics*. 2023;11(12):2654. doi: 10.3390/math11122654
- 3D-IRCAdB. Available online: <https://www.ircad.fr/research/3dircadb/>
- Harari CM, Magagna M, Bedoya M, Lee FT Jr, Lubner MG, Hinshaw JL, Ziembiewicz T, Brace CL. Microwave Ablation: Comparison of Simultaneous and Sequential Activation of Multiple Antennas in Liver Model Systems. *Radiology*. 2016 Jan;278(1):95-103. doi: 10.1148/radiol.2015142151. Epub 2015 Jul 2. PMID: 26133361; PMCID: PMC4699493.
- LeBrun A, Ma R, Zhu L. MicroCT image based simulation to design heating protocols in magnetic nanoparticle hyperthermia for cancer treatment. *J Therm Biol*. 2016 Dec;62(Pt B):129-137. doi: 10.1016/j.jtherbio.2016.06.025. Epub 2016 Jul 7. PMID: 27888926.
- Gorman J, Tan W, Abraham J. Numerical Simulation of Microwave Ablation in the Human Liver. *Processes*. 2022;10(2):361. doi: 10.3390/pr10020361.

Determination of the Optimal Parameters for Microwave Ablation of Liver Tumor

Nikola Bošković, Branislav Radjenović, Marija Radmilović-Radjenović*

Institute of Physics, University of Belgrade, Belgrade, Serbia

Abstract

Microwave ablation is a minimally invasive cancer treatment with high survival and low recurrence rates. Despite the unquestionable benefits of microwave ablation, the interaction between the medical tool and the tissue may cause damage to the surrounding tissue, which can be removed by clarifying the conditions for their development. In addition to clinical methods, computer simulation has proven to be a very effective tool to optimize microwave ablation performance. This study aimed to determine the optimal input power for complete microwave tumor ablation with an adequate safety margin while avoiding injury to surrounding healthy tissue. The liver tumor model was based on a real tumor labeled 1.02 in the 3D-IRCAdB-01 database. Calculations were performed for a 10-slot microwave antenna with a frequency of 2.45 GHz using COMSOL Multiphysics. The obtained simulation results revealed that with proper input power, the necrotic tissue was mainly located in the tumor with minimal damage to the surrounding healthy tissue. This study may represent a step forward in planning individual microwave ablation procedures for each patient. (International Journal of Biomedicine. 2024;14(2):291-294.)

Keywords: liver tumor • microwave ablation • ablation zone • necrotic tissue

For citation: Bošković N, Radjenović B, Radmilović-Radjenović M. Determination of the Optimal Parameters for Microwave Ablation of Liver Tumor. International Journal of Biomedicine. 2024;14(2):291-294. doi:10.21103/Article14(2)_OA9

Introduction

Liver cancer is not only one of the most common cancers in the world, but it is also the fastest-growing cause of cancer-related death.⁽¹⁻⁴⁾ Microwave ablation (MWA) at 2.45 GHz is considered as a minimally invasive procedure with a higher overall survival rate than external beam radiation therapy and proton beam therapy.^(5,6) Furthermore, MWA is highly recommended as a rapid treatment with a short recovery time for COVID-19 patients with liver tumors.⁽⁷⁾ Although the success rate of eliminating small liver tumors by MWA is higher than 85% for large tumors, the completion rates slightly decrease.^(8,9)

The mechanism underlying MWA is associated with an increase in temperature above the normal physiological threshold to kill cancer cells with minimal damage to surrounding tissue.⁽¹⁰⁾ A microwave antenna radiates a rapidly oscillating electromagnetic field that causes frictional heating of water molecules in the soft tissues around the field source.⁽¹¹⁾ The production of reliable near-spherical ablation zones depends on the antenna design. Recently, a compact multi-slot coaxial antenna was built to achieve an optimal

ablation shape and proper impedance matching to the target tumor without damaging the surrounding healthy tissues.⁽¹²⁾ Besides clinical studies, the role of computational models in predicting microwave ablation outcomes has significantly increased.^(13,14)

In this study, simulations were performed using a full three-dimensional (3D) MWA model,⁽¹⁵⁾ which was developed and tested using the COMSOL Multiphysics platform.⁽¹⁶⁾ A realistic tumor model based on a 3D CT scan of the tumor labeled as 1.02 in the 3D-IRCAdB-01 liver tumors database (3D-IRCAdB)⁽¹⁷⁾ was given special emphasis. The main goal of this study was to determine the optimal input power to ensure complete tumor 1.02 (3D-IRCAdB) ablation with minimal damage to the surrounding healthy tissue. Estimating the optimal power will ensure the best ratio of necrotic tissue to healthy tissue.

Methodology

To simulate microwave tissue ablation,⁽¹⁸⁾ the model must contain three fundamental components. The antenna probe model contains a microwave field production in the

tissue. In the heat transfer equation, the second component describes the microwave field and blood perfusion as sources of heat and heat sinks, respectively. The third component deals with the effect of the heat on the destruction of the tumor cells. All components of the MWA model are affected by various material parameters that depend on tissue characteristics. Modeling MWA as a multiphysics problem involves modeling multiple physical phenomena, such as electromagnetic wave propagation, heat transfer, and tissue damage, that occur during the procedure.⁽¹⁸⁾ Equations governing the calculations of the electric field distribution through the tissue and the heat generated by the electromagnetic field during MWA^(18,19) have been described in previous publications.

In contrast to the frequently used spherical tumor geometry, which is artificial, our simulation model is based on a real tumor labeled as 1.02, which belongs to a female in the database 3D-IRCADb-01, which contains several sets of CT scans of patients (3D-IRCADb).⁽¹⁷⁾ This tumor is relatively large (2.80 cm × 2.34 cm × 2.30 cm) and has an irregular shape, as shown in Figure 1.

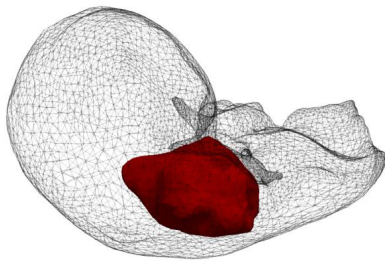


Fig. 1. Schematic view of the liver (triangulated surface) with tumor 1.02 taken from the database (3D-IRCADb)⁽¹⁷⁾ (solid surface).

To determine the optimal input power, numerical simulations were performed for tumor 1.02 from the database (3D-IRCADb)⁽¹⁷⁾ exposed to a frequency of 2.45 GHz and an input power in the range of 25–45 W. The parameters of the biological materials used in the numerical simulations were obtained from the literature.^(10,19)

Results

Figure 2 shows the isocontours representing the tumor (triangulated surface) and surrounding healthy tissue (solid light brown surface). The optimal value of the input power corresponded to total tumor ablation with minimal damage to healthy tissues. An input power of 25 W did not ensure complete ablation of the tumor backside. When 35 W was applied, the ablation zone covered the entire tumor, but there was significant damage to healthy tissue. When the whole tumor was destroyed, the isocontours that best fit the necrotic tissue were achieved for an input power of 30 W, while healthy tissue was preserved.

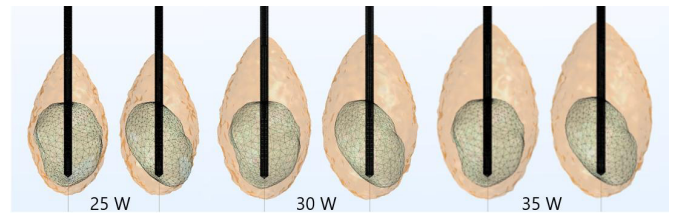


Fig. 2. Isocontours composed of the totally ablated region (solid surface) after 600 s of MWA of tumor 1.02 (3D-IRCADb)⁽¹⁷⁾ (triangulated surface) for input power of 25, 30, and 35 W).

Figure 3 shows the significance of the proper choice of the input power and ablation time. The ablation time was shortened from 600 to 560, 540, or 520 s when a power of 35, 40, or 45 W was applied, respectively. However, even though the ablation time was shorter, the healthy surrounding tissues were heavily damaged compared with those treated with 30 W for 600 s. These results indicate that the most efficient and safest MWA procedure is not always related to higher input power and shorter ablation time. Due to the dimensions of the tumor and its irregular shape, the formed ablation zones were elongated with a greater length along the shaft of the antenna than the transverse diameter. Elongated shapes are undesirable ablation patterns that cause damage to healthy tissues even if the ablation time is shorter.

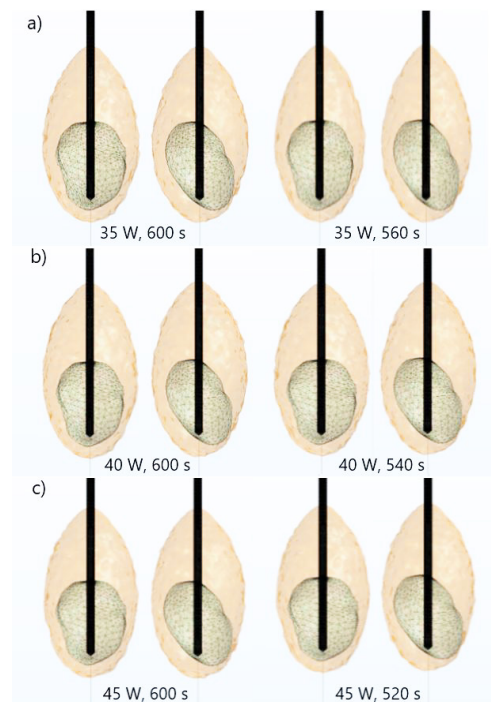


Fig. 3. Totally ablated regions (solid surface) around liver tumor 1.02 (3D-IRCADb)⁽¹⁷⁾ (triangulated surface) for MWA with an input power of a) 35 W, b) 40 W, and c) 45 W during various ablation times.

Figure 4a shows the isocontours calculated for the optimal power of 30 W at temperatures of 40°C, 60°C, 70°C, 80°C, and 90°C.

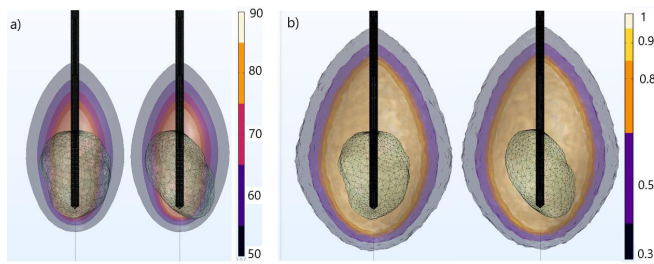


Fig. 4. Isocontours of a) temperature (50 oC, 60 oC, 70 oC, 80 oC, and 90 oC) and b) fraction of damage (0.3, 0.5, 0.8, 0.9, and 1) corresponding to the front (left) and back (right) sides of the liver tumor 1.02⁽¹⁷⁾ (triangulated surface).

The absorbed energy is converted into thermal energy, leading to an increase in tissue temperature. Close to the antenna, where the heat source is strong, the temperature is higher. The temperature increases with the ablation time, reaching a maximum inside the tumor region, where all cancer cells are killed. The temperature decreased as the distance from the antenna decreased, where the heat source weakened. Blood perfusion limits the extent of the heated area. Figure 4b illustrates isocontours related to damage fractions of 0.6, 0.7, 0.8, 0.9, and 1 for an optimal input power of 30 W. The ablation zones were elongated because of the size and irregular shape of the tumor (1.02 3D-IRCAdB).⁽¹⁷⁾ The active and passive heating zones can be distinguished. An active heating zone emerges within the tissue closest to the device, with high energy intensity and rapid absorption by tissue. On the other hand, the passive zone appears outside the active zone, far from the antenna.

Discussion

The study aimed to determine the optimal input power for efficient and safe microwave liver tumor ablation. For this purpose, full three-dimensional simulations within COMSOL Multiphysics, a finite element method-based platform, were applied.⁽¹⁶⁾ Calculations were performed for a model of a real liver tumor labeled as 1.02 in the database 3D-IRCAdB-01 (3D-IRCAdB)⁽¹⁷⁾ exposed to radiation from a 10-slot antenna operating at a frequency of 2.45 GHz. The optimal value of the input power of 30 W was estimated so that the whole tumor could be completely treated with minimal damage to the healthy tissue. The difference between ablation times when the input power was 35, 40, and 45 W, compared with that at 30 W, was approximately 7%, 10%, and 13%, respectively. Ablation time decreased with increasing input power. However, higher input power values may result in undesirable ablation zone shapes, leading to significant damage to healthy tissue. Regardless of the input power, the maximum temperature values were reached inside the tumor regions, where all cancer cells were destroyed. The fraction of damage increased as the ablation time increased. Although a multi-slot coaxial antenna produces a more localized heating pattern for spherical tumors, for realistic tumor shapes, the ablation zones are usually elongated.

Determining the optimal ratio of necrotic tissue to healthy tissue is important for improving the microwave ablation procedure to destroy the maximal part of the tumor while conserving the healthy tissue. It was confirmed that two-dimensional models are not sufficient and that full three-dimensional simulations are necessary for predicting the optimal conditions for microwave ablation, which may be incorporated into medical procedure planning.

Sources of Funding

The authors acknowledge that this research was supported by the Science Fund of the Republic of Serbia (GRANT No. 7739583, SimSurgery).

Conflicts of interest

The authors declare no conflict of interest.

References

1. Watson J, Hydon K, Lodge P. Primary and secondary liver tumours. *InnovAiT* 2016; 9(8):477-82. doi: 10.1177/1755738016653419
2. Sia D, Villanueva A, Friedman SL, Llovet JM. Liver Cancer Cell of Origin, Molecular Class, and Effects on Patient Prognosis. *Gastroenterology*. 2017 Mar;152(4):745-761. doi: 10.1053/j.gastro.2016.11.048. Epub 2016 Dec 30. PMID: 28043904.
3. Chen JG, Zhu J, Zhang YH, Chen YS, Lu JH, Zhu YR, Chen HZ, Shen AG, Wang GR, Groopman JD, Kensler TW. Liver cancer mortality over six decades in an epidemic area: what we have learned. *PeerJ*. 2021 Feb 3;9:e10600. doi: 10.7717/peerj.10600. PMID: 33604165; PMCID: PMC7866902.
4. Linn YL, Chee MY, Koh YX, Teo JY, Cheow PC, Chow PKH, Chan CY, Chung AYY, Ooi LLPJ, Goh BKP. Actual 10-year survivors and 10-year recurrence free survivors after primary liver resection for hepatocellular carcinoma in the 21st century: A single institution contemporary experience. *J Surg Oncol*. 2021 Jan;123(1):214-221. doi: 10.1002/jso.26259. Epub 2020 Oct 23. PMID: 33095920.
5. Villard C, Soler L, Gangi A. Radiofrequency ablation of hepatic tumors: simulation, planning, and contribution of virtual reality and haptics. *Comput Methods Biomech Biomed Engin*. 2005 Aug;8(4):215-27. doi: 10.1080/10255840500289988. PMID: 16298844.
6. Facciorusso A, Di Maso M, Muscatiello N. Microwave ablation versus radiofrequency ablation for the treatment of hepatocellular carcinoma: A systematic review and meta-analysis. *Int J Hyperthermia*. 2016 May;32(3):339-44. doi: 10.3109/02656736.2015.1127434. Epub 2016 Jan 21. PMID: 26794414.
7. Afaghi P, Lapolla MA, Ghandi K. Percutaneous microwave ablation applications for liver tumors: recommendations for

*Corresponding author: Prof. Marija Radmilović-Radjenović, Institute of Physics, University of Belgrade, Belgrade, Pregrevica 118, Serbia. E-mail: marija@ipb.ac.rs

- COVID-19 patients. *Heliyon*. 2021 Mar 6;7(3):e06454. doi: 10.1016/j.heliyon.2021.e06454. PMID: 33748501; PMCID: PMC7966996.
8. Gartshore A, Kidd M, Joshi LT. Applications of Microwave Energy in Medicine. *Biosensors (Basel)*. 2021 Mar 26;11(4):96. doi: 10.3390/bios11040096. PMID: 33810335; PMCID: PMC8065940.
 9. Itoh S, Ikeda Y, Kawanaka H, Okuyama T, Kawasaki K, Eguchi D, Korenaga D, Takenaka K. Efficacy of surgical microwave therapy in patients with unresectable hepatocellular carcinoma. *Ann Surg Oncol*. 2011 Dec;18(13):3650-6. doi: 10.1245/s10434-011-1831-z. Epub 2011 Jun 15. PMID: 21674268.
 10. Tehrani MHH, Soltani M, Kashkooli FM, Raahemifar K. Use of microwave ablation for thermal treatment of solid tumors with different shapes and sizes-A computational approach. *PLoS One*. 2020 Jun 15;15(6):e0233219. doi: 10.1371/journal.pone.0233219. PMID: 32542034; PMCID: PMC7295236.
 11. Karampatzakis A, Kühn S, Tsanidis G, Neufeld E, Samaras T, Kuster N. Antenna design and tissue parameters considerations for an improved modelling of microwave ablation in the liver. *Phys Med Biol*. 2013 May 21;58(10):3191-206. doi: 10.1088/0031-9155/58/10/3191. Epub 2013 Apr 19. PMID: 23603829.
 12. Ge M, Jiang H, Huang X, Zhou Y, Zhi D, Zhao G, Chen Y, Wang L, Qiu B. A multi-slot coaxial microwave antenna for liver tumor ablation. *Phys Med Biol*. 2018 Sep 6;63(17):175011. doi: 10.1088/1361-6560/aad9c5. PMID: 30102247.
 13. Racila M, Crolet JM. Numerical simulation of thermoablation in living tissues. *Computer Methods in Biomechanics and Biomedical Engineering* 2011;14(sup1): 279-80.
 14. Chiang J, Wang P, Brace CL. Computational modelling of microwave tumour ablations. *Int J Hyperthermia*. 2013 Jun;29(4):308-17. doi: 10.3109/02656736.2013.799295. PMID: 23738698; PMCID: PMC3768158.
 15. Radjenović B, Sabo M, Šoltes L, Prnova M, Čičak P, Radmilović-Radjenović M. On Efficacy of Microwave Ablation in the Thermal Treatment of an Early-Stage Hepatocellular Carcinoma. *Cancers (Basel)*. 2021 Nov 18;13(22):5784. doi: 10.3390/cancers13225784. PMID: 34830937; PMCID: PMC8616542.
 16. Heat Transfer Module 1986-2020. Burlington (MA): COMSOL, Inc. <https://www.comsol.com/heat-transfer-module>
 17. 3D-IRCADb. Available online: <https://www.ircad.fr/research/3dircadb/>
 18. Radmilović-Radjenović M, Bošković N, Sabo M, Radjenović B. An Analysis of Microwave Ablation Parameters for Treatment of Liver Tumors from the 3D-IRCADb-01 Database. *Biomedicines*. 2022 Jul 1;10(7):1569. doi: 10.3390/biomedicines10071569. PMID: 35884874; PMCID: PMC9312906.
 19. Bošković N, Radmilović-Radjenović M, Radjenović B. Finite Element Analysis of Microwave Tumor Ablation Based on Open-Source Software Components. *Mathematics*. 2023;11:2654.
-



**IX International School and Conference on Photonics
Belgrade, Serbia, August 28th – September 1st 2023**

Vinča Institute of Nuclear Sciences
Mike Petrovića Alasa 12-14, P.O.Box 522, 11351 Belgrade, Serbia
Phone: +381 11 3408 101; Fax: +381 11 8066 425
E-mail: photonica2023@ipb.ac.rs, www.photonica.ac.rs

Dr. Nikola Bošković
Institute of Physics Belgrade,
Belgrade, Serbia

Belgrade, May 22nd, 2023

Dear Dr. Bošković,

On behalf of the Organizing Committee of the International School and Conference on Photonics, we are pleased to invite you to the **PHOTONICA 2023** conference scheduled from **28th August** until **1st September 2023** in **Belgrade, Serbia**. This conference will be organized by the Vinča Institute of Nuclear Sciences, Belgrade, Serbia, the Optical Society of Serbia and the Serbian Academy of Sciences and Arts.

It is our special pleasure to invite you to attend the meeting and present a **progress report lecture (20 min)**. The lecture is expected to contain information about your recent research in your field of expertise, with a brief introduction to the field that would be appreciated by graduate students.

We would be honored if you could accept this invitation and accordingly send us the title of your lecture, to be included in the Conference Announcement. The abstract of the lecture, 1 page in length, should be emailed to us by the 15th of June 2023 to be published in the Book of Abstracts.

Kindly, as an invited speaker, the Organizers will cover your conference fee.

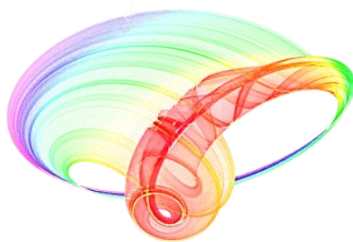
If you have any questions please do not hesitate to contact us.

Yours sincerely,

Dušan K. Božanić, Ph.D.
Chair of the Organizing Committee

cell: +381 64 1775986
e-mail: bozanic@vin.bg.ac.rs
photonica2023@ipb.ac.rs
website: <http://www.photonica.ac.rs/>

Book of abstracts



IX International School and Conference on Photonics

PHOTONICA2023

with joint events:

Understanding interaction light - biological surfaces: possibility for new electronic materials and devices

&

Biological and bioinspired structures for multispectral surveillance

&

Quantum sensing integration within microfluidic Lab-on-a Chips for biomedical applications

&

Advanced Biophysical Methods for Soil Targeted Fungi-Based Biocontrol Agents

August 28 - September 01, 2023, Belgrade, Serbia

Editors

Jelena Potočnik, Maja Popović, Dušan Božanić

Vinča Institute of Nuclear Sciences – National Institute of the Republic of Serbia, University of Belgrade

Belgrade, 2023

I.7	Polymeric SERS-fluidic platforms for the non-destructive optical analysis of liquid samples <i>C. Credi</i>	21
I.8	Rapid and sensitive cancer detection with fluorescence lifetime imaging microscopy <i>W. Su, M. Ji, J. Ma, R. Guo and L. Mi</i>	22
I.9	Photonic integrated circuits based on linearly coupled waveguide arrays <i>J. Petrovic</i>	23
I.10	Excursion of a biophysicist to the quantum world <i>A. Dér</i>	24
I.11	Light-enhanced transdermal drug delivery <i>R. Boukherroub</i>	25
I.12	Luminescent thermometry using lanthanide and transition metal-activated phosphors <i>Ž. Antić</i>	26
I.13	Black box certification of resources for photonic quantum technologies <i>S. Neves, L. dos Santos Martins, V. Yacoub, P. Lefevbre, I. Šupić, D. Markham and E. Diamanti</i>	27
I.14	Femtosecond laser direct writing of fiber optic microstructure devices <i>X. Shu</i>	28
I.15	Microscopic theory of transport and optics in superlattices and applications to metabolomics and novel device functionalities <i>M.F. Pereira, A. Apostolakis, H. Zafar, V. Vaks and V. Anfertev</i>	29
I.16	Blue and red diode pumped low-cost ultrafast lasers for biomedical applications <i>B. Resan</i>	30

Progress Reports

P.1	Broadband photonic quantum memory in atomic ensembles <i>K. Shinbrough, B.D. Hunt, S. Park, K. Oolman, T. Loveridge, J.G. Eden and V.O. Lorenz</i>	32
P.2	Measuring the dipolar interaction shift of the BEC critical temperature <i>M. Krstajić</i>	33
P.3	Crystal structure, optical properties and photo/electrocatalytic activity of nanostructured $\text{Zn}_{1-x}\text{Fe}_y\text{O}_{(1-x+1.5y)}$ <i>V. Rajić, S. Marković, M. Popović, M. Novaković, Lj. Veselinović, I. Stojković Simatović, S.D. Skapin, S. Stojadinović and V. Rac</i>	34
P.4	Synchrotron radiation photoemission spectroscopy study of the valence band electronic structure of Ag-Ag ₂ S Janus nanoparticles for the development of nanomotors propelled by NIR light <i>D. Danilović, D.K. Božanić, J. Pajović, G.A. Garcia, L. Nahon, T. Marić and V. Djoković</i>	35
P.5	Photosensitizer potential of doped and undoped nanostructured TiO ₂ <i>M. Matijević, L. Korićanac, Đ. Nakarada, J. Žakula, M. Stepić, M. Radoičić, M. Mojović, M. Petković and M.D. Nešić</i>	36
P.6	Application of laser-induced breakdown spectroscopy for the determination of trace metals in oils <i>M. Vinić</i>	37

P.7	Influence of thin oxide layer to photoacoustic signal of nano-mechanical structures <i>K.Lj. Đorđević, S.P. Galović, M.A. Dragaš, D.K. Markushev and D.D. Markushev</i>	38
P.8	Modeling microwave ablation for tumor treatment using open-source software components <i>N. Boskovic, M. Radmilovic-Radjenovic and B. Radjenovic</i>	39

Contributed Papers

1. Quantum optics and ultracold systems

QO.1	Exploiting the quantumness of coherent states: toward macroscopic quantum light <i>C. Hermann Avigliano</i>	42
QO.2	Anomalous diffusion and mixed dynamics in a classical Bose-Hubbard chain <i>D. Markovic and M. Cubrovic</i>	43
QO.3	Correlated photon pairs by Four Wave Mixing in alkali vapor for imaging application <i>M.M. Ćurčić, D. Arsenović and B. Jelenković</i>	44
QO.4	Transport of cold bosonic atoms in optical lattices <i>I. Vasić and J. Vučićević</i>	45
QO.5	Experimental and theoretical study of the phase response of M_x magnetometer to modulating transversal magnetic field <i>M.M. Ćurčić, A. Milenković, A. Bunjac, T. Scholtes and Z. Grujić</i>	46
QO.6	Spontaneous emission of three-level ladder-type atom coupled to one-dimensional rectangular waveguide <i>Lj. Stevanović and M. Perić</i>	47
QO.7	Quantized vortices in dipolar BECs when crossing the superfluid-supersolid phase transition <i>M. Sindik, A. Recati, S.M. Roccuzzo, L. Santos and S. Stringari</i>	48

2. Nonlinear optics

NO.1	Absorption coefficients and refractive index changes in a strongly prolate and strongly oblate ellipsoidal quantum dot <i>V. Pavlovic and Lj. Stevanovic</i>	50
NO.2	Impact of nonlinearity on the zero-mode lasing in optical lattices <i>M. Nedić, G. Gligorić, J. Petrovic and A. Maluckov</i>	51
NO.3	The modulation instability triggered band relaxation in photonic Chern insulator <i>A. Mančić, M. Nedić, D. Leykam and A. Maluckov</i>	52
NO.4	Coupled vortex generator in active multi-core fibers <i>P.P. Beliće, G. Gligorić and A. Maluckov</i>	53
NO.5	Electric-field induced SHG (EFISHG) in graphene? <i>J. Woeste, N. Stojanovic and M. Gensch</i>	54
NO.6	Rogue wave clusters of the nonlinear Schrödinger equation composed of Akhmediev breathers and Kuznetsov-Ma solitons <i>S.N. Nikolić, S. Alwashahi, N.B. Aleksić and M.R. Belić</i>	55

Modeling microwave ablation for tumor treatment using open-source software components

N. Boskovic, M. Radmilovic-Radjenovic and B. Radjenovic

Institute of Physics, Belgrade, Serbia

e-mail: nikolab@ipb.ac.rs

Microwave ablation (MWA) is a minimally invasive medical procedure with a short recovery time for treating various types of cancers. During MWA, a small needle-like probe is inserted inside the tumor. Inside the probe there is a microwave radiator (antenna) that delivers microwave energy, causing tissue heating, and effectively produces necrosis of the tumor tissue. The primary goal of modeling and studying of MWA is to determine ablation zone caused by the particular combination of radiator, input power, time and position of the probe. MWA should cause total necrosis of tumor tissue and minimal damage to surrounding healthy tissue. Simulation of MWA requires calculation of electromagnetic wave propagation, heat transfer, and tissue damage. Physical processes can be described using partial differential equations (PDEs). Multiple effects such as blood flow and change of water content inside the tissue with temperature have a major influence on the MWA.

In our study we have created the complete geometry of MWA including a multi-slot coaxial antenna [1], a real liver tumor taken from the database [2], and the surrounding liver tissue using Gmsh [3]. Geometry is meshed and PDEs are solved using Finite Elements Method (FEM) via GetDP package [4]. The MWA occurs at 2.45 GHz, with an input power of 13 W, during 600 s. The electric field is calculated in frequency domain, while temperature distribution and necrosis are calculated in the time domain using the custom fast fully explicit stable Euler scheme. We have calculated all quantities required in the MWA, including temperature and distribution of tissue necrosis over time, Fig. 1, with results comparable to Comsol [5].

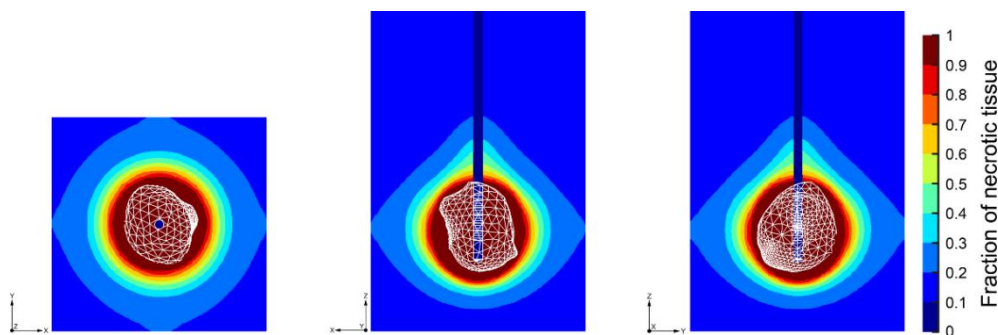


Figure 1. Fraction of necrotic tissue at different cross-sections at 600 s. The shape of the tumor is marked in white and is located in the zone of total tissue damage.

REFERENCES

- [1] M. Radmilović-Radjenović *et al.*, Bioengineering 9, 656 (2022).
- [2] M. Radmilović-Radjenović *et al.*, Biomedicines 10, 7 (2022).
- [3] Gmsh. Available online: <https://gmsh.info>.
- [4] GetDP. Available online: <https://getdp.info>.
- [5] Comsol Multiphysics. Available online: www.comsol.com.

Open-Source Software for Microwave Ablation Analysis

Nikola Bošković
Institute of Physics
University of Belgrade
Belgrade, Serbia
nikolab@ipb.ac.rs

Marija Radmilović-Radjenović
Institute of Physics
University of Belgrade
Belgrade, Serbia
marija@ipb.ac.rs

Branislav Radjenović
Institute of Physics
University of Belgrade
Belgrade, Serbia
bradjeno@ipb.ac.rs

Abstract—In this paper, we use a full 3D finite element method for microwave ablation simulation based on open-source software. A real large tumor taken from the database is used and two probes are used for treatment. The effects of using power control and changing the size and shape of the ablation with the same applied energy are shown.

Keywords—Finite element analysis, microwave ablation, open-source software.

I. INTRODUCTION

Microwave ablation (MWA) is an established tumor treatment procedure as a viable alternative to surgical resection [1], [2]. During the MWA procedure, a source of microwave radiation (antenna) is inserted into the tumor, interacting with microwave radiation heats the tissue typically above 60 °C when immediate tissue necrosis occurs. The MWA system usually operates at 2.4 GHz, and the most commonly used coaxial slot antennas are only a few millimeters in diameter [3], [4]. As MWA is performed via radiation, the coaxial antenna is usually placed in a dielectric probe, which isolates the antenna from the tissue. During MWA, the probes are typically navigated using an ultrasound imaging system, and temperature sensors can be placed at multiple points [5].

The MWA system can be configured based on specific requirements and adapted to tissue type, tumor size and location. The size of the ablation is a function of time, input power, antenna radiation characteristics, and spatial position. A shorter duration of procedure is recommended to maximize effectiveness and reduce complications, usually around 10 to 15 minutes, with input power generally below 100 W. Single probe MWA is generally recommended for smaller tumors up to 3 cm in diameter. Microwave radiation penetrates tissue well, so with high power and prolonged duration, the ablation will continue to increase, and eventually can cause organ failure and death.

The main issue in MWA is determining the exact parameters that will cause total tumor necrosis with safety margins, and minimal damage to the surrounding healthy tissue [6]. The ablation shape is preferably spherical with minimal damage to healthy tissue. Real tumors are often irregular in shape, and can be much larger than 3 cm in diameter. The use of a single probe for treatment of large tumors leads to excessive damage to healthy tissue [7]. Much better results and low invasiveness can be achieved by using lower power antenna arrays placed at optimal points in the tumor [8].

Numerical simulations can be used to evaluate ablation development under given conditions and to provide optimal parameters for MWA procedure [9]–[11]. MWA prediction requires a multiphysics approach: calculation of electromagnetic field propagation through tissue, tissue heating and estimation of necrosis as a function of time and temperature. Tissues represent a complex medium where during MWA tissue is heated by radiation, but heat is also transferred by conduction (between objects) and convection (with fluids). The liver is particularly rich with blood vessels, so the blood during MWA acts as a coolant, which greatly affects the process of MWA. The material parameters of tumor and healthy tissue are different, so the shape of the tumor will affect the development of ablation.

In this paper, we evaluate the optimal parameters of the MWA for a large real liver tumor of irregular shape taken from database [12], [13]. The numerical approach is described in more detail in [10]. The geometry and meshing are made using Gmsh [14]. The equations describing MWA are solved using the finite element method (FEM), with the general FEM solver GetDP [15]. We used two multi-slot antennas and investigate the effects of power control during MWA.

II. METHODOLOGY

The propagation of the radiation through the tissue can be described by the wave equation for the electric field, as in:

$$\nabla^2 \vec{E} - \mu_r k_0^2 \left(\epsilon_r - \frac{j\sigma}{\omega\epsilon_0} \right) \vec{E} = 0, \quad (1)$$

where \vec{E} , $\mu_r = 1$, $\omega = 2\pi f$, k_0 , ϵ_r , σ are the electric field vector, relative permeability, angular frequency, vacuum propagation constant, permittivity of the vacuum and electric conductivity, respectively. The bio-heat equation describes temperature transfer within tissues as:

$$\rho c \frac{\partial T}{\partial t} = \nabla \cdot (k \nabla T) + \rho_b \omega_b c_b (T_b - T) + \frac{\sigma |\vec{E}|^2}{2}, \quad (2)$$

where ρ , c , T , t , k are tissue density, specific heat capacity, temperature, time, thermal conductivity, and ρ_b , ω_b , c_b , $T_b = 37^\circ\text{C}$ are density, perfusion rate, specific heat capacity and arterial blood temperature, respectively. Since the liver has a very high water content of about 78%, which drastically changes to less than 20% when the tissue is heated to above 100 °C due to evaporation [16], specific heat capacity should be replaced with effective specific heat capacity c' as in (3) where $W(T)$ represents the change in water content with temperature.

This research was supported by the Science Fund of the Republic of Serbia, The Program IDEAS, GRANT No. 7739583, SimSurgery.

Thermal conductivity depends on temperature as in (4), where k_0 is tissue thermal conductivity measured at the base temperature T_0 and given in Table I.

$$c' = c - 2260 \frac{\partial W}{\partial T},$$

$$W(T) = \begin{cases} 0.778 \cdot \left(1 - e^{\frac{T-106}{3.42}}\right), & 70^\circ\text{C} \leq T \leq 100^\circ\text{C} \\ 7.053 - 0.064096 \cdot T, & 100^\circ\text{C} \leq T \leq 104^\circ\text{C} \\ 0.778 \cdot e^{\frac{T-80}{34.37}}, & T > 104^\circ\text{C} \end{cases} \quad (3)$$

$$k(T) = k_0 + 0.00161|T - T_0| \quad (4)$$

TABLE I. TISSUE PARAMETERS.

Parameter	Tissue		
	Liver	Tumor	Blood
k_0 (W/m°C)	0.52	0.57	0.5
c (J/kg/°C)	3540	3960	3600
ρ (kg/m³)	1079	1040	1060

Blood perfusion has an extremely large impact on the MWA because it acts as a coolant. This will continue until the blood coagulate at about 60 °C, and blood perfusion can be described as:

$$\omega_b = \begin{cases} 2.1 \times 10^{-5} T + 3.5 \times 10^{-3}, & T \leq 60^\circ\text{C} \\ 0, & T > 60^\circ\text{C} \end{cases} \quad (5)$$

ϵ_r , σ also depend on temperature as:

$$\epsilon_r = a_1 \cdot \left(1 - \frac{1}{1 + e^{(a_2 - a_3 T)}}\right) \quad (6)$$

$$\sigma = b_1 \cdot \left(1 - \frac{1}{1 + e^{(b_2 - b_3 T)}}\right) \quad (7)$$

TABLE II. COEFFICIENTS USED IN (6) AND (7).

Coefficient	Tissue	
	Liver	Tumor
a_1	44.3	54.8
a_2	5.223	5.223
a_3	0.0524	0.0524
b_1	1.69	2
b_2	6.583	6.583
b_3	0.0598	0.0598

The specific absorption rate (SAR) determines how much radiation is absorbed by the tissue and can be calculated as:

$$SAR = \frac{\sigma}{2\rho} |\vec{E}|^2. \quad (8)$$

The tissue temperature damage Ω can be estimated using the Arrhenius equation:

$$\frac{\partial \Omega}{\partial t} = A e^{\left(\frac{-\Delta E}{RT}\right)}, \quad (9)$$

where $A = 7.39 \times 10^{39}$ 1/s, $\Delta E = 2.577 \times 10^5$ J/mol, and $R = 8.314$ J/(K mol) are the frequency factor, the activation energy for the irreversible damage reaction and the universal gas constant, respectively. From Ω , we can calculate fraction of necrotic tissue θ_d as:

$$\theta_d = 1 - e^{-\Omega} \quad (10)$$

III. MODEL

In this paper, we use two identical coaxial probes with 10 slots [10] and a large asymmetric tumor taken from the database [12], [13]. The model is shown in Fig. 1.

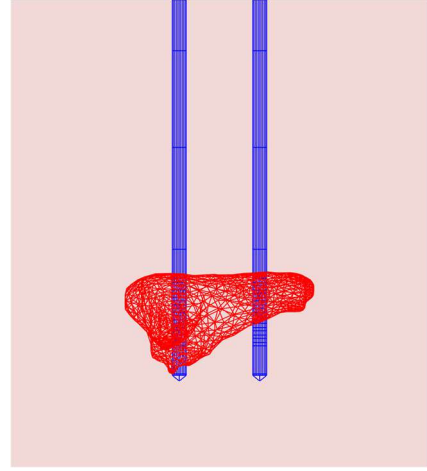


Fig. 1. Two probes (blue) and liver tumor (red) inside the computational domain (liver). The dimensions of the tumor are: 35.4 mm \times 24.7 \times 19.2 mm.

The tumor shown in Fig. 1 is very irregular and elongated. The 10-slot coaxial antenna creates highly spherical ablation zones with low input powers. With increasing power, the increase in ablation volume is mostly oriented towards the power source, so ablation is shaped like a comet tale, hence the treatment of the tumor in Fig. 1 with single probe would be highly invasive, with massive damage to healthy tissue.

In the MWA simulation, we have two types of processes: almost instantaneous propagation of electromagnetic waves and slow tissue heating. We solve (1) in the frequency domain and use the obtained electric field vector in (2), which should be solved in time domain. This is done using an Explicit Euler scheme with conditions implemented to ensure the stability of the scheme [10]. Since the material parameters change with temperature (time), the electric field needs to be calculated from (1) for each time step, so finding the optimal parameters for MWA by simulation of multiple combinations can be an extremely long process.

Using (8) and the material parameters for the initial $T = 37^\circ\text{C}$, we can get the initial SAR distribution. If the tumor is mostly covered by a high SAR, about 30dBW/kg and more, this would guarantee a very fast destruction of the tumor. In Fig. 2, we can see the initial SAR with a single probe for input power of 20 W, 30 W and 40 W.

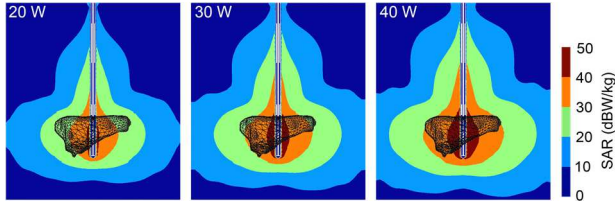


Fig. 2. SAR simulations with single probe and different input powers. The tumor is shown with black lines.

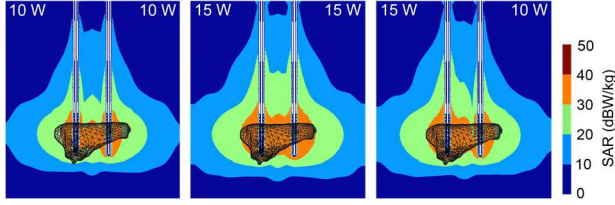


Fig. 3. SAR simulations with two probes and different input powers.

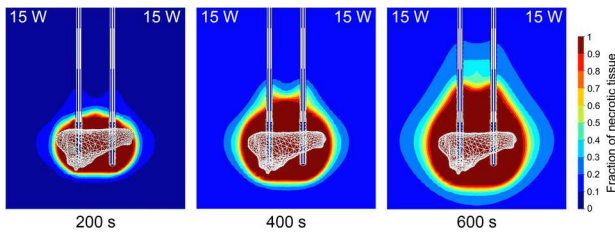


Fig. 4. Fraction of necrotic tissue with two probes with an input power of 15 W per probe during 600s. The tumor is shown with white lines.

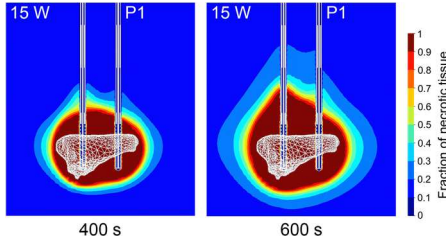


Fig. 5. Fraction of necrotic tissue with two probes with an input power of 15 W per probe, where probe P1 is turned off from 200 s to 400 s, during 600s. At 200 s results are the same as in Fig. 4.

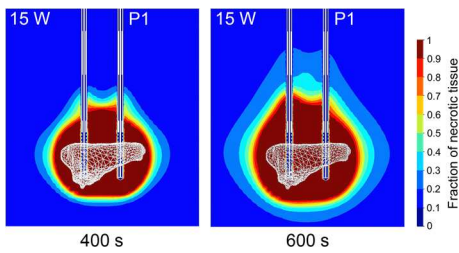


Fig. 6. Fraction of necrotic tissue with two probes with an input power of 15 W per probe, where probe P1 is turned off from 400 s to 600 s, during 600s. At 200 s results are the same as in Fig. 4.

The orange and red zones in Figs. 2-3 represent zones of very high radiation where tumor ablation would occur almost instantaneously, while zones with lower values would represent the likely development of ablation over time. As we can see with higher power and longer time the ablation would progress towards the power source further away from tumor, increasing unnecessary destruction of healthy tissue. In Fig. 2 for an input power of 20 W, large parts of the tumor are outside the orange zone.

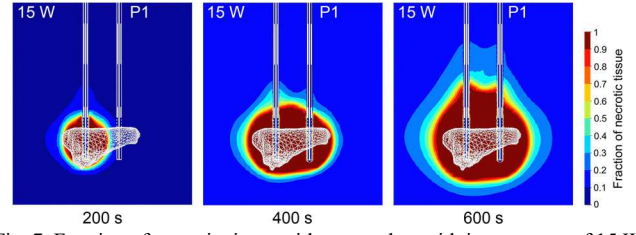


Fig. 7. Fraction of necrotic tissue with two probes with input power of 15 W per probe, where probe P1 is turned off from 0 s to 200 s, during 600s.

The orange zone grows around tumor for 30 W, and for 40 W tumor is completely inside the orange zone. From this it can be concluded that using a single 40 W probe would probably cause tumor destruction in a very short time, a slightly longer time would be required for the 30 W case, and a much longer time for the 20 W case.

In Fig. 3, we have the distribution of power using two probes, which enables better concentration of radiation in certain areas with lower power. In the first case with 10 W per probe, we have a smaller parts of the tumor outside the orange zone than in the case with the same total power with single probe. The green zones are more focused around the tumor and spread less towards the power source, signifying smaller invasiveness. For the case with 15 W per probe, we can see that a very small fraction of the tumor is outside the orange zone, suggesting that this configuration can give satisfactory results. Third case show what would happen if we have one probe with 15 W and the other with 10 W, where we have SAR as a combination of the previous cases.

In Fig. 4 we see the progression of the fraction of necrotic tissue during 600 s with an input power of 15 W per probe. We can see that ablation zone at 400 s is highly spherical around tumor, and spreads towards power source at 600 s. Size and ablation propagation is in agreement with the initial SAR results.

Using a different constant power per probe in multi-probe setup will generate asymmetric ablation zones, but varying the power during MWA and controlling the growth of ablation during MWA would be ideal. In Fig. 5 we have the same case as in Fig. 4 up to 200 s, when probe P1 is turned off until 400 s, and we can see that asymmetric shape of ablation is created with less invasiveness, and with 26.3% less volume than in the Fig. 4. In Fig. 6 we have the case when P1 is turned off from 400 s, and we can see that asymmetry is much less pronounced and ablation volume is 9.6% smaller than in Fig. 4. In Fig. 7 we have the final case when probe P1 is turned on at 200 s, and final results are similar to the previous case, but the ablation volume is 19% smaller than that in Fig. 4. In all cases from Figs. 5-7, total energy is the same, but the results vary significantly in both shape and size.

Solving the MWA equations in practice is possible using numerical methods, such as FEM. In FEM, complex geometry is divided into many small simple subdomains (meshing), called finite elements. Numerical approximation can be performed on finite elements using simple functions. The quantity, quality, and size of finite elements directly affect the accuracy and stability of the approximation. As a general rule, the finite element size should be equal to or less than $\lambda_g/10$, where λ_g is the guided wavelength. The approximation is stable when the use of smaller finite elements has very small effect on the observed result.

The number of finite elements directly affects the duration of the simulation and required computational resources. The quality of the finite element is another important factor in FEM. Degenerated finite elements can cause large approximation errors. We used the same approach as in [10], where we used a combination of structured, unstructured and mixed meshing, obtaining an extremely stable solution.

IV. CONCLUSION

This paper shows the possibility of creating different ablation zones using two probes in the simplest case where one probe has constant power during the entire process, and the other is turned off for 200 s, but in different phases during MWA. The entire simulation process is based on open-source software. Instead of simple power control, changing the power in both probes based on the feedback would allow the creation of highly specific ablation zones with minimal invasiveness.

REFERENCES

- [1] Z. Wang et al., "Microwave ablation versus laparoscopic resection as first-line therapy for solitary 3-5-cm HCC," *Hepatology (Baltimore, Md.)*, vol. 76, no. 1, pp. 66-77, July 2022.
- [2] S. Itoh et al., "Efficacy of Surgical Microwave Therapy in Patients with Unresectable Hepatocellular Carcinoma," *Ann Surg Oncol*, vol. 18, no. 13, pp. 3650-3656, Dec. 2011.
- [3] F. Hojjatollah and P. Punit, "Antenna Designs for Microwave Tissue Ablation," *Crit. Rev. Biomed. Eng.*, vol. 46, no. 6, pp. 495-521, Dec. 2018.
- [4] H. Huang et al., "A review of antenna designs for percutaneous microwave ablation," *Physica medica*, vol. 84, pp. 254-264, Mar. 2021.
- [5] G. Yang et al., "A Systemic Study on the Performance of Different Quantitative Ultrasound Imaging Techniques for Microwave Ablation Monitoring of Liver," in *IEEE Trans. Instrum. Meas.*, vol. 72, pp. 1-11, 2023.
- [6] M. Cavagnaro, C. Amabile, P. Bernardi, S. Pisa and N. Tosoratti, "A Minimally Invasive Antenna for Microwave Ablation Therapies: Design, Performances, and Experimental Assessment," in *Trans. Biomed. Eng.*, vol. 58, no. 4, pp. 949-959, April 2011.
- [7] H. Luyen, F. Gao, S. C. Hagness and N. Behdad, "High frequency microwave ablation for targeted minimally invasive cancer treatment," *The 8th European Conference on Antennas and Propagation (EuCAP 2014)*, The Hague, Netherlands, 2014, pp. 1478-1482.
- [8] R. L. Cazzato et al., "Large nearly spherical ablation zones are achieved with simultaneous multi-antenna microwave ablation applied to treat liver tumours," *Eur Radiol*, vol. 30, no. 2, pp. 971-975, Feb. 2020.
- [9] M. Radmilović-Radjenović, N. Bošković, B. Radjenović, "Computational Modeling of Microwave Tumor Ablation," *Bioengineering*, vol. 9, no. 11, pp. 656, Nov. 2022.
- [10] N. Bošković, M. Radmilović-Radjenović, B. Radjenović, "Finite Element Analysis of Microwave Tumor Ablation Based on Open-Source Software Components," *Mathematics*, vol. 11, no. 12, pp. 2654, Jun. 2023.
- [11] W. Schramm, D. Yang and D. Haemmerich, "Contribution of Direct Heating, Thermal Conduction and Perfusion during Radiofrequency and Microwave Ablation," *2006 International Conference of the IEEE Engineering in Medicine and Biology Society*, New York, NY, USA, 2006, pp. 5013-5016.
- [12] M. Radmilović-Radjenović, N. Bošković, M. Sabo, B. Radjenović, "An Analysis of Microwave Ablation Parameters for Treatment of Liver Tumors from the 3D-IRCAdb-01 Database," *Biomedicines*, vol. 10, no. 7, pp. 1569, July 2022.
- [13] L. Solere et al., "3D image reconstruction for comparison of algorithm database: A patient-specific anatomical and medical image database," *IRCAD Tech Rep*, Strasbourg, France, 2010, pp. 1.
- [14] C. Geuzaine, J.-F. Remacle, "Gmsh: A three-dimensional finite element mesh generator with built-in pre- and post-processing facilities," *Int. J. Numer. Meth. Eng.*, vol. 79, no. 11, pp. 1309-1331, Sep. 2009.
- [15] P. Dular, C. Geuzaine, F. Henrotte and W. Legros, "A general environment for the treatment of discrete problems and its application to the finite element method," in *IEEE Trans. Magn.*, vol. 34, no. 5, pp. 3395-3398, Sept. 1998.
- [16] D. Yang, M. C. Converse, D. M. Mahvi and J. G. Webster, "Expanding the Bioheat Equation to Include Tissue Internal Water Evaporation During Heating," in *IEEE Trans. Biomed. Eng.*, vol. 54, no. 8, pp. 1382-1388, Aug. 2007.

Accurate Shallow-Buried Object Detection Using Bistatic Drone-Mounted Ground Penetrating Radar

Nikola Bošković^{#1}, Aleksandar Atanasković^{*#2}, Nebojša Dončov^{*#3}

[#]Institute of Physics Belgrade, Belgrade, Serbia

^{*}Faculty of Electronic Engineering, Niš, Serbia

¹nikolab@ipb.ac.rs, ²aleksandar.atanaskovic, ³nebojsa.doncov}@elfak.ni.ac.rs

Abstract — This paper shows a study of possible scenarios of using bistatic drone-mounted ground penetrating radar configuration for an accurate shallow-buried object detection. Objects of interest are anti-personnel landmines, which are often made of plastic, with a small amount of metal parts. Because of payload limitations, the system must be small, lightweight and highly efficient. The system is intended in a microwave range of 0.6 GHz - 2.6 GHz. Signal reflections are recorded in frequency domain which correlates to Stepped Frequency Continuous Wave measurements and processed through Inverse Fast Fourier Transformation for time domain analysis. Recording in multiple spatial positions enables B-scans generation for object detection. Polarimetric approach and its effects on target detection accuracy will be investigated in the paper.

Keywords — airborne radar, ground penetrating radar, frequency-domain analysis, land mine detection.

I. INTRODUCTION

Ground penetrating radar (GPR) is a system designed for remote sensing of the underground objects. It sends electromagnetic waves toward the ground. On contact with buried objects with different electromagnetic properties, fractions of the waves are returned to the GPR system. By processing the returned waves, profiling and visualization of the underground object can be done, [1]. GPR can be coupled with the air or directly with the ground. Ground coupled are typically mounted on platform and move above screening area, [2]. They are most appropriate for flat and bare terrain. Harsh, eroded, and hazardous areas are more suitable for air coupled GPR, [3]

It can be mounted on the drone and scan an area above any terrain with higher speed, but would have limitations in system size and available power supply. Signals levels would be lower and wave would have more complex propagation in comparison with ground coupled systems, [3]-[4].

GPR radar in a static position can obtain one-dimensional information about object below, depth (A-scan). Moving the GPR system along the straight line, multiple depth profiles can be obtained and combined, forming a two-dimensional depth-space profile, called B-scan. Image of the buried object would typically have hyperbolic shape, due to the different travel time as the system moving. Reconstruction of the real object shape can be done with some of the migration techniques, [1].

Most GPR systems are configured to work with two or more antennas. Bistatic systems use two antennas, one for

transmitting and the second for signal receiving. Scan moving is typically done in three scenarios. Common offset (CO), where both antennas are at a fixed distance while moving. Common midpoint (CMP) where both antennas are moved in an opposite direction from the same point. Wide angle reflection and refraction (WARR) where only receiver is moving away from transceiver, [5]. CO is the most popular and can be used with a single drone, [3].

GPR radars usually work in time domain, typically as Impulse radar. With the technological advancement and availability of the cheap technology, working in frequency domain is a viable choice, [3]-[6]. In Stepped Frequency Continuous Wave (SFCW) radar signal is formed from a series of pulses with a uniform frequency step between them. Frequency domain signal can be transformed to time domain with Inverse Fast Fourier Transformation (IFFT). Single position can obtain time curve, depth, in the same manner as working in time domain natively. SFCW GPR systems are Ultra-Wideband (UWB), where range and resolution are determined by bandwidth and the number of frequency steps. It can provide a high dynamic range and low noise floor [2].

Soil is a very complex propagation environment, heterogeneous, with high losses. Dielectric properties are especially sensitive to water content, hence soil can change its dielectric constant very fast. Dielectric profile of the soil (ground wave velocity) is necessary for depth estimation of any object. GPR radars can be used to obtain this data, [7].

Detection of the anti-personnel landmines (APL) using drone mounted GPR radar is of great practical significance [2], [3]. APL represent shallow-buried object, filled with explosive, and is typically activated when the victim step on it. They are typically in the shape of the disk and consist of the explosive charge, casing, and fuse mechanism. Metal detector can detect metallic casing, but it cannot differentiate between APLs or any other metal object. Since electromagnetic waves do not penetrate through metal, high reflection would occur, and GPR can be used to do through profiling of the object, greatly reducing the number of false positive.

In the case of the APLs with a minimal content of metal, GPR waves would penetrate through APLs and signal reflection intensity would depend on the contrast between dielectric constants between APL and soil. Dielectric constant of the explosive used in APL are generally around 3.1, for soil

it can be from around 2 to more than 16, depending on the water content, [2]. Plastic casing would have a different dielectric constant, and there is usually additional small air layer inside. All, this means that APL will have a unique electromagnetic signature, which can be used for detection.

High signal losses and large amount of clutter possess a significant problem in APL detection. Polarization of the antenna is determined by the orientation of the electric field vector, which is perpendicular to the direction of the propagation. Antenna with linear polarisation would have polarization mostly oriented around one axis. Receiving and transmitting antenna have same polarization for maximal signal transfer, but each antenna would receive and send a certain amount of the signal with orthogonal polarisation. Long object parallel to the electric field would have the best detection. Buried object can have random orientation, and influence the polarisation of the signal, hence collecting information with multiple antenna polarization can provide additional information whether for better description of the target or for clutter removal, [8].

In this paper we have investigated GRP detection of the buried plastic APL, rotated in 3D plane. Scenario is designed and simulated in CST MWS, results are exported in the form of S -parameters, and processed in Matlab.

II. GPR SCENARIO SETUP

In the model, we have used two identical antipodal Vivaldi antennas, with fixed distance of $D = 0.3$ m, between them. Antennas are x -polarized and y -polarized, depending on the orientation, Fig. 1. We have used three different pairs: copolarized xx , yy , and orthogonally polarized xy pair. Antennas are positioned at $H = 0.2$ m above surface, Fig. 2. System is configured to function as CO, with step size of $M = 0.05$ m, moving along y -axis. At each step, S -parameters are calculated. There are a total of 13 steps which cover scanning from 0 to 0.6 m.

Plastic APLs are generally composed of plastic encasing, explosive charge and firing mechanism. Parts are not airtight, and there is usually a small air layer in-between. We have modelled APL as an explosive disk with dielectric constant $\epsilon_r = 3.1$, and loss tangent $\tan\delta = 0.02$. Plastic casing is presented with layer of Teflon $\epsilon_r = 2.1$, $\tan\delta = 0.0002$. In-between there is a layer of air. For the soil, we have chosen the one with very similar dielectric constant as a worst-case scenario for detection, dry loamy soil with $\epsilon_r = 2.44$, $\tan\delta = 0.0014$.

In majority of studies, APLs are considered being completely horizontal. In reality, this is not the case, and APL will have a small offset from the horizontal plane, and this can have an impact on detection. Most important issue in GPR is removing unwanted reflections and enhance weak signals originating from the target. For that purpose, in this model, we have run identical simulations without APL model. Hence, all reflections not originating from the target can be removed.

S -parameters are imported in Matlab, and the first step is to transfer data to the time domain. Simulation is done from 0.6 GHz to 2.6 GHz, and data is exported in 201 steps, with a frequency step size of 10 MHz.

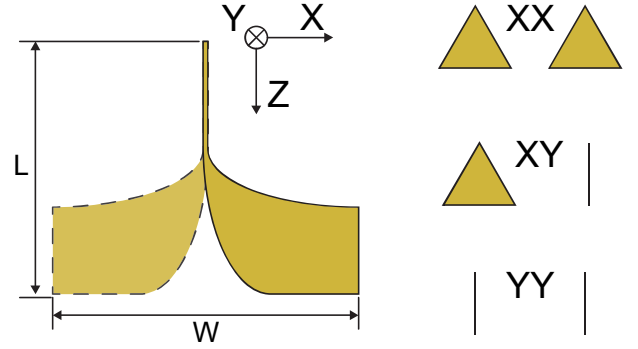


Fig. 1. Antipodal Vivaldi antenna used in simulation oriented along x -axis. Two identical antennas are used with different orientation. Triangle represents orientation along x -axis, while line represents rotation for 90° around z -axis, and orientation along y -axis. $L = 0.15$ m, $W = 0.18$ m.

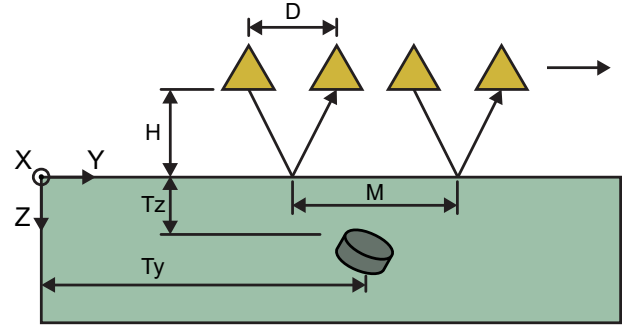


Fig. 2. GPR scenario with two antennas in CO configuration. Buried APL is rotated for 20° around x - and y -axis. $D = 0.3$ m, $H = 0.2$ m, $Tz = 0.1$ m, $Ty = 0.3$ m, $M = 0.05$ m.

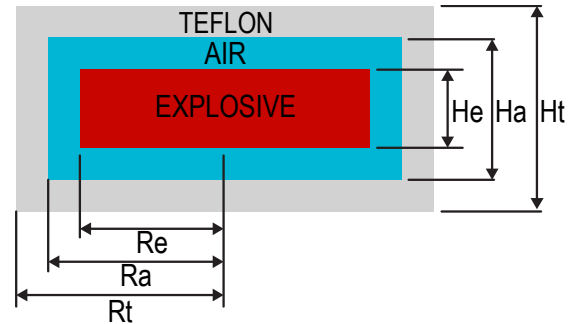


Fig. 3. Model of the APL used in the simulation. Disk, which represents explosive charge, is placed in the center, with layers of air, and Teflon. $He = 0.02$ m, $Ha = 0.03$ m, $Ht = 0.04$ m, $Re = 0.045$ m, $Ra = 0.04$ m, $Rt = 0.055$ m.

Frequency steps from 0 to 0.6 GHz are filled with zeros (zero padding), and complex conjugate in negative frequency plane is constructed. Now we can apply IFFT and obtain a time domain signal. This is done for all positions, and now it is possible to obtain B-scan. In order to actually see the target, we have to remove all much stronger reflections, which is possible by subtracting signals obtained without the target.

III. WAVE PROPAGATION

In bistatic radar, we are interested in the transmission parameter S_{21} . In time domain, this represents time travel from transmitter through air (t_1), soil to the target (t_2), and again through soil (t_2), air to the receiver (t_1), Fig. 4.

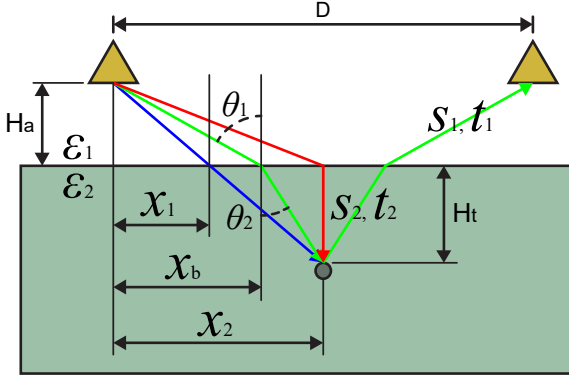


Fig. 4. Bistatic radar ray path between two different mediums. Green path is the actual propagation path, the blue line represents the path when $\epsilon_1 = \epsilon_2$, the red path represent case when $\epsilon_1 \ll \epsilon_2$. t_1, s_1 and t_2, s_2 are time and length of the path through medium 1 and medium 2, respectively.

When traveling between mediums of different dielectric constants, refraction will occur according to Snell's law, as $\epsilon_1 \sin \theta_1 = \epsilon_2 \sin \theta_2$. True inflection point x_b will be located between two extremes. When there is no difference between dielectric constants wave will travel in a straight line, and when $\epsilon_{r1} \ll \epsilon_{r2}$, inflection point will happen at x_2 , [9]. x_b location can be approximated as

$$x_b = x_2 + \sqrt{\frac{\epsilon_{r1}}{\epsilon_{r2}}} (x_1 - x_2). \quad (1)$$

Total travel time between the transmitter, target and receiver can be expressed as

$$t = 2t_1 + 2t_2 = 2 \frac{s_1}{v_1} + 2 \frac{s_2}{v_2} \quad (2)$$

$$v_i \approx \frac{c_0}{\sqrt{\epsilon_{ri}}}. \quad (3)$$

Travel times can be expressed in relation to path lengths, s_1 and s_2 . Wave speed in medium v_i is a critical parameter, and it is dependent on the medium dielectric constant ϵ_{ri} as in (3). Distance of the antenna and the target from horizontal plane, H_a and H_t can be expressed in terms of path length and angles θ_1 and θ_2 as

$$H_a = s_1 \cos \theta_1 \quad (4)$$

$$H_t = s_2 \cos \theta_2. \quad (5)$$

Each time when wave transits between two different medium previously described processes will be repeated.

IV. SIMULATION RESULTS

There are 13 total positions with step of 0.05 m, where simulations are done. In order to enhance image quality, cubic interpolation between positions is performed, creating data with step size of 0.005 m. Elongated target would have the highest detection when it is oriented parallel with the polarization direction, [8].

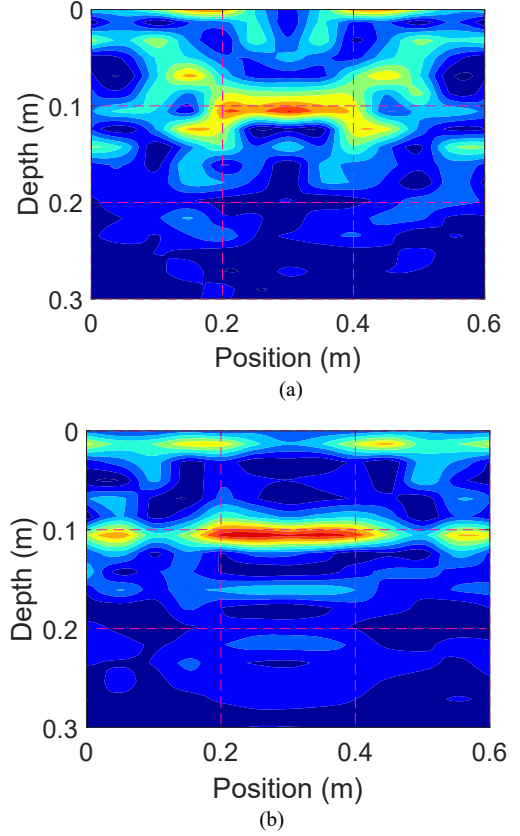


Fig. 5. B-scan of the APL parallel with the horizontal plane: (a) xx -orientation, (b) yy -orientation.

In Fig. 5, B-scan of the APL presented in Fig. 3, in scenario given in Fig. 2, is shown. APL is parallel with the horizontal plane.

Antennas are moving along y -axis and are in co-polarized orientation. In both cases, the position of the target is fairly accurate and similarly estimated. In case of the xx -orientation, we are detecting stronger scattering in the direction of the x -axis, and similarly for the yy -orientation. Since the target is horizontal disk, both polarization are equally parallel to the target.

When we offset APL with horizontal rotation, we can see a completely different situation. In Fig. 6a and Fig. 6b we can see strong scattering all around the target position, for both xx - yy - and orientation. Target is a multi-layered object which is not parallel to the polarisation direction, which would have a high possibility of exhibiting depolarisation features. Depolarisation is an effect of changing current polarization of the electromagnetic wave upon interaction with complex object. In the co-polarized antenna pair, the receiving antenna expects a particular type of linear polarisation. If the polarisation is modified, accurate detecting of the target can be extremely difficult.

Orthogonally polarized antenna pair can be used for the detection of randomly oriented objects. In Fig. 6c, we can see that scattering is much smaller and that position of target is detected.

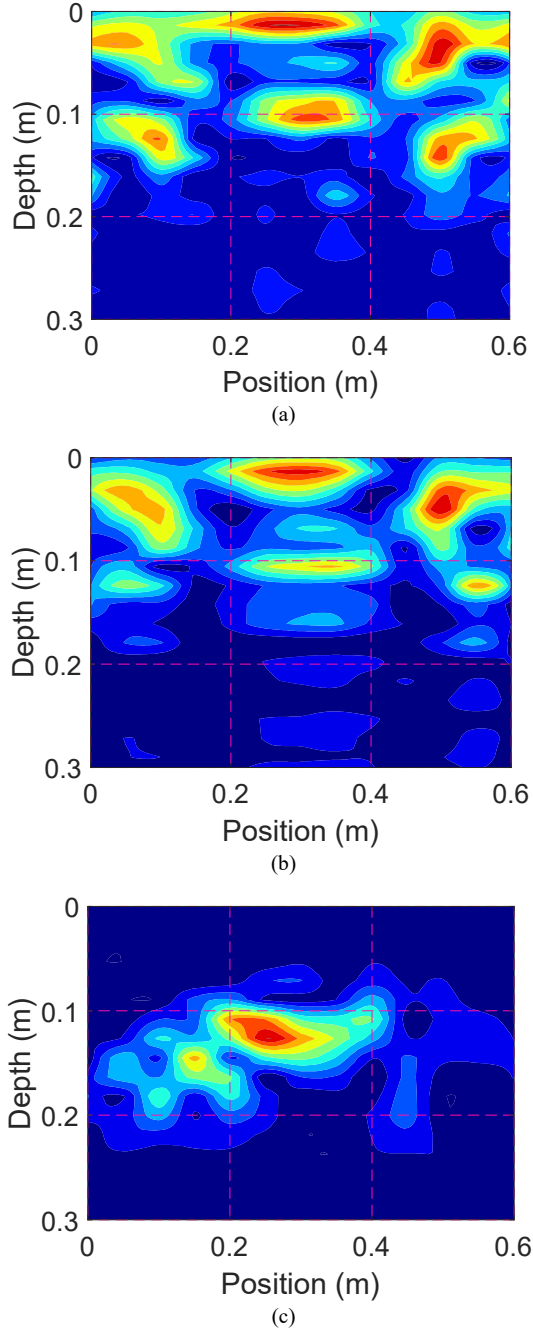


Fig. 6. B-scan of the APL for the 20° offset from horizontal position: (a) xy-orientation, (b) yy-orientation, (c) xy-orientation.

V. CONCLUSION

In this paper, we have tested GRP detection of a randomly oriented model of multi-layered APL. We have shown that with the use of single linear polarisation, even small offset from horizontal plane make accurate estimation of the target position extremely difficult. Using an orthogonally polarized antenna pair gives superior results. Combining data from multiple polarization with the neural network learning model can give an opportunity to accurately characterize APL in arbitrary orientation.

ACKNOWLEDGMENT

This work is supported by the NATO Science for Peace and Security Programme, grant number SPS G5953.

REFERENCES

- [1] Daniels D., *Ground Penetrating Radar*, 2nd Edition, London, United Kingdom: IEE, 2004.
- [2] Daniels, D.J., "A review of GPR for landmine detection," *Sens. Imaging*, vol. 7, pp. 90–123, 2006.
- [3] Šipoš, Danijel, and Dušan Gleich., "A Lightweight and Low-Power UAV-Borne Ground Penetrating Radar Design for Landmine Detection," *Sensors*, vol. 20, no. 8: 2234, 2020.
- [4] N. Diamanti and A. P. Annan, "Air-launched and ground-coupled GPR data," in *Proc. 2017 11th EUCAP*, Paris, France, 2017, pp. 1694-1698.
- [5] N. Diamanti, E. J. Elliott, S. R. Jackson, A. P. Annan; "The Warr Machine: System Design, Implementation and Data," *Journal of Environmental and Engineering Geophysics*; vol. 23, no 4, pp. 469–487, 2018.
- [6] G. Tronca, I. Tsilicalou, S. Lehner and G. Catanzariti, "Comparison of pulsed and stepped frequency continuous wave (SFCW) GPR systems," in *Proc 2018 17th Int. Conf. on GPR*, Rapperswil, Switzerland, 2018, pp. 1-4.
- [7] S. Kaufmann, A. Klotzsche, H. Vereecken and J. van der Kruk, "Simultaneous multi-channel GPR measurements for soil characterization," in *Proc 2018 17th Int. Conf. on GPR*, Rapperswil, Switzerland, 2018, pp. 1-4.
- [8] H. -H. Sun, Y. H. Lee, C. Li, L. F. Ow, M. L. M. Yusof and A. C. Yucel, "The Orientation Estimation of Elongated Underground Objects via Multipolarization Aggregation and Selection Neural Network," in *IEEE Geoscience and Remote Sensing Letters*, vol. 19, pp. 1-5, 2022.
- [9] E. M. Johansson, J. E. Mast, "Three-dimensional ground-penetrating radar imaging using synthetic aperture time-domain focusing," in *Proc. SPIE2275, Advanced Microwave and Millimeter-Wave Detectors*, vol. 2275, 1994.

The Influence of the Drone-Mounted Antenna Angular Position for Bistatic FL GPR Detection of Shallowly Buried Metallic Objects

Aleksandar Atanasković¹, Nebojša Dončov², and Nikola Bošković³

^{1,2} Faculty of Electronic Engineering, University of Niš, Niš, Serbia

³ Institute of Physics Belgrade, Belgrade, Serbia

{¹aleksandar.atanaskovic, ²nebojsa.doncov}@elfak.ni.ac.rs, ³nikolab@ipb.ac.rs

Abstract—Analysis of influence of antenna angles of bistatic forward-looking drone-mounted ground penetrating radar (FL GPR) on A-scan is examined in this paper through EM simulation. To detect shallowly buried metallic objects, scenarios with fixed transmitting and receiving antennas and different forward-looking angles, from 0 to 30 degree with step of 7.5 degree, are studied. Objects of interest are anti-personnel landmines considered to be fully metallic, placed in several positions between transmitter and receiver. The system is intended to operate in a microwave range of 0.6 GHz - 2.6 GHz. A Ricker waveform, which is the negative, normalized second derivative of a Gaussian waveform is used as transmitting signal. Signal reflections are recorded in the time domain. After filtering and time gating, only a signal reflected from buried landmine at a certain position is obtained and analyzed for different transmitting and receiving antennas angles.

Index Terms— Bistatic radar, ground penetrating radar, radar signal processing, ultra wideband radar

I. INTRODUCTION

Ground penetrating radar (GPR) represents a term that describes a remote sensing technique used to determine a presence and location of underground objects or interfaces [1]. The technology deployed for GPR depends on the application as well as the target type and its material. The most often used sensing technology is one based on electromagnetic (EM) waves propagation through the ground [2] due to its ability to penetrate relatively deep into the soil (depending on EM waves and soil parameters), to detect both metal and plastic objects and to operate in different soil conditions.

In general, GPR systems can be identified as ground-coupling and air-coupling systems. Ground-coupled GPR systems are usually mounted on a platform that moves above the screening area [3]. As such, they are generally suitable for areas that are flat and without any plants or trees. In a case of more hazardous objects detection and for harsh and eroded terrain, air-coupled GPR systems, such as one where system is mounted on a drone flying over the terrain, are more suitable [4]. Antennas are one of vital components of both systems, so different antenna types have been employed for either ground- or air-coupling GPR [1].

GPS systems can operate in monostatic or quasi-monostatic and bistatic GPR configurations defined whether the transmitting and receiving antennas are placed close to each other or far away in terms of operating wavelengths. Both configurations can be further grouped as forward-looking (FL) and down-looking (DL) GPR depending on whether the antenna is looking ahead from the drone on which is mounted or is oriented normal to the terrain [5-7]. FL GPR system is much more suitable than DL GPR for shallowly buried object detection due to oblique and near grazing incident sensing that reduces dominant reflection from air-ground interface.

Some numerical and experimental analysis regarding the impact of transmitting and receiving bowtie antennas separation, height above the ground and input impedance of antenna on bistatic DL GPR system performance for nonmetallic object detection was presented in [8]. In [9], a nonmetallic object detection was also performed both numerically and experimentally for variable elevation angle and height of transmitting and receiving horn antennas of bistatic FL GPR system. In general, both papers showed that performances of considered GPR systems are, among other things, influenced significantly by the configurations and positions of the antennas.

In order to further study this impact, in this paper we perform an EM analysis on how different antenna angular positions influence bistatic drone-mounted FL GPR performance for shallowly buried objects detection. We consider scenarios with fixed transmitting and receiving Vivaldi antennas whose FL angles vary from 0 to 30 degree with a step of 7.5 degree. Objects of interest are anti-personnel landmines considered to be fully metallic, placed in several positions between transmitter and receiver. Bistatic FL GPR is intended to operate in a microwave range of 0.6 GHz - 2.6 GHz. A Ricker waveform, which is the negative, normalized second derivative of a Gaussian waveform is used as transmitting signal. Signal reflections are recorded in the time domain. After filtering and time gating, only a signal reflected from buried landmine at a certain position is obtained and analyzed for different transmitting and receiving antennas angles.

II. GPR SCENARIO

In the considered scenario, two identical antipodal Vivaldi Antennas [10] (Fig. 1) were used, placed at a distance of $D = 1\text{ m}$, raised above the ground $H = 0.5\text{ m}$, oriented at appropriate angles in relation to the direction towards the ground, marked as θ_{TX} and θ_{RX} (Fig. 2). The antennas are designed to work in the frequency range of $0.6\text{ GHz} - 2.6\text{ GHz}$. The S_{11} parameter of the designed antenna is shown in Fig. 3a, while the radiation pattern at central frequency of 1.6 GHz is shown in Fig. 3b. From the radiation pattern, it can be seen that the gain of the designed antenna is 5.08 dB and the beamwidth is 182 degrees . The target, represented by metallic anti-personnel landmine with diameter $2r = 0.14\text{ m}$ and height $h = 0.06\text{ m}$ is located at a depth of $H_t = 0.3\text{ m}$. Different positions of the target (D_t) were considered. The soil is modelled as an ideal single-layer structure with dielectric constant $\epsilon_r = 6$ (dry soil). The Ricker waveform defined by (1) was used as the excitation signal, as in:

$$W(t) = -(2\xi(t - \chi)^2 - 1)e^{-\xi(t-\chi)^2} \quad (1)$$

where $\xi = \pi^2 f^2$, $\chi = \sqrt{2}/2$ and $f = 1\text{ GHz}$. The waveform of the used signal is shown in Fig. 4.

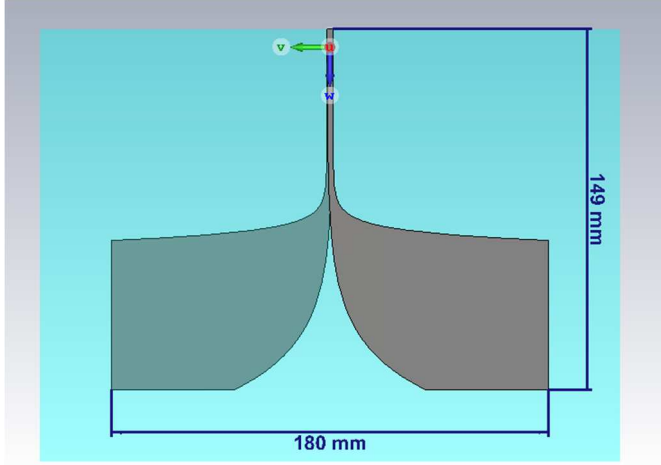


Fig. 1. Designed antipodal Vivaldi antenna used in simulation.

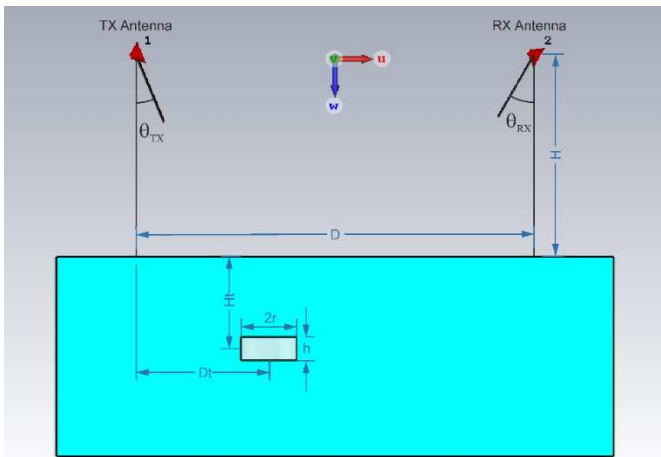


Fig. 2. GPR scenario.

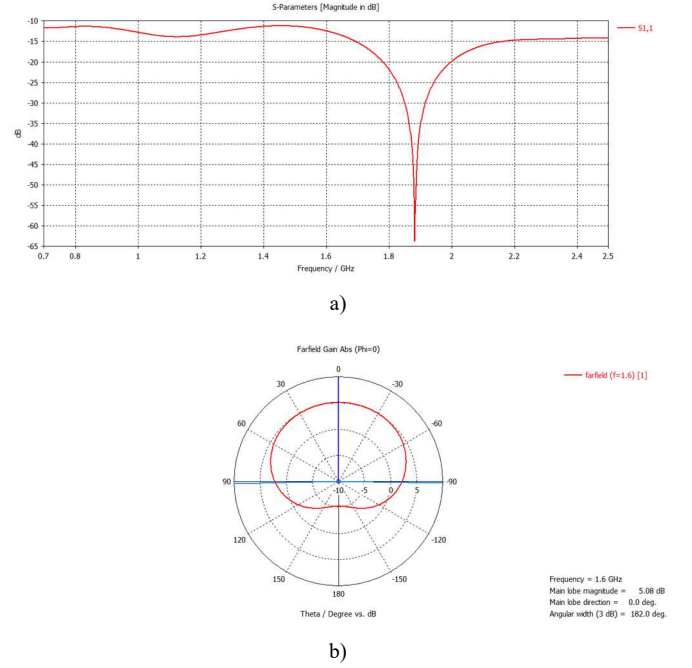


Fig. 3. Parameters of designed Vivaldi antenna: a) S_{11} ; b) Radiation pattern.

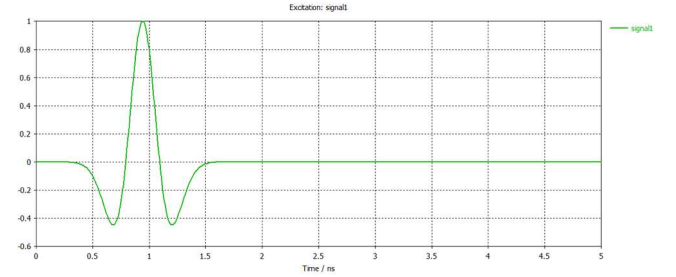


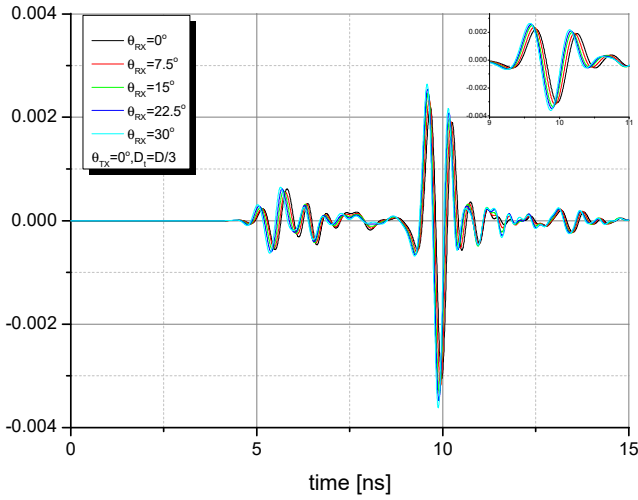
Fig. 4. Waveform of the used Ricker signal.

To remove unwanted reflections that do not originate from the target, identical simulations were performed with and without the target. In this way, the model was calibrated, i.e., all reflections that do not come from the target were removed. Simulations for this considered scenario were performed for 5 different angles of the transmitting (θ_{TX}) and receiving (θ_{RX}) antennas (from 0 to 30 degree with a step of 7.5 degree) and for four different positions of the mine (D_t) between the transmitting and receiving antenna (from 0 m to 1 m with a step of $1/3\text{ m}$).

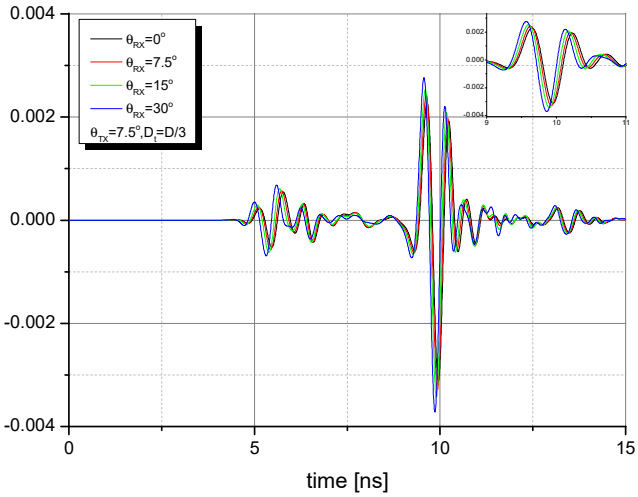
III. SIMULATION RESULTS

To detect when the signal reflected from the target has the maximum value, the A-scan for the described GPR scenario was considered. The angles of the antennas and the target position were considered as parameters. Figs. 5 and 6 show A-scan for different combination of the parameters (D_t , θ_{TX} and θ_{RX}). It can be observed that the intensity of the reflected signal increases as the antenna angular orientation approaches the angle between the target and the antenna. Also, it can be observed that the peak of A-scan occurs a bit earlier, which can be explained by the fact that by rotating the antenna, the centre of the antenna's radiation moves and thus shortens the distance

between the antenna and the target, which results in a shorter time required for the signal to travel through path transmitting antenna - target - receiving antenna. Based on the presented results, it can be concluded that the signal reflected from the target would be of the highest intensity if both the receiving and transmitting antennas are oriented towards the target. The simulation of such a case for target position $D_t = D/3$, when the angle of the transmitting antenna is 22 degrees and the angle of the receiving antenna is 40 degrees, is shown in Fig. 7. In this case the signal detected from the target is nearly twice as strong compared to the previously observed cases. This means that in the case of optimal orientation of the antennas towards the target, we have a higher reflection from the target and, therefore, a higher probability of detection.



a)



b)

Fig. 5. A-scan for $D_t = D/3$ and different angles θ_{RX} : a) $\theta_{TX} = 0$ deg (down-looking); b) $\theta_{TX} = 7.5$ deg.

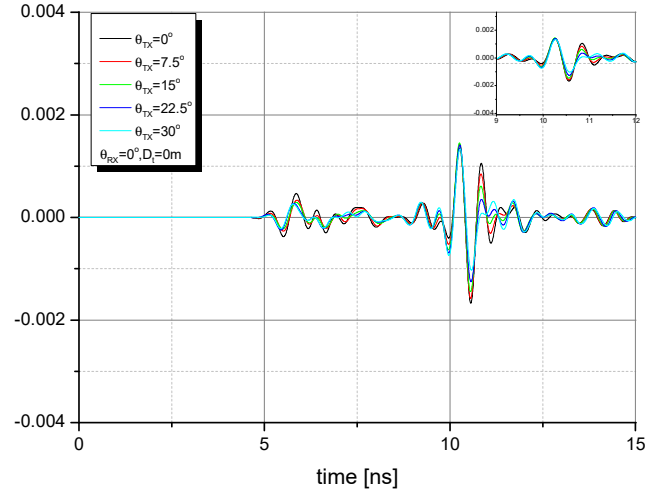


Fig. 6. A-scan for $D_t = 0$ m, $\theta_{RX} = 0$ deg (down-looking) and different angles of θ_{TX} .

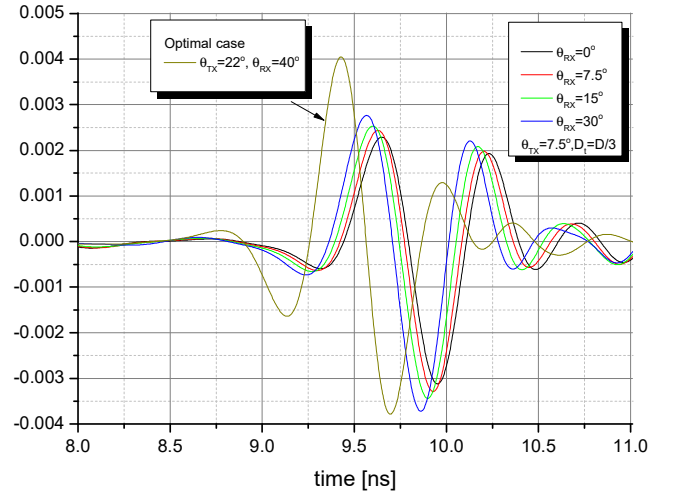


Fig. 7. A-scan for $D_t = D/3$ and optimal position of the transmitting and receiving antennas.

IV. CONCLUSION

In this paper, the intensity of the reflected signal from a metal shallowly buried target with a bistatic forward-looking GPR radar was considered. We have shown that the angular orientation of the transmitting and receiving antennas affects the intensity of the reflected signal. For the considered scenario with antipodal Vivaldi antennas, the optimal angular orientation of the antennas significantly affects the strength of the reflected signal, which in the optimal case can be twice as strong compared to the signal obtained with randomly selected antenna positions. We can conclude that by optimally adjusting the angles of the antennas, a higher intensity A-scan is obtained, that is, the probability of reliable detection of shallowly buried metal targets increases. Further research will be related to the investigation of the optimal angular orientation

of the antennas for the case of space scanning in order to obtain B-scans, when one and/or both antennas change their spatial position relative to each other, approaching or moving away from each other.

ACKNOWLEDGMENT

This work is supported by the NATO Science for Peace and Security Programme, grant number SPS G5953.

REFERENCES

- [1] D. J. Daniels, *Ground Penetrating Radar*, 2nd edition, IET: London, UK, 2004.
- [2] R. Persico, *Introduction to Ground Penetrating Radar: Inverse and Data Processing*, Hoboken, NJ: Wiley, 2014.
- [3] D. J. Daniels, "A review of GPR for landmine detection," *Sensing and Imaging*, vol. 7, pp. 90–123, 2006.
- [4] D. Šipoš, D. Gleich., "A Lightweight and Low-Power UAV-Borne Ground Penetrating Radar Design for Landmine Detection," *Sensors*, vol. 20, no. 8: 2234, 2020.
- [5] D. Comite, F. Ahmad, T. Dogaru, M. G. Amin, "Adaptive Detection of Low-Signature Targets in Forward-Looking GPR Imagery," *IEEE Geoscience and Remote Sensing Letters*, vol. 15, no. 10, October 2018, pp. 1520-1524.
- [6] D. Comite, F. Ahmad, M. G. Amin, T. Dogaru, "Forward-Looking Ground-Penetrating Radar: Subsurface target imaging and detection: A review," *IEEE Geoscience and Remote Sensing Magazine*, vol. 9, no. 4, December 2021, pp. 173-190.
- [7] M. Garcia-Fernandez, G. Alvarez-Narciandi, Y. A. Lopez, "Analysis and Validation of a Hybrid Forward-Looking Down-Looking Penetrating Radar Architecture," *Remote Sensing*, 2021, 12, 1206.
- [8] X. Gao, F. J. W. Podd, W. van Verre, D. J. Daniels and A. J. Peyton., "Investigating the Performance of Bi-Static GPR Antennas for Near-Surface Object Detection," *Sensors*, vol. 19, no. 1:170, 2019.
- [9] Yu Zhang, Dan Orfeo, Dylan Burns, Jonathan Miller, Dryver Huston, Tian Xia, "Buried nonmetallic object detection using bistatic ground penetrating radar with variable antenna elevation angle and height," *Proc. SPIE 10169, Nondestructive Characterization and Monitoring of Advanced Materials, Aerospace, and Civil Infrastructure 2017*, 1016908 (19 April 2017).
- [10] A. Z. Hood, T. Karacolak and E. Topsakal, "A Small Antipodal Vivaldi Antenna for Ultrawide-Band Applications", *IEEE Antennas and Wireless Propagation Letters*, vol. 7, pp. 656 – 660, 2008.

Log-Periodic Antenna Consideration for Advanced GPR Applications

Nikola Bošković
Institute of Physics Belgrade,
University of Belgrade
Belgrade, Serbia
nikolab@ipb.ac.rs

Nebojša Dončov
Faculty of Electronic Engineering,
University of Niš
Niš, Serbia
nebojsa.doncov@elfak.ni.ac.rs

Abstract— Ground Penetrating Radar is a device for imaging object buried in the ground, estimations of physical properties, size and position of the underground structure. It is of special interest in dangerous and hardly accessible areas. For such a purpose radar system on the remote controlled drone is highly desirable in which antenna plays a very important role.

Keywords—antenna, radiation pattern, printed antenna, UWB GPR.

I. INTRODUCTION

GPR (Ground Penetrating Radar) is a device which is commonly used for non-invasive profiling of the structures which are buried underground. GPR operates by sending and receiving electromagnetic waves from antenna into the ground, [1]. Received signals would go through post processing blocks and image of the detected object can be generated. GPR would typically operate in the frequency range from 50 MHz to 3 GHz. Ground medium is vastly different from air, hence main problem in GPR is to provide efficient signal transmission through ground, [2]. GPR system configuration would depend on the particular use case, but would generally operate in close proximity to the ground and GPR would be placed on the moving vehicle.

GPR can be used in archaeology, studying glaciers, ice sheets, soils, peatlands, biomonitoring, etc. One of the particular interesting applications is detection of the small object such as landmines. Due to dangerous environment it is preferable to place GPR on unmanned aerial vehicle (UAV). Such GPR configuration impose certain demands on the overall design. System needs to be light-weight, energy efficient, and compact dimensions. Wide frequency bandwidth is necessary to achieve resolution necessary for small object detection. Lower frequency provides better ground penetration but require a large antenna size.

Recent advances in UWB (Ultra-Wideband) technologies, antenna design and microelectronics enable that GPR can cover frequency ranges from 500 MHz to 3 GHz with a single antenna and hardware. Multiple scanning scenarios are possible with using two UAV, such as that transmitting UAV is stationary, while receiving UAV is moving.

Having good GPR antenna is essential for good imaging results. Bandwidth of the antenna is often observed as a frequency bandwidth where S_{11} is lower than -10 dB, which

is not entirely correct because UWB antennas often suffers from massive radiation pattern degradation through bandwidth. Good radiation pattern should have a gain variation less than 2 dB, sidelobe levels below -20 dB in comparison to the main lobe, undeformed main lobe.

II. GPR ANTENNA

Among antennas often used for GPR are: dipoles, bow-tie antennas, TEM horns, Vivaldi antenna, spiral antennas, [3], [4]. Antenna type which can be of particular interest as UWB, light-weight and cheap solution for UAV is printed log-periodic antenna. Printed log-periodic antenna is similar to the standard structure consisting of multiple wires which is mostly used in rooftop as terrestrial television antennas. Printing antenna on dielectric enables creating very thin conductor lines, and functioning on much higher frequency. Depending on the chosen radiating elements and spatial configuration multiple variations are possible.

Dimensions of the adjacent elements such as L1 and L2, W1 and W2, R1 and R2 all have the same ratio of 0.89, Fig. 1. Also, dipoles' ends form a lines which form an angle, hence by selecting dimensions of the first element, dimensions of the other elements can be quickly obtained. Overall maximal dimensions of the antenna are determined by the lowest working frequency and the number of elements, where higher number of elements yields smoother and better characteristics. The longest dipole should be resonant at lowest frequency, and the shortest dipole should be resonant at the highest frequency.

In this case dipoles are printed in the balanced microstrip technology, [5]. Dipoles are printed on the single dielectric but from the both sides. Each arm of the dipole is from the opposite side, and adjacent dipoles are alternating in order to provide required phase shift for efficient end-fire radiation. Typical coaxial connector is unbalanced structure, hence balun is used for the transition and mode conversion. At the end of the antenna matching resistor is placed in order to prevent any remaining power reflection and radiation degradation.

Structures is created on dielectric Rogers 5880 with dielectric constant $\epsilon_r = 2.2$, height of $H = 3.175$ mm, metal thickness of 0.035 mm. Structure is composed of the 20 dipoles.

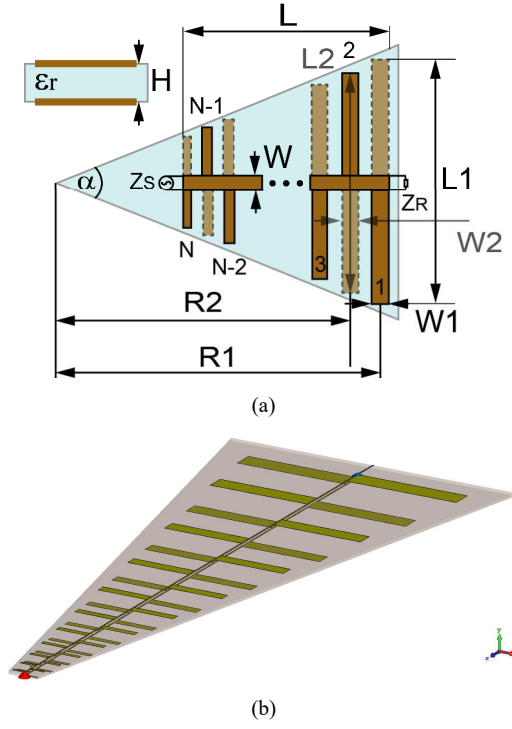


Fig. 1. Printed UWB log-periodic antenna. (a) Plane view with relevant elements, (b) 3D model. ($L = 650$ mm, $L1 = 248$ mm, $W = 1.6$ mm, $W1 = 22.4$ mm, $R1 - R2 = 78.4$ mm; $L2 = 0.89 L1$, $LN = 0.89 LN-1$).

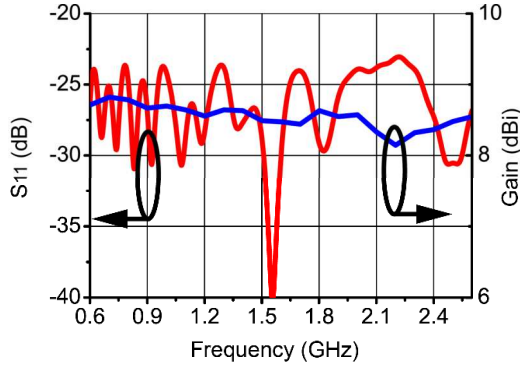
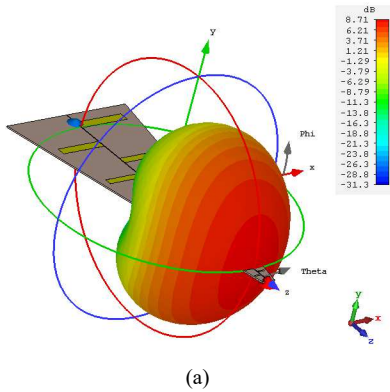


Fig. 2. S_{11} and gain variation versus frequency.



III. RESULTS

Antenna is simulated and analyzed in the frequency range from 0.6 GHz to 2.6 GHz. Antenna gain and S_{11} parameters are shown in Fig. 2. Gain is exceptionally flat, with variation of less than 0.5 dB in the observed bandwidth, and with level around 8.5 dBi. In Fig. 3, 3D radiation patterns are shown at 0.6 GHz, 1.6 GHz, and 2.6 GHz.

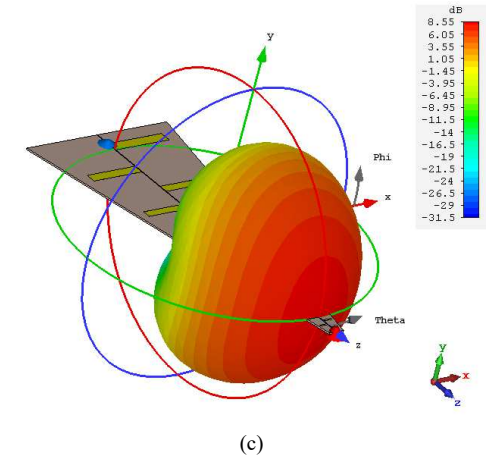
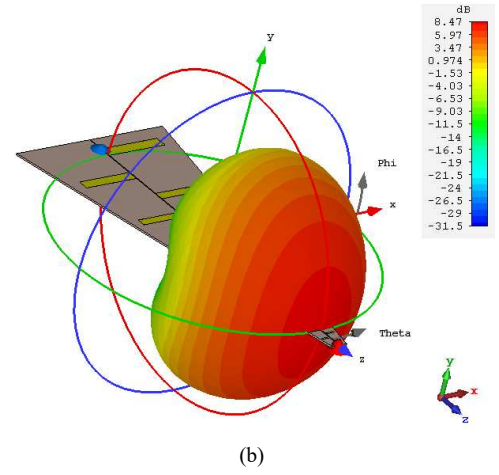


Fig. 3. 3D radiation pattern of the antenna at (a) 0.6 GHz, (b) 1.6 GHz (c) 2.6 GHz.

TABLE I. ANTENNA DIMENSION AND MASS

Length	Min / Max width	Mass aprox.	Reduced mass aprox.
650 mm	30 / 250 mm	0.85 kg	0.2 kg

It can be seen that radiation pattern is almost identical, there is no sidelobes, or any kind of deformation. In comparison with spiral antenna in [4], this solution has around 5 dB higher gain and the gain and radiation pattern are much more stable in the considered frequency range than in [4].

Antenna plane has shape of isosceles trapezoid, with length and two opposite dimensions at the start and the end of the antenna given in Table I. Approximate mass of the given structure is 0.85 kg. Radiation is entirely done through metallic dipoles, and dielectric is used as a support structure, hence it is possible to remove majority of the dielectric, by simple cutting it out, this can reduce the mass of the antenna for more than four times, to about 0.2 kg. This can actually be beneficial for radiation characteristics, because removing excess dielectric would also remove the surface waves.

Standard patch antenna has extremely narrowband S_{11} . Commonly used approach to achieve wideband S_{11} is to use slots in the ground plane (Defected Ground Structure). One of the consequences of such approach typically asymmetrical bilateral radiation. Bow-tie antennas and similar structures have symmetrical bilateral radiation. Gain is fairly limited. In order to achieve unilateral radiation,

reflector can be used. This also can be challenging if stable UWB characteristics are required. In comparison with popular Vivaldi, TEM horn antennas [6], [7], Log-periodic antenna is planar array, where practically each radiating element can control specific part of the bandwidth therefore, fine grain control over radiation is possible. Each radiating element of the array can be specially optimized, if needed different radiating elements can be used, also with pin diodes is possible to have different elements physically present at the same time, and use fast switching as needed. Branching planar antennas in multiple arrays is generally simple.

One of the simplest ways to increase the depth of penetration is to increase the transmitter power, [8], hence providing higher levels of reflected signals. This will reduce the time of operation of the UAV through increased power consumption. Much more efficient way to achieve the same effect is through passive antenna structure.

IV. CONCLUSION

In this work, a printed UWB log-periodic antenna, as main sensor on GPR intended to be used on UAV, is considered. Antenna shows an excellent stability in the observed bandwidth, which open opportunities for multiple improvements. Antenna elements can be individually modified, antenna can be part of the larger array, adding and controlling reflector can be further enhance and significantly improve radiation in the desired plane. Its applicability for UAV GPR system will be tested both numerically and experimentally in future research.

ACKNOWLEDGMENT

This work is supported by the NATO Science for Peace and Security Programme, grant number SPS G5953.

REFERENCES

- [1] Harry M. Jol, "Ground Penetrating Radar Theory and Applications", Elsevier, 2009.
- [2] C. Warren and A. Giannopoulos, "Experimental and Modeled Performance of a Ground Penetrating Radar Antenna in Lossy Dielectrics," *IEEE Journal of Selected Topics in Applied Earth Observations and Remote Sensing*, vol. 9, no. 1, pp. 29-36, Jan. 2016.
- [3] Balanis, C.A., "Antenna Theory and Design", John Wiley & Sons, New York, 1997.
- [4] Bousbaa, W, Medkour, H, Bouttout, F, Messali, Z. "Fully planar frequency independent square Archimedean spiral antenna with impedance transformer for ground penetrating radars", *Microw Opt Technol Lett*. 2021; 63: 295– 309.
- [5] N. Boskovic, B. Jokanovic and M. Radovanovic, "Printed Frequency Scanning Antenna Arrays With Enhanced Frequency Sensitivity and Sidelobe Suppression," *IEEE Transactions on Antennas and Propagation*, vol. 65, no. 4, pp. 1757-1764, April 2017.
- [6] A. Ahmed, Y. Zhang, D. Burns, D. Huston and T. Xia, "Design of UWB Antenna for Air-Coupled Impulse Ground-Penetrating Radar," *IEEE Geoscience and Remote Sensing Letters*, vol. 13, no. 1, pp. 92-96, Jan. 2016.
- [7] D. Šipoš and D. Gleich, "Design of a full polarimetric GPR system for landmine detection," *2020 International Conference on Systems, Signals and Image Processing (IWSSIP)*, pp. 357-360, 2020.
- [8] Jol, H.M., "Ground penetrating radar antennae frequencies and transmitter powers compared for penetration depth, resolution and reflection continuity", *Geophysical Prospecting*, vol. 43, pp. 693–709, 1995.

3-Phase Feeding for CP Antenna Elements

Miloš Radovanović

*Institute of Physics & School of Electrical Engineering,
University of Belgrade, Serbia*
rmilos@ipb.ac.rs, rm135051p@student.etf.bg.ac.rs
<https://orcid.org/0000-0003-1063-7972>

Nikola Bošković

*Institute of Physics,
University of Belgrade, Serbia*
nikolab@ipb.ac.rs
<https://orcid.org/0000-0002-6316-4120>

Abstract—This paper is intended to draw attention to underutilized principle of multiphase feeding structures of circular polarized (CP) printed antennas, and especially advantages of using tree phase feeding structures over the more conventional quadrature feeds, like increasing axial ratio (AR) bandwidth. This is done by constructing simple tri-pole radial slot antenna and feeding it by a phasing structure derived from a cross between double-Y baluns and the theory of 3-phase static phase converters.

Keywords—Axial ratio, CP antennas, double-Y baluns, multiphase feeding, phase converters, printed antennas, 3-phase.

I. INTRODUCTION

Unlike with the linearly polarized (LP) antennas which are usually band limited by impedance matching, with most printed CP antennas, bandwidth-limiting factor tends to be the AR. Since it was recognized [1] for the first time, the potential of array-element sequential rotation and phasing, was widely applied in CP-array designs to improve AR, going as far as to use a LP elements in CP arrays [2].

For achieving CP in a single antenna radiating element designers have several options: among which are intrinsically CP elements like spirals [3] and helicoids [4]; simultaneous excitations of two orthogonal modes [5]; perturbation coupling of orthogonal modes [6]; and independently driving element modes in quadrature with feeding networks [7].

Recently the possibility of 3-phase driving of a single antenna element was investigated and utilized in several broad band designs [8]–[10], attaining same benefits of AR-bandwidth improvement, as was previously achievable only with sequentially rotated arrays. These designs utilize series line phase shifter element driving, Wilkinson power divider with negative delay/lumped element phase shifter, and a parallel delay line phase shifters respectively.

Another way of achieving symmetric 3-phase driving of a symmetric three port network from a single-phase energy source can be borrowed from theory of poly-phase electrical machines and power distribution systems, namely from static phase converters, history of which is neatly summed in [11]. In short, Ferraris developed a way of running a standard 3-phase motor of a single-phase power source, Arno built a static phase converter from it, and Maggs [12] made an improved version, replacing a coil with a capacitor (Fig.1.a, b). When not used for static phase converters, and without rest of similar concerns of power distribution systems, even better phase symmetry is possible combining these two configurations and using both inductive and capacitive phasing (Fig.1.c).

II. ANTENNA CONSTRUCTION

A. Reactive loading phase Converter-Shifter

To achieve AR of one at the central operating frequency of tri-port CP antenna, antenna must be supplied with three

equal currents, with a sequential phase shift of 120 degrees, in direct or reverse sequence, depending on desired variant of CP (left- or right-handed). With this scheme from phase converters, this perfect symmetry off currents, two reactively loaded ports, must see two equal (1) but opposite reactances: X_L and X_C (Fig.2.). Those reactances, by opposing the two of the mesh currents flowing thru the generator branch of the circuit, induce a third mesh current flowing through both, but not the generator, and being orthogonal to the first two, and so must also be adequately sized for the orthogonal current to be exactly a square-root-of-three times larger (1) than the current flowing thru the generator.

$$\sqrt{3}R_{Z0} = X_{L0} = X_{C0} = R_G/\sqrt{3} \quad (1)$$

$$\sqrt{3}R_{Z0} \cong X_{L0} = X_{C0} < R_G/\sqrt{2} \quad (2)$$

where R_G and R_{Z0} represent generator resistance and resistance per phase of the given system, respectively. Remaining requirement from (1) relating R_Z to the R_G is less strict, as it is only relevant for the optimal transfer of power (minimum reflection coefficient), at the central frequency, and can be loosen to that of (2), which consider the whole operating bandwidth, rather than focusing only on the central frequency.

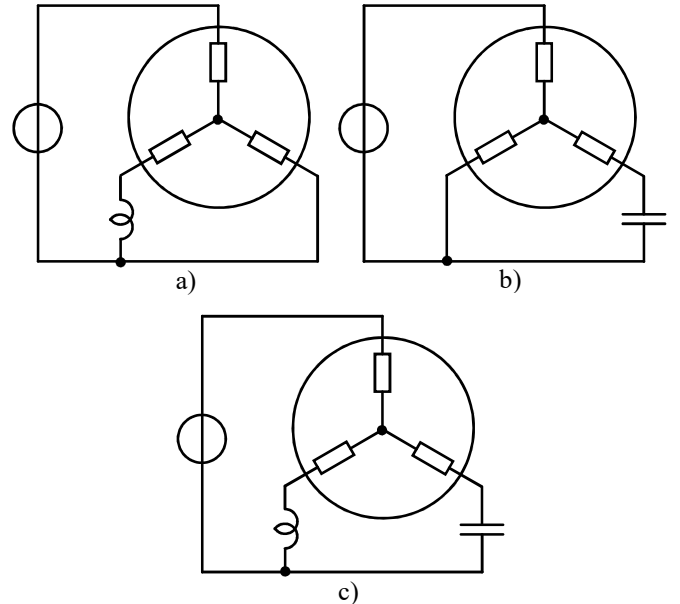


Fig. 1. a) Ferraris single phase driving of 3-phase induction motor from Ferraris–Arno static phase converters; b) Maggs 3-phase pilot induction motor single phase driving for capacitor–Ferraris–Arno type static phase converters; c) Fully balanced L-C 3-phase induction motor single phase driving for improved reverse sequence symmetric component suppression.

B. Double-Y junction / Radial Slot Antenna

Although the double-Y junction is famously used in double-Y baluns, since they were first constructed, it was known, but somewhat less commonly, that double-Y baluns have a stop-band [13] at their resonant frequency and can radiate similarly to single-Y junction [14] even if fully matched. This radiation can be enhanced by using stub lines of length equal or longer than quarter wavelength [13]. This radiation effect is also increased with changing the impedance ratios of balanced to unbalanced lines, as well as, with using inherently lossy tapered and wide high impedance slot lines.

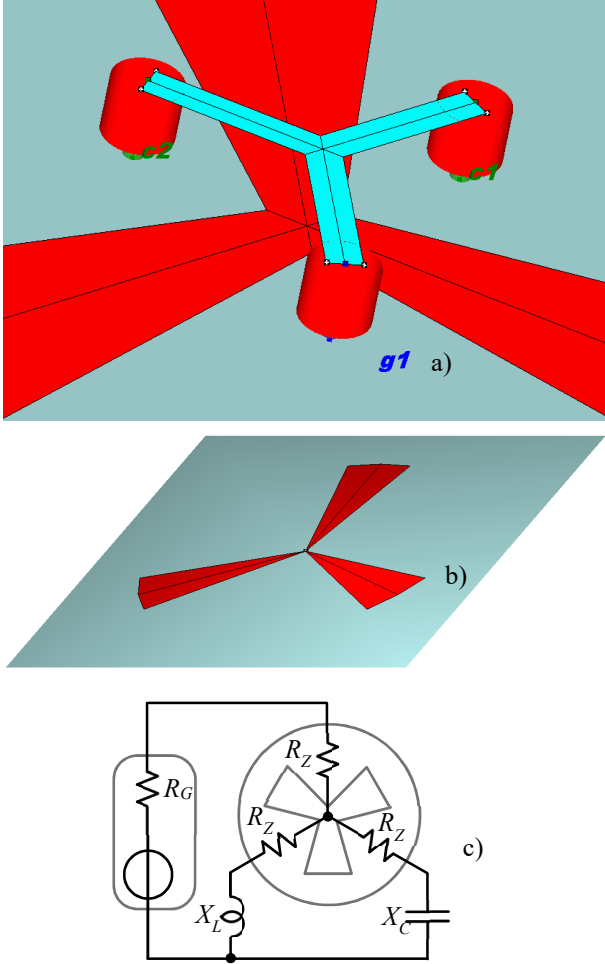


Fig. 2. Simulation model: a) Double-Y junction of microstrip-to-slotline feeding structure. (c1 – concentrated capacitive load, c2 – concentrated inductive load, g1 – exciting generator); b) Tri-pole radial slot CP antenna c) Simplified antenna equivalent circuit with radiating elements represented by radiation resistances R_Z .

III. SIMULATION AND DISCUSSION OF RESULTS

Described antenna model was simulated with full-wave EM solver [15] but with few simplifications of details not needed to show off the merits of the concept. Those simplifications include not including dielectric substrate or implementing final impedance transformer normalize impedance to 50Ω , as well as using lumped L and C loadings instead realizing them with transmission line stubs. Also, simulation uses infinite perfectly conducting ground plane, with upper, and lower half-spaces, and omits using a reflector. Also putting element in an array was not attempted yet.

This work was supported by the Ministry of Education, Science, and Technological Development of the Republic of Serbia.

Having all this facts on mind, this antenna model archives fractional AR (of below 2 or 6dB) bandwidth of 24%, reflection losses smaller then -20dB and Co-polar right CP gain of 4.36 dB.

A. Impedance match

Above given reflection loss, that is impedance match, was calculated for generator impedance of RG between 150Ω and 182Ω (Fig.3. a,b), which represent two extreme values of matching either a central frequency or AR-band edges. Better compromise value can be chosen between them, but this had no real purpose prior to implementing practical impedance transformer to match the future physical antenna prototype to the 50Ω port required for measurement. Because of this for all the rest of the results, a referent port impedance was arbitrary chosen to be 150Ω .

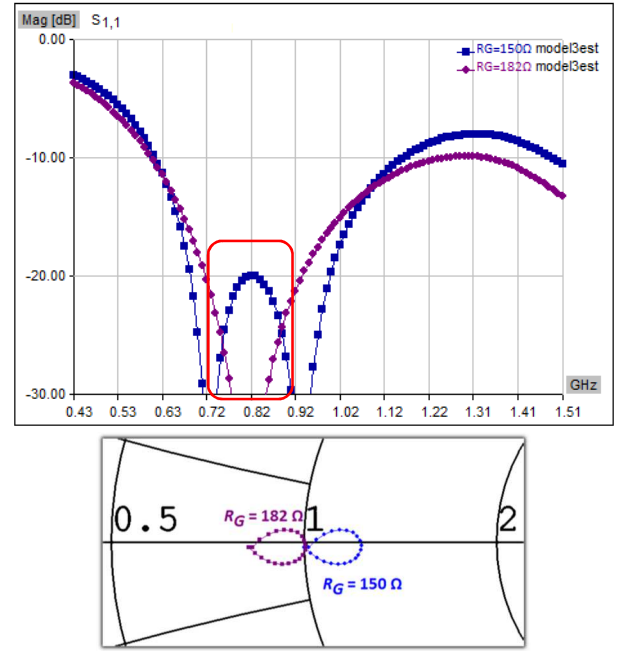


Fig. 3. Reflection losses for two different generator impedances a) Frequency dependence of $|S_{11}|$ with useful band marked b) Magnified Smith chart in band reflections.

B. Realized gains and Radiation patterns

Simulated antenna exhibited a single lobe in elevation sweep for both total and right-handed CP radiation pattern, while having three equally spaced lobes for all three (Total, R-CP and L-CP) radiation patterns in azimuthal sweep patterns parallel to the ground surface. This was summarized in a 3d plots (Fig.4.). Frequency sweep of main axis realized gains for R-CP and L-CP are given on Fig.5, and assume $R_G = 150 \Omega$.

C. Axial ratio and feeder currents

Since AR is the focus of this paper, we will examine it more thoroughly (Fig.6.) and try to explain its properties by analyzing feeder current (Fig.7.) its properties.

On Fig.6, it can be observed that AR in the operating band resembles a parabola, which contrasts with usual single [1] or quadrature feed CP antenna elements like CP patches which have an absolute value-like frequency dependency. This can be explained by noticing (Fig.7.a, b) that both magnitude and phase of two phasing reactances have tendency to cancel out their respective detuning when leaving resonant frequency

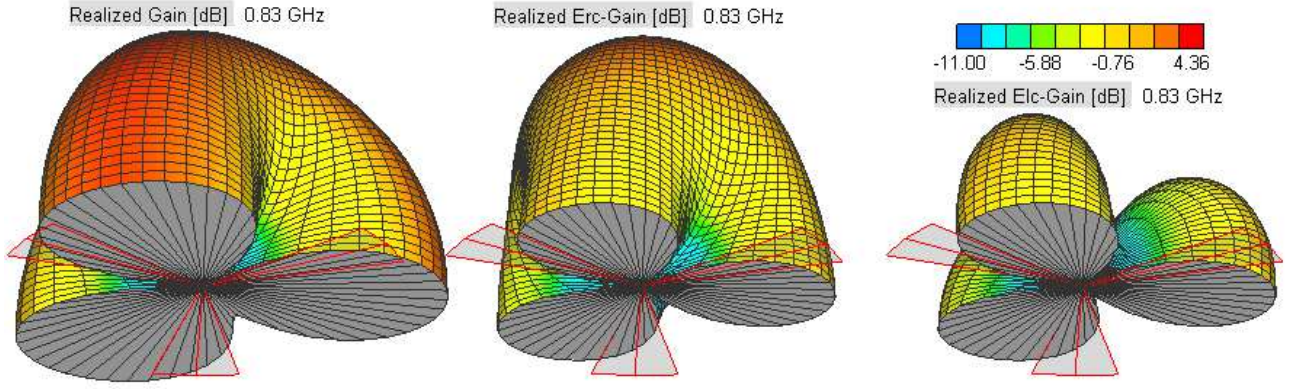


Fig. 4. Upper half-space 3D radiation patterns for: a) Total field realized gain; b) R-CP realized Gain (co-polarized); c) L-CP (cross-polarized).

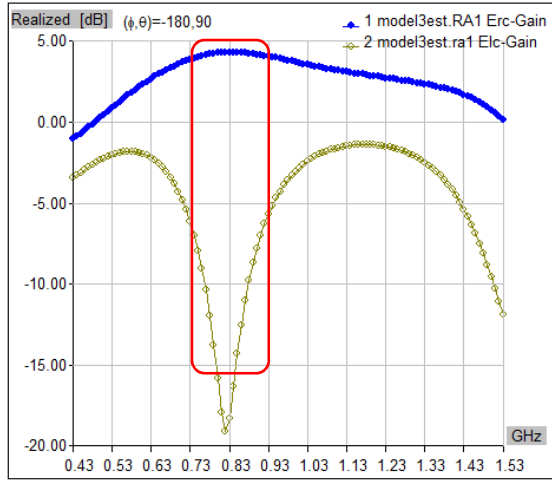


Fig. 5. Frequency dependence of R-CP and L-CP main axis realized gains, with useful band marked.

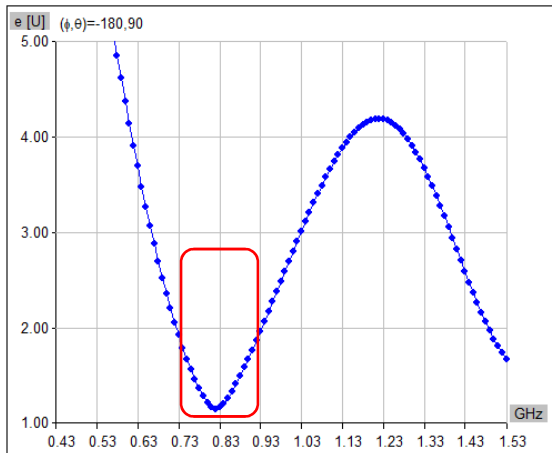


Fig. 6. Axial ratio of simulated antenna, with useful band marked.

and taking over dominant role in providing quadrature component to form pure CP. This ensures that detuning only happens as a second order effect, increasing the useful AR bandwidth.

IV. CONCLUSION

Antenna design presented in this paper was merely a proof of concept and shown without rigorous derivation, and is intended for further improvement. Proposed design can achieve wideband and stable circular polarization, and significant size reduction in comparison with the existing solutions.

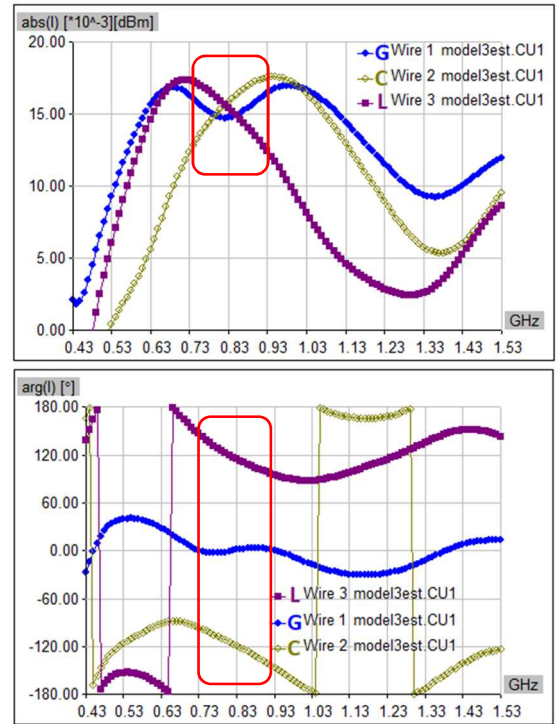


Fig. 7. Currents of the feeding circuit (blue/G – generator current; magenta/L – inductive loading; yellow/C – capacitive loading) a) Magnitude variation showing crossover around central frequency; b) Phase variation showing going in and out of 120 degrees phase relations.

ACKNOWLEDGMENT

Authors would like to thank the company WIPL-D d.o.o., Belgrade, for providing the simulation software used in this research.

REFERENCES

- [1] T. Teshirogi, M. Tanaka, and W. Chujo, Wide-band circularly polarized array antenna with sequential rotations and phase shift of elements, International Symposium on Antennas and Propagation, ISAP, Tokyo, Japan, 1985, pp. 117–120
- [2] Huang, John. "A technique for an array to generate circular polarization with linearly polarized elements." IEEE Transactions on antennas and propagation 34, no. 9 (1986): 1113-1124.
- [3] Mao, S.G., Yeh, J.C. and Chen, S.L., 2009. Ultrawideband circularly polarized spiral antenna using integrated balun with application to time-domain target detection. IEEE Transactions on Antennas and Propagation, 57(7), pp.1914-1920.
- [4] Djordjevic, Antonije R., Alenka G. Zajic, Milan M. Ilic, and Gordon L. Stuber. "Optimization of helical antennas [antenna designer's notebook]." IEEE Antennas and Propagation Magazine 48, no. 6 (2006): 107-115.
- [5] Shen, Liang. "The elliptical microstrip antenna with circular polarization." IEEE transactions on antennas and propagation 29, no. 1 (1981): 90-94.
- [6] Sajal, Sayeed, and Saeed I. Latif. "Hybrid perturbation technique applied to stacked patches for circular polarization." In 2018 IEEE international conference on electro/information technology (EIT), pp. 0638-0640. IEEE, 2018.
- [7] Wang, Shi Tong, Sheng Sun, Hucheng Sun, Shiwen Yang, and Jun Hu. "A quadrature - hybrid - integrated reconfigurable feeding network for wideband quad - polarization - agile antenna design." International Journal of RF and Microwave Computer - Aided Engineering 31, no. 6 (2021): e22641.
- [8] Lin, Chen, et al. "A three-fed microstrip antenna for wideband circular polarization." IEEE antennas and wireless propagation letters 9 (2010): 359-362.
- [9] Fartookzadeh, M. and Armaki, S.M., 2014. Serial - feed for a circular patch antenna with circular polarization suitable for arrays. International Journal of RF and Microwave Computer - Aided Engineering, 24(5), pp.529-535.
- [10] Theunis, Robin, Maarten Baert, Paul Leroux, and Wim Dehaene. "Highly broadband circular polarized patch antenna with 3 phase feed structure." In 2017 11th European Conference on Antennas and Propagation (EUCAP), pp. 2197-2200. IEEE, 2017.
- [11] Chhabra, R. L. (1974). Optimization of phase converter parameters and effects of voltage variation on their performance. Iowa state university.
- [12] Maggs, A. H. (1946). Single-phase to three-phase conversion by the Ferraris–Arno system. Journal of the Institution of Electrical Engineers - Part II: Power Engineering, 93(32), 133–136. doi:10.1049/ji-2.1946.0030
- [13] Schiek, B., and J. Kohler. "An improved microstrip-to-microslot transition." IEEE Transactions on Microwave Theory and Techniques 24.4 (1976): 231-233.
- [14] Lewin, L. "Spurious radiation from a microstrip Y junction." IEEE Transactions on Microwave Theory and Techniques 26.11 (1978): 893-894.
- [15] WIPL-D software package

Three-dimensional simulations of the microwave tissue ablation

Nikola Bošković, Marija Radmilović-Radjenović, Branislav Radjenović

Institute of Physics, University of Belgrade, Pregrevica 118, 11080 Belgrade, Serbia

Contact: B. Radjenović (bradjeno@ipb.ac.rs)

Abstract. Microwave ablation (MWA) is a minimally invasive thermal ablation modality based on increasing the temperature above the normal physiological threshold to kill cancer cells with minimal damage to the surrounding. The objective of the study is to assess the role of optimal conditions in the efficacy of MWA in treating malignant tissues. For this purpose, a three-dimensional simulation model is developed and tested within the COMSOL Multiphysics software package [1]. Figure 1a shows the liver (triangular surface) with early-stage HCC (1.64 cm × 1.71 cm × 3.81 cm) (solid red surface) of patient 16 (male, born in 1950) in the 3D-IRCADb-01 database [2]. The proper choice of input power should be estimated before the procedure begins to attain the desired ablation zone. As can be seen from Figure 1b, when a power of 10 W was applied, the tumor was not completely ablated. Application of 15 W to the significant damage to healthy tissue. The application of 13 W provides treatment for the entire tumor with minimal damage to the surrounding tissue [3].

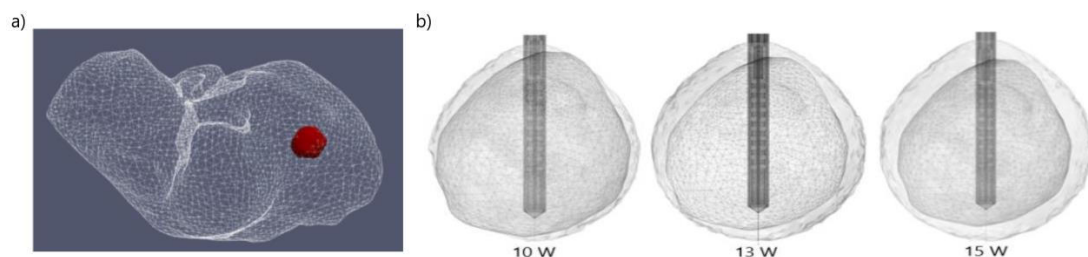


Figure 1. a) Three-dimensional simulation model of HCC (solid red surface), which belonged to patient 16 in the 3D-IRCADb-01 database [2] and b) ablated regions (solid gray surfaces) around the HCC [2] (triangulated surface) after 600 s of microwave ablation at 2.45 GHz and three different values of the input power.

This research was supported by the support of the Science Fund of the Republic of Serbia, GRANT 7739583, SimSurgery.

REFERENCES

- [1] Comsol Multiphysics. 1986–2020. Burlington (MA): COMSOL, Inc. Available online: <https://www.comsol.com/comsol-multiphysics>.
- [2] 3D-IRCADb. Strasbourg (F): IrcadFrance. Available online: <https://www.ircad.fr/research/data-sets/liver-segmentation-3d-ircadb-01>.
- [3] M. Radmilović-Radjenović., N. Bošković, B. Radjenović, “Computational Modeling of Microwave Tumor Ablation”, *Bioengineering* 9 (2022), 656(1-23).

Effectiveness of two-antenna microwave ablation of large hepatocellular carcinoma

Marija Radmilović-Radjenović, Nikola Bošković, Branislav Radjenović

Institute of Physics, University of Belgrade, Pregrevica 118, 11080 Belgrade, Serbia

Contact: M. Radmilović-Radjenović (marija@ipb.ac.rs)

Abstract. In the treatment of tumors, certain types of cancer cells have been found to denature at elevated temperatures (which are slightly lower than temperatures normally injurious to healthy cells). Conventional microwave ablation techniques for treating hepatocellular carcinoma (HCC) typically used only a single antenna to deliver energy, resulting in relatively small ablation zones and increased risks of local tumor residual, intrahepatic recurrences, or distant metastases. It was shown that two-antenna configurations are less invasive than the single-antenna configuration. Ablation zones created using two antennas are smaller causing less damage to the healthy tissue as compared to those created using a single antenna. Two-antenna configurations produce more uniform thermal profiles and higher peripheral tissue temperatures. Three-dimensional simulation results obtained within the Comsol software package [1] for a) a single-antenna and b) two-antenna microwave ablation of tumor [2] are shown in Figure 1. As can be observed, a single-antenna configuration leads to larger damage to the healthy surrounding tissue. On the other hand, the two-antenna configuration provides complete ablation of the tumor with small damage to healthy tissue.

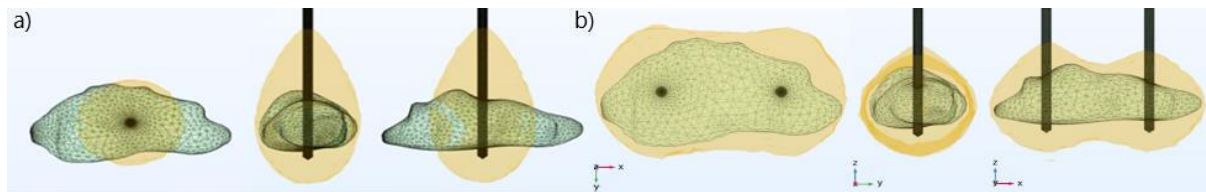


Figure 1. Isocontours related to ablated regions (solid gray surfaces) around the HCC [2] (triangulated surface) after 600 s of a) a single-slot and b) two-antenna microwave ablation.

This research was supported by the support of the Science Fund of the Republic of Serbia, GRANT 7739583, SimSurgery.

REFERENCES

- [1] Comsol Multiphysics. 1986–2020. Burlington (MA): COMSOL, Inc. Available online: <https://www.comsol.com/comsol-multiphysics>.
- [2] 3D-IRCADb. Strasbourg (F): IrcadFrance. Available online: <https://www.ircad.fr/research/data-sets/liver-segmentation-3d-ircadb-01>.

SIMULATION STUDIES OF SURGICAL ELECTRODE DESIGN TO PREVENT SPARKING ENHANCED BURNS

Marija Radmilović-Radjenović, Nikola Bošković, Branislav Radjenović

Institute of Physics, University of Belgrade, Pregrevica 118, 11080 Belgrade, Serbia

E-mail: marija@ipb.ac.rs

Proper care and handling of electrosurgical equipment are essential to patient and personnel safety. Burns that destroy layers of the patient's skin often linked to a medical mistake are largely preventable. This paper is dealing with the design of surgical electrodes as one of the extremely important factors for the formation of burns during standard procedures.

1. Introduction

The main mechanism responsible for skin burns during electrocautery is the electrical breakdown characterized by a voltage that electrically breaks down gas in the interelectrode gap enabling current flow through the ionized gas. The breakdown voltage usually obeys the standard scaling law. Further development of the discharge depends on several parameters such as the geometry of the electrode arrangements and the gap spacing. Results of extensive studies reveal that various electrode configurations correspond to different electric field distributions although the same voltage is applied leading to the dissimilar breakdown voltages.

2. Method

In the past few decades, computer modeling and simulations have evolved into very effective tools for studying sparking during various *electrosurgical* procedures and for developing new instrument designs. In this paper, the effects of the electrode shape on the sparking have been studied by using software package COMSOL [1] based on the multi-component plasma fluid model. Our goal was to determine both a minimum voltage necessary for sparking and locations where sparks start as crucial factors for the formation of burns during electrocautery. For that purpose, calculations were carried out for DC argon discharges having in mind that the main advantage of argon coagulation is constant, a minimum depth of the thermal effect. The emphasis was put on generations of sparks between various electrode arrangements (cylinder-cylinder, sphere-sphere cylinder-sphere, cylinder-cone, sphere-cone, and cone-cone). Electrosurgical sparks have been distinguished both for the positive and negative cycles. It was found that mechanisms of electrical spark formation are not equal in both directions introducing the electrical asymmetries.

3. Results

The obtained simulation results shown in Figure 1 agree well with the experimental data taken from literature [2] revealing that the sparking formation is strongly affected by the electrode configuration. Sparking occurs most easily when both electrodes are cylindrical and the most difficult when one electrode is a cone. The highest voltages are required for triggering sparks between arrangements with one cone electrode. It was found that the field is more uniform in the cylinder-cylinder configuration, while highly non-uniform in the cylinder-cone configuration. For a configuration with one or two spherical electrodes, breakdown voltages are higher up to 10 V and 8 V, respectively. When one electrode is a cone, the breakdown voltage is higher from 4 V up to 46 V.

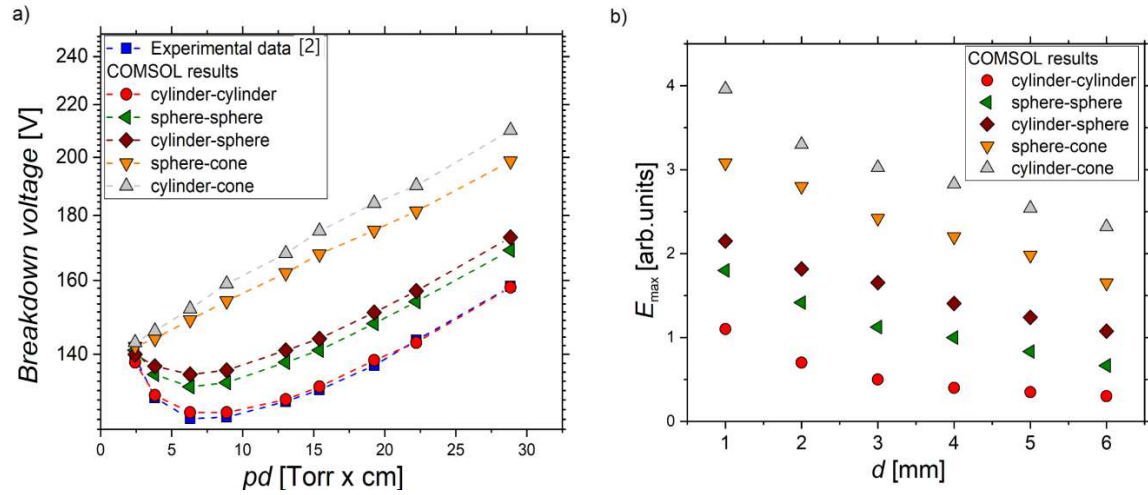


Figure 1. a) The breakdown voltage curves and b) maximum electrical field for various electrode configurations. The experimental data [2] are presented by blue squares.

This study was supported by the Science Fund of the Republic of Serbia, The Program IDEAS, GRANT No. 7739583, SimSurgery.

4. References

- [1] COMSOL Multiphysics. Stockholm, Sweden, www.comsol.com.
- [2] Meek JM and Craggs JD 1953. *Electrical breakdown of gases*. (Oxford, UK: Oxford Press).

The thermal effect during microwave ablation treatment of Hepatocellular Carcinoma

Marija Radmilović-Radjenović, Nikola Bošković, and Branislav Radjenović

Institute of Physics Belgrade, University of Belgrade, Pregrevica 118, 11080 Belgrade, Serbia

Contact: M. Radmilović-Radjenović (marija@ipb.ac.rs)

Abstract. Hepatocellular Carcinoma (HCC) accounts for more than 75% of all liver cancers representing the fourth major cause of cancer-related death [1]. One of the most persuasive treatments for HCC is microwave ablation (MWA) particularly recommended for COVID-19 patients with liver tumors as a minimally invasive procedure with a short recovery time. For this study, calculations were performed using the COMSOL Multiphysics software package based on the finite element method [2]. Simulation conditions include a 10-slots antenna operating at microwave frequency of 2.45 GHz, the input power of 10 W, and parameters corresponding to the liver tissue (healthy and tumoral) taken from ref. [3]. The antenna immersed into the tissue radiates energy that is converted into the heat invading the tissue (Fig. 1a). The absorbed energy converted into thermal energy leads to an increase in the tissue temperature (Fig.1b). The region where $\Delta T = T - T_b \geq 15$ °C (T_b is the blood temperature) is mainly located inside the tumor indicating a small risk of damaging healthy tissue (Fig. 1c). The damage zone is concentrated around the tip and slots of the antenna, while the backward heating effect is smaller as depicted in Fig. 1d.

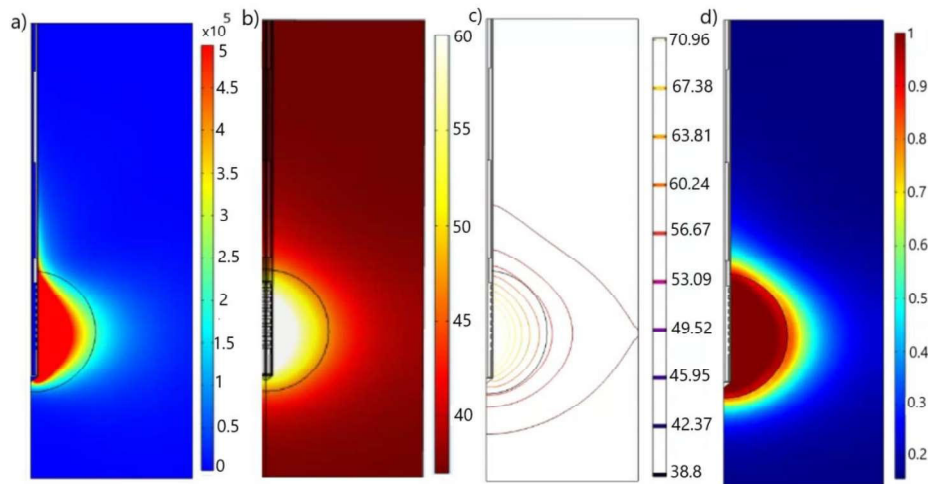


Figure 1. a) The total power dissipation density (expressed in W/m³). b) The temperature (expressed in °C) distributions in the liver tissue after 600 s of microwave ablation. c) Spatial distribution of ($\Delta T = T - T_b$). d) Fraction of necrotic tissue after 600 s of microwave ablation.

Acknowledgements. This research was supported by the Institute of Physics Belgrade, through the grant by the Ministry of Education, Science and Technological Development of the Republic of Serbia and by the Science Fund of the Republic of Serbia, GRANT 7739583, SimSurgery.

REFERENCES

- [1] J.M. Llovet, R.K. Kelley et al. *Nat. Rev. Dis. Primers* **7** (2021), 6.
- [2] Comsol Multiphysics. Available online: www.comsol.com
- [3] B. Radjenović, M. Sabo et al., *Cancers* **13** (2021), 5784.

Numerical Simulation of Microwave Tumor Ablation

Nikola Bošković

Institute of Physics, University of Belgrade, Pregrevica 118, 11080 Belgrade, Serbia
e-mail: nikolab@ipb.ac.rs

Branislav Rađenović

Institute of Physics, University of Belgrade, Pregrevica 118, 11080 Belgrade, Serbia
e-mail: bradjeno@ipb.ac.rs

Marija Radmilović-Rađenović

Institute of Physics, University of Belgrade, Pregrevica 118, 11080 Belgrade, Serbia
e-mail: marija@ipb.ac.rs

Abstract. Microwave ablation (MWA) is a minimally invasive, fast-recovery treatment for cancer cell destruction using microwave radiation. Computer modeling has proven to be an effective tool for optimizing the performance of MWA, enabling ablation size control to guarantee tumor necrosis with minimal damage to healthy tissues [1]. The higher the level of predictability achieved in simulations, the easier it is to plan a safer, more effective, and less time-consuming treatment procedure [2]. Mathematical models of MWA consist of three fundamental components: modeling tissue and heat transport in tissues, modeling the microwave electromagnetic field generated by antennas, and modeling the effect of heating on tumor cells. Wave propagation occurs in nanoseconds and must be solved in the frequency domain, while tissue heating is much slower process and must be solved in the time domain [3]. We developed an application framework for modeling MWA based on open-source software components that is suitable for use not only by scientists but also engineers and medical personnel. We demonstrate that using smart meshing procedures significantly reduces computational costs and simulation time. An accurate, custom-explicit Euler time loop was designed to obtain temperature values and estimate tissue necrosis across the computational domain during microwave ablation [3].

Keywords: Computational modeling; Finite-element method; Microwave ablation; Numerical simulations.

References

- [1] **M. Radmilović-Rađenović, N. Bošković, B. Rađenović.** An Analysis of Microwave Ablation Parameters for Treatment of Liver Tumors from the 3D-IRCADb-01 Database. *Biomedicines*, 2022, 10, 7, 1569. <https://doi.org/10.3390/biomedicines10071569>
- [2] **N. Bošković, S. Nikolić, B. Rađenović, M. Radmilović-Rađenović.** Safety and Effectiveness of Triple-Antenna Hepatic Microwave Ablation. *Bioengineering*, 2024, 11, 11, 1133. <https://doi.org/10.3390/bioengineering11111133>
- [3] **N. Bošković, M. Radmilović-Rađenović, B. Rađenović.** Finite Element Analysis of Microwave Tumor Ablation Based on Open-Source Software Components. *Mathematics*, 2023, 11, 12, 2654. <https://doi.org/10.3390/math11122654>

ON THE EFFICIENCY OF TRIPLE ANTENNA MICROWAVE ABLATION

Nikola Bošković¹, Srdjan Nikolić^{2,3}, Branislav Radjenović¹, Marija Radmilović-Radjenović¹

¹Institute of Physics, University of Belgrade, Pregrevica 118, 11080 Belgrade, Serbia

²Institute of Oncology and Radiology of Serbia, Pasterova 14, Belgrade, Serbia

³Faculty of Medicine, University of Belgrade, Dr Subotica 8, 11000 Belgrade, Serbia

ABSTRACT

Microwave ablation is a minimally invasive, highly efficient procedure for treating the various types of cancers, during which tumor cells are destroyed with hyperthermia caused by microwave radiation from small probe inserted in tumor. With enough power and time much larger tumors can be destroyed at the expense of the significant damage of the healthy tissue, which can be minimized with spatially distribution of the power with multi-probe setup. Finite element method can be used to accurately estimate the processes occurring during the ablation, but due to complexity requires significant computation resources and time. In the multi-probe setup number of possible combination is massive, and with each new probe complexity of the calculation rise significantly. In multi-probe setup, identical probes are typically arranged symmetrically around the center of the tumor in the form equilateral shape such as triangle or square. If have the complete calculations with single probe, we can generate virtual computational domain with any multi-probe setup, and obtain fairly good starting estimation almost instantly. Chosen setups can be than simulated with the full simulation. All procedures involving modeling, meshing, and calculation are done using open-source software.

Keywords: microwave ablation, two antenna configuration, finite element

Authors acknowledge that this research was supported by the Science Fund of the Republic of Serbia, The Program IDEAS, GRANT No. 7739583, SimSurgery.

THREE-DIMENSIONAL MODELING OF RADIOFREQUENCY ABLATION THERAPIES

Nikola Bošković

Institute of Physics, University of Belgrade

Marija Radmilović-Radjenović

Institute of Physics, University of Belgrade

Branislav Radjenović

Institute of Physics, University of Belgrade

ABSTRACT

Currently, the use of RFA has been well described as a primary or adjuvant treatment modality of limited but unresectable hepatocellular carcinoma, liver metastasis, especially colorectal cancer metastases, primary lung tumors, renal cell carcinoma, boney metastasis and osteoid osteomas. The role of RFA in the primary treatment of early stage breast cancer is still evolving. A challenging problem of radiofrequency ablation (RFA) in liver surgery is to accurately estimate the shapes and sizes of RFA lesions. The aim of this paper is to use computer modeling of the Bio-Heat equation to demonstrate factors influencing RF ablation tissue heating. Computer modeling demonstrates the importance of energy deposition, tumor and background tissue electrical and thermal conductivity, and perfusion on RF ablation outcomes.

Keywords: radiofrequency ablation, tumor configuration, finite element

Authors acknowledge that this research was supported by the Science Fund of the Republic of Serbia, The Program IDEAS, GRANT No. 7739583, SimSurgery.

II. INTERNATIONAL CONGRESS ON ADVANCED RESEARCH AND APPLICATIONS

ON THE EFFICIENCY OF RADIOFREQUENCY TUMOR ABLATION

Marija Radmilović-Radjenović¹, Srdjan Nikolić^{2,3}, Nikola Bošković¹, Branislav Radjenović¹

¹*Institute of Physics, University of Belgrade, Pregrevica 118, 11080 Belgrade, Serbia*

²*Institute of Oncology and Radiology of Serbia, Pasterova 14, Belgrade, Serbia*

³*Faculty of Medicine, University of Belgrade, Dr Subotica 8, 11000 Belgrade, Serbia*

ABSTRACT

Radiofrequency ablation (RFA) is a minimally invasive procedure that uses electrical energy and heat to destroy cancer cells. RFA is usually considered a treatment option only if you're not a good candidate for surgery for some reason, such as your overall health or the presence of many small tumors in an organ. RFA is most commonly used to treat a spot of cancer that is causing problems such as pain or other discomfort and is generally not used as the primary treatment for most cancers. The radiologist uses imaging tests to guide a thin needle through the skin or an incision and into the cancer tissue. High-frequency energy passes through the needle and causes the surrounding tissue to heat up, killing the nearby cells. Computer modeling evolved into a very powerful tool for the determination of optimal conditions for RFA. We have developed a simulation package based on the finite element method to determine conditions enabling the efficiency of RFA. **Keywords:** radiofrequency ablation, necrotic tissue, three-dimensional simulation, finite element

Authors acknowledge that this research was supported by the Science Fund of the Republic of Serbia, The Program IDEAS, GRANT No. 7739583, SimSurgery.

6. INTERNATIONAL MEDITERRANEAN CONGRESS 13-15 August 2024, Rome - Italy

THE EFFICIENCY AND SAFETY OF TRIPLE ANTENNA MICROWAVE ABLATION

Nikola Bošković, Marija Radmilović-Radjenović, Branislav Radjenović

Institute of Physics Belgrade, University of Belgrade, Pregrevica 118, 11080 Belgrade, Serbia

ABSTRACT

Microwave ablation is a minimally invasive, highly efficient procedure for treating the various types of cancers, during which tumor cells are destroyed with hyperthermia caused by microwave radiation from small probe inserted in tumor. With enough power and time much larger tumors can be destroyed at the expense of the significant damage of the healthy tissue, which can be minimized with spatially distribution of the power with multi-probe setup. Finite element method can be used to accurately estimate the processes occurring during the ablation, but due to complexity requires significant computation resources and time. In the multi-probe setup number of possible combination is massive, and with each new probe complexity of the calculation rise significantly. In multi-probe setup, identical probes are typically arranged symmetrically around the center of the tumor in the form equilateral shape such as triangle or square. If have the complete calculations with single probe, we can generate virtual computational domain with any multi-probe setup, and obtain fairly good starting estimation almost instantly. Chosen setups can be than simulated with the full simulation. All procedures involving modeling, meshing, and calculation are done using open-source software.

Keywords: microwave ablation, two antenna configuration, finite element

Authors acknowledge that this research was supported by the Science Fund of the Republic of Serbia, The Program IDEAS, GRANT No. 7739583, SimSurgery.

ON THE EFFICIENCY OF RADIOFREQUENCY TUMOR ABLATION

Marija Radmilović-Radjenović

Nikola Bošković

Branislav Radjenović

Institute of Physics, University of Belgrade, Belgrade, Serbia

ABSTRACT

Radiofrequency ablation (RFA) is a minimally invasive procedure that uses electrical energy and heat to destroy cancer cells. RFA is usually considered a treatment option only if you're not a good candidate for surgery for some reason, such as your overall health or the presence of many small tumors in an organ. RFA is most commonly used to treat a spot of cancer that is causing problems such as pain or other discomfort and is generally not used as the primary treatment for most cancers. The radiologist uses imaging tests to guide a thin needle through the skin or an incision and into the cancer tissue. High-frequency energy passes through the needle and causes the surrounding tissue to heat up, killing the nearby cells. Computer modeling evolved into a very powerful tool for the determination of optimal conditions for RFA. We have developed a simulation package based on the finite element method to determine conditions enabling the efficiency of RFA. Keywords: radiofrequency ablation, necrotic tissue, three-dimensional simulation, finite element

Authors acknowledge that this research was supported by the Science Fund of the Republic of Serbia, The Program IDEAS, GRANT No. 7739583, SimSurgery.

THREE-DIMENSIONAL MODELING OF RADIOFREQUENCY ABLATION THERAPIES

Marija Radmilović-Radjenović

Nikola Bošković

Branislav Radjenović

Institute of Physics, University of Belgrade, Belgrade, Serbia

Currently, the use of RFA has been well described as a primary or adjuvant treatment modality of limited but unresectable hepatocellular carcinoma, liver metastasis, especially colorectal cancer metastases, primary lung tumors, renal cell carcinoma, bony metastasis and osteoid osteomas. The role of RFA in the primary treatment of early stage breast cancer is still evolving. A challenging problem of radiofrequency ablation (RFA) in liver surgery is to accurately estimate the shapes and sizes of RFA lesions. The aim of this paper is to use computer modeling of the Bio-Heat equation to demonstrate factors influencing RF ablation tissue heating. Computer modeling demonstrates the importance of energy deposition, tumor and background tissue electrical and thermal conductivity, and perfusion on RF ablation outcomes.

Keywords: radiofrequency ablation, tumor configuration, finite element

ON THE EFFICIENCY OF RADIOFREQUENCY TUMOR ABLATION

Marija Radmilović-Radjenović, Nikola Bošković, Branislav Radjenović
Institute of Physics, University of Belgrade, Belgrade, Serbia

Radiofrequency ablation (RFA) is a minimally invasive procedure that uses electrical energy and heat to destroy cancer cells. RFA is usually considered a treatment option only if you're not a good candidate for surgery for some reason, such as your overall health or the presence of many small tumors in an organ. RFA is most commonly used to treat a spot of cancer that is causing problems such as pain or other discomfort and is generally not used as the primary treatment for most cancers. The radiologist uses imaging tests to guide a thin needle through the skin or an incision and into the cancer tissue. High-frequency energy passes through the needle and causes the surrounding tissue to heat up, killing the nearby cells. Computer modeling evolved into a very powerful tool for the determination of optimal conditions for RFA. We have developed a simulation package based on the finite element method to determine conditions enabling the efficiency of RFA.

Keywords: radiofrequency ablation, necrotic tissue, three-dimensional simulation, finite element

Authors acknowledge that this research was supported by the Science Fund of the Republic of Serbia, The Program IDEAS, GRANT No. 7739583, SimSurgery.

THREE-DIMENSIONAL MODELING OF RADIOFREQUENCY ABLATION THERAPIES

Marija Radmilović-Radjenović,

Nikola Bošković,

Branislav Radjenović

Institute of Physics, University of Belgrade, Belgrade, Serbia

ABSTRACT

Currently, the use of RFA has been well described as a primary or adjuvant treatment modality of limited but unresectable hepatocellular carcinoma, liver metastasis, especially colorectal cancer metastases, primary lung tumors, renal cell carcinoma, bony metastasis and osteoid osteomas. The role of RFA in the primary treatment of early stage breast cancer is still evolving. A challenging problem of radiofrequency ablation (RFA) in liver surgery is to accurately estimate the shapes and sizes of RFA lesions. The aim of this paper is to use computer modeling of the Bio-Heat equation to demonstrate factors influencing RF ablation tissue heating. Computer modeling demonstrates the importance of energy deposition, tumor and background tissue electrical and thermal conductivity, and perfusion on RF ablation outcomes.

Keywords: radiofrequency ablation, tumor configuration, finite element

Authors acknowledge that this research was supported by the Science Fund of the Republic of Serbia, The Program IDEAS, GRANT No. 7739583, SimSurgery.

EFFICIACY OF MICROWAVE TUMOR ABLATION USING TWO ANTENNAS

**Nikola Bošković,
Marija Radmilović-Radjenović,
Branislav Radjenović**

Institute of Physics Belgrade, University of Belgrade, Pregrevica 118, 11080 Belgrade, Serbia

ABSTRACT

Microwave ablation is a well-established method for treating cancer, with a high survival rate and low recurrence rates. It is recommended for the treatment of small tumors in the early stages of the disease. Destruction of the tumor cells occurs as a consequence of the heating caused by the interaction of the microwave radiation with the tissue. In this article we are investigating the destruction of the real large elongated tumor taken from the database with maximum dimensions of $56.8 \text{ mm} \times 27.6 \text{ mm} \times 22.4 \text{ mm}$, using two identical parallel positioned probes with multi-slot coaxial antennas. Electromagnetic field propagation is calculated using the Finite Element Method in the frequency domain, while temperature and tissue damage distribution is calculated in the time domain. Frequency domain calculation is repeated for each time step with the updated temperature dependent material parameters. All procedures involving modeling, meshing, and calculation are done using open-source software.

Keywords: microwave ablation, two antenna configuration, finite element

Authors acknowledge that this research was supported by the Science Fund of the Republic of Serbia, The Program IDEAS, GRANT No. 7739583, SimSurgery.

PHYSICS-BASED STUDIES OF SURGICAL ELECTRODE DESIGN TO PREVENT SPARKING ENHANCED SKIN BURNS DURING ELECTROCAUTERY

Marija Radmilović-Radjenović

Institute of Physics, University of Belgrade

Branislav Radjenović

Institute of Physics, University of Belgrade

Nikola Bošković

Institute of Physics, University of Belgrade

ABSTRACT

Objectives- Proper care and handling of electrosurgical equipment are essential to patient and personnel safety. Burns that destroy layers of the patient's skin often linked to a medical mistake are largely preventable. This paper is dealing with the design of surgical electrodes as one of the *extremely* important factors for the formation of burns during standard procedures.

Methods- Simulations have been performed by using the COMSOL simulation package for various electrode configurations (cylinder-cylinder, sphere-sphere, cylinder-sphere, cylinder-cone, sphere-cone, and cone-cone) representing shapes of surgical electrodes. The primary goal was to determine the location and the voltage required for sparking.

Results- The obtained simulation results agree well with the experimental data taken from literature revealing that the sparking formation is strongly affected by the electrode configuration. Sparking occurs most easily when both electrodes are cylindrical and the most difficult when one electrode is a cone. It was also found that the sparking mechanism is not the same in both directions between the active electrode and passive metal plate due to electrical asymmetries.

Conclusions- Electrical asymmetries may lead to differences in breakdown voltage even to 40%. Since the asymmetry is the cause of undesirable direct current burns and neuromuscular electrostimulation, and the conformity process does not take into account the sparking phenomena, the certification process for this class of equipment must change. Results presented here can be used to establish practices for the safe use of the electrocautery device and to prevent injury to patients and staff.

EFFICIACY OF MULTISLOT ANTENNA IN MICROWAVE TUMOR ABLATION

Marija Radmilović-Radjenović, Nikola Bošković, Branislav Radjenović

Institute of Physics Belgrade, University of Belgrade, Pregrevica 118, 11080 Belgrade, Serbia

ABSTRACT

Microwave ablation (MWA) is a thermal ablation modality based on increasing the temperature above the normal physiological threshold to kill cancer cells with minimal damage to surrounding tissues. MWA is highly recommended for COVID-19 patients with cancers as a safe and minimally invasive therapeutic options with a short recovery time. The objective of the study was to assess the role of the antenna design in the efficacy of MWA in treating malignant tissues. For this study, the finite elements method (FEM) is used to solve coupled electromagnetic-field and heat-transfer equations, including all details of multislot antenna design and properties of healthy and tumoral tissue. Calculations were performed by using the COMSOL Multiphysics softwer package (www.comsol.com). The obtained simulation results reveal that precisely localized heating distributions and heating effectiveness can be achieved by using a multi slot antenna probe than a single slot antenna. In further improvements of the design and optimization of microwave ablation devices, a numerical model of the antenna-tissue system plays a crucial role in providing vital information on the thermal behavior of the tissue.

Keywords: finite element, multislot antenna, microwave ablation

Authors acknowledge that this research was supported by the Science Fund of the Republic of Serbia, The Program IDEAS, GRANT No. 7739583, SimSurgery.

**THE DEVELOPMENT OF A THREE-DIMENSIONAL MODEL OF
ELECTROSURGICAL PROCEDURES**

Prof. Dr. Branislav Radjenović,

Institute of Physics, University of Belgrade, Serbia

ORCID: 0000-0002-8756-1008,

Prof. Dr. Marija Radmilović-Radjenović,

Institute of Physics, University of Belgrade, Serbia

ORCID: 0000-0001-8931-859X,

Dr. Nikola Bošković,

Institute of Physics, University of Belgrade, Serbia

ORCID: 0000-0002-6316-4120,

ABSTRACT

Nowadays more than 90% of all surgical operations use electrosurgery as the preferred way to cut, coagulate, ablate, and desiccate tissue. Despite the unquestionable benefits of electrosurgery, the interaction of the electrosurgical tools with the tissue may result in tissue damage. Besides the experimental methods, computer modeling is proven to be an effective approach to improve the performance of electrosurgery. The study is aimed to create a multiphysics software package for simulation of electrosurgery, from the current flow through the tissue to the topology changes of the tissue due to thermal effects with greater physical fidelity than already implemented in existing simulators. Realistic tissue modeling involving continuum thermo-mechanics model is included. The main goal is transferring the treatment plan based on the simulation outputs into an accurate and safe electrosurgical procedure.

The primary aim of this study is a better understanding of the effect of various conditions (electrode geometry, the applied voltage, pulse waveforms, power) on the prevention of sparking between electrodes during an electrosurgical procedure. The simulation model has been developed based on a multi-component plasma fluid model. Calculations were performed for different electrode arrangements (cylinder-cylinder, sphere-sphere, and cylinder-sphere) representing the shapes of surgical electrodes. The obtained simulation results could be useful for determining which electrode configuration will more easily lead to the sparking, to prevent complications of electrocautery procedures.

Keywords: Multi-component, electrosurgery, skin burns.

This research was supported by the support of the Science Fund of the Republic of Serbia, GRANT 7739583, SimSurgery.

THREE-DIMENSIONAL MODELING OF MICROWAVE TUMOR ABLATION

Prof. Dr. Marija Radmilović-Radjenović,
Institute of Physics, University of Belgrade, Serbia
ORCID: 0000-0001-8931-859X,
Prof. Dr. Branislav Radjenović,
Institute of Physics, University of Belgrade, Serbia
ORCID: 0000-0002-8756-1008,
Dr. Nikola Bošković,
Institute of Physics, University of Belgrade, Serbia
ORCID: 0000-0002-6316-4120,

ABSTRACT

Computer modeling is confirmed to be an effective tool to improve the performance of microwave tumor ablation. Most of the existing numerical models of microwave ablation of tumors are two-dimensional axis-symmetric within the assumption of a homogeneous medium. Since tumors have no regular shapes, the development of three-dimensional predictive models of the microwave ablation procedure including all details of the targeted tissue characteristics and the antenna design is essential for further ablation studies with a promising possibility of application in the treatment planning adjusted for each patient.

Conventional microwave ablation technique for treating liver tumor typically used only a single antenna to deliver energy, resulting in relatively small ablation zones and increased risks of local tumor residual, intrahepatic recurrences, or distant metastases. It was reported that using multiple antennas enables creation of substantially larger ablation zones.

It was shown that two-antenna configurations are less invasive than the single-antenna configuration. Ablation zones created using two antennas are smaller causing less damage to the healthy tissue as compared to those created using a single antenna. Two-antenna configurations produce more uniform thermal profiles and higher peripheral tissue temperatures.

Keywords: Computer, microwave ablation, treatment plan.

This research was supported by the support of the Science Fund of the Republic of Serbia, GRANT 7739583, SimSurgery.

APPLICATION OF MULTI-COMPONENT FLUID MODEL IN STUDIES OF THE ORIGIN OF SKIN BURNS DURING ELECTROSURGICAL PROCEDURES

Prof. Dr. Branislav RADJENović

Institute of Physics, University of Belgrade, Belgrade, Serbia (Responsible Author)

ORCID ID: 0000-0002-8756-1008

Dr. Nikola BOŠKOVIĆ

Institute of Physics, University of Belgrade, Belgrade, Serbia

ORCID ID: 0000-0002-6316-4120

Prof. Dr. Marija RADMILOVIĆ-RADJENović

Institute of Physics, University of Belgrade, Belgrade, Serbia

ORCID ID: 0000-0001-8931-859X

ABSTRACT

The primary aim of this study is a better understanding of the effect of various conditions (electrode geometry, the applied voltage, pulse waveforms, power) on the prevention of sparking between electrodes during an electrosurgical procedure. The simulation model has been developed based on a multi-component plasma fluid model. Calculations were performed for different electrode arrangements (cylinder-cylinder, sphere-sphere, and cylinder-sphere) representing the shapes of surgical electrodes. The obtained simulation results could be useful for determining which electrode configuration will more easily lead to the sparking, to prevent complications of electrocautery procedures.

Keywords: Multi-component, electrosurgery, skin burns.

COMPUTATIONAL MODELING OF MICROWAVE TUMOR ABLATION**Prof. Dr. Marija RADMILOVIĆ-RADJENOVIĆ**

Institute of Physics, University of Belgrade, Belgrade, Serbia (Responsible Author)

ORCID ID: 0000-0001-8931-859X**Prof. Dr. Branislav RADJENOVIĆ**

Institute of Physics, University of Belgrade, Belgrade, Serbia

ORCID ID: 0000-0002-8756-1008**Dr. Nikola BOŠKOVIĆ**

Institute of Physics, University of Belgrade, Belgrade, Serbia

ORCID ID: 0000-0002-6316-4120,**ABSTRACT**

Computer modeling is confirmed to be an effective tool to improve the performance of microwave tumor ablation. Most of the existing numerical models of microwave ablation of tumors are two-dimensional axis-symmetric within the assumption of a homogeneous medium. Since tumors have no regular shapes, the development of three-dimensional predictive models of the microwave ablation procedure including all details of the targeted tissue characteristics and the antenna design is essential for further ablation studies with a promising possibility of application in the treatment planning adjusted for each patient.

Keywords: Computer, microwave ablation, treatment plan.

FINITE ELEMENT ANALYSIS OF MICROWAVE TUMOR ABLATION USING OPEN SOURCE SOFTWARE COMPONENTS

Nikola BOŠKOVIĆ

Institute of Physics Belgrade, University of Belgrade, Pregrevica 118, 11080 Belgrade, Serbia

Marija RADMILOVIĆ RADJENović

Institute of Physics Belgrade, University of Belgrade, Pregrevica 118, 11080 Belgrade, Serbia

Branislav RADJENović

Institute of Physics Belgrade, University of Belgrade, Pregrevica 118, 11080 Belgrade, Serbia

ABSTRACT

Microwave ablation is a procedure for treating various types of cancers during which a small needle-like probe is inserted inside the tumor, which delivers microwave energy, causes tissue heating, and effectively produces necrosis of the tumor tissue. Mathematical models of microwave ablation involve the simultaneous modeling of multiple physical phenomena that occur during the procedure, including electromagnetic wave propagation, heat transfer, and tissue damage. In this study, a complete model of a microwave ablation procedure based on open-source software components is presented. First, the comprehensive procedure of mesh creation the complete geometric arrangement of the microwave ablation, including a multi-slot coaxial antenna, a real liver tumor taken from the database, and the surrounding liver tissue are described. It is demonstrated that utilizing smart meshing procedures significantly reduces the usage of computational resources and simulation time. An accurate custom Explicit Euler time loop was designed to obtain temperature values and estimate tissue necrosis across the computational domain during the time of microwave ablation. The simulation results obtained by solving the electromagnetic field using the finite element method in the frequency domain are shown and analyzed.

Keywords: computational physics; microwave ablation; necrotic tissue; open-source software

**FINITE ELEMENT ANALYSIS OF THE EFFICIENCY OF MULTISLOT ANTENNA IN
MICROWAVE TUMOR ABLATION**

Dr. Marija RADMILOVIĆ-RADJENOVIC

Institute of Physics Belgrade, University of Belgrade, Pregrevica 118, 11080 Belgrade, Serbia

Dr. Nikola BOŠKOVIĆ

Institute of Physics Belgrade, University of Belgrade, Pregrevica 118, 11080 Belgrade, Serbia

Dr. Branislav RADJENOVIC

Institute of Physics Belgrade, University of Belgrade, Pregrevica 118, 11080 Belgrade, Serbia

Abstract

Microwave ablation is a medical procedure that uses high-frequency electromagnetic waves to create heat and destroy abnormal or cancerous tissue in the body. It is a minimally invasive alternative to surgery that is often used to treat liver, lung, kidney, and bone cancer, as well as other conditions such as benign tumors, nodules, and cysts. Microwave ablation is generally considered a safe and effective treatment option for certain types and stages of cancer. It is often performed on an outpatient basis, which means that patients can go home the same day as the procedure. However, like any medical procedure, there are some potential risks and side effects associated with microwave ablation, such as pain, bleeding, infection, and damage to nearby organs or tissues. Patients should discuss the benefits and risks of this treatment with their healthcare provider before deciding whether it is right for them. For this study, the finite elements method (FEM) is used to solve coupled electromagnetic-field and heat-transfer equations, including all details of multislot antenna design and properties of healthy and tumoral tissue. The obtained simulation results reveal that precisely localized heating distributions and heating effectiveness can be achieved by using a multi slot antenna probe than a single slot antenna.

Keywords: finite element, multislot antenna, microwave ablation

**SIMULATION OF MICROWAVE TUMOR ABLATION BASED ON MULTIPHYSICS
SOFTWARE PACKAGE**

Dr. Branislav Radjenović

Institute of Physics, University of Belgrade, Serbia

Dr. Nikola BOŠKOVIĆ

Institute of Physics, University of Belgrade, Serbia

Dr. Marija RADMILOVIĆ-RADJENOVIĆ

Institute of Physics, University of Belgrade, Serbia

Abstract

Modeling the MWA as a multiphysics problem involves the simultaneous modeling of multiple physical phenomena that occur during the procedure, including electromagnetic wave propagation, heat transfer, and tissue damage. These phenomena are interrelated, and modeling them together can provide a more accurate and comprehensive understanding of the behavior of tissue during the procedure. The first stage encompasses the accurate modeling of the microwave radiation of the antenna. The second stage involves modeling the interaction between the tissue and antenna radiation, heat transfer, blood flow effects, etc. The third stage requires estimating cell death due to heating. While the material parameters of the antenna components can generally be observed as constant during ablation, the material properties of the healthy tissue and tumor are temperature (time) dependent. Tumor shape is patient-specific, so a general approach with a spherical or static tumor model is not accurate. The water concentration in the tissue changes with increasing temperature, which effectively changes the physical properties of the tissue.

Keywords: Multiphysics, microwave ablation, tissue.

Acknowledgements. This study was supported by the Science Fund of the Republic of Serbia, The Program IDEAS, GRANT No. 7739583, SimSurgery.

**APPLICATION OF THE MULTI-COMPONENT PLASMA FLUID MODEL IN
SIMULATION OF ELECTROSURGICAL PROCEDURE**

Prof. Dr. Branislav Radjenović,

Institute of Physics, University of Belgrade, Serbia

Dr. Nikola Bošković,

Institute of Physics, University of Belgrade, Serbia

Prof. Dr. Marija Radmilović-Radjenović,

Institute of Physics, University of Belgrade, Serbia

ABSTRACT

This paper reports on safety challenges regarding sparking as a source of skin burns during electrosurgery. Some risks of complications often depend on a surgeon's knowledge of instruments and safety aspects of technical equipment. In this study, sparking-enhanced skin burns were studied based on the multi-component plasma fluid model. Calculations were performed for different electrode arrangements (cylinder-cylinder, sphere-sphere, and cylinder-sphere) representing shapes of surgical electrodes. The primary goal was to determine the location where sparking starts, as it is one of the *extremely* important factors for the formation of burns during electrosurgery. It was shown that electrode shape and dimension objectively stipulate several factors that may lead to sparking causing severe burns. Sparking occurs most easily when both electrodes are cylindrical. For configurations with one or two spherical electrodes, minimum voltages required for sparking are higher up to 25% and 48%, respectively. With the decreasing radius of the cylindrical electrode, the breakdown voltage may decrease even to 41%. Electrical asymmetries appear to be a response to the non-symmetry of the electric field between the electrodes used in electrosurgery leading to differences in breakdown voltage even to 70%. Results presented here are useful for understanding which electrode configuration will more easily lead to the sparking, to prevent complications of electrocautery procedures.

Acknowledgements. This study was supported by the Science Fund of the Republic of Serbia, The Program IDEAS, GRANT No. 7739583, SimSurgery.

Keywords: Softwer package, Finite Element Method, electrosurgery.

**MINIMALLY INVASIVE TREATMENT OF AN EARLY STAGE
HEPATOCELLULAR CARCINOMA**

Dr. Nikola Bošković,

Institute of Physics, University of Belgrade, Pregrevica 118, Belgrade, Serbia

Prof. Dr. Branislav Radjenović

Institute of Physics, University of Belgrade, Pregrevica 118, Belgrade, Serbia

Prof. Dr. Marija Radmilović-Radjenović

Institute of Physics, University of Belgrade, Pregrevica 118, Belgrade, Serbia

ABSTRACT

Microwave ablation (MWA) is a minimally invasive procedure that uses microwave energy to destroy cancerous tumors. It is typically used to treat small tumors in the liver, kidney, and lungs, as well as other parts of the body. During the procedure, a needle-like probe is inserted through the skin and guided to the tumor using imaging techniques such as ultrasound or CT scan. Once the probe is in place, microwave energy is used to heat and destroy the tumor cells. Microwave tumor ablation has several advantages over traditional cancer treatments such as surgery, chemotherapy, and radiation therapy. It is a minimally invasive procedure that can be performed on an outpatient basis, which means that patients can often go home the same day. It also has a shorter recovery time than traditional cancer treatments, and there is less pain and scarring associated with the procedure.

For this study, three-dimensional simulations were performed by using the COMSOL Multiphysics software package for MWA of real tumor taken from the 3D-IRCADb-01 Database. The obtained simulation results reveal that two-antenna configurations produce more uniform thermal profiles and higher peripheral tissue temperatures. The obtained simulation results reveal that two-antenna configurations produce more uniform thermal profiles and higher peripheral tissue temperatures.

Acknowledgements. This study was supported by the Science Fund of the Republic of Serbia, The Program IDEAS, GRANT No. 7739583, SimSurgery.

Keywords: Two-antenna configuration, microwave ablation, ablation zone, tissue

THREE DIMENSIONAL SIMULATION OF MICROWAVE TUMOR ABLATION

Marija Radmilović-Radjenović

Institute of Physics, University of Belgrade, Pregrevica 118, Belgrade, Serbia

Nikola Bošković

Institute of Physics, University of Belgrade, Pregrevica 118, Belgrade, Serbia

Branislav Radjenović

Institute of Physics, University of Belgrade, Pregrevica 118, Belgrade, Serbia

Microwave ablation is recognized as a minimally invasive, fast-recovery treatment for destroying cancer cells using the heat generated by microwave energy. Despite the unquestionable benefits of microwave ablation, the interaction of the microwave applicator with the tissue may result in localized heating and damage to the surrounding tissue. The majority of the tissue damage can be removed by clarifying the conditions for their development. In addition to experimental methods, computer modeling has proven to be an effective tool for optimizing the performance of microwave ablation. Numerical methods that enable ablation size control are required to guarantee tumor destruction and minimize damage to healthy tissues. Various values of input power and ablation time correspond to different tumor shapes ensuring the preservation of healthy tissues. Since tumors have no regular shapes, the optimal conditions can be estimated by performing full three-dimensional simulations without axial symmetrical approximation.

A critical component of MWA systems is the applicator consists of an antenna for coupling applied microwave (MW) power from a generator to the targeted tissue. For large tumors, two-antenna configurations lead to less invasive microwave ablation than using the single-antenna configuration. Ablation zones created using two antennas are smaller causing less damage to the healthy tissue as compared to those created using a single antenna. For this study, three-dimensional simulations were carried out by using the COMSOL Multiphysics software package based on finite element method for modelling one and two-antenna thermal ablation of tissue. The obtained simulation results show that a single-antenna configuration leads to larger damage to the healthy surrounding tissue. On the other hand, the two-antenna configuration provides complete ablation of the tumor with small damage to healthy tissue. In other words, ablation zones created using two antennas are smaller causing less damage to the healthy tissue as compared to those created using a single antenna.

This research was supported by the support of the Science Fund of the Republic of Serbia, GRANT 7739583, SimSurgery.

Computer Modeling of Microwave Ablation in the Thermal Treatment of Hepatocellular Carcinoma

Marija Radmilović-Radjenović, Nikola Bošković, Branislav Radjenović,
Institute of Physics, University of Belgrade, Serbia

ABSTRACT

Microwave ablation is recognized as a minimally invasive, fast-recovery treatment for destroying cancer cells using the heat generated by microwave energy. Despite the unquestionable benefits of microwave ablation, the interaction of the microwave applicator with the tissue may result in localized heating and damage to the surrounding tissue. The majority of the tissue damage can be removed by clarifying the conditions for their development. In addition to experimental methods, computer modeling has proven to be an effective tool for optimizing the performance of microwave ablation. Numerical methods that enable ablation size control are required to guarantee tumor destruction and minimize damage to healthy tissues. Various values of input power and ablation time correspond to different tumor shapes ensuring the preservation of healthy tissues. The optimal conditions can be estimated by performing full three-dimensional simulations.

A critical component of MWA systems is the applicator consists of an antenna for coupling applied microwave (MW) power from a generator to the targeted tissue. For large tumors, two-antenna configurations lead to less invasive microwave ablation than using the single-antenna configuration. Ablation zones created using two antennas are smaller causing less damage to the healthy tissue as compared to those created using a single antenna. For this study, three-dimensional simulations were carried out by using the COMSOL Multiphysics software package based on finite element method for modelling one and two-antenna thermal ablation of tissue. The obtained simulation results reveal that two-antenna configurations produce more uniform thermal profiles and higher peripheral tissue temperatures.

Keywords: Microwave ablation, ablation zone, tumoral tissue.

FINITE ELEMENT MODELING OF MICROWAVE TISSUE ABLATION

Marija Radmilović-Radjenović

Institute of Physics, University of Belgrade, Serbia

Nikola Bošković

Institute of Physics, University of Belgrade, Serbia

Branislav Radjenović

Institute of Physics, University of Belgrade, Serbia

Microwave ablation (MWA) is recognized as a minimally invasive, fast-recovery treatment for destroying cancer cells using the heat generated by microwave energy. Despite the unquestionable benefits of microwave ablation, the interaction of the microwave applicator with the tissue may result in localized heating and damage to the surrounding tissue. The majority of the tissue damages can be removed by clarifying the conditions for their development. In addition to experimental methods, computer modeling has proven to be an effective tool for optimizing the performance of microwave ablation. Furthermore, because the thermal spread in biological tissue is difficult to measure, developing a predictive model from procedural planning to execution may have a substantial influence on patient care. MWA system is composed of high-power MW sources, ablation applicators for delivering power from the generator to the target tissue, cooling systems, energy-delivery control algorithms, and imaging guidance systems. A critical component of MWA systems is the applicator consists of an antenna for coupling applied microwave (MW) power from a generator to the targeted tissue. It was shown that two-antenna configurations lead to less invasive microwave ablation than using the single-antenna configuration. Ablation zones created using two antennas are smaller causing less damage to the healthy tissue as compared to those created using a single antenna. For this study, three-dimensional simulations were carried out by using the COMSOL Multiphysics software package based on finite element method for modelling two-antenna thermal ablation of tissue. The obtained simulation results reveal that two-antenna configurations produce more uniform thermal profiles and higher peripheral tissue temperatures.

Keywords: Two-antenna configuration, microwave ablation, ablation zone, tissue

Acknowledgements. This study was supported by the Science Fund of the Republic of Serbia, The Program IDEAS, GRANT No. 7739583, SimSurgery.

**DEVELOPMENT OF THREE-DIMENSIONAL MULTIPHYSICS SOFTWARE
PACKAGE FOR SIMULATION OF ELECTROSURGICAL PROCEDURE**

Prof. Dr. Branislav RADJENOVIC

Institute of Physics, University of Belgrade, Serbia

Dr. Nikola BOŠKOVIĆ

Institute of Physics, University of Belgrade, Serbia

Prof. Dr. Marija RADMILOVIĆ-Radjenović

Institute of Physics, University of Belgrade, Serbia

ABSTRACT

Nowadays more than 90% of all surgical operations use electrosurgery as the preferred way to cut, coagulate, ablate, and desiccate tissue. Despite the unquestionable benefits of electrosurgery, the interaction of the electrosurgical tools with the tissue may result in tissue damage. Besides the experimental methods, computer modeling is proven to be an effective approach to improve the performance of electrosurgery. The study is aimed to create a multiphysics software package for simulation of electrosurgery, from the current flow through the tissue to the topology changes of the tissue due to thermal effects with greater physical fidelity than already implemented in existing simulators. Realistic tissue modeling involving continuum thermo-mechanics model is included. The main goal is transferring the treatment plan based on the simulation outputs into an accurate and safe electrosurgical procedure.

Keywords: Softwer package, Finite Element Method, electrosurgery

Acknowledgements. This study was supported by the Science Fund of the Republic of Serbia, The Program IDEAS, GRANT No. 7739583, SimSurgery.

THREE-DIMENSIONAL SIMULATIONS OF MICROWAVE TISSUE ABLATION

Prof. Dr. Marija RADMILOVIĆ-Radjenović
Institute of Physics, University of Belgrade, Serbia

Prof. Dr. Branislav RADJENOVIC
Institute of Physics, University of Belgrade, Serbia

Dr. Nikola BOŠKOVIĆ
Institute of Physics, University of Belgrade, Serbia

ABSTRACT

Microwave ablation (MWA) is recognized as a powerful thermal modality for minimally invasive treatment of tumoral tissue and cardiac arrhythmias, neuromodulation, endometrial ablation, and other applications. MWA system is composed of high-power MW sources, ablation applicators for delivering power from the generator to the target tissue, cooling systems, energy-delivery control algorithms, and imaging guidance systems. A critical component of MWA systems is the applicator consists of an antenna for coupling applied microwave (MW) power from a generator to the targeted tissue. It was shown that two-antenna configurations lead to less invasive microwave ablation than using the single-antenna configuration. Ablation zones created using two antennas are smaller causing less damage to the healthy tissue as compared to those created using a single antenna. For this study, three-dimensional simulations were carried out by using the COMSOL Multiphysics software package for two-antenna thermal ablation of tissue. The obtained simulation results reveal that two-antenna configurations produce more uniform thermal profiles and higher peripheral tissue temperatures.

Keywords: Two-antenna configuration, microwave ablation, ablation zone, tissue

Acknowledgements. This study was supported by the Science Fund of the Republic of Serbia, The Program IDEAS, GRANT No. 7739583, SimSurgery.

APPLICATION OF TWO-ANTENNA CONFIGURATIONS FOR MICROWAVE TISSUE ABLATION

Marija RADMILOVIĆ-RADJENović

Branislav RADJENović

Nikola BOŠKOVIĆ

Institute of Physics, University of Belgrade, Serbia

ABSTRACT

Microwave ablation (MWA) emerges as a powerful thermal modality for minimally invasive treatment of unresectable tumors and cardiac arrhythmias, neuromodulation, endometrial ablation, and other applications. MWA system is composed of high-power MW sources, ablation applicators for delivering power from the generator to the target tissue, cooling systems, energy-delivery control algorithms, and imaging guidance systems. A critical component of MWA systems is the applicator consists of an antenna for coupling applied microwave (MW) power from a generator to the targeted tissue. It was shown that two-antenna configurations lead to less invasive microwave ablation than using the single-antenna configuration. Ablation zones created using two antennas are smaller causing less damage to the healthy tissue as compared to those created using a single antenna. For this study, three-dimensional simulations were carried out by using the COMSOL Multiphysics software package for two-antenna thermal ablation of tissue. The obtained simulation results reveal that two-antenna configurations produce more uniform thermal profiles and higher peripheral tissue temperatures.

Keywords: Two-antenna configuration, microwave ablation, ablation zone, tissue

Acknowledgements. This study was supported by the Science Fund of the Republic of Serbia, The Program IDEAS, GRANT No. 7739583, SimSurgery.



DEVELOPMENT OF MULTIPHYSICS SOFTWARE PACKAGE FOR SIMULATION OF ELECTROSURGERY PROCEDURE

Branislav RADJENović

Nikola BOŠKOVIĆ

Marija RADMILOVIĆ-RADJENović

Institute of Physics, University of Belgrade, Serbia

ABSTRACT

Nowadays more than 90% of all surgical operations use electrosurgery as the preferred way to cut, coagulate, ablate, and desiccate tissue. Despite the unquestionable benefits of electrosurgery, the interaction of the electrosurgical tools with the tissue may result in tissue damage. Besides the experimental methods, computer modeling is proven to be an effective approach to improve the performance of electrosurgery. The study is aimed to create a multiphysics software package for simulation of electrosurgery, from the current flow through the tissue to the topology changes of the tissue due to thermal effects with greater physical fidelity than already implemented in existing simulators. Realistic tissue modeling involving continuum thermo-mechanics model is included. The main goal is transferring the treatment plan based on the simulation outputs into an accurate and safe electrosurgical procedure.

Keywords: Softwer package, Finite Element Method, electrosurgery.

Acknowledgements. This study was supported by the Science Fund of the Republic of Serbia, The Program IDEAS, GRANT No. 7739583, SimSurgery.

APPLICATION OF TWO-ANTENNA CONFIGURATIONS FOR MICROWAVE TISSUE ABLATION

Prof. Dr. Marija Radmilović-Radjenović

Institute of Physics, University of Belgrade, Serbia

Dr. Nikola Bošković

Institute of Physics, University of Belgrade, Serbia

Prof. Dr. Branislav Radjenović

Institute of Physics, University of Belgrade, Serbia

ABSTRACT

Microwave ablation (MWA) emerges as a powerful thermal modality for minimally invasive treatment of unresectable tumors and cardiac arrhythmias, neuromodulation, endometrial ablation, and other applications. MWA system is composed of high-power MW sources, ablation applicators for delivering power from the generator to the target tissue, cooling systems, energy-delivery control algorithms, and imaging guidance systems. A critical component of MWA systems is the applicator consists of an antenna for coupling applied microwave (MW) power from a generator to the targeted tissue. It was shown that two-antenna configurations lead to less invasive microwave ablation than using the single-antenna configuration. Ablation zones created using two antennas are smaller causing less damage to the healthy tissue as compared to those created using a single antenna. For this study, three-dimensional simulations were carried out by using the COMSOL Multiphysics software package for two-antenna thermal ablation of tissue. The obtained simulation results reveal that two-antenna configurations produce more uniform thermal profiles and higher peripheral tissue temperatures.

Keywords: Two-antenna configuration, microwave ablation, ablation zone, tissue

Acknowledgements. This study was supported by the Science Fund of the Republic of Serbia, The Program IDEAS, GRANT No. 7739583, SimSurgery.

FINITE ELEMENT ANALYSIS OF EFFICIENCY OF TWO-ANTENNA CONFIGURATION FOR MICROWAVE TISSUE ABLATION

Branislav Radjenović, Nikola Bošković and Marija Radmilović-Radjenović

Institute of Physics, University of Belgrade, Serbia

ABSTRACT

Microwave ablation (MWA) emerges as a powerful thermal modality for minimally invasive treatment of unresectable tumors and cardiac arrhythmias, neuromodulation, endometrial ablation, and other applications. MWA system is composed of high-power MW sources, ablation applicators for delivering power from the generator to the target tissue, cooling systems, energy-delivery control algorithms, and imaging guidance systems. A critical component of MWA systems is the applicator consists of an antenna for coupling applied microwave (MW) power from a generator to the targeted tissue. It was shown that two-antenna configurations lead to less invasive microwave ablation than using the single-antenna configuration. Ablation zones created using two antennas are smaller causing less damage to the healthy tissue as compared to those created using a single antenna. For this study, three-dimensional simulations were carried out by using the COMSOL Multiphysics software package for two-antenna thermal ablation of tissue. The obtained simulation results reveal that two-antenna configurations produce more uniform thermal profiles and higher peripheral tissue temperatures..

Keywords: Two-antenna configuration, microwave ablation, ablation zone, tissue

Acknowledgements. The authors acknowledge that this research was supported by the Science Fund of the Republic of Serbia, The Program IDEAS, GRANT No. 7739583, SimSurgery.

COMPARISON BETWEEN SINGLE-SLOT AND TWO-ANTENNA CONFIGURATION FOR MICROWAVE TISSUE ABLATION

Nikolal Boskovic, Marija Ivanovic, and Branislav Radjenovic

Institute of Physics, University of Belgrade, Serbia

ABSTRACT

Conventional microwave ablation technique for treating liver tumor typically used only a single antenna to deliver energy, resulting in relatively small ablation zones and increased risks of local tumor residual, intrahepatic recurrences, or distant metastases. It was reported that using multiple antennas enables creation of substantially larger ablation zones. For this study, three-dimensional simulations were performed by using the COMSOL Multiphysics software package for single-slot and two-antenna thermal ablation of tissue. Three-dimensional simulation results reveal that two-antenna configurations are less invasive than the single-antenna configuration. Ablation zones created using two antennas are smaller causing less damages to the healthy tissue as compared to those created using a single antenna. Two-antenna configurations produce more uniform thermal profiles and higher peripheral tissue temperatures.

Authors M.R.-R., N.B. and B.R. acknowledge that this research was supported by the Science Fund of the Republic of Serbia, The Program IDEAS, GRANT No. 7739583, SimSurgery.



8th INTERNATIONAL ZEUGMA CONFERENCE ON SCIENTIFIC RESEARCH



THREE-DIMENSIONAL SIMULATIONS OF THE MICROWAVE ABLATION OF LIVER TUMORS FROM THE 3DIRCADb-01 DATABASE

Marija Radmilović-Radjenović, Nikola Bošković, Marija Ivanović, and Branislav Radjenović

Institute of Physics Belgrade, University of Belgrade, Pregrevica 118, 11080 Belgrade, Serbia

Abstract

Microwave ablation (MWA) is a minimally invasive thermal ablation modality based on increasing the temperature above the normal physiological threshold to kill cancer cells with minimal damage to surrounding. Simulation techniques are powerful tools for determining the optimal conditions necessary for microwave ablation to be efficient and safe for treating liver tumors. Owing to the complexity and computational resource consumption, most of the existing numerical models are two-dimensional axisymmetric models that emulate actual three-dimensional cancers and the surrounding tissue, which is often far from reality. Different tumor shapes and sizes require different input powers and ablation times to ensure the preservation of healthy tissues that can be determined only by the full three-dimensional simulations. This study aimed to tailor microwave ablation therapeutic conditions for complete tumor ablation with an adequate safety margin, while avoiding injury to the surrounding healthy tissue. Three-dimensional simulations were performed for a multi-slot microwave antenna immersed in two tumors obtained from the 3D-IRCADb-01 liver tumors database. For this purpose, three-dimensional simulation model is developed and tested within COMSOL Multiphysics software package (www.comsol.com). The finite elements method (FEM) is used to solve coupled electromagnetic-field and heat-transfer equations, including all details of a 10-slot antenna design and properties of healthy and tumoral tissue. The obtained simulation results reveal that proper determination of the optimal input power and ablation time ratio may lead to precisely localized heating distributions and formation of the optimal ablation zones. In further improvements of the design and optimization of microwave ablation devices and microwave ablation procedure, a numerical methods may play a pivotal role in providing vital information on the thermal behavior of the tissue. The developed three-dimensional predictive model of the microwave ablation procedure with all details of the tissue antenna design is a prerequisite, not only for further ablation studies but also for planning the MWA procedure for each patient individually.

Authors M.R.-R., N.B. and B.R. acknowledge that this research was supported by the Science Fund of the Republic of Serbia, The Program IDEAS, GRANT No. 7739583, SimSurgery.

THREE-DIMENSIONAL SIMULATIONS OF THE MICROWAVE TISSUE ABLATION

Marija Radmilović-Radjenović
Nikola Bošković
Marija Ivanović
Branislav Radjenović

Institute of Physics Belgrade, University of Belgrade, Pregrevica 118, 11080 Belgrade, Serbia

ABSTRACT

Microwave ablation (MWA) is a minimally invasive thermal ablation modality based on increasing the temperature above the normal physiological threshold to kill cancer cells with minimal damage to surrounding. The objective of the study is to assess the role of the optimal conditions in the efficacy of MWA in treating malignant tissues. For this purpose, three-dimensional simulation model is developed and tested within COMSOL Multiphysics software package (www.comsol.com). The finite elements method (FEM) is used to solve coupled electromagnetic-field and heat-transfer equations, including all details of a 10-slot antenna design and properties of healthy and tumoral tissue. The obtained simulation results reveal that proper determination of the optimal input power and ablation time ratio may lead to precisely localized heating distributions and formation of the optimal ablation zones. In further improvements of the design and optimization of microwave ablation devices and microwave ablation procedure, a numerical method may play a pivotal role in providing vital information on the thermal behavior of the tissue.

Keywords: three-dimensional simulation, microwave ablation, multislot antenna

This research was supported by the Institute of Physics Belgrade, through the grant by the Ministry of Education, Science and Technological Development of the Republic of Serbia. M.R.-R., N.B. and B.R. acknowledge the support of the Science Fund of the Republic of Serbia, GRANT 7739583, SimSurgery.

**SIMULATION STUDIES OF THE EFFECT OF THE INPUT POWER ON THE
PERFORMANCE OF MICROWAVE TISSUE ABLATION**

Prof.Dr. Marija Radmilović-Radjenović

Institute of Physics, University of Belgrade, Serbia

ORCID NO: 0000-0001-8931-859X

Marija Ivanović

Institute of Physics, University of Belgrade, Serbia

Dr. Nikola Bošković

Institute of Physics, University of Belgrade, Serbia

ORCID NO: 0000-0002-6316-4120

Prof. Dr. Branislav Radjenović

Özyeğin Üniversitesi, Mimarlık ve Tasarım Fakültesi

ORCID NO: 0000-0002-8756-1008

Abstract

Microwave ablation (MWA) is a promising modality for treating cancerous tumor cells in patients who are non-surgical candidates. MWA system is composed of high-power MW sources, ablation applicators for delivering power from the generator to the target tissue, cooling systems, energy-delivery control algorithms, and imaging guidance systems. A critical component of MWA systems is the applicator consists of an antenna for coupling applied microwave (MW) power from a generator to the targeted tissue.

When the tissue is exposed to the microwave field, the energy from the field is absorbed by the tissue, leading to the heating of the cancer cells. Antenna radiates energy throughout the biological tissue, and this energy is converted into heat that invades the tissues. The absorbed power density is extremely high close to the antenna and decreases with distance. The absorbed energy converted into thermal energy causes an increase in the tissue temperature. As the distance from the antenna increases, the heat source becomes weaker, so the blood can maintain the tissue at a normal body temperature. It appears that the perfusion of blood limits the extent of the heated area. Many factors such as antenna design and the input power affect the formation of ablation zones.

For this study, calculations were performed by using the COMSOL Multiphysics software package (www.comsol.com) to investigate how the input power affects the tumoral tissue. Besides axial-symmetric, calculations were also carried out by using full three-dimensional (3D) model for real Hepatocellular carcinoma (HCC) listed in the 3D-IRCADb-01 liver tumors database. The obtained simulation results reveal that the input power plays a significant role during MWA and determination of its proper value depending on the tumoral shape may provide creation of optimal ablation zones and thus leading to minimal damages of healthy tissues.

Keywords: Microwave ablation, tissue, ablation zone

FINITE ELEMENT ANALYSIS OF THE EFFICIENCY OF MULTISLOT ANTENNA IN MICROWAVE TISSUE ABLATION

Marija Radmilović-Radjenović

Institute of Physics Belgrade, University of Belgrade

Marija Radmilović-Radjenović

Institute of Physics Belgrade, University of Belgrade

Nikola Bošković

Institute of Physics Belgrade, University of Belgrade

Marija Ivanović

Institute of Physics Belgrade, University of Belgrade

Branislav Radjenović

Institute of Physics Belgrade, University of Belgrade

Objectiv- Microwave ablation (MWA) is a thermal ablation modality based on increasing the temperature above the normal physiological threshold to kill cancer cells with minimal damage to surrounding tissues. MWA is highly recommended for COVID-19 patients with cancers as a safe and minimally invasive therapeutic options with a short recovery time. The objective of the study was to assess the role of the antenna design in the efficacy of MWA in treating malignant tissues. **Method-** For this study, the finite elements method (FEM) is used to solve coupled electromagnetic-field and heat-transfer equations, including all details of multislot antenna design and properties of healthy and tumoral tissue. Calculations were performed by using the COMSOL Multiphysics software package (www.comsol.com).

Results- The obtained simulation results reveal that precisely localized heating distributions and heating effectiveness can be achieved by using a multi slot antenna probe than a single slot antenna.

Conclusions- In further improvements of the design and optimization of microwave ablation devices, a numerical model of the antenna-tissue system plays a crucial role in providing vital information on the thermal behavior of the tissue.

Keywords: finite element, multislot antenna, microwave ablation

4th INTERNATIONAL CONGRESS
OF MULTIDISCIPLINARY STUDIES
IN MEDICAL SCIENCES

18-20 February 2022/Antalya – Turkey

COMPUTATIONAL STUDIES OF ANTENNA DESIGNS FOR MICROWAVE TISSUE ABLATION

Marija RADMILOVIĆ-RADJENOVIĆ

*Prof. Dr., Institute of Physics, University of Belgrade, Serbia
ORCID NO: 0000-0001-8931-859X*

Nikola BOŠKOVIĆ

*Dr., Institute of Physics, University of Belgrade, Serbia
ORCID NO: 0000-0002-6316-4120*

Branislav RADJENOVIĆ

*Prof. Dr., Institute of Physics, University of Belgrade, Serbia
ORCID NO: 0000-0002-8756-1008*

ABSTRACT

Microwave ablation (MWA) is recognized as a powerful thermal modality for minimally invasive treatment of unresectable tumors and cardiac arrhythmias, neuromodulation, endometrial ablation, and other applications. MWA system is composed of high-power MW sources, ablation applicators for delivering power from the generator to the target tissue, cooling systems, energy-delivery control algorithms, and imaging guidance systems. A critical component of MWA systems is the applicator consists of an antenna for coupling applied microwave (MW) power from a generator to the targeted tissue.

Significant efforts were made to suppress the backward current on the surface of the coaxial cable outer conductor by adding chokes and sleeves and to keep the electric fields concentrated around the antenna tip. It also can be achieved by creating a better coupling between the antenna and the surrounding tissue by loading the antenna with a dielectric material with electrical permittivity closer to that of the tissue. A variety of antenna designs have been developed for MWA to transfer MW power to the tissue efficiently. The selection of the appropriate antenna designs provide well match between the yield electric field radiation patterns and the targeted tissue.

For this study, calculations were performed by using the COMSOL Multiphysics software package (www.comsol.com) for various antennas designed for site-specific thermal ablation of tissue. The obtained simulation results reveal that antenna designs strongly affect the pattern of the radiated electric fields. It is desirable to select antenna geometries that yield electric field radiation patterns that are well matched to the tissue regions targeted for ablation. The use of active cooling minimizes unintended heating along the feeding transmission line and antenna chokes/ sleeves and adjusts the length of ablation zones.

Keywords: Antenna design, Microwave ablation, Ablation zone, Tissue

Acknowledgements. This research was supported by the Science Fund of the Republic of Serbia, GRANT 7739583, SimSurgery.